Breathing Stones:

Developing laser-based spectroscopic methods to study moisture transport by historic limestone



Dáire Elaine Browne
St. Cross College
University of Oxford

A thesis submitted for the degree of
Doctor of Philosophy

Hilary Term 2023

Breathing Stones: Developing laser-based spectroscopic methods to study moisture transport by historic limestone

Dáire Elaine Browne

St. Cross College
University of Oxford

A thesis submitted for the degree of
Doctor of Philosophy

Hilary Term 2023

Abstract

The deterioration of porous building materials occurs *via* physical, chemical and biological decay processes which are facilitated by the presence of water. Current methods of measuring moisture content in building stones have inherent limitations, with many requiring laboratory calibration and providing only limited spatial and temporal resolution, thus offering minimal insight into the water transport kinetics. The aim of this thesis is to develop and apply a laser-based spectroscopic technique as a novel method to measure the moisture dynamics of porous building stones, in order to enhance understanding of durability and assess the efficacy of conservation treatments for limestone deterioration. In particular, this work applies the highly sensitive and selective technique of cavity ring-down spectroscopy (CRDS) to measure the release of water and its artificially enriched isotopologues from a selection of commonly used building limestones, with a focus on those used in the historic centre of Oxford, and for comparison, a sandstone.

This thesis begins with an overview of the deterioration processes and conservation treatments of porous building stones, with particular focus on limestone and the application of $Ca(OH)_2$ nanoparticles, known as nanolimes. Following this, a review of the current methods of measuring and monitoring moisture content, considering their advantages and disadvantages, is presented. In order to achieve the research aim, an understanding of the material and the technique is required, and thus, the fundamental theory of gas and liquid transport within porous media, and that of laser absorption spectroscopy and optical techniques is detailed. The development of the near-infrared cavity ring-down spectrometer and the prerequisite measurements required are also described.

The application of the developed instrument to the research aim is presented in the form of three peer-reviewed publications. The first paper describes the first measurements of moisture content and flux from limestone samples using CRDS, with the determined drying kinetics consistent with the well-established two-phase drying behaviour exhibited by porous media. The CRDS measurements are benchmarked

against the traditional method of gravimetric analysis, and the spectroscopic mass determined is in excellent agreement with the gravimetric mass. The selectivity and sensitivity of the CRDS instrument is then shown in measurements of isotopically labelled water, and the drying kinetics are shown to be self-consistent when monitoring HDO and H_2O. Following this, the flux of isotopically labelled water is measured under varying relative humidities, and a departure from the distinct two-phase drying behaviour with increasing humidity is observed.

Building on this work, the second paper investigates the drying behaviour of five commonly used building limestones, and a sandstone for comparison. The relationship between the pore size distribution and the drying kinetics is investigated, and while an increase in the phase I drying time is observed with increasing porosity, no clear link with the phase II behaviour is determined. Further investigations into the relationship between the drying kinetics and environmental conditions is achieved through measurements under varying temperatures. An activation energy associated with phase II drying behaviour is determined for a subset of the stones investigated and is found to be comparable with others reported in the literature.

Finally, while the effectiveness and compatibility of conservation treatments has been assessed, a surprisingly small number of studies have investigated their impact on the water transport kinetics. The final paper presents a first investigation into the effect of an ethanol dispersed nanolime on the drying kinetics of a limestone sample, conducted at a variety of temperatures. The presence of nanolime is confirmed in the samples through an increase in the dry mass, observable colour change and decrease in surface roughness following treatment. No changes in the total mass of water released, the phase I drying time or the phase II behaviour are measured, however, small but reproducible increases in the phase I evaporation flux are observed following treatment. The phase II activation energy also remains unchanged, indicating that there is little-to-no change in the internal surfaces.

This thesis presents proof-of-principle, laboratory-based measurements of water transport kinetics in porous building materials using the highly sensitive, selective and quantitative technique of cavity ring-down spectroscopy. The high temporal resolution and versatility of the instrument having thus been demonstrated under varying environmental conditions, this thesis provides the groundwork for future studies concerning water transport kinetics, other degrading species of interest such as pollutants, and conservation treatments.

Acknowledgements

First and foremost, I wish to thank Grant and Heather for their guidance, support and willingness to venture into this strange and unknown interdisciplinary field with me. Thank you both for all the time and effort over the years, and for providing endless encouragement and inspiration which enabled so much of my progress. I am forever grateful to Rob for his enormous contribution to my studies, without whom the completion of this work would not have been possible (nor half as enjoyable). Thank you for always having your door open and letting me take over one of your office chairs for lengthy discussions which would meander through ideas, results, and occasionally into whatever unrelated topics came into our minds.

My time in the Ritchie Group has been incredible and it is due to the wonderful people I have worked with over the years, all of whom have always been willing to help and provide endless support (and delicious treats). A big thank you to Nick for being a fantastic office mate all these years, for always being a listening ear and providing excellent advice, and for reminding me to take breaks and enjoy the lunchtime lap; to Sam for being my Part II/DPhil buddy with endless knowledge and enthusiasm for everything, and for making everyday in the office so much more enjoyable; to Lorenzo for being incredibly kind, patient and funny, and for always checking in to see how I was; to Graham for his fantastic one-liners which always made me smile, for always knowing the answer and where to find something in the lab, and for all the LabVIEW help; to John for his incredible wealth of knowledge and always being willing to explain, and for providing invaluable design help; to Gus for all his wisdom and fantastic stories over the years; to Dom for all the great laps and conversations, and for always being good craic; and to Charlie for always being supportive and making me laugh, and for all the times we would sit and share stories and photos of adorable nephews. Thank you to everyone else in the group who I have spent such a wonderful time with, including Katherine, An, Hamza, Robin, Eleanor, Alex, Evan, Scott, Tom, and so many others! I am also incredibly grateful to all those who work behind the scenes in the PTCL and in the workshops, especially Paul, Andy, Kevin, Sue and Mary.

I would like to thank all those in OxRBL for accepting a physical chemist into

their midst and helping me find my feet in this new area. In particular, I wish to thank Hong for all her help in preparing samples and explaining how to use all the different equipment. This research was made possible due to funding provided by the EPSRC through the Centre for Doctoral Training for Science and Engineering for Arts, Heritage and Archaeology, and I am extremely grateful for all the opportunities and people this has introduced me to. Thank you also to Dr. Robert Jacobs in the Surface Analysis Facility for performing the nitrogen adsorption measurements, the British Geological Survey for performing the mercury intrusion porosimetry measurements, and Dr. Jorge Otero for his advice regarding the application of consolidants.

During my GCSEs and A-Levels, I was incredibly lucky to be tutored by Dr. Sean Fee, and while this DPhil is definitely the result of many people who helped me along the way, the initial spark and interest in chemistry is entirely due to him. Without his incredible teaching, endless support and sarcasm, I never would have thought of studying chemistry at university, never mind staying on for more, and I will forever be grateful to him.

Finally, and most importantly, I would like to thank all my friends and family who have supported me over the years. While I have been away from home, I have been incredibly lucky to have fantastic friends who were willing to meet up and make memories I will forever cherish. Above all, the support and love of my family, especially my parents, has made this journey possible and ensured that I reached the end. Thank you for always being there when I call, encouraging me to ask questions, helping me pick up the pieces when things haven't completely worked out, and teaching me that anything is possible if you try.

List of publications

- **Determining water transport kinetics in limestone by dual-wavelength cavity ring-down spectroscopy**
  Dáire E. Browne, Robert Peverall, Grant A. D. Ritchie and Heather A. Viles
  Analytical Chemistry, **2022**, *94*, 3126 – 3134

- **Direct monitoring of drying kinetics of building limestones using cavity ring-down spectroscopy**
  Dáire E. Browne, Robert Peverall, Grant A. D. Ritchie and Heather A. Viles
  Construction and Building Materials, **2023**, *369*, 130554

- **Investigating the effect of nanolime treatment on the drying kinetics of Clipsham limestone**
  Dáire E. Browne, Robert Peverall, Grant A. D. Ritchie and Heather A. Viles
  Heritage Science, **2023**, *11*, 114

Contents

Abstract i

Acknowledgements iii

List of publications v

1 Introduction 1

1.1 Motivation for the research 1

1.2 Protecting and consolidating limestone 6

1.3 Methods of monitoring moisture 13

1.3.1 Destructive techniques 13

1.3.2 Probe-based methods 16

1.3.3 Infrared thermography 17

1.3.4 Electrical based methods 18

1.3.5 Time domain reflectometry 21

1.3.6 Microwave meters 23

1.3.7 Optical fibre sensors 24

1.3.8 Neutron radiography 26

1.3.9 Nuclear magnetic resonance 27

1.4 Aims and objectives 29

2 Gas and liquid transport in porous media 31

2.1 General description of gas and liquid transport 31

2.1.1 Liquid flow 31

2.1.2 Gas transport 34

2.1.3 Thermodynamics of water 35

2.2 Two-phase drying 42

2.3 The pore size distribution 52

2.3.1 Important parameters for describing porosity 53

2.3.2 Methods for probing the pore network 54
2.4 Conclusions 68

3 Development of an atmospheric pressure cavity ring-down spectrometer 71
3.1 Laser absorption spectroscopy 71
3.1.1 Beer–Lambert Law 73
3.1.2 The width and shape of spectral lines 74
3.2 Properties of optical cavities 78
3.3 Theory of cavity ring-down spectroscopy 82
3.4 Instrument development 83
3.4.1 Sample measurement and its relation to mass flux 88
3.4.2 Control and acquisition 90
3.5 Initial characterisations and measurements of water 93
3.5.1 Spectroscopy of water 93
3.5.2 Pressure broadening of H_2O transitions in N_2 94
3.5.3 Investigating the water continuum 96
3.5.4 Determination of % relative humidity 97
3.5.5 Measuring isotopically labelled species 99
3.6 Conclusions 101

4 Determining water transport kinetics in limestone by dual-wavelength cavity ring-down spectroscopy 103
4.1 Introduction 104
4.2 Materials and methods 106
4.2.1 Cavity ring-down spectroscopy 106
4.2.2 Stone samples: Clipsham limestone 109
4.2.3 Experimental procedure 110
4.3 Results and discussion 110
4.3.1 Drying kinetics under dry flows 110
4.3.2 Isotope detection for moisture flux determination 116
4.4 Conclusions 121

5 Direct monitoring of drying kinetics of building limestones using cavity ring-down spectroscopy 123
5.1 Introduction 124
5.2 Materials and methods 126

5.2.1 Cavity ring-down spectroscopy . . . 126
5.2.2 Stone samples . . . 128
5.2.3 Experiment procedure . . . 132
5.3 Analysis . . . 133
5.4 Results and discussion . . . 134
5.4.1 Stone comparison data . . . 134
5.4.2 Temperature dependence . . . 138
5.5 Conclusions . . . 143

6 Investigating the effect of nanolime treatment on the drying kinetics of Clipsham limestone 145
6.1 Introduction . . . 146
6.2 Materials and methods . . . 148
6.2.1 Stone type: Clipsham limestone . . . 148
6.2.2 Consolidant and application procedure . . . 149
6.2.3 Characterisation of consolidants and their impacts . . . 150
6.2.4 Cavity ring-down spectroscopy . . . 151
6.3 Analysis of the drying kinetics . . . 154
6.4 Results and discussion . . . 156
6.4.1 Characterisation of consolidation . . . 156
6.4.2 Sample variation and reproducibility of the drying kinetics . . . 160
6.4.3 Temperature dependence of the drying kinetics . . . 163
6.5 Conclusions . . . 165

7 Discussion, conclusions and future work 167
7.1 Discussion and conclusions . . . 167
7.2 Future work . . . 171

Bibliography 175

A Supplementary Information – Gas and liquid transport in porous media 205
A.1 Derivation of the Langmuir isotherm . . . 205
A.2 Mercury intrusion porosimetry measurements . . . 207
A.3 Nitrogen adsorption measurements . . . 207

B Supplementary Information – Determining water transport kinetics in limestone by dual-wavelength cavity ring-down spectroscopy **209**

B.1 Stone samples: Clipsham limestone 209

B.2 Spectroscopic nomenclature 209

B.3 Wavelength calibration 210

B.4 Reproducibility 210

B.5 Phase II diffusivity and % relative humidity 212

C Supplementary Information – Investigating the effect of nanolime treatment on the drying kinetics of Clipsham limestone **213**

C.1 Scanning electron microscopy results 213

C.2 Sample variation and reproducibility of the drying kinetics 213

C.3 Temperature dependence of the drying kinetics 215

D Statements of authorship for multi-authored papers **217**

The world lives between those who say it cannot be done and those who say it can. And in my experience, those who say that it can be done are usually telling the truth. It's just a matter of thinking creatively.

— Sir Terry Pratchett

Chapter 1

Introduction

1.1 Motivation for the research

Since the desire first arose for humankind to construct buildings, monuments and memorials and to preserve culture for future generations, the use of stone materials has been a prominent choice[1–3]. The appeal of natural stone is its perceived durability, the impression that it is a material that will withstand the test of time, and for a lay observer, this belief is perpetuated with the survival of many historic cities and the world's cultural heritage sites. All natural stones, however, are affected by weathering, and upon being quarried, cut and utilised for construction, their susceptibility increases due to the influence of additional anthropogenic factors[4]. Thus, this impression of longevity neglects to account for those structures which did not survive, and for earlier conservation efforts of stone replacement and the dressing back of historic buildings[5].

The weathering of natural stones, whether in a building or natural outcrop, is a complex process which is dependent on the specific material and the environment, and occurs due to physical, chemical and biological processes[4,6]. Physical weathering is caused by freeze–thaw mechanisms[7], salt weathering[8], and thermal, hygric and wet–dry cycling[9]. For example, freeze–thaw mechanisms cause mechanical damage *via* ice segregation, in which ice lenses are formed by the accumulation of moisture in a small pores or existing cracks, and in favourable conditions, the ice lenses undergo progressive growth and wedge the stone material apart[7,9]. Chemical weathering encompasses reactions of the chemical components of the geomaterial with atmospheric

constituents, such as water (H_2O), oxygen (O_2), carbon dioxide (CO_2) and pollutants such as sulfur dioxide (SO_2) and nitrogen dioxide (NO_2)[4,10], resulting in chemical change, followed by disintegration. Biodeterioration of natural stones occurs due to the biological activity of cyanobacteria, microalgae, lichens and fungi[9]. The subsequent formation of these biofilms can result in the trapping of moisture within the stone, leading to further weathering processes[11]. A necessary environmental component for all three weathering processes, or at least one that certainly accelerates the weathering process, is the moisture both internally and externally to the material[4,12]. The deterioration of stone-built heritage is clearly multifaceted and heterogeneous, and thus, its understanding and reduction requires knowledge about the specific material properties, the interactions between the material and its weathering processes and water in particular, and the resultant changes in the material[4].

The research reported in this thesis focuses on the study of limestone, a commonly used building stone[13–17] due to its widespread occurrence through the geological column[5]. From observations of natural landscapes, it can be concluded that erosion is a gradual and uniform process, both temporally and spatially[5]. Such erosion mainly occurs *via* the karst process, as identified by Livingston[18]. The karst process is the dissolution of limestone by rainwater, which is normally acidified by the uptake of CO_2 or organic acids, and is described by:

$$CaCO_{3(s)} + H_2O_{(\ell)} + CO_{2(g)} \rightleftharpoons Ca(HCO_3)_{2(s)} \tag{1.1}$$

Notably, calcite (the most stable polymorph of $CaCO_3$) has a low solubility in pure water, 11 mg/L at 25 °C, which is enhanced in the presence of atmospheric CO_2 to 43 mg/L[18]. This process is significant over geological time periods, resulting in the formation of distinct relief forms[19], for example, solution flutes, decantation runnels and solution spikes. However, Livingston highlighted that in polluted environments, such as those found in cities, dissolution increases through wet and dry deposition processes.

Wet deposition is exemplified by the presence of acidity in rainwater in excess of

naturally occurring acids and is usually the result of human activity[18]. This contribution mainly consists of sulfuric acid (H_2SO_4) with a smaller, and more variable, amount of nitric acid (HNO_3). When acid rain reaches the limestone surface it is neutralised, for example, by the reaction:

$$CaCO_{3(s)} + H_2SO_{4(aq)} \rightleftharpoons CaSO_{4(aq)} + H_2O_{(\ell)} + CO_{2(g)} \tag{1.2}$$

In dry deposition, sulfur bearing acidic gases and/or particulate matter react with the carbonate surface to produce gypsum ($CaSO_4 \cdot 2H_2O$), requiring the presence of moisture on the stone surface[10]. Gypsum has a much higher solubility than calcite (2 g/L vs. 43 mg/L in the presence of CO_2)[18], and the dissolution of gypsum occurs *via* the following reaction:

$$CaSO_4 \cdot 2H_2O_{(s)} \rightleftharpoons CaSO_{4(aq)} + 2H_2O_{(\ell)} \tag{1.3}$$

It is this significant difference in solubility that contributes to the damaging effects of gypsum because during wet periods, gypsum will dissolve and be transported into the internal pore structure of the stone. Upon drying, gypsum re-deposits and due to its higher specific volume compared to calcite, exerts pressures on the material and causes further physical damage, such as bursting or flaking[10,20].

Depending on the façade, different damage patterns will be observed as dry deposition can affect all surfaces of a building, while wet deposition will only affect the exposed surfaces[21,22]. Thus, if the surface is exposed to rainfall, then the gypsum formed will be washed away, resulting in "white areas"[20] as the surface gradually recedes, exposing the retreating original stone. On the other hand, if the stone is relatively sheltered, preventing run-off, the gypsum accumulates and incorporation of carbonaceous particles and aerosols results in a "black crust" being observed[10].

Oxford stone and its decay

The heritage buildings of Oxford have been constructed primarily from Jurassic oolitic limestone, resulting in Oxford's iconic cityscape[23–25]. Oxford's oldest architectural structure, constructed in the eleventh century from locally sourced Coral rag, is St.

Michael's Church tower on Cornmarket Street. This local rubble stone was also used in the construction of the city walls, the Castle tower and elsewhere. However, upon the larger construction projects of the University buildings and colleges in the $13-15^{\text{th}}$ centuries, this rubble stone was considered unsuitable, and instead the stones were supplied from Wheatley and Headington quarries, with Taynton and other quarries near Burford providing the freestones used for dressings and sculptural details. The Renaissance architects brought fresh demands, requiring the construction of whole buildings in freestone to realise their classical ambitions. The Taynton quarries were unable to supply the demand, and a new source of stones was required, found in the local Headington quarries. The seventeenth century saw the Headington freestone hailed as a new discovery and it saw widespread use across the city. However, by the 18^{th} century, its unsuitability had been realised due to its extreme susceptibility to the weathering processes discussed in Section 1.1, resulting in blistering and disintegration, and a substitute was sought.

It was at this time that Bath stone first arrived in Oxford, coinciding with the Gothic Revival period of the 19^{th} century, but the later stages showed a return to the local quarries of Taynton and Milton. However, lack of care in the selection of these stones resulted in rapid erosion of the less durable Milton stone, and again, a new substitute was sought. It was the construction of the University's Examination Schools by Sir Thomas Jackson which introduced Clipsham limestone, from Lincolnshire, to Oxford. The high durability of this stone led it to be seen as the solution to Oxford's decaying infrastructure and climatic environment, resulting in its use for restoration and refacing of many buildings in the 20^{th} century, for example, the refacing of Wadham college[26]. Portland stone, although used throughout the rest of the country, and famously by Sir Christopher Wren in the construction of St. Paul's Cathedral in London[27], was not widely used in Oxford except in the construction of the Ashmolean Museum, owing to the strong contrast between the almost white tones of Portland stone and the honey coloured tones of most stones used in Oxford. In response to the increasing cost and supply issues of English limestones, and the globalised market, the introduction of French limestones, including

Savonnières limestone which was used for refacing the roadside façade of Magdalen College[26], has occurred within the last 100 years. These types of limestone are still used today in restoration and for the facing of new developments which must be in keeping with the surrounding architectural style.

The stones selected for use in Oxford are all oolitic limestones which consist primarily of small fragments of shell or fossil surrounded by concentric layers of calcium carbonate, and embedded in calcitic cement[5,23]. While oolitic limestones are chemically homogenous, although many are not completely pure $CaCO_3$, they are highly variable in physical properties such as porosity, hardness and petrology, and this results in differences in durability[28]. The oolitic limestones used in Oxford date from various periods within the Jurassic era, and thus, in comparison to many geologically older limestones, they have not experienced the intense diagenesis processes[1] and are found to be less crystalline, less dense, and therefore, less resilient to many decay processes[30]. Thus, in the built environment, these limestones often experience rapid, catastrophic decay, characterised by the hollowing of exposed surfaces[28], as shown in Figure 1.1.

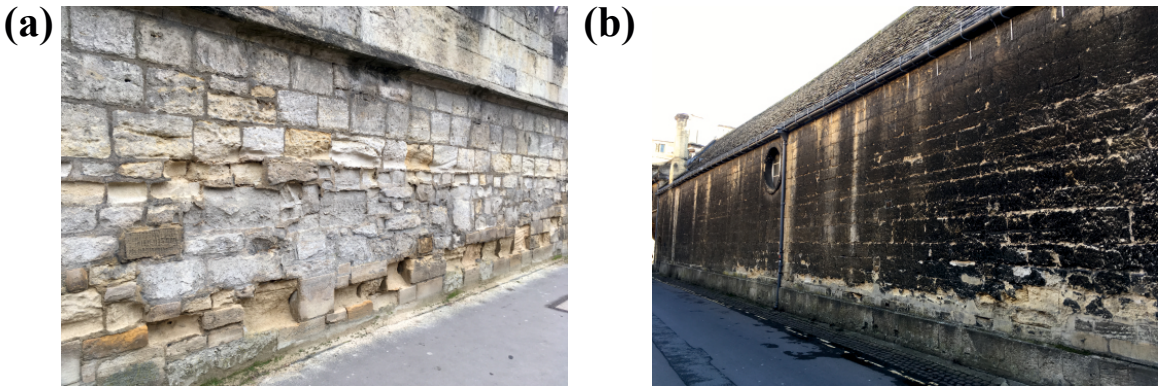


Figure 1.1: **(a)** Rapid, catastrophic decay of a section of wall constructed from Headington stone[31] – Longwall Street, Oxford; **(b)** Soot-encrusted and deteriorating 14th century Headington stone[23] – New College Lane, Oxford. *Images: Author's own.*

This rapid, catastrophic decay occurs due to initial exposure to polluted and moist atmospheric conditions which accelerate chemical reactions, followed by a cycling of

[1] "...physical, chemical and biological processes which bring about compaction, cementation, recrystallisation and other modifications to the original sediment, and form rocks."— M. E. Tucker, *Sedimentary Petrology: An Introduction to the Origin of Sedimentary Rocks*, **2001**[29]

environmental conditions which encourage the formation of gypsum crusts and, subsequently, allow the inner core to soften. Once the outer crust is breached, leading to the formation of blisters and scales, the weakened core undergoes rapid weathering, leading to granular disaggregation and flaking. Smith and Viles[28] propose that this process occurs in areas where dry deposition or mixed process regimes dominate, with a significant contribution from salt weathering and freeze–thaw processes. This decay exhibits temporal and spatial variability which is controlled by the presence of moisture on and within the stone structure.

The distribution of moisture within the stone is determined by the environmental conditions and the material properties, as these control the water transport kinetics. Evaporation is the main route through which moisture is lost from the stone, and drives water flow through the material[32]. Therefore, improved knowledge of the evaporation process for stone materials would provide important information for understanding the deterioration processes and patterns explained above. This thesis describes the development and application of a sensitive and quantitative laser-based spectroscopic system, based on cavity ring-down spectroscopy (CRDS), which is designed specifically to detect water and its isotopologues in order to elucidate water transport in these stone materials. The spectrometer is used to investigate five of the oolitic limestones used in Oxford city, and for comparison, a British sandstone which is often used for construction and repair. The stones selected were Portland limestone (Whit and Base Bed), Clipsham limestone, Bath limestone, Savonnières limestone and Stoke Hall sandstone. This bespoke CRDS instrument is benchmarked against established methods for investigating petrophysical properties.

1.2 Protecting and consolidating limestone

The deterioration of stone can lead to material loss in the form of blistering, delamination, disintegration and fragmentation. It is often desirable, and necessary, to apply a consolidant which re-establishes cohesion between the stone material, restoring strength and providing resistance to further decay mechanisms[33,34]. The effectiveness

of a consolidant is assessed by its performance in terms of its compatibility with the stone, durability, depth of penetration, effect on appearance, and effect on porosity and moisture transfer[33]. While no item on this list could be considered unreasonable, finding one treatment which fulfils all these requirements is extremely difficult and has resulted in a wide variety of materials being considered. The earliest known example is from the first century B.C.E. where Vitruvius[35] describes the preservation of a vermilion fresco on stone by the application of molten Phoenician wax. The ability to apply waxes in the liquid form, allowing deeper penetration before they harden, is a desirable feature. However, this advantage becomes a risk for materials which have exposure to the sun and reach high temperatures which could soften the consolidation[33,34]. Waxes also have the tendency to acquire dirt and grime, resulting in the stone acquiring an unsightly appearance.

Consolidants that are widely used, as reported in the scientific literature, are based on alkoxysilanes and alkyl alkoxysilanes[33,34,36–40], predominantly methyltrimethoxysilane (MTMOS) and tetraethoxysilane (TEOS). These silanes are hydrolysed to form silanols which then polymerise in a condensation reaction to form silica which fills the pores[34], as shown in Figure 1.2.

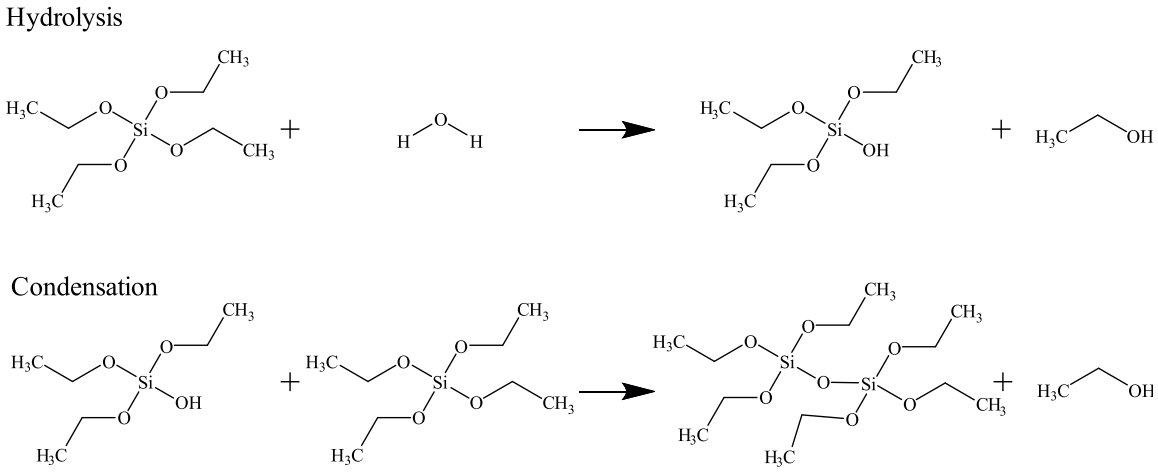


Figure 1.2: Hydrolysis and condensation reaction for tetraethoxysilane (TEOS) which continues until all alkoxy groups have been released and silica is formed.

This hydrolysis reaction and polymerisation occurs after the treatment has been applied to the stone, and therefore, good penetration by the consolidant is reported[33].

While this consolidant is considered very effective for the treatment of siliceous sandstones, its compatibility with limestones has long been called into question[34,36,40]. In sandstones, the resultant silica gel is able to form silicate bonds with the hydroxyl groups on the sandstone surface. These groups, however, do not exist in the majority of carbonate stones; therefore, the consolidation is purely *via* physical binding[41]. It is important to note that treatment with alkoxysilanes results in the formation of a hydrophobic gel[36,41] which can trap moisture within the material, leading to further deterioration. Another drawback is that the consolidant tends to form brittle gels, which under the high capillary pressures generated by the pore network, leads to shrinkage and cracking during the drying process[42]. Interpretation of whether these microcracks are beneficial can differ, with Pápay and Török[38] stating that these microcracks provide additional pathways for water vapour transport and partial evaporation.

The traditional use of limewater, an aqueous suspension of $Ca(OH)_2$, is perhaps a more natural, and more compatible, choice for the consolidation of limestone materials[33–35,43,44]. While $Ca(OH)_2$ itself does not provide any consolidating action, it reacts with atmospheric carbon dioxide, as shown in Equation 1.4, to form calcium carbonate — the main component of the limestone matrix.

$$Ca(OH)_{2(aq)} + CO_{2(g)} \rightarrow CaCO_{3(s)} + H_2O_{(\ell)} \tag{1.4}$$

However, while this process meets the requirement of compatibility, various drawbacks have been reported in terms of penetration, durability, appearance and effect on porosity and moisture. The low solubility of $Ca(OH)_2$ in water (1.7 g/L at 20 °C[45]) means that successive applications are required to achieve consolidation. The large amount of water involved, therefore, introduces the risk of freeze–thaw weathering, salt migration, substrate dissolution and reprecipitation[43], which may outweigh the hypothetical benefits of the consolidation achieved. The majority of the lime is deposited near the surface, reportedly within the outer millimetres of the stone[33,34,43]. This combined with the limiting rate of carbonation arising from the difficulty of CO_2 permeating through the material, can result in the formation of a thin, hard calcium

carbonate shell surrounding the inner deteriorated stone. This outer shell will have different physical properties, and due to differences in size and morphology, it may have limited durability[43].

An alternative consolidant is barium hydroxide, due to its increased solubility in water (49.1 g/L at 25 ℃[46]) and the chemical and physical similarities between barium carbonate and calcium carbonate[33,34,43,47]. Barium hydroxide offers the additional advantage that it may react with gypsum to form barium sulfate:

$$Ba(OH)_{2(aq)} + CaSO_{4(s)} \rightarrow BaSO_{4(s)} + Ca(OH)_{2(aq)} \tag{1.5}$$

The barium sulfate product has a much lower solubility than calcium sulfate and calcium carbonate, and therefore, may limit further weathering and reduce the damage caused by the dissolution and recrystallisation of gypsum, as described previously in Section 1.1. The calcium hydroxide product may also go on to react with atmospheric CO_2, offering additional consolidation. However, similar to limewater, there have been reports of a surface hardened layer which subsequently exfoliates and leaves the original stone unprotected[33,43].

A more attractive alternative to increase the concentration in solution, rather than using a more soluble compound such as barium hydroxide, is to use a dispersion of calcium hydroxide. However, aqueous calcium hydroxide dispersions are unstable, with a fast sedimentation rate resulting in the formation of a white film when applied to surfaces[48,49]. Giorgi, Dei and Baglioni[48] proposed the use of a dispersion of slaked lime particles ($3 - 4$ μm) in propan-1-ol as an alternative, comparing its kinetic stability with an aqueous dispersion. It was proposed that the greater kinetic stability was due to a combination of electrostatic and hydrophobic interactions between the particles and medium, preventing sedimentation and aggregation[48,50]. Following this study by Giorgi, Dei and Baglioni[48], research has been carried out into the development, use and evaluation of dispersions with progressively smaller $Ca(OH)_2$ particles for consolidation, including two European Commission projects: STONECORE (Stone conservation for the refurbishment of buildings)[51] and NANO-CATHEDRAL (Nanomaterials for conservation of European architectural heritage developed by research

on characteristic lithotypes)[52]. The goal of using these so-called nanolimes is that the smaller nanometre sized $Ca(OH)_2$ particles will achieve greater penetration through the material.

The use of alcohol dispersions offers the advantage of limiting carbonation by CO_2 before the particles are deposited[34,49]. However, studies by Rodriguez-Navarro *et al.*[53,54] show that the nanoparticles can partially transform to Ca-alkoxides as a function of temperature and time, and this process is dependent on the alcohol used. They showed that there is a greater conversion of $Ca(OH)_2$ into Ca-alkoxide for ethanol dispersions compared to isopropanol, supposedly due to ethanol's shorter alkyl chain allowing more effective adsorption on the $Ca(OH)_2$ surface as a consequence of steric effects. The formation of Ca-alkoxides reduces the carbonation of both dispersions, with a lower degree of carbonation observed for ethanol dispersions. Thus, this implies that for effective consolidation, freshly prepared dispersions should be used. Also, if storage is required, because the conversion into Ca-alkoxides displays Arrhenius type behaviour, the dispersions should be kept at low temperatures ($T < 5$ ℃).

The carbonation reaction, stated in Equation 1.4, has been the focus of many studies, and its rate and yield have been shown to have a critical dependence on the relative humidity. Rodriguez-Navarro, Elert and Ševčík[55] determined that at room temperature (18 ± 2 ℃), the carbonation reaction only occurs in the presence of water *via* a dissolution–precipitation reaction. This carbonation process follows Ostwald's step rule[56] which states that if a reaction can form several products, the least stable polymorph which is closest in free energy to the original state will form first. These researchers determined that initially, $Ca(OH)_2$ undergoes carbonation to form amorphous calcium carbonate ($CaCO_3 \cdot nH_2O$; ACC). Following dissolution of ACC, the metastable vaterite and aragonite polymorphs form before transforming into stable calcite *via* dissolution–precipitation. They confirmed the crucial presence of water for carbonation by storing nanolime in a 0 % relative humidity (RH) environment at room temperature for 2 months, after which no ACC or any other calcium carbonate phase was found. A study by Beruto and Botter[57] determined that the

carbonation reaction was catalysed by multilayer water vapour adsorption, and that a significant increase in carbonation rate occurred when $RH \geq 70$ %. This result is consistent with a study by Daniele, Taglieri and Quaresima[58] who reported an improved carbonation yield from 65 % to 93 % upon increasing the RH from 40 % to 90 %. The general consensus, therefore, is that to achieve effective carbonation and consolidation, following application of nanolimes, the substrates should be stored in high humidity ($RH > 70$ %) conditions.

Despite the use of nanometre sized particles of $Ca(OH)_2$, research conducted on different limestones[59–62] has reported limited penetration of the consolidant, and evidence of accumulation beneath the surface due to back-migration during solvent evaporation[63]. This back-migration has been linked to the kinetic stability of the dispersions, and research has sought to minimise this effect[64–67]. The kinetic stability of the dispersion has been measured using UV–Vis spectroscopy, by analysing the absorbance at $\lambda = 600$ nm. This absorption is proportional to the turbidity of the dispersion, which decreases as a function of time as the particles agglomerate and settle. Borsoi *et al.*[64] describe a conceptual relationship between the moisture transport properties of the substrate and the kinetic stability of the dispersion. In this study, they found that for coarse porous stones, such as Maastricht limestone (pore sizes $= 35 - 40$ μm), solvents with low kinetic stability and high boiling points, *e.g.*, butanol or water, improve deposition with no significant back-migration. For improved penetration and deposition in fine porous stones, *e.g.*, Migné limestone (pore sizes $= 0.5 - 2$ μm), solvents with lower boiling points and high kinetic stability should be used, such as ethanol or isopropanol. These findings were confirmed experimentally, with a penetration depth of $20 - 25$ mm found using butanol dispersions on Maastricht limestone.

A follow-up study by Borsoi *et al.*[65] investigated the addition of water to ethanol dispersions in an effort to reduce kinetic stability while limiting back-migration. They found that the addition of a small amount of water (5 %) notably reduced the kinetic stability, improving penetration and limiting back-migration when applied to Maastricht limestone. Otero *et al.*[67] also investigated the addition of water, with

the aim of consolidating lime mortars, and reported that the greatest improvement was upon using a $50 - 50$ % alcohol–water dispersion. This implies that, while the conceptual model proposed by Borsoi *et al.*[64] can provide a starting point in terms of improving in-depth deposition, experimental tests for each material are required in order to determine the most appropriate solvent.

A large proportion of the literature, however, focuses on studying the application and efficacy of nanolimes (typically in pure alcohol dispersions) on different substrates[68–73], investigating the impact of application procedure[62,74–76] and environmental conditions[77–79]. These studies have assessed the effectiveness and compatibility of the consolidation in terms of penetration depth (phenolphthalein test, scanning electron microscopy), superficial cohesion (Scotch tape test), hardness (drilling resistance measurements), degree of carbonation (X-ray diffraction, phenolphthalein test, Raman spectroscopy), durability (salt crystallisation test, ultrasonic pulse velocity), and aesthetics (colorimetry). Surprisingly, only a small subsection of these studies have addressed the effect of consolidation on porosity and water uptake[58,60,67,69,71,72,74], determined using mercury intrusion porosimetry and water absorption by capillarity. These studies all report a reduction (*ca.* 5 %) in the substrate porosity, but only Borsoi *et al.*[60] and Otero, Starinieri and Charola[72] investigated the impact of consolidant on water uptake and drying, with both studies reporting that the treated stones had increased drying times due to changes in the substrate pore network. This represents an undesirable finding in terms of consolidation and weathering, as it indicates that nanolime treatments may result in accumulation of moisture and/or salts, leading to increased weathering by mechanisms such as freeze–thaw or salt migration[33]. Since the methods developed during the course of the work reported on here are inherently sensitive to drying kinetics, they are appropriate for assessing changes in the effects of consolidation.

1.3 Methods of monitoring moisture

As clearly mentioned in the previous sections, improved knowledge of moisture transport kinetics and distributions within stone materials is of great importance for understanding the deterioration processes and assessing the effectiveness of consolidation treatments. A wide range of techniques have been developed to measure, and monitor, the moisture content of porous materials, varying in their accessibility, reliability, cost, and applicability for use at field sites. In principle, many of these can be used to deduce drying kinetics, but are more useful for on-site diagnostics, often requiring absolute calibration, while others are clearly laboratory based. This section, however, provides a general overview with which to place the work of this thesis into context. The principles behind the most widely used techniques, along with their advantages and disadvantages, are presented here, and summarised in Table 1.1.

1.3.1 Destructive techniques

Gravimetric analysis

A direct and simple method of determining the moisture content of stones is *via* gravimetric analysis which involves the drying and weighing of samples. The sample of interest is weighed to determine its wet weight, m_w, and then is oven-dried, typically at 103 ℃, until it reaches a constant weight, m_d[84,85,90]. The percentage moisture content by weight is calculated:

$$\% \text{ Moisture content by weight} = \frac{m_w - m_d}{m_d} \times 100 \tag{1.6}$$

As an easy to use and inexpensive technique, gravimetric analysis is typically used as the reference method against which other methods are compared, as it provides precise quantitative measurements. A disadvantage of this technique is that in order to measure the moisture content of stone at a field site, stone fragments must be broken off or collected[11,80,83], which is an undesirable requirement for heritage sites. Additionally, the oven-drying of some samples can cause chemical alteration and prevent repeated measurements[90]. Therefore, to gain an accurate measurement

Table 1.1: Comparative assessment of the most commonly used techniques to measure moisture content in porous building materials.

Technique	Advantages	Disadvantages	References
Gravimetric analysis	Easy, inexpensive, direct measurement	Destructive, low spatial and temporal resolution, total mass change only	11 80–90
Carbide meters	Fast, easy, can be used *in situ*	Destructive, low spatial and temporal resolution	84,85, 90,91
Gravimetric replacement materials	Simple, inexpensive, monitoring possible	Invasive, slow response, low spatial resolution	84,85, 91–93
Relative humidity probes	Simple, inexpensive, monitoring possible	Invasive, not suitable for high saturation, low spatial resolution	11,85, 94,95
Infrared thermography	Simple, spatial distributions	Qualitative, surface measurement, easily misinterpreted	11, 84,85, 96–101
Hand-held moisture meters	Simple, inexpensive, temporal or spatial distributions possible	Calibration required, limited penetration, influenced by salts	11,25,84, 83,85,95, 96,102–107
Electrical resistivity tomography	2D- or 3D-spatial distribution, can be applied *in situ*	Calibration required, technically difficult, influenced by salts and porosities	11,25,85, 83,92,94, 104,106, 108–110
Time domain reflectometry	Can be applied *in situ*, temporal distributions	Invasive, calibration required, influenced by temperature	11,84, 83,85, 111–113
Microwave meters	Can be applied *in situ*, unaffected by salts	Calibration required, limited depth information	11,85, 95,110, 114–116
Fibre Bragg grating sensors	Small, light-weight, robust, high sensitivity	Invasive, calibration required, influenced by temperature	117–120
Neutron radiography	High sensitivity, quantitative, temporal or spatial distributions	Expensive, requires specialist training, strict safety procedures	84,85, 121–125
Neutron magnetic resonance	High sensitivity, quantitative, temporal or spatial distributions	Calibration required, technically difficult, requires specialist training	84,85,101, 126–133

of the moisture content, or to obtain a spatial distribution, a large number of samples is required[83]. The ability to monitor temporal changes in the moisture content at a field site is also limited due to the destructive nature of the technique.

Alternatively, and more commonly, studies are conducted using surrogate samples, allowing an understanding of the moisture content and transport kinetics for materials typically found in heritage sites. While exposure trials have been conducted to study the effect of pollutants[134], erosion by wind and rain[135] or consolidation effectiveness[70], the majority of studies for studying moisture transport kinetics are conducted under controlled laboratory conditions. Typically, the experiments are carried out with static temperature and relative humidity in containers with controlled air flow and the samples are weighed at regular time intervals[81,82,86–89]. However, as this technique measures the total mass change of the sample, it cannot distinguish between the loss of moisture and other species, such as volatile decomposition products[85].

Chemical analysis

For gravimetric measurements, samples must be taken off-site to be assessed, resulting in delays. An alternative, and (relatively) faster, method is the use of carbide meters for the determination of moisture content[84,85,90]. A drill powder sample is obtained from the structure and a known amount is combined with calcium carbide (CaC_2) within a sealed vessel. The calcium carbide reacts with the moisture present in the powder sample to produce acetylene gas (C_2H_2) and the gas pressure in the vessel rises. Using gravimetric calibration curves, this measurement is converted into a direct measurement of the moisture content. This technique has the advantage that is easy to perform and can be used *in situ*. The disadvantages, however, are that it is destructive both in terms of obtaining the sample by drilling, and because the reaction with calcium carbide destroys the sample, preventing further tests. As a result, the method cannot be used to investigate moisture transport kinetics. This technique can also result in an underestimation of the moisture content due to moisture loss during the sample preparation, such as moisture evaporation while drilling due to the

drill bit heating up[84,91]. Similar to using gravimetric analysis at field sites, it has low spatial and temporal resolution unless a large number of samples are obtained.

1.3.2 Probe-based methods

Gravimetric replacement materials

As already discussed, one of the drawbacks of gravimetric analysis is the limited number of samples that can be obtained at field sites. An alternative method is to employ a replacement material which can be inserted and removed from a drilled hole in the substrate, and to determine the moisture content of the material gravimetrically at regular intervals[84,85]. Typically, wooden dowels are used as the probe as they are a relatively inexpensive material. However, the dowels require time to equilibrate with their surroundings, and as the dowels may swell over time, they must be significantly smaller than the borehole to allow removal for measurements[85]. As a consequence, there is a small air gap between the dowel and the material, allowing interaction with the external conditions and potentially providing an evaporation route through which moisture is lost. This method is commonly used for comparison with other techniques and to provide point measurements in order to determine areas for larger study[92]. It has been noted that it is unclear whether the presence of the wooden dowels affects the water movements in the stone[93], and that as the wooden dowels have different material characteristics, the measurements cannot be related to absolute moisture content.

Sandrolini and Franzoni[91] proposed the use of the drill powders and fragments collected from the stone itself during drilling as the replacement material to ensure chemical and physical compatibility. They conducted a study to compare the moisture content of these fragments and powder with the actual moisture content of the stone assembly. The material was reinserted into the boreholes and sealed to ensure equilibrium, and upon reaching a steady state, the moisture content was determined gravimetrically. They reported that the fragments provide a good representation of the moisture content, but that the powders return systematically higher values due to the increased surface area resulting in greater water adsorption, and therefore,

higher moisture content. Although this method is moderately invasive due to the requirement for boreholes, it can be used to provide time-resolved measurements at a field site. Thus, this technique is more suitable as a method of monitoring moisture content, rather than one which provides detailed measurements of transport kinetics.

Relative humidity (RH) probes

The moisture content of a stone can be determined indirectly through the use of a RH probe, making the assumption that the water vapour concentration in the surrounding air of a borehole is in equilibrium with the moisture content of the stone[11,85]. To ensure that there is no moisture exchange with the external environment, the borehole is typically sealed with a polymer. The measured RH is converted into moisture content using sorption isotherms[85], which quantifies the equilibrium between the air humidity and the water content of a porous medium at a specific temperature[136]. Using this technique, temporal monitoring of a field site is possible as, depending on the probe, it can be continuously logging data. However, again, this can only provide point measurements at a site. To ensure accurate readings, there must be good contact between the probe and the stone, which can cause difficulties and may prevent the recovery of all the probes[94]. The measurement of the relative humidity is also influenced by the presence of salts[95], and therefore, this technique could provide alternative information regarding the presence and composition of salts in the substrate. Additionally, the general consensus reported in the literature is that successful application of RH probes only occurs in indoor or arid conditions[11,85,95], as the probes rapidly equilibrate with their surroundings to a constant reading of 100 % RH, thus limiting their usefulness as a monitoring technique and preventing measurements of transport kinetics.

1.3.3 Infrared thermography

Infrared thermography offers a quick, non-destructive method for mapping moisture distributions within building materials[11,84,85]. This method is based on detecting emission in the infrared spectral range (approximately $8-20$ μm) and relating this to

surface temperature by the Stefan–Boltzmann and Planck laws[99]. The assumption is that the cold temperature anomalies are due to evaporative cooling, indicating the presence of moisture, while the warm anomalies relate to structural conditions[11]. However, this is only a qualitative method as the results are dependent on various factors, such as weather conditions, properties of the surface materials, distance and angle to target, presence of metals or heat sources, and incidence of sunlight[97,98,101]. Thus, without knowledge of the underlying structure and the environment, the assumption that colder areas are due to moisture is often a misconception, and the results may be misinterpreted. Infrared thermography is, therefore, generally used as an initial survey tool, allowing large-scale mapping of the building before targeted surveys are conducted using more specialised techniques[96,97,101], and provides no information on water transport kinetics.

1.3.4 Electrical based methods

Hand-held moisture meters

The presence of moisture within a porous material will influence its electrical properties, which can be measured using hand-held meters, a non-destructive, relatively inexpensive and easy to use technique. These moisture meters can be broadly divided into two categories, depending on the property they measure in the material: *capacitance* meters measure the dielectric constant of a material, and relate the moisture content to the attenuation in a radio frequency signal after it has passed through the material of interest[85,103]; while *resistivity* meters apply a current to the material through two (or more) electrodes and measure the potential difference at the electrodes, following which, the resistivity is calculated using Ohm's law and related to moisture content[85,103]. It is important to note that hand-held meters do not directly measure the moisture content, and that typically they have been calibrated for use on wood materials, providing readings in terms of *% wood moisture equivalent*[103]. Therefore, to relate these readings to absolute moisture values for masonry materials requires further calibration, which is typically achieved using gravimetric analysis[84].

An ideal moisture meter would show a direct 1:1 relationship between the meter reading and the absolute moisture content, allowing measurements to be taken across the entire range.

A study by Eklund *et al.*[103], however, investigating the relationship between the meter readings for different commercial hand-held moisture meters and the absolute moisture content determined gravimetrically, found that there is no linear relationship between the different meter readings or the absolute moisture content. This study determined that the meter readings can be influenced by the presence of metals, air gaps within the material, the operator's hand position and pressure applied, and the time at which readings are taken, *i.e.*, immediately upon contact or allowing the readings to stabilise. An example of the response measured for two capacitance meters (CEM DT-128 and Brookhuis FMW-T) and one resistivity meter (GE Protimeter) for Clipsham limestone is shown in Figure 1.3, showing the inconsistent relationship observed. Thus, as these techniques can only give measurement of the relative moisture content on the surface of the material, they are generally used as a semi-quantitative method to map and limit the area over which more advanced techniques are used[25,96,104,106].

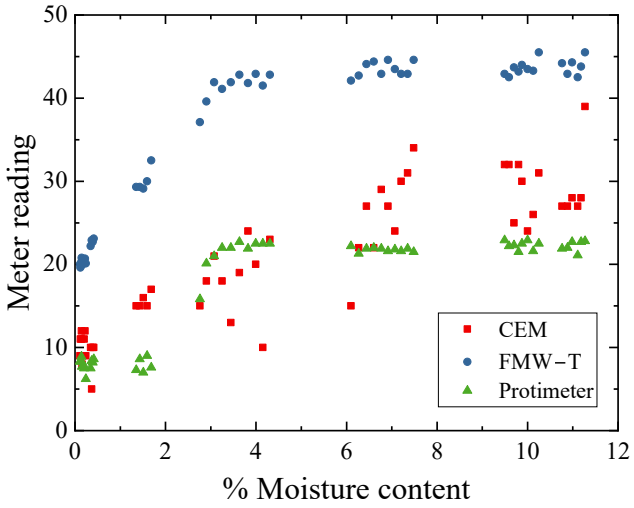


Figure 1.3: A plot of the meter readings obtained using two capacitance meters (CEM DT-128 and Brookhuis FMW-T) and one resistivity meter (GE Protimeter) against the percentage moisture content of a Clipsham limestone sample, calculated using Equation 1.6. *Data: Author's own*[137].

One of the main limitations noted by several studies[11,83,85,103,105] is that the read-

ings are influenced by the presence of salts, as these will increase the conductivity of pore water, reducing the resistivity, and therefore, leading to an overestimation of moisture content. Wilhelm, Viles and Burke[105] conducted a study investigating this effect, and found that both resistivity and capacitance meters reported higher readings for salt-contaminated stones versus non-contaminated stones. They observed a greater effect under high RH (95 %) conditions and after the samples had reached sorption equilibrium. Therefore, without knowledge of the salt contamination on-site, care must be taken in interpreting results obtained with electrical based measurements.

It has been noted that these meters have limited penetration, which is affected by the electrode separation and the degree of contact with the material of interest[85,95]. Due to the presence of rough, uneven surfaces which may have many joints and voids, these techniques may have limited applicability in heritage environments[85]. To overcome this limitation, some studies have investigated placing the sensors within the material, similar to RH probes, to measure the internal moisture content[102,107]. However, as previously stated, these measurements can only provide an insight into the relative moisture content, and without gravimetric calibration, cannot give absolute values or be used to study moisture transport.

Electrical resistivity tomography (ERT)

Hand-held moisture meters provide quick, simple, qualitative measurements of the relative moisture content at a specific point on the surface of interest, and therefore require a large number of measurements to obtain a spatial distribution. Using the same principles as resistivity meters, electrical resistivity tomography (ERT) uses 50 or more electrodes to obtain a 2D- or 3D-distribution of the electrical resistivity[11,83,85]. Although this technique originally required the use of metal screws inserted into boreholes within the rock to establish an electrical connection[83], a non-invasive method using self-adhesive medical electrodes was developed by Sass and Viles[92] for use in heritage environments where monument protection would prohibit invasive drilling. They determined that there was no significant difference between

the contact resistances for the drilled-in and self-adhesive electrodes, although for adhesion, the surfaces must be dry, with electrode detachment observed following rainfall[108].

As this method measures the electrical resistivity, similar to the hand-held moisture meters, determination of the absolute moisture content requires an experimentally derived calibration, which is a source of possible errors[83]. Sass and Viles[108] derived a conversion curve based on Archie's law[138] and laboratory resistivity measurements for a selection of limestones and dolomites, allowing application to measurements conducted on Oxford limestone buildings. This conversion has a defined range of $50 - 5000\,\Omega$m, as they note that resistivity values below 50 Ωm correspond to amounts of water larger than the available pore space. Thus, when applying this technique to masonry walls, and especially heritage structures, interpretation of the results should be in light of the porosity variations and requires site-specific calibrations[108,110].

As with resistivity meters, the measurements are also influenced by the presence of salts, which can be accounted for by measuring the pore water resistivity from drilled samples[25]. However, as with the restrictions on inserting electrodes into boreholes, collection of these samples is not always possible[109], and therefore, without the use of additional techniques, the user is unable to determine whether low resistivity measurements are the result of high moisture content, the presence of salts or a combination of both[94,106].

Studies report high penetration of up to 40 cm using this technique[25,104,106], allowing in-depth spatial mapping of a structure at a specific time. However, without repeated measurements, it cannot provide an insight into temporal, or long-term, trends[104], and similar to the resistivity meters, without calibration, it only provides relative interpretations which do not yield information on water transport kinetics.

1.3.5 Time domain reflectometry (TDR)

Time domain reflectometry (TDR) measurements are based on the difference between the relative dielectric constant for water ($\varepsilon_r \approx 78$ at 25 °C for 1.8 GHz[139], microwave

region) and that for dry building materials ($\varepsilon_r \approx 3-5$[83]). In TDR measurements, an electromagnetic signal is propagated along a probe which is in contact with the material of interest, and the amplitude and time interval of the reflected wave is measured[11,84,85,111]. The dielectric constant of the surrounding medium is related to the time taken, Δt, for the signal to travel along the length, L, and return by the following equation:

$$\varepsilon_r = \left(\frac{c\Delta t}{2L}\right)^2 \tag{1.7}$$

where c is the speed of light. Thus, the presence of moisture within the surrounding material will alter the dielectric constant, resulting in changes in the time taken for the reflected signal to be detected[84,111].

However, determination of the absolute moisture content requires both individual probe calibration[84,111], and calibration to the material and water[85]. Calibration of the probe length is achieved by inserting the probes into materials with well-known dielectric constants, and to ensure high accuracy across a wide range, these materials are typically selected to have very different dielectric constants, for example, water and air, or water and benzene[113]. Gravimetric calibration is the most reliable method and consists of wetting the material to a reference moisture content and measuring the dielectric constant[112]. It is important to ensure that the water content is equally distributed throughout the whole sample[113], and the temperature of the measurement is known, as the dielectric constant is temperature dependent[83].

TDR allows continuous monitoring of the moisture content[85,95]. However, as the measurements are integrated over the depth of the probe, it is unable to provide spatial profiles[85] and is susceptible to any moisture movement along the probe[11]. Typical TDR devices consist of two probes which must be embedded parallel within the material. For accurate measurements, there must be good contact between the probes and the material, as the presence of air gaps will affect the measurements[84], and could also become filled with water from rainfall, altering the readings[95]. Weiss and Sass[95] observed that abrupt changes in measurements can occur if the sensors' position and contact with the material changes, as shown in Figure 1.4, and installa-

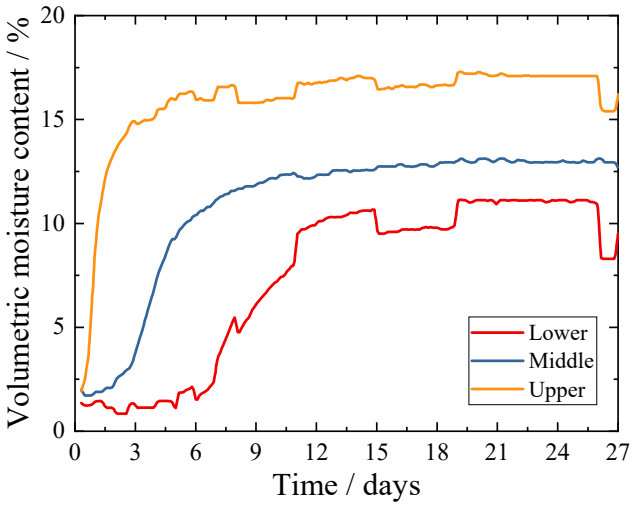


Figure 1.4: A plot of the volumetric moisture content against time, measured using time domain reflectometry at three heights. Lower: 5 cm above the rock base; Middle: 10 cm above the rock base; Upper: 15 cm above the rock base. *Adapted from Weiss and Sass* [95].

tion of TDR devices is technically difficult to achieve in masonry [11,84,85]. While this technique could be used to measure water transport kinetics, gravimetric calibration would be required to determine absolute moisture content. Thus, the majority of its application as reported in the literature has been on *in situ* monitoring rather than water transport studies.

1.3.6 Microwave meters

Microwave meters provide an alternative dielectric moisture measurement also based on the difference between the relative permittivity of water and most building materials [11,85]. Generally for microwave permittivity, a transmitter sends a microwave signal and a receiver on a different side of the object or in an adjacent borehole measures the attenuation in the signal in order to determine the moisture content [85,110]. Hand-held microwave meters have also been developed which produce an electromagnetic wave and measure the proportion of the energy which is reflected [114,115]. This is different from the TDR configuration, in which ε_r is deduced from the temporal evolution of a reflected signal, and thus, these microwave meters do not measure the moisture at a specified depth, but rather the moisture present in an integrated volume down to the specified depth [110,115].

Nevertheless, the hand-held microwave meters are a non-destructive technique which are easy to use, can be used *in situ*, and in the frequency range commonly used ($1 - 10$ GHz), the influence of salts can be neglected [11,85,110,116]. As with all methods which measure a property of the material rather than directly measure the moisture content, calibration is required to convert the reported readings into absolute moisture content. This is commonly achieved using gravimetric analysis in controlled laboratory conditions, and a linear calibration curve is commonly reported [95,110,114–116]. Similar to TDR calibration, it is important to ensure a homogeneous water distribution throughout the material [95,114]. Indeed, Orr *et al.* [114] report inversions of the reflected signal as a result of non-linear interactions with inhomogeneous moisture distributions.

Despite a linear calibration indicating equal responsiveness across the range of moisture contents from saturated to dry, Sass [110] reported difficulty in converting the on-site measurements to absolute moisture content due to the measured readings falling below the range determined gravimetrically. Sass proposes that this limitation is a result of the lithology of the site being different from that used in the laboratory. Another difficulty in calibration is that, although this measurement is based on the average properties over the integrated area, microwaves decay exponentially as they propagate through a material [115], and the sensors are strongly affected by moisture in the volume closest to the sensor [95,110,114]. Thus, in most applications, microwave measurements are used semi-quantitatively to provide an initial spatial distribution of the relative moisture content [110,115].

1.3.7 Optical fibre sensors

The direct monitoring of moisture within masonry is possible through the use of optical fibre sensors, in particular fibre Bragg grating (FBG) sensors. These sensors are coated with a hygroscopic material which, in the presence of moisture, expands and induces a proportional deformation in the FBG structure [117–120].

A Bragg grating is formed within the fibre core by the mechanism of photo-induced refractive index modulation, and can be inscribed through a variety of tech-

niques[140,141]. This modulation causes the FBG to act as a wavelength specific filter, in which light is preferentially reflected at the Bragg wavelength, λ_B[118]. The Bragg wavelength is dependent on the effective refractive index of the fibre at the grating location, n_{eff}, and the fibre grating interval, Λ, by the following equation:

$$\lambda_B = 2n_{\text{eff}}\Lambda \tag{1.8}$$

The effective refractive index and fibre grating interval are both sensitive to temperature and strain variations. Thus, using a moisture sensitive polymer, which expands and induces a strain effect on the FBG in the presence of moisture, will lead to a shift in the Bragg wavelength, given by the following equation:

$$\frac{\Delta\lambda_B}{\lambda_B} = (1 - P_e)\varepsilon_{RH} + (1 - P_e)\varepsilon_T + \xi\Delta T \tag{1.9}$$

where P_e is the photoelastic constant of the fibre, ε_{RH} and ε_T represent the strain induced by moisture and temperature expansion, respectively, ξ is the thermal-optical coefficient, and ΔT is the change in temperature.

Optical fibre sensors are small and light-weight[117,120], and measurements are obtained by inserting the sensor into boreholes within the structure[118]. Determination of the absolute moisture content is obtained through calibration of $\Delta\lambda_B$ with relative humidity and temperature changes[117,118], both of which must be accounted for as the relative humidity varies as a function of temperature. Studies report linear relationships between the wavelength and both the relative humidity and temperature[117–119].

The sensitivity of the sensors is dependent on the fibre and polymer coating properties. If the polymer coating induces anisotropic strain on the fibre, then optical birefringence can occur, and this leads to a broadening of the FBG signal[120]. Chai *et al.*[119] investigated the effect of varying the thickness of a polyimide coating on the response time to water absorption and desorption, and the sensitivity. They determined that both the sensitivity and response time increase as a function of thickness, with the response time to absorption ($\approx$ 110 s for a 121 μm thick coating) being approximately a quarter that of desorption.

A comparison of the performance of a FBG sensor and a capacitance based *RH* sensor in monitoring the moisture content of a limestone block during wetting and drying cycles was conducted by Sun *et al.*[118]. The FBG sensor showed a faster response to wetting, while the capacitance sensor showed a more gradual change, which was theorised to be due to its larger volume. During the drying phase, the capacitance sensor maintained its saturated reading while the FBG sensor responded rapidly. Despite these promising findings, the use of FBG sensors in moisture monitoring in heritage environments and water transport studies remains quite limited.

1.3.8 Neutron radiography

Neutron radiography is based on the principle that when thermal neutrons, released from a radioactive source, interact with nuclei, energy is lost and a lower energy neutron results[84,85,121–125]. The neutron capture cross-section for water is an order of magnitude larger than for the main elements found in building stones[122], and therefore, neutrons are easily transmitted through dry stones but are strongly absorbed by interaction with water. Thus, by measuring the number of neutrons following the interaction of a building stone and a neutron source, the density of water can be determined. However, when neutrons interact with nuclei, the majority of them are scattered and can reach the detector. This causes the transmission of the neutron beam to be overestimated, with a corresponding underestimation of the attenuation and sample density[122,125]. Hassanein *et al.*[122] developed a correction algorithm to account for this scattering contribution and determine the total neutron attenuation, and report a $50 - 100$ % increase in water content as a result.

While neutron radiography is a highly sensitive technique, it is an expensive method, requiring specially trained personnel and access to a neutron source with high intensity beams[121]. As it involves a radioactive source, strict safety procedures must be followed, and this has been observed to interfere with some studies. Dewanckele *et al.*[125] report that when measuring water uptake, the water contents determined with gravimetric analysis are significantly higher than those obtained using neutron radiography. The authors hypothesise two potential explanations for this, the first

being the underestimation of the background scattering previously mentioned. The second, and more likely, is that due to requirement of safe radiation levels, the samples were left for an additional 15 minutes in contact with the water following the last neutron radiograph, before gravimetric analysis could be carried out.

Neutron radiography offers both a visualisation and quantification of the moisture content in the stone[123,125], allowing it to be determined as a function of both height and time, and thus, can be used to investigate water transport kinetics. However, the neutron radiograph results in a 2D image, meaning the results are a summation of the water content across the thickness of the sample[125], and therefore, cannot distinguish between surface content and deep layers, limiting its spatial resolution.

1.3.9 Nuclear magnetic resonance (NMR)

The presence of hydrogen nuclei within a solid can be measured using nuclear magnetic resonance (NMR), which has its basis in the interaction of an external magnetic field with the magnetic dipole moment of a nuclear spin with a non-zero angular momentum quantum number[84,85,132,133]. When a sample is exposed to a static external magnetic field of magnitude B_0, the nuclei in the sample become partially polarised, resulting in a macroscopic magnetisation, $\vec{\mathbf{M}}$, in the same direction as the static field[133]. Application of a radio frequency pulse at a characteristic frequency, ω_L, applied perpendicular to the static magnetic field (which defines the z-direction), results in precession of the macroscopic magnetisation from its equilibrium position at frequency ω_L around the axis of the external magnetic field. This characteristic frequency, known as the Larmor frequency, for an unshielded nucleus is given by:

$$\omega_L = \gamma B_0 \tag{1.10}$$

where γ is the gyromagnetic ratio of the nucleus. The net magnetisation decays due to two independent relaxation processes, resulting in a characteristic free induction decay signal. Longitudinal relaxation describes the recovery of the magnetic component in the direction of the external magnetic field to its equilibrium value, *i.e.*, spin-lattice relaxation, and this occurs with a characteristic relaxation time constant T_1.

The transverse relaxation time, T_2, describes the decrease in magnetisation in the transverse plane, *i.e.*, the dephasing or loss of coherence. In proton NMR relaxometry, this decay signal is proportional to the magnetisation, which is given by:

$$M_{xy}(t) = M_0 \exp\left(\frac{-t}{T_2}\right) \tag{1.11}$$

The initial amplitude, M_0, is directly proportional to the number of hydrogen nuclei present, and therefore, following calibration, the absolute water content within a sample can be determined. This relaxation time constant, T_2, can provide information on the different physical states of water[84] and can determine the amount of water present in different pores, as water present in smaller pores will have shorter relaxation times[129,133]. Thus, using conventional proton NMR, studies have been conducted into the moisture distribution, absorption, drying and characterisation of pore space for a variety of building materials[126–128,130,131]. Comparison of the NMR-determined moisture transport properties with those obtained using gravimetric analysis have shown good agreement[126,128].

A limitation of conventional NMR is that it is a laboratory-based technique and requires samples to be an appropriate dimension for use in the spectrometer[85]. In response to this, portable one-sided NMR devices have been developed, such as the NMR MOUSE[142] and NMR MOLE[143]. However, due to the inhomogeneous magnetic field, these devices have limited sample penetration. For example, the NMR MOUSE has a 2 mm maximum depth of penetration, and thus, for accurate readings, flat surfaces are required to ensure good contact[85,101]. These devices also have a low signal-to-noise ratio, requiring a number of acquisitions[129,132], which can be a time-consuming process and has lead to the recommendation of surveying restricted areas on-site[101]. The use of a single-sided probe, however, allows moisture content to be determined as a function of depth, thus providing information on moisture transport[129,132]. Camaiti *et al.*[129] assessed the performance of a hydrophobic polymer on stone using a single-sided probe, and compared the results with conventional magnetic resonance imaging, reporting good agreement between the two techniques.

The imaging provides visualisation of the water distributed across the whole sample, while the single-sided probe provides measurements on the pore scale.

1.4 Aims and objectives

The main aim of this project is to develop and evaluate a novel technique suitable for quantitative investigations into moisture transport within limestone to allow assessment of the efficacy of conservation treatments for limestone deterioration. This is addressed by the following research objectives:

1. To develop a real-time, high-resolution non-destructive quantitative technique based on laser spectroscopy to monitor water evaporation from limestone, and with the potential to detect specifically and sensitively other degrading chemicals;

2. To demonstrate the universality of the developed instrument in measuring the drying kinetics for different limestones under varying environmental conditions;

3. To investigate the impact of conservation treatments on the water transport kinetics of limestone under different environmental conditions.

The attainment of the aims and objectives are addressed in the remainder of this thesis. Chapters 2 and 3 contain the fundamental theory required to achieve the research aims. Chapter 2 describes the principles of gas and liquid transport through porous media, applying this theory to the understanding of the evaporation of water from stones. A review of the methods of determining pore networks is provided, with focus on the use of mercury intrusion porosimetry and nitrogen adsorption measurements. Chapter 3 describes the fundamental theory of laser absorption spectroscopy and optical techniques employed in this thesis, before detailing the development of the near-infrared cavity ring-down spectrometer and the prerequisite measurements needed before application to the research aims.

Chapters 4, 5 and 6 present the application of the instrument developed to the research aims in the form of three peer-reviewed papers. Chapter 4 describes the first

measurements of moisture content and fluxes from limestone samples using cavity ring-down spectroscopy, including determination of transport kinetics in environments of varying relative humidity. Chapter 5 builds on this work through the application of this technique to a selection of building limestones, and comparison with a sandstone, to demonstrate the universality of the method. Further investigation into the influence of the environmental conditions is achieved by measurements under varying temperatures. Finally, Chapter 6 presents an investigation into the impact of conservation treatments, specifically an ethanol based nanolime consolidant, on the drying kinetics of a limestone sample, conducted at a variety of temperatures. This thesis concludes with a discussion of the findings, a review of the general conclusions and the potential avenues for future work.

Chapter 2

Gas and liquid transport in porous media

The description of the drying of porous media can be generalised in terms of a well-established multi-phase process, which involves both liquid and vapour transport through the material. Usually this is dominated by two main phases which ultimately depend upon evaporation. In this chapter, the background pertinent to understanding transport through porous media is described, considering both saturated and unsaturated liquid flow, and the importance of diffusion in gas transport. Following this, important thermodynamic properties of water are detailed, including adsorption on surfaces and the equilibrium between the liquid and vapour phase. Using this background theory, a description of the two-phase drying process and the associated kinetic parameters is presented using an exemplar data set. The transport properties are dependent on the characteristics of the porous material, both in terms of porosity and connectivity. Descriptions of porous media and methods of characterising the pore network conclude the chapter, where some experimental data pertinent to the samples studied in this thesis are also presented.

2.1 General description of gas and liquid transport

2.1.1 Liquid flow

When a drop of liquid is placed in contact with a solid surface, its contact area will either expand or contract depending on the interactions at the interface that is formed[144]. Figure 2.1(a) shows a cross-section of a liquid drop placed on a solid surface. The three interfaces shown each have an associated surface tension, γ_i, which

is the free energy change required to increase the surface area of a medium by unit area, and therefore, exerts a force which acts in the direction to oppose the increase in surface area of the medium[144,145]. We define the surface tension between the gas and liquid, $\gamma_{g\ell}$, the surface tension between the liquid and solid, $\gamma_{\ell s}$, and the surface tension between the solid and the gas, γ_{sg}. The solid and liquid interfaces meet at the defined contact angle, θ:

$$\cos\theta = \frac{\gamma_{sg} - \gamma_{\ell s}}{\gamma_{g\ell}} \tag{2.1}$$

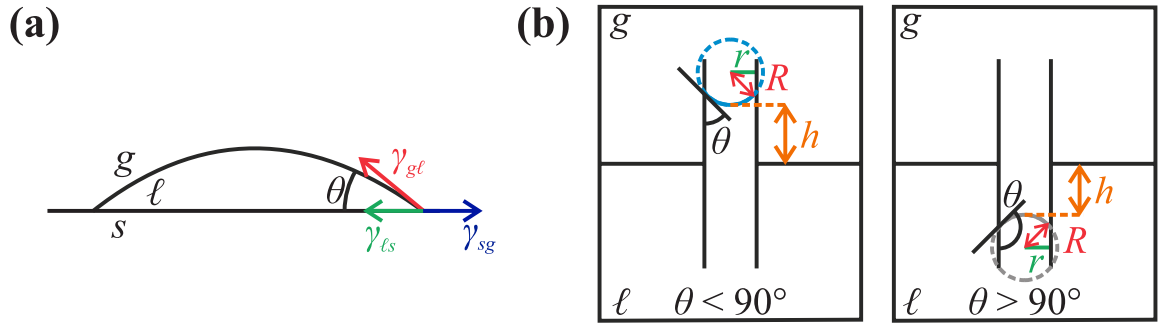


Figure 2.1: **(a)** Cross-section of a liquid drop placed on a solid surface. Note: θ is the contact angle between the solid and liquid interfaces; γ_i are the surface tensions of the solid-gas (sg), solid-liquid ($s\ell$) and liquid-gas ($g\ell$) interfaces. **(b)** Schematic of the capillary action of a wetting liquid ($\theta < 90°$) and non-wetting liquid ($\theta > 90°$).

The degree of wetting of the surface depends on the contact angle, θ, and complete wetting occurs when $\gamma_{sg} \geqslant \gamma_{\ell s} + \gamma_{g\ell}$, and thus, $\theta = 0°$. Partial wetting occurs when $\gamma_{sg} < \gamma_{\ell s} + \gamma_{g\ell}$ and $0° < \theta < 180°$, causing the formation of a droplet on the surface. If $\theta < 90°$, the surface is hydrophilic or *wetting*, and if $\theta > 90°$, it is hydrophobic or *non-wetting*.

Within stone materials, such as limestones, where there exists a pore network through which liquid and gas transport can occur, liquids, such as water, are transported through the network through the action of capillarity. When a capillary of radius r is brought into contact with a liquid, the system acts to minimise the interfacial surface tensions and a meniscus is formed between the liquid and gas phase in the capillary[144]. The shape of the meniscus is part of a sphere of radius R and is related to the radius of the capillary tube, r, by $R = r/\cos\theta$. Wetting liquids have a negative meniscus, and the liquid will absorb into the capillary and rise a height, h,

above the external liquid-gas surface to reach an equilibrium such that the hydrostatic pressure balances the additional force provided by the surface tension, as shown in Figure 2.1(b). A non-wetting liquid, however, will exhibit a positive curvature, with the surface tension providing a force component resisting the flow of liquid into the capillary and the level will be below that of the external liquid-gas surface.

In the absence of a compensatory hydrostatic force, a wetting fluid will continue to flow along a capillary driven by the pressure difference ΔP across the meniscus, where ΔP is described by the Washburn equation[146] for a capillary radius, r, such that:

$$\Delta P = \frac{-2\gamma_{g\ell}\cos\theta}{r} \tag{2.2}$$

This equation forms the basis of several different methods for determining the pore size distribution (explained in Section 2.3).

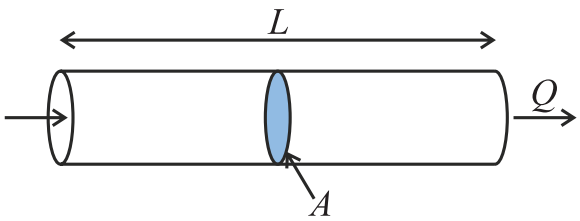


Figure 2.2: A schematic of Darcy's law through a porous medium of length L. The flux of liquid, $\dot{q}$, is determined by the flow rate, Q, through a cross-sectional area, A.

When a porous medium is in contact with a reservoir of wetting liquid, it will absorb liquid until saturation of the material occurs. The flux of liquid, $\dot{q}$, through a saturated porous material is determined by the flow rate, Q, of liquid per cross-sectional area, A, *i.e.*, $\dot{q} = Q/A$, as shown in Figure 2.2. Darcy's law[147] states that the flux of liquid over a length L is proportional to the pressure difference, ΔP, across the material, that is:

$$\dot{q} = \frac{-k_{\text{int}}}{\eta L}\Delta P \tag{2.3}$$

where k_{int} is the intrinsic permeability of the medium [m^2] and η is the viscosity of the liquid [$\text{kg m}^{-1}\ \text{s}^{-1}$]. This equation can be simplified to:

$$\dot{q} = -K\vec{\mathbf{F}} \tag{2.4}$$

i.e., the flux is equal to a constant term, K, which is dependent on the material and liquid [m s^{-1}], and a force term, $\vec{\mathbf{F}}$.

However, in many cases and especially in the work pertinent to this thesis, it is flux through an unsaturated system which is important. In this case, the flux depends upon the volume fraction of liquid present in the material, θ_ℓ, which is defined as the ratio of liquid volume to bulk volume of the material. Thus, an extension of Darcy's law[90] is relevant, which states that:

$$\dot{q} = -K(\theta_\ell)\nabla\Psi(\theta_\ell) \tag{2.5}$$

where $K(\theta_\ell)$ is the same constant as defined in Equation 2.4, except it is now also dependent on the volume fraction, θ, and $\Psi(\theta_\ell)$ is the capillary potential [m], the negative gradient of which is a force (term).

Using the continuity equation[148], which states that the flux of mass into a system is equal to the flux out of it plus accumulation within the system, that is:

$$\frac{\partial\theta}{\partial t} + \nabla\dot{q} = 0 \tag{2.6}$$

and defining a parameter $D_\ell = K(\theta)[\mathrm{d}\Psi/\mathrm{d}\theta]$, then Equation 2.5 rearranges to:

$$\frac{\partial\theta}{\partial t} = \nabla D_\ell \nabla\theta \tag{2.7}$$

where D_ℓ is the capillary liquid diffusivity [m^2 s^{-1}], a quantity which is dependent on the porous material and the liquid.

2.1.2 Gas transport

For the work discussed in this thesis, the key transport process for gaseous molecules is that of diffusion[149]. Diffusion is the movement of matter from an area of high concentration to one of lower concentration as a result of random movements. Fick's first law[150] states that for an isotropic medium, one in which the structure and diffusion properties are uniform in all directions relative to any point, the diffusive flux, $\mathcal{F}$, through an area of cross-section A is proportional to the concentration gradient measured normal to the area:

$$\mathcal{F} = -D\frac{\partial C}{\partial x} \tag{2.8}$$

where C is the concentration, x the coordinate normal to the cross-sectional area and D is the diffusion coefficient. The diffusion coefficient can be described by the Stokes–Einstein equation:

$$D = \frac{k_B T}{6\pi\eta r} \tag{2.9}$$

where k_B is Boltzmann's constant, T is the temperature, η is the viscosity of the fluid and r is the radius of the diffusing species. The time-dependent change in concentration in one dimension is equal to the difference between the flux of molecules entering from an area of high concentration and the flux of molecules diffusing to an area of low concentration, and results in Fick's second law[150]:

$$\frac{\partial C}{\partial t} = D\frac{\partial^2 C}{\partial x^2} \tag{2.10}$$

Fick's second law is the key equation for understanding the diffusion of vapour during the drying process, as shown in Section 2.2.

2.1.3 Thermodynamics of water

Adsorption on surfaces

When a gas is brought into contact with a solid surface, the pressure of the gas is observed to decrease. This is due to the gas molecules adsorbing onto the surface, and this pressure decrease will continue until the rate of adsorption equals the rate of desorption, that is, equilibrium is reached[151].

If the interactions between the adsorbate (gas) and adsorbent (solid) are long-range weak interactions, that is van der Waals interactions, then the process is known as *physisorption*. In physisorption, the enthalpy of adsorption is typically the same order of magnitude as the enthalpy of vaporisation for the adsorbate. If, however, a chemical reaction occurs between the adsorbate and the substrate, then the phenomenon is known as *chemisorption*. As the process involves the formation and destruction of chemical bonds, the enthalpies of adsorption are much larger than those observed in physisorption, being in the range of those typically observed for chemical reactions. For both physisorbed and chemisorbed molecules, the desorption process requires an activation energy to raise the molecules from the bottom of the potential

energy well[152] and desorption is a first order rate process with a rate coefficient, k_{des}, that can be expressed using an Arrhenius relationship:

$$k_{\text{des}} = A \exp\left(\frac{-E_a}{RT}\right) \tag{2.11}$$

where A is the pre-exponential factor and E_a is the activation energy for desorption.

The adsorbed and free gas molecules exist in an equilibrium and the extent of adsorption is dependent on the temperature, the identity of the adsorbate, the nature and availability of the adsorbent, and the pressure of the gas[145]. The relationship between the fraction of surface covered and the gas pressure is described by an adsorption isotherm, the simplest of which is the Langmuir isotherm which has two key assumptions[153]:

(a) Adsorption of a gas molecule can only occur at a finite number of identical sites on the surface of the solid, *i.e.*, only monolayer coverage is possible — this assumes that the surface is atomic in structure with potential energy wells as the sites of adsorption, and if the depth of the wells $\ll k_B T$ then the assumption will break down;

(b) The ability for a gas molecule to bind to a site is independent of neighbouring molecules and the quantum states of the molecule are the same for all sites — if the adsorbed molecules have significant attractive or repulsive interactions, or the surface is significantly heterogeneous, this assumption will break down.

The Langmuir isotherm can be derived from statistical thermodynamics, as shown in Appendix A.1, and is given by:

$$\theta = \frac{KP_\theta}{1 + KP_\theta} \tag{2.12}$$

where θ is the fractional coverage of the surface, K is the equilibrium constant and P_θ is the pressure at which equilibrium between adsorption and desorption occurs. At low pressures, $KP_\theta \ll 1$ and $\theta = KP_\theta$, while at high pressures, $KP_\theta \gg 1$ and $\theta \approx 1$, as shown in Figure 2.3. The Langmuir isotherm, therefore, predicts that the

maximum amount of adsorbate corresponds to monolayer coverage, and while this is true for chemisorption, it is not the case for physisorption, where multiple adsorbed layers are formed.

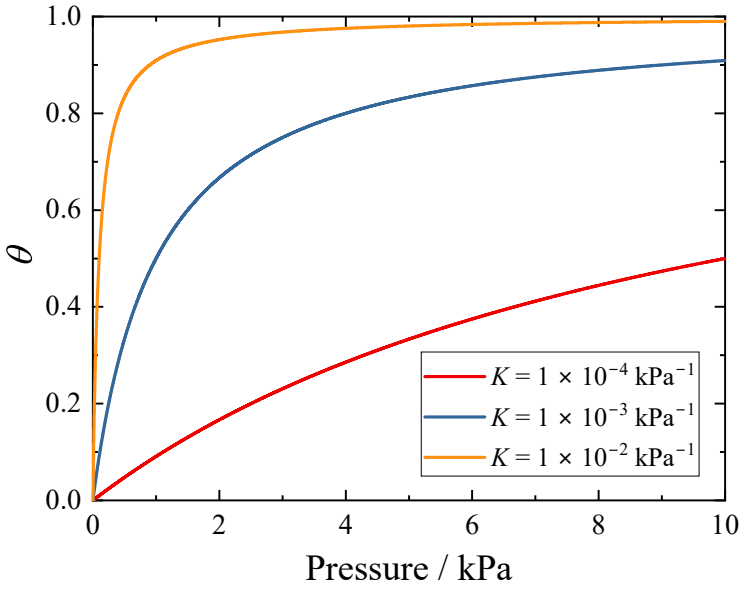


Figure 2.3: Langmuir isotherms plotted using Equation 2.12 with three different values of equilibrium constant, K.

The temperature dependence of the equilibrium constant K from Equation 2.12 can be investigated, and the enthalpy of adsorption can be obtained by application of the van't Hoff equation:

$$\left(\frac{\partial \ln K}{\partial T}\right)_{\theta} = \frac{\Delta H_{\text{ads}}}{RT^2} \tag{2.13}$$

The enthalpy of adsorption determined using this method is based on the assumption that it is independent of the surface coverage. However, for many surfaces it has been observed that the enthalpy of adsorption decreases as θ increases, that is, a larger amount of energy is required to desorb a mole of gas when only a small fraction of the surface is covered[151].

In the case of physisorption, when multiple adsorbed layers are formed, the enthalpy of adsorption approaches the enthalpy of vaporisation for the adsorbate[151,154]. To account for multilayer adsorption, the Brunauer–Emmett–Teller (BET) isotherm[155] was developed. This is an extension of the Langmuir isotherm, and thus, follows the

same assumptions concerning the adsorption onto the surface. One additional assumption which arises is that the enthalpy of adsorption is determined for the first layer, and the enthalpy of vaporisation of the adsorbate applies to subsequent layers[149]. The BET isotherm is given by:

$$\frac{1}{W\left(\frac{P_0}{P}-1\right)} = \frac{1}{W_m C} + \frac{C-1}{W_m C}\left(\frac{P}{P_0}\right) \tag{2.14}$$

where W is the weight of gas adsorbed at relative pressure P/P_0, in which P is the equilibrium pressure and P_0 is the saturation vapour pressure at the absorption temperature, W_m is the specific weight of the adsorbate as a monolayer and C is the BET constant. Figure 2.4 shows a simulation of Equation 2.14 as a function of relative pressure for different values of C.

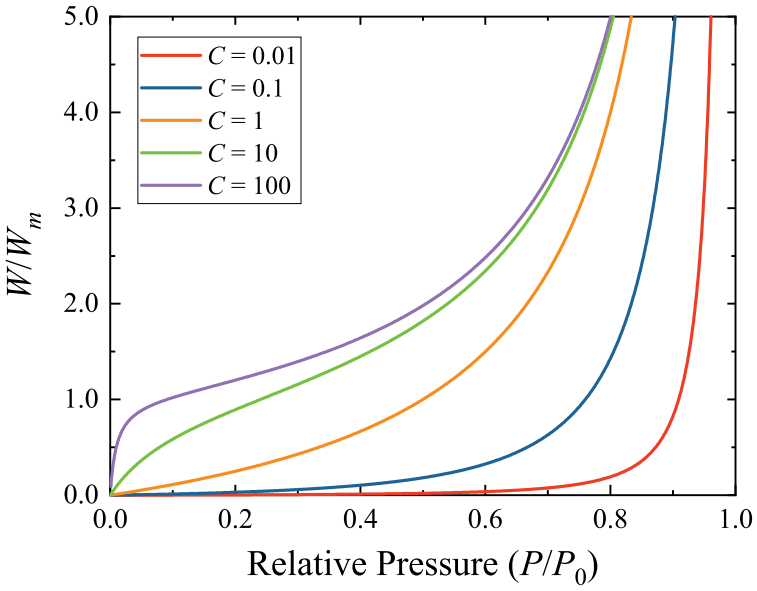


Figure 2.4: BET isotherms plotted using Equation 2.14 with different values of the BET constant, C.

The BET isotherm has been applied to the study of water adsorption isotherms on various substrates, such as silica and calcite[156–158], and in these studies it was found that as the surface coverage increases above monolayer coverage, the enthalpy of adsorption approaches the enthalpy of vaporisation for water ($\Delta H_{\text{vap}} = 44$ kJ mol^{-1}). Meyer and Hackerman[157] investigated how the free energy of adsorption and enthalpy of adsorption varied with specific surface area, and how the integral

enthalpies varied with surface coverage, for three forms of silica — fused, crystalline, and etched. The free energy of adsorption increased for fused and crystalline silica, while decreasing for etched silica, as the specific surface area increased. The integral enthalpies showed a dependence on the crystalline particle size, theorised to be due to the larger particle size resulting in a greater electrostatic force field and subsequent polarization of the hydroxyl groups on the silica surface. Thus, at a given surface coverage, the integral enthalpy of adsorption decreased from the crystalline silica, which have the largest particle sizes, to the fused samples. For a number of samples reported in this study by Meyer and Hackerman the enthalpy of adsorption is less than the enthalpy of vaporisation, but no explanation is given for this behaviour.

Okhrimenko *et al.*[158], in contrast, studied water adsorption isotherms for the three anhydrous calcium carbonate polymorphs — calcite, vaterite and aragonite — and found that all samples adsorb significant amounts of water and exhibit the same trend in enthalpy of adsorption and surface coverage, as shown in Figure 2.5. The enthalpy of adsorption is high at submonolayer coverage but decreases as the coverage increases. The theory and application of the BET method is discussed in more detail in Section 2.3.2.

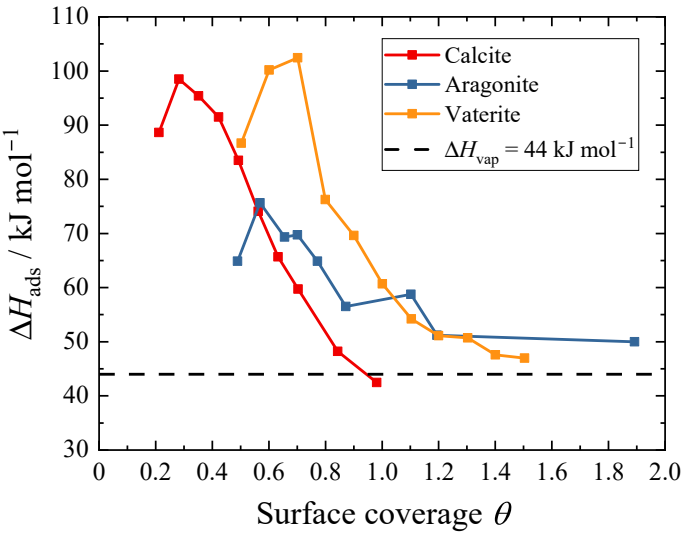


Figure 2.5: Enthalpy of adsorption as a function of surface coverage θ measured over the temperature range $T = 273 - 293$ K for calcite, aragonite and vaterite. The dashed horizontal line represents the enthalpy of vaporisation for water at 298.15 K. *Adapted from Okhrimenko et al.*[158].

Determination of % relative humidity

The rates of gas and liquid transport through a porous medium are dependent on the environmental conditions, such as temperature and % relative humidity (RH). The % RH indicates the concentration of water vapour in the environment relative to the maximum concentration that could be present at the same temperature. Thus, determination of the % RH requires an understanding of how the maximum concentration of water vapour varies with temperature.

Equilibrium between the liquid and vapour phase occurs when the Gibbs free energy for the two phases are equal, and therefore, can only exist under certain temperature and pressure conditions. The Clausius–Clapeyron[149,153] equation describes how the pressure and temperature of the system must vary in order to maintain equilibrium between a liquid and vapour phase, assuming the vapour phase behaves as an ideal gas:

$$\frac{\mathrm{d}\ln P}{\mathrm{d}T} = \frac{\Delta H_{\mathrm{vap}}}{RT^2} \tag{2.15}$$

A relationship between the logarithm of pressure and temperature can then be determined and is encompassed in the Antoine equation[159], which is a semi-empirical description of the vapour pressure, P_v, as a function of temperature, which has the following form:

$$\log P_v = A - \frac{B}{T + C} \tag{2.16}$$

where A, B and C are component specific parameters. Using the reported parameters for water[160,161], the vapour pressure for water can be determined as a function of temperature between $288.15 - 323.15$ K ($15 - 50$ ℃) as shown in Figure 2.6(a).

The % RH can therefore be determined using the following equation:

$$\%\, RH = \frac{P_{\mathrm{H_2O}}}{P_v} \times 100 \tag{2.17}$$

where P_v is the water vapour pressure at the temperature of interest and $P_{\mathrm{H_2O}}$ is the experimentally measured water pressure, further details of which will be given in Section 3.5.4. Determination of the % RH is also important for the calculation of the wet bulb temperature. The wet bulb temperature, T_h, is defined as the temperature

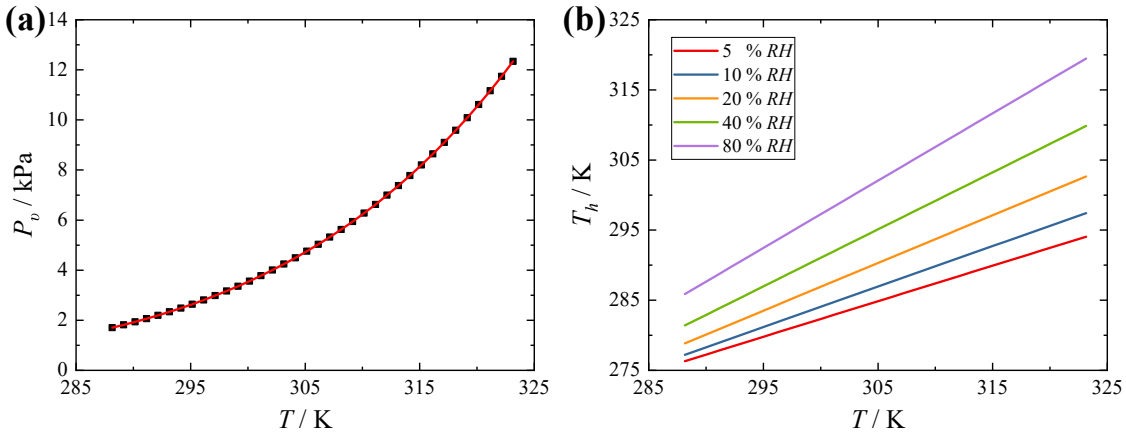


Figure 2.6: **(a)** Plot of the vapour pressure determined using Equation 2.16 as a function of temperatures used in this work. **(b)** Plot of the wet bulb temperature as a function of air temperature for different % relative humidities, determined using Equation 2.18.

a volume of air would measure if it were cooled adiabatically at constant pressure to saturation by evaporation of water into it[162]. The latent enthalpy of evaporation is provided by the volume of air. Thus, the wet bulb temperature is dependent on the saturated water vapour pressure and the air temperature, T_{air}. Stull[163] proposed the following empirical expression for the wet bulb temperature using the % RH and T_{air}:

$$\begin{aligned} T_h = {} & T_{\text{air}} \tan^{-1}[0.151977(\%\, RH + 8.313659)^{1/2}] \\ & + \tan^{-1}[T_{\text{air}} + \%\, RH] - \tan^{-1}(\%\, RH - 1.676331) \\ & + 0.00391838(\%\, RH)^{3/2} \tan^{-1}(0.023101\%\, RH) - 4.686035 \end{aligned} \tag{2.18}$$

Figure 2.6(b) shows the wet bulb temperature as a function of air temperature between 288.15 − 323.15 K for different % RH. Understanding of the wet bulb temperature, and its variation with % RH and air temperature, is important in the understanding of the drying processes of porous materials, especially the evaporation process. When a porous material is saturated with water, it is assumed that the gas immediately above the surface is saturated and the surface temperature is equal to the wet bulb temperature[164,165]. The difference between the wet bulb temperature and the air temperature controls the rate of evaporation from the surface.

Isotopologues of water

The question arises as to how to differentiate between water present in the environment and water contained in the sample, and in this work, this is addressed through the use of isotopologues. An isotope is an atomic species with the same atomic number but different mass number, *i.e.*, a different number of neutrons, for example, hydrogen (^{1}H) and deuterium (^{2}H $\equiv$ D), whereas when a molecule has a different isotopic composition but same chemical formula, it is known as an isotopologue. This is useful because isotopologues have almost identical physico-chemical properties, but clearly have differences which enables them to be distinguished. Water has three hydrogen-based isotopologues: H_2O, D_2O and HDO; when D_2O is in the presence of H_2O, proton exchange occurs and HDO is formed:

$$H_2O + D_2O \rightleftharpoons 2HDO \tag{2.19}$$

This isotope-exchange process reaches a thermodynamic equilibrium which, assuming ideal mixing, can be described by the following equilibrium constant:

$$K_{eq} = \frac{(2\delta)^2}{(x-\delta)(y-\delta)} \tag{2.20}$$

where x, y and δ are the number of moles of H_2O, D_2O and HDO, respectively. Simonson[166] reports a liquid phase equilibrium constant of 3.82 at 298.15 K and 100 kPa, and thus, using Equation 2.20, the thermodynamic number of moles for the three isotopologues can be determined for different mixtures, as shown in Figure 2.7. For the work in this thesis, described in Sections 3.5.5 and 4.3.2, a 10:1 mixture of H_2O and D_2O was produced, and thus, using Equation 2.20, the thermodynamic liquid equilibrium mixture should contain H_2O, D_2O and HDO in approximately the ratios 83:1:16.

2.2 Two-phase drying

This thesis is concerned with the moisture transport kinetics of limestone, and in particular focuses on the drying processes. The main route through which water leaves a porous material is through evaporation, and it is the evaporation process which

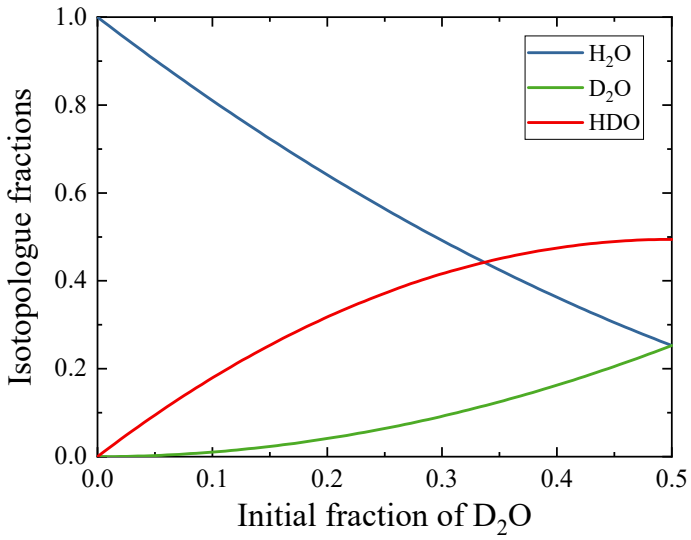


Figure 2.7: Plot of the equilibrium isotopologue fractions determined using Equation 2.20 as a function of initial fraction of D_2O.

drives capillary flow and distributes water through a building structure, controlling the damaging mechanisms such as rising damp and salt crystallisation [90]. The drying of porous materials generally follows a two-phase process [81,90,164,165,167] — a constant drying rate period (phase I) followed by a falling drying rate period (phase II). This is now outlined in more detail.

A schematic of the moisture transport during the drying processes of porous materials is shown in Figure 2.8. Assuming the material is initially fully saturated, Figure 2.8(a), a continuous liquid phase exists throughout the porous solid, and water is supplied to the surface through connected pathways. The water content at the surface is, therefore, sufficiently high that the gas above the surface is fully saturated and there exists a concentration gradient between the surface and the gas above which drives the evaporation process. The rate of evaporation is controlled by the external conditions, and providing the process is conducted under controlled conditions, this will occur at a constant rate. This phase of drying is, therefore, known as the constant drying rate period or phase I, and is reported to be independent of the transport processes within the material [90,164]. The constant drying period is maintained provided that the flow rates through the porous material are sufficient to maintain the surface water content.

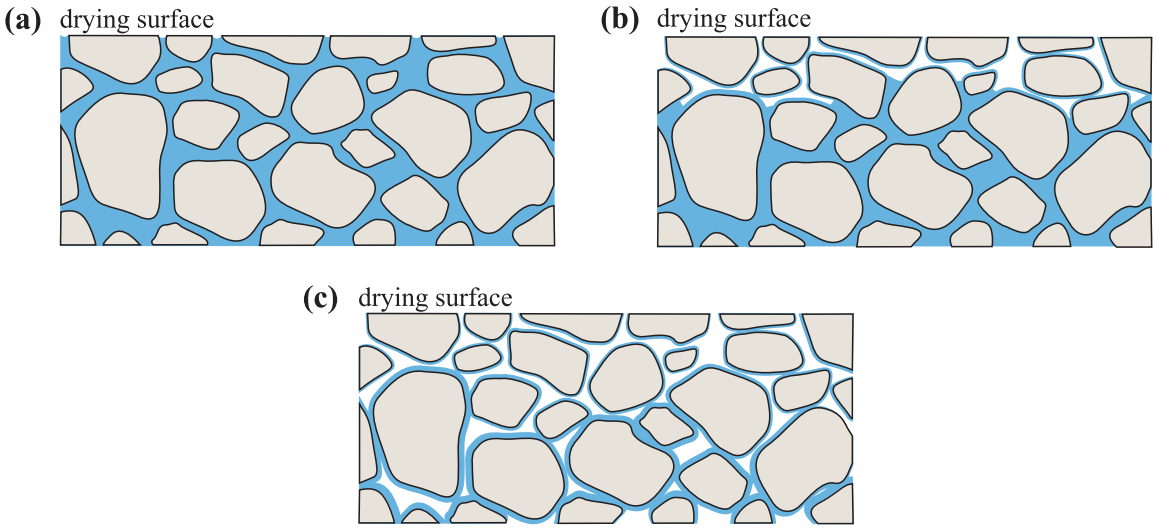


Figure 2.8: Schematic of the moisture transport during the drying processes of porous materials **(a)** initial fully saturated state; **(b)** phase I drying during which capillary transport dominates; **(c)** phase II drying which is dominated by vapour transport.

As the drying proceeds, the water content in the material decreases and the drying front recedes within the material, as shown in Figure 2.8(b). Eventually, the liquid phase becomes discontinuous, Figure 2.8(c), and the water content reaches a critical value at which the flux to the surface is no longer sufficient to maintain the constant evaporation rate. As the rate of evaporation begins to fall, phase II drying begins and this is controlled by the unsaturated flow within the material. Thus, the phase II drying rate is dependent on the phase transitions occurring within the capillary pores and transport *via* the vapour phase[168,169].

Drying kinetic parameters

In drying experiments, it is the change in moisture content as a function of time which is measured, regardless of the method employed. These results are often presented in terms of the normalised mass difference, Δm_n, which may be calculated as:

$$\Delta m_n(t) = \frac{m_{\mathrm{H_2O}}(t)}{m_d} \tag{2.21}$$

where $m_{\mathrm{H_2O}}$ is the mass of water present in the sample and m_d is the dry mass of the sample. Figure 2.9(a) shows an example of the normalised mass difference as a function of time from data collected during the course of this work on drying

limestone. The two-phase drying behaviour is clearly evident. The phase I period is shown with a linear fit and phase II with an exponential decay.

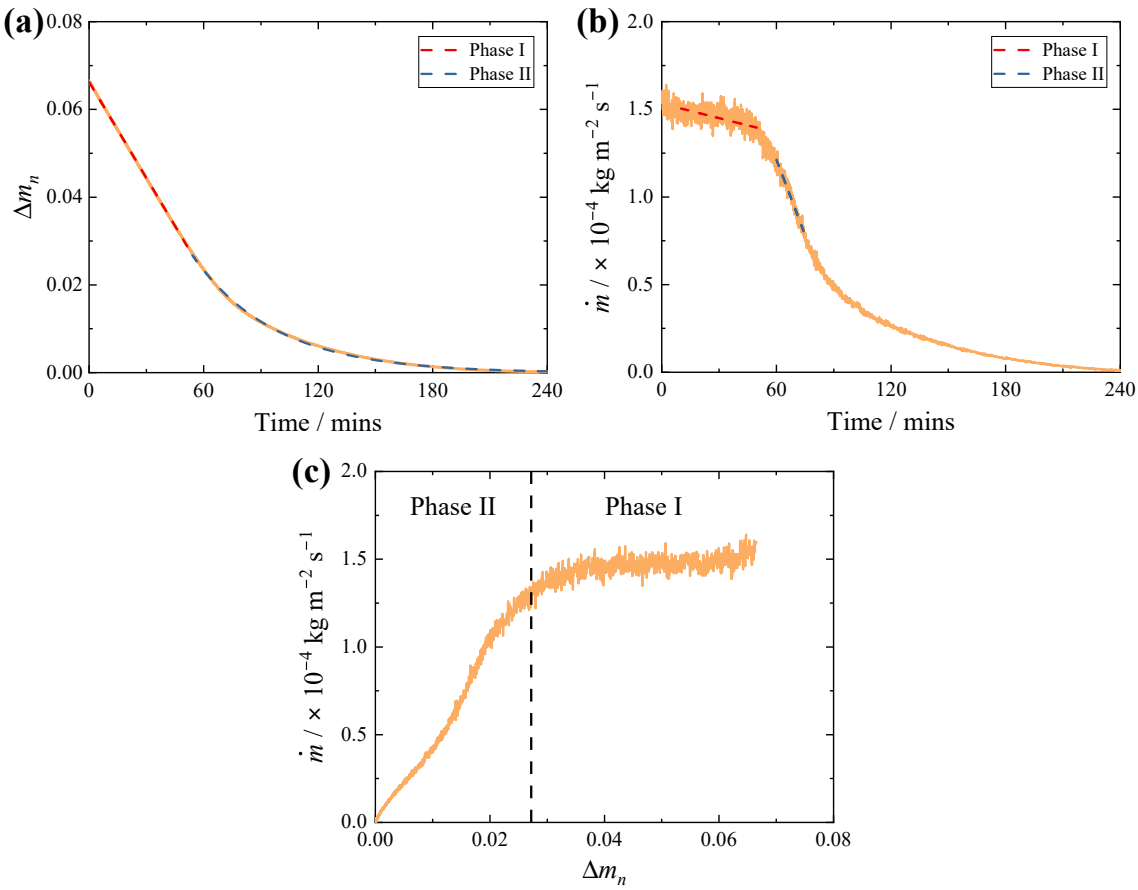


Figure 2.9: **(a)** A plot of the normalised mass difference, Δm_n, as a function of time for a limestone sample dried with a dry flow (1.5 slm N_2) at $T = 298$ K. **(b)** A plot of the mass flux, $\dot{m}$, as a function of time, showing the linear fits to phase I and II to determine the critical time, t_c. **(c)** A Krischer curve showing the mass flux, $\dot{m}$, as a function of normalised mass difference, Δm_n.

As previously described, the main process by which water is lost from a porous material is due to evaporation, and therefore, the data can be presented in terms of the mass flux, $\dot{m}(t)$, from the exposed surface area, A:

$$\dot{m}(t) = \frac{1}{A}\frac{\mathrm{d}m_{\mathrm{H_2O}}}{\mathrm{d}t} \tag{2.22}$$

Using the data presented in Figure 2.9(a), the mass flux has been calculated and is shown in Figure 2.9(b). From Figure 2.9(b) it can be observed that the mass flux at the beginning is nearly a constant value, in accordance with the theory that under

controlled conditions phase I drying would occur at a constant rate, and a linear fit to this region allows determination of the constant drying rate, $\dot{m}_{\mathrm{CST}}$.

The value that $\dot{m}_{\mathrm{CST}}$ should be is a widely debated topic. Some researchers report that the constant drying rate should be, and is found to be, equal to the rate of evaporation from a free water surface, for example, Hall *et al.*[167], Scherer[164], and Bakhshi and Mobasher[168]. However, other researchers[81,170,171] report constant drying rates which differ, and in some cases, are higher than the free water evaporation. Tournier *et al.*[81] hypothesise that the higher evaporation rate of porous materials is due to the greater evaporating surface area caused by the presence of the pores. Bakhshi and Mobasher report an evaporation rate of 1.25 $\times 10^{-4}$ kg m^2 s^{-1} at a pressure of 1.7 kPa, which is lower than the constant drying rate shown in Figure 2.9(b), although comparison is limited due to the differences in conditions as the experiments in this thesis were conducted at atmospheric pressure, and the temperature at which Bakhshi and Mobasher conducted their experiments is not stated.

Phase I is maintained until the water content reaches a critical value and the flow to the surface can no longer maintain this constant rate of evaporation. The critical time, t_c, is defined as the time at which phase I ends and is determined as the intercept between two tangents fitted to $\dot{m}(t)$, denoted by dotted lines in Figure 2.9(b). This parameter is found using an iterative process, based on the analysis described by Castro and Coelho Pinheiro[172], in which the intercept of the two tangents is determined, and this value is set as the upper limit for the tangent to phase I. The process is repeated until a constant value of t_c is determined. The critical saturation, S_c, is defined as the percentage of water remaining in the sample at the end of phase I[82]. Finally, the mass flux, $\dot{m}$, can alternatively be presented in a Krischer curve[88] which plots $\dot{m}$ as a function of the moisture content, as shown in Figure 2.9(c), clearly showing the two-phase behaviour.

The phase I rate of evaporation is driven by the concentration gradient which exists between the surface and the gas above, and thus, the mass flux can be expressed as:

$$\dot{m} = h_m(\rho_{v,\mathrm{surf}} - \rho_{v,\mathrm{gas}}) \tag{2.23}$$

where $\rho_{v,\text{surf}}$ and $\rho_{v,\text{gas}}$ are the vapour densities at the surface of the porous medium and the gas above, respectively, and h_m is the mass transfer coefficient[88,165]. The mass flux is due to convection, and therefore, there is simultaneously a net heat flux, $\dot{q}$, between the porous medium and the environment. The net heat flux is equal to the sum of the heat exchanged *via* vapour flux and the convective heat exchanged between the environment and the material[165]:

$$\dot{q} = h(T_{\text{gas}} - T_{\text{surf}}) - L\dot{m} \tag{2.24}$$

where h is the heat transfer coefficient, T_{gas} and T_{surf} is the gas and surface temperatures, respectively, and L is the latent enthalpy of evaporation (2.5×10^6 J kg^{-1})[88,165].

It is assumed that during phase I the gas above the surface is fully saturated and the surface temperature is equal to the wet bulb temperature[88,164,165], and therefore, $\rho_{v,\text{surf}} = \rho_{v,\text{sat}}$ and $T_{\text{surf}} = T_h$. Due to this saturated vapour layer, it is assumed that there is no heat transfer to the sample and it is all used for evaporation of liquid water. Thus, Equations 2.23 and 2.24 can be rearranged as follows:

$$h_m = \frac{\dot{m}_{\text{CST}}}{\rho_{v,\text{sat}} - \rho_{v,\text{gas}}} \tag{2.25}$$

$$h = \frac{L\dot{m}_{\text{CST}}}{T_{\text{gas}} - T_h} \tag{2.26}$$

Determination of $\rho_{v,\text{sat}}$, $\rho_{v,\text{gas}}$ and T_h using the methods described in Section 2.1.3, when combined with experimental measures of $\dot{m}_{\text{CST}}$, allows evaluation of h_m and h.

Phase I ends when the drying front has receded within the material, resulting in the liquid phase becoming discontinuous and decreasing the flow rate to the surface. Lehmann *et al.*[86] defined a characteristic length, L_c, which is the distance between the evaporating surface and the drying front at the end of phase I, and is determined by capillarity, gravitational and viscous forces. The origin of this characteristic length was illustrated by Lehmann *et al.* using a pair of capillaries, of radius r_1 and r_2, respectively, which are hydraulically connected by a permeable interface, as shown in Figure 2.10.

Initially, the capillaries are completely saturated with water, but as evaporation occurs, capillary menisci are formed with radius R. The largest curvature that the

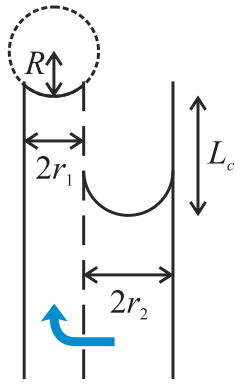


Figure 2.10: A schematic of a pair of capillaries, of radius r_1 and r_2, respectively, that are hydraulically connected by a permeable interface, adapted from Lehmann *et al.*[86]. The characteristic length, L_c, is the distance between the evaporating surface and the drying front, and R is the radius of the meniscus. Water flows (blue arrow) from the large pore to the small capillary as the drying front recedes.

meniscus in the large capillary can attain is equal to the radius of its pore[86,164], *i.e.*, $R = r_2$, and this defines the maximum capillary pressure attainable. As further evaporation occurs from the system, the curvature of the larger pore cannot change, however, the smaller pore can continue to decrease and this results in a pressure difference between the two capillaries. Therefore, as evaporation proceeds and the larger capillary meniscus recedes, water flows into the smaller capillary and the characteristic length increases. It is this capillary mass flow which can support the rate of evaporation and explains why it is observed that larger pores empty first during the drying process[164]. The smaller pore also has a maximum radius of curvature, equal to its pore radius, and therefore, the maximum capillary head pressure, ΔH_{cap}, is given by:

$$\Delta H_{\text{cap}} = \frac{2\gamma}{\rho g}\left(\frac{1}{r_1} - \frac{1}{r_2}\right) \tag{2.27}$$

where γ is the surface tension of water (0.072 N m^{-1}), ρ is the density of water (997.07 kg m^{-3}) and g is the gravitational acceleration (9.81 m s^{-2}).

As the drying front recedes, unsaturated flow within the porous material becomes increasingly important in maintaining the evaporation rate from the surface. Thus, to account for viscous effects and unsaturated flow during evaporation, the evaporation volumetric flux, $\dot{v} = \dot{m}/\rho$, is expressed using the unsaturated variant of Darcy's law

(Equation 2.5) as:

$$\dot{v} = K(\theta)\frac{\Delta H_v}{L_c} \tag{2.28}$$

where $K(\theta)$ is the unsaturated hydraulic conductivity and ΔH_v is the viscous head pressure. By equating the capillary head pressure and viscous head pressure, the characteristic length, L_c, is defined as:

$$L_c = \frac{2\gamma K(\theta)}{\dot{v}\rho g}\left(\frac{1}{r_1} - \frac{1}{r_2}\right) \tag{2.29}$$

Thus, determination of the characteristic length requires knowledge of the unsaturated hydraulic conductivity, which as previously stated in Section 2.1.1 is dependent on the volume fraction, θ, and estimates of the distribution of water content above the drying front.

Prime *et al.*[88] applied this theory of characteristic lengths to the understanding of drying experiments conducted in which the heights of cylindrical samples of Lixhe limestone were varied. They found that the phase I drying flux and duration increased with increasing height, up to a limit of 30 mm, above which both parameters remained constant. They compared this experimental distance with the theoretical characteristic length determined using Equation 2.29, and obtained a characteristic length range of $1.7 - 10$ cm as the degree of surface saturation varies from $50 - 90$ %. They note that only an order of magnitude estimate can be obtained using Equation 2.29 due to its dependence on the unsaturated hydraulic conductivity, which can only be estimated from water retention curves. It should be noted that for the research described in this thesis, the sample lengths are smaller than the characteristic lengths determined by both Prime *et al.* and Lehmann *et al.*[86]. This ensures that once the end of phase I drying has been reached for the samples used in this study, vapour phase transport in phase II is the dominant behaviour.

The phase II drying is well described by Fick's second law, Equation 2.10:

$$\frac{\partial C}{\partial t} = D_{\mathrm{II}}\frac{\partial^2 C}{\partial x^2}$$

where C is the moisture concentration, x is the distance over which moisture transfer occurs, and D_{II} is the phase II diffusion coefficient. Setting C_i as the initial moisture

concentration, the initial boundary condition is:

$$t = 0, \quad C = C_i, \quad 0 \leq x \leq L$$

where L is the thickness of the sample. Assuming the bottom surface of the sample is impermeable, the boundary condition at the bottom is:

$$\text{at} \quad x = 0, \quad \mathcal{F} = -D_{\text{II}} \frac{\partial C}{\partial x} = 0$$

For phase II drying, the concentration at the top surface is equal to the ambient moisture concentration, C_*, and thus, the boundary condition for the top surface is:

$$\text{at} \quad x = L, \quad C = C_*$$

Thus, the phase II diffusion coefficient, D_{II}, is dependent on the moisture concentration. However, assuming the moisture is uniformly distributed, the solution to Equation 2.10 is given by[150]:

$$\frac{C - C_i}{C_* - C_i} = 1 - \frac{4}{\pi} \sum_{n=0}^{\infty} \frac{(-1)^n}{2n+1} \exp\left\{\frac{-D_{\text{II}}(2n+1)^2\pi^2 t}{4L^2}\right\} \cos\left\{\frac{(2n+1)\pi x}{2L}\right\} \tag{2.30}$$

Integrating Equation 2.30 over the sample thickness L allows the mass of water released by the sample in phase II drying at a given time t, $m(t)$, to be obtained and related to the total mass of water released, $m(\infty)$. This is given by[150]:

$$\frac{m_{\text{H}_2\text{O}}(t)}{m_{\text{H}_2\text{O}}(\infty)} = 1 - \sum_{n=0}^{\infty} \frac{8}{(2n+1)^2\pi^2} \exp\left\{\frac{-D_{\text{II}}(2n+1)^2\pi^2 t}{4L^2}\right\} \tag{2.31}$$

It has been reported that the higher terms with $n > 0$ in Equation 2.31 can be neglected during phase II drying, provided that 60 % of the moisture has been lost[168]. To investigate this statement, a simulation of Equation 2.31 for $n = 0$, and $n = 0$, 1, 2 was conducted for $D_{\text{II}} = 5 \times 10^{-9}$ m^2 s^{-1} and $D_{\text{II}} = 1 \times 10^{-8}$ m^2 s^{-1}, assuming $L = 5 \times 10^{-3}$ m (the length that best characterises the geometry of the sample and the design of the experiment), and the results are presented in Figure 2.11.

From Figure 2.11, it can be observed that the additional terms only result in changes at the beginning of the simulation, and confirms that following 60 % water

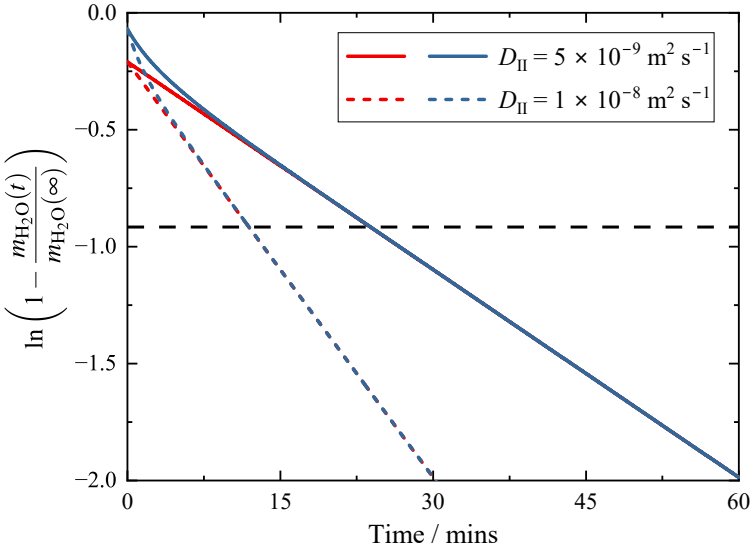


Figure 2.11: A plot of $\ln\left(1 - m_{H_2O}(t)/m_{H_2O}(\infty)\right)$ against time, simulated using Equation 2.31, for $n = 0$ (shown in red), and $n = 0$, 1, 2 (shown in blue), for $D_{II} = 5 \times 10^{-9}$ m^2 s^{-1} and $D_{II} = 1 \times 10^{-8}$ m^2 s^{-1}, assuming $L = 5 \times 10^{-3}$ m. A horizontal line for 60 % water loss is shown.

loss from the material, the higher terms can be neglected. Therefore, the phase II diffusivity can be determined from a linear relationship between the logarithmic terms and time, as follows:

$$\ln\left(1 - \frac{m_{H_2O}(t)}{m_{H_2O}(\infty)}\right) - \ln\left(\frac{8}{\pi^2}\right) = \frac{-D_{II}\pi^2 t}{4L^2} \tag{2.32}$$

As previously noted, the phase II drying is also dependent on the evaporation of liquid water present on the pore surfaces to allow transport *via* the vapour phase. In Section 2.1.3 it was noted that the desorption process has an activation energy associated with it. It is also important to note, that on average, the water vapour diffusing through the porous medium will undergo many surface interactions. Thus, the phase II drying process can be characterised by an activation energy, E_a, which can be determined if an Arrhenius relationship for the phase II diffusivity is assumed[172,173]:

$$D_{II}(T) = D_0 \exp\left(\frac{-E_a}{RT}\right) \tag{2.33}$$

where D_0 is a temperature-independent pre-exponential factor, R is the gas constant and T is the absolute temperature. The activation energy can therefore be determined from the gradient of a linear fit to a plot of $\ln(D_{II})$ against $1/T$.

2.3 The pore size distribution: describing and measuring porous media

It is due to the presence of a pore network within a porous material that water can be absorbed and permeate throughout its internal structure. Thus, understanding of the transport and drying kinetics requires an understanding of the porosity and the pore network present in the materials of interest.

Sedimentary rocks, such as limestone, are formed through the cementation and compaction of carbonate grains and skeletal material[29], resulting in the formation of an intergranular porosity. The porosity of the material may be reduced or gained due to further diagenetic processes[29,90], such as dissolution, compaction and dolomitisation. Therefore, the pore network found in such sedimentary materials will be highly complex, with varying pore sizes and shapes, and will be dependent on the specific material under investigation. Fitzner and Basten[174] proposed a classification of the pore spaces, a schematic of which is shown in Figure 2.12, to describe the complex pore networks found in sedimentary material.

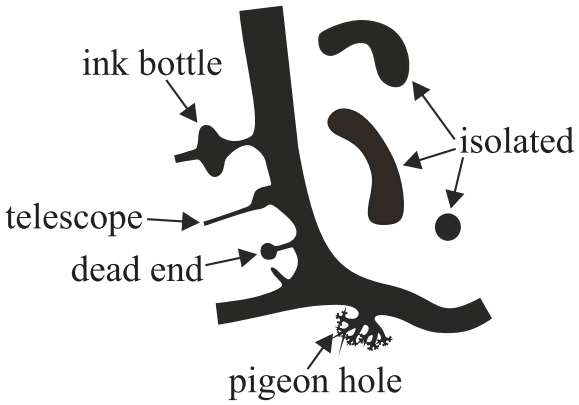


Figure 2.12: Classification of pore spaces using the transmission or penetration criterion. *Adapted from Fitzner and Basten*[174].

However, accurate measurement of such a system is complex, and most methods rely on the oversimplification that the pore network is constructed of cylindrical pores, the size of which is determined using the Washburn equation (Equation 2.2). A classification system based on pore diameters[175] was proposed as follows:

(i) *Macropores*: pore diameters exceeding 0.05 μm;

(ii) *Mesopores*: pore diameters between 0.002 μm and 0.05 μm;

(iii) *Micropores*: pore diameters not exceeding 0.002 μm.

Using the assumption of cylindrical pore geometries, different methods of measuring the porosity and pore network have been developed. These have allowed the various important parameters to be determined that elucidate the percolation properties, which underlie the drying kinetics of the materials of interest. These are now described in the following section.

2.3.1 Important parameters for describing porosity

As demonstrated in Figure 2.12, there exist two different types of porosity — open (or connected) and closed (or disconnected) porosity. For the movement of gases and liquids, it is the open porosity and its connectivity which determines the transport properties of the material. Measurement of the pore network relies on intrusion of a liquid or gas into the material, and therefore, only measures the open porosity[90]. The total intrusion volume is thus equal to the open pore volume of the sample, V_{p}. The bulk volume, V_{b}, of a sample is the total volume of the sample including all pores (both open and closed) as well as the interstitial spaces between particles. The skeletal volume, V_{s}, is the volume of the solid material only, and therefore, is determined by subtracting the pore volume from the bulk volume, *i.e.*, $V_{\mathrm{s}} = V_{\mathrm{b}} - V_{\mathrm{p}}$. From the bulk and skeletal volumes, the corresponding bulk, ρ_{b}, and skeletal, ρ_{s}, densities can be determined, and the open porosity, ϕ, which is defined as[90]:

$$\phi = \frac{(\rho_{\mathrm{s}} - \rho_{\mathrm{b}})}{\rho_{\mathrm{s}}} \tag{2.34}$$

As the porosity of the material increases, the greater the amount of water which can be adsorbed, and therefore, the longer the drying time of the material.

The flow of liquid through the material is described by Darcy's law, Section 2.1.1, which defines the intrinsic permeability, k_{int}, of the material. Measurement of the pore network and its connectivity is, therefore, important in understanding the flow of liquid and can be related to k_{int}. As the pore system is complex, with varying sizes

and connectivity, the path for fluid flow is rarely straight from point A to point B, as demonstrated in Figure 2.13(a). The tortuosity, ξ, is the ratio of the actual distance travelled between the two points, L_t, to the minimum, or straight line, distance between the same two points, L_s [90]; ξ can take a minimum value of unity. Related to this is the tortuosity factor, τ_c, itself defined as ξ/β, where the constriction factor, β, is defined as the ratio of the area of the largest pore with diameter D_{max}, as shown in Figure 2.13(b), to the area of the smallest pore with diameter D_{min}. The tortuosity factor characterises the efficacy of diffusion of fluids through a porous media [176].

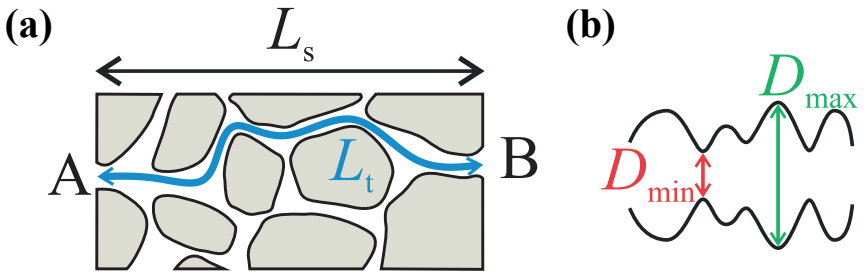


Figure 2.13: **(a)** A schematic showing the straight line distance, L_s, and the tortuous path, L_t, from point A to B; **(b)** A schematic showing the minimum and maximum pore diameters which determines the constriction factor, β.

Clearly the pore structure and tortuosity are important in defining the moisture transport in both phase I and II drying. However, particularly for phase II, the vapour phase adsorption and desorption become important. Thus, knowledge of the available adsorption sites and the internal surface area will aid in understanding the differences observed in the vapour transport.

2.3.2 Methods for probing the pore network

Determination of the open porosity can be achieved through measuring the penetration of liquids or gases into the pore network, for example, using water saturation methods or helium pycnometry. These methods, however, are unable to determine the size and connectivity of the pores and instead methods such as mercury intrusion porosimetry and gas adsorption are required. The various methods are now described, with emphasis particularly on presenting parameters derived using mercury intrusion porosimetry and gas adsorption for the stones used throughout this thesis.

Liquid saturation methods

Determination of the porosity using liquid saturation methods is based on calculating the difference in the saturated mass (m_s) and dry mass (m_d) for a given volume (V) of sample:

$$\phi = \frac{m_s - m_d}{V\rho_\ell} \tag{2.35}$$

where ρ_ℓ is the density of the liquid (usually water)[90]. There are two approaches to achieving saturation — by vacuum saturation or the boiling water method. In vacuum saturation, the sample is placed in a chamber which is evacuated and is then filled with water and returned to atmospheric pressure, leaving the sample to soak for several hours. Alternatively, the boiling water method places the sample in a large container of water which is then brought to the boiling point for several hours. The sample is then left to cool in the water and weighed. In both cases, all water must be completely removed from the samples (to determine m_d) and this is usually achieved by oven-drying the samples at 105 ℃ until they reach constant weight. This, however, may cause alteration of the material structure or composition[177]. Additional problems may arise in achieving saturation, which is dependent on the sample, for example, low porosity samples with small pore sizes will require longer soaking times. Thus, comparison of the two methods shows a large variation in results[90] and for many samples, water may be unsuitable due to its interactions with the material under investigation.

Helium pycnometry

Helium can be considered a non-absorbing, ideal gas which can be used to probe the porosity of building materials. The principle of helium pycnometry is based on Boyle's law which describes the variation of the pressure of a given mass of ideal gas with volume at constant temperature. In a two-chamber pycnometer, a reference cell of known volume is filled with helium at a predetermined pressure. A valve is opened allowing the helium to expand into the second chamber containing a known volume of the sample of interest. Once equilibrium has been reached, the pressure is measured and from this, the skeletal volume, V_s, is determined, and therefore, the porosity of

the sample can be calculated[178,179].

Helium pycnometry is a relatively quick, simple and highly repeatable method of determining porosity. For example, Beck *et al.*[180] reported good agreement between the results obtained using hydrostatic weighing and helium pycnometry for Tuffeau limestone. The sample remains undamaged following measurements, and therefore, can be used in future tests. However, as this method relies on the ideal behaviour of the gas, frequent calibrations are required and variations in the temperature and pressure of the gas must be accounted for in calculations[178]. If the gas absorbs on the surface, then the porosity determined will be higher than the true porosity value, hence the preference for using helium. It has been noted, however, that the use of helium can still result in the overestimation of volumes when the sample has a large specific area[179]. For accurate skeletal volume determination, it is important that equilibrium pressure is reached. If the sample has low porosity or bulk gas diffusivity, this may require longer stabilisation times, and therefore, this increases the chances of temperature and pressure variation[178]. It is also important to note that this method only allows determination of the open porosity, and not the pore size distribution.

Mercury intrusion porosimetry (MIP)

MIP is a ubiquitous method for investigating the pore size distribution and connectivity in porous media, and is utilised in this work to procure sample data which has been further analysed. Mercury is a non-wetting fluid, *i.e.*, it does not absorb spontaneously into pores, and therefore, must be forced into the pore network under increasing pressure. Similar to vacuum saturation methods, the sample is placed in a chamber which is evacuated to remove all contaminants. Mercury is then introduced to the sample, and the amount of mercury entering the sample is monitored as a function of pressure, producing an intrusion curve, as shown in Figure 2.14(a). An extrusion curve is also measured by measuring the amount of mercury released from the pores as the pressure is reduced. MIP measurements were obtained by the British Geological Survey for all stone samples used in this thesis, and the petrophysical properties were determined using the following methods and calculations,

described using Clipsham limestone as exemplar data. Table 2.1 reports the mercury intrusion results for all stone samples used in this thesis.

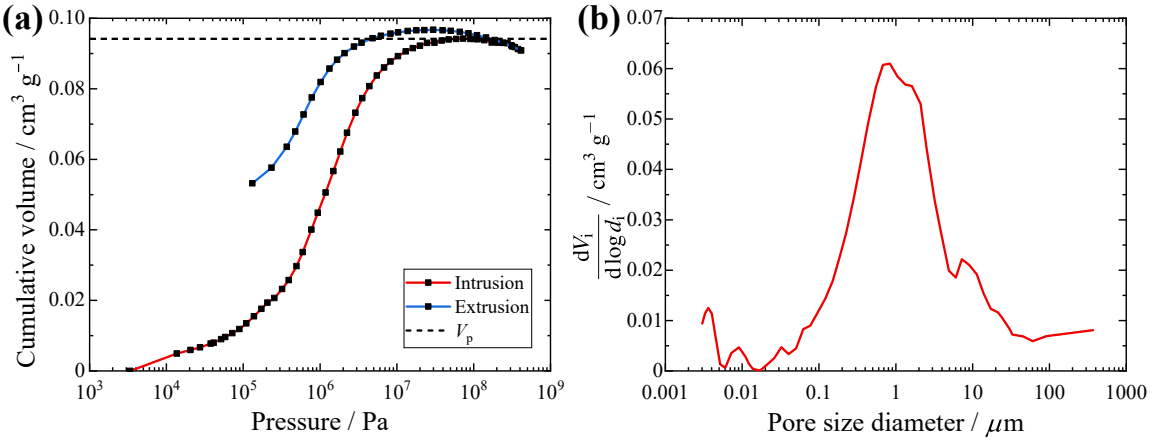


Figure 2.14: **(a)** Raw data measured using mercury intrusion porosimetry, consisting of the cumulative volume against pressure for Clipsham limestone; **(b)** Pore size distribution as commonly reported in literature.

As stated previously in Section 2.3.1, the total intrusion volume is equal to the open pore volume of the sample, V_p, and can be determined directly from the intrusion data, shown by the asymptote in Figure 2.14(a), and thus, for Clipsham limestone, $V_p = 0.09419$ cm^3 g^{-1}. The bulk volume, V_b, of the sample is determined by the difference in mercury volume contained in a receptacle with and without the sample present. As mercury is a non-wetting liquid, and therefore, will not enter the pores, cracks and interparticle voids unless pressure is applied, this difference in volumes is equal to the bulk volume at low pressure. The skeletal volume, V_s, is determined by subtracting the pore volume from the bulk volume, *i.e.*, $V_s = V_b - V_p$. From the bulk and skeletal volumes, the corresponding densities can be determined, *e.g.*, for Clipsham, $\rho_b = 2.14 \pm 2 \times 10^{-4}$ g cm^{-3}, and $\rho_s = 2.68 \pm 2 \times 10^{-4}$ g cm^{-3} (precision determined from instrumental parameters). The bulk and skeletal densities reported in Table 2.1 are in good agreement with literature values[177,181,182], and the skeletal densities are very close to the reported crystallographic densities for calcite, 2.71 g cm^{-3}, and quartz, 2.65 g cm^{-3} [177]. Using Equation 2.34, the open porosity of the samples can therefore be determined, *e.g.*, the Clipsham limestone used in this thesis has an open porosity, ϕ, of 20.16 %.

Table 2.1: Physical properties of the stone samples used in this study determined by mercury intrusion porosimetry by British Geological Survey. V_p = total intrusion volume; A_p = total pore area; ρ_b = bulk density; ρ_s = skeletal density; ϕ = open porosity; d_p = peak pore diameter; d_m = mean pore diameter; P_c = threshold pressure; ℓ_c = characteristic length; σ/σ_0 = conductance formation ratio; k_{int} = intrinsic permeability; τ_c = tortuosity.

Stone	Stoke Hall SH	Portland Whit Bed PWB	Portland Base Bed PBB	Clipsham C	Bath B	Savonnières S
V_p / cm^3 g^{-1}	0.045	0.083	0.085	0.094	0.095	0.172
A_p / m^2 g^{-1}	0.565	1.394	1.339	0.809	1.666	1.465
ρ_b / g cm^{-3}	2.3302	2.2016	2.1874	2.1400	2.1494	1.8253
ρ_s / g cm^{-3}	2.5973	2.6904	2.6951	2.6803	2.7018	2.6624
ϕ / %	10.54	18.17	18.54	20.16	20.44	31.44
d_p / μm	3.84	0.28	0.18 13.95	0.84	0.55	0.15 21.33
d_m / μm	0.32	0.24	0.25	0.47	0.23	0.47
P_c / kPa	295.26	3947.31	80.24	22.39	1336.89	55.61
ℓ_c / μm	4.22	0.32	15.54	55.70	0.93	22.42
σ/σ_0	0.017	0.042	0.021	0.006	0.020	0.030
k_{int} / $\times 10^{-15}$ m^2	1.34	0.02	22.44	82.38	0.08	66.75
τ_c	2.111	2.025	2.021	2.002	1.999	1.875

The advantage of mercury intrusion porosimetry, in comparison with liquid saturation methods and helium pycnometry, is that a pore size distribution can be determined from the intrusion curve using the Washburn equation, Equation 2.2, which relates the applied pressure to the minimum pore size into which mercury can be forced. For mercury, the surface tension, $\gamma_{g\ell}$, is 0.485 N m^{-1}, and the contact angle, θ, is 130°. A pore size distribution is then given by the derivative of the cumulative intrusion volume, and this is commonly displayed in the literature as a lognormal distribution, as shown in Figure 2.14(b) for Clipsham limestone. The peak pore diameter, d_p, is defined as the maximum in the lognormal pore size distribution, and d_p is 0.84 μm for Clipsham. The pore size distributions determined by MIP for the other stones investigated in this thesis are shown in Appendix A.2.

As previously stated in Section 2.1.1, the Washburn equation assumes the pores have a cylindrical shape, with a circular opening, and therefore, a pore wall area can be determined by $A_i = 4V_i/d_i$, where V_i is the incremental intrusion volume and d_i is the average pore diameter determined for the increment. Figure 2.15(a) shows a plot of the cumulative pore area as a function of pore diameter for Clipsham limestone, with a total pore area, A_p, equal to 0.809 m^2 g^{-1}. The mean pore diameter, d_m, is calculated using $d_m = 4V_p/A_p$, and d_m is 0.47 μm for Clipsham.

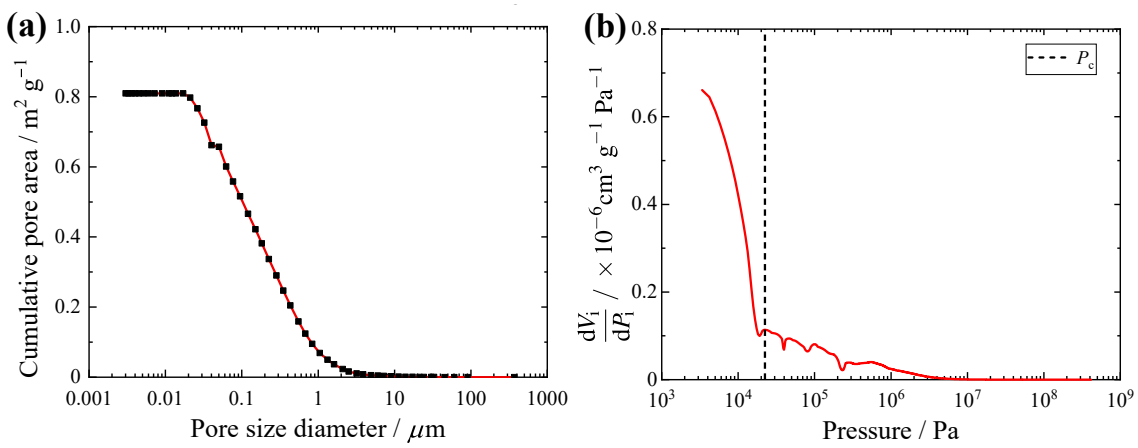


Figure 2.15: **(a)** A plot of the cumulative pore area, determined using $A_i = 4V_i/d_i$, against pore size diameter; **(b)** A plot of the differential volume against pressure, allowing determination of the threshold pressure, and therefore, the characteristic length.

Typically, mercury intrusion curves are sigmoidal shaped, with the point of inflection representing the threshold pressure, P_c, at which mercury can penetrate into the interior of the sample[90]. P_c therefore defines a characteristic length, ℓ_c, which represents the largest diameter of a "test sphere" which can percolate through the pore network. The threshold pressure is determined as the pressure corresponding to the maximum in the differential volume against pressure plot, shown in Figure 2.15(b), excluding the initial decrease. For Clipsham limestone, P_c is equal to 22.39 kPa, and using the Washburn equation (Equation 2.2), corresponds to a characteristic length, ℓ_c, of 55.70 μm. Determination of the characteristic length is important in determining other petrophysical properties, such as the intrinsic permeability which is important for understanding saturated and unsaturated flow.

Katz and Thompson[183] proposed the following relation for intrinsic permeability, k_{int}, assuming cylindrical pore geometry:

$$k_{\text{int}} = \frac{1}{226}\ell_{\text{c}}^2\left(\frac{\sigma}{\sigma_0}\right) \tag{2.36}$$

where ℓ_{c} is the characteristic length previously determined, σ is the electrical conductivity of the material saturated with salt solution of electrical conductivity σ_0. The constant value of 1/226 arises from the assumptions of a cylindrical pore geometry and a very broad pore size distribution, further details of which can be found in Katz and Thompson[183]. As the intrinsic permeability k_{int} is dependent on ℓ_{c}^2, the value of intrinsic permeability can vary over a wide range[90], for example, for the different stones used in this thesis, k_{int} varies from 10^{-17} to 10^{-14} m^2. It is important to note that to use Equation 2.36, the conductance formation ratio, σ/σ_0, must also be measured for the stones under investigation, and this was carried out by the British Geological Survey. Katz and Thompson[183–185] showed good agreement between measured gas permeability values and the intrinsic permeability values calculated using Equation 2.36 for 50 different sedimentary rocks with permeabilities ranging from 5 $\times 10^{-14}$ m^2 to 5 $\times 10^{-12}$ m^2.

As noted in Section 2.3.1, the efficacy of diffusion through a porous material can be characterised by the tortuosity factor, τ_{c}[176]; which is given, assuming cylindrical uniform diffusion paths, by:

$$\tau_{\text{c}} = 2.23 - 1.13V_{\text{p}}\rho_{\text{b}} \tag{2.37}$$

provided that $0.05 \leq V_{\text{p}}\rho_{\text{b}} \leq 0.95$, where V_{p} is the total intrusion volume and ρ_{b} is the bulk density. Therefore, values of τ_{c} are limited to 1.157 to 2.173; for Clipsham limestone, τ_{c} is equal to 2.002.

It is important to acknowledge that several key assumptions are involved in the analysis and transformation of mercury intrusion data that has been set out above. First, the transformation of the mercury intrusion volume into a pore size distribution, using the Washburn equation, assumes that the pores have a cylindrical geometry, and this assumption is reiterated in the determination of other petrophysical parameters

such as permeability and tortuosity. Furthermore, Carniglia[176] defines a cylindrical diffusion path as one in which "the variation in its radius does not exceed the width of a pore group radius interval". In reality, the majority of pores are not regularly shaped and have quite irregular and convoluted shapes[90,186]. Thus, mercury intrusion porosimetry results in an oversimplification of the pore network.

Second, mercury intrusion analysis also assumes that all pores are equally open to the outer surface, and therefore, in contact with the mercury[186]. Instead, most pores are located within the interior of the sample and can only be accessed following percolation through a range of pore sizes and shapes. Thus, if there is a large interstitial void which is only accessible *via* a smaller pore, it would fill at a relatively low pressure only if it was in direct contact with the mercury. However, it will not be filled until the higher pressure required to fill the smaller pore is reached, and at this point, both pores will become filled. This results in the larger pore volume being assigned to the higher pressure interval, and therefore, being associated with the smaller diameter. This effect is commonly referred to as the ink-bottle effect[187–189]. Therefore, rather than interpreting mercury intrusion results as a pore size distribution, it is more accurate to interpret the results as describing the percolation properties of the material, measuring the pressure required to enter the pore throats. The impact of the ink-bottle effect is observed in the hysteresis between the intrusion and extrusion curves shown in Figure 2.14(a). During extrusion, the narrower pore throats break and trap large volumes of mercury in these internal voids[188].

Finally, it is important to note the range of pores accessible using mercury intrusion. In general, pressures up to 414 MPa are applied in mercury intrusion experiments which corresponds to pore diameters of 3 nm[188]. That is, mercury intrusion porosimetry only describes the macro- and mesopore structure and does not access the micropores. Therefore, when mercury intrusion porosities are compared with other methods, such as helium pycnometry or nitrogen adsorption measurements, the porosity may be underestimated, as reported by Beck *et al.*[180].

Nitrogen adsorption

Gas adsorption techniques, such as nitrogen adsorption, allow a greater range of pore diameters to be measured, and inclusion of the micropores results in improved accuracy in surface area measurements[189]. Gas adsorption measurements are based on the principles of physisorption, as described in Section 2.1.3, in particular, multilayer adsorption. As stated previously, it is assumed that the adsorbent surface is a uniform array of adsorption sites and there is no interaction between the adsorbed species, meaning the physically adsorbed species are adsorbed in a random manner across the entire surface[190]. Assuming there are no lateral interactions between the adsorbed molecules, each layer therefore acts as an idealised monolayer. Thus, in physisorption measurements, initially a monolayer is formed in which all the adsorbed species are in contact with the surface layer of the adsorbent. Following this, multilayer adsorption occurs in which the adsorbed molecules in the first monolayer act as sites for adsorption of the second layer, and so forth[175,190]. The thermodynamic stability of the multilayer film depends on the attractive interactions between the gas and wall, and between gas molecules, as well as the curvature of the interface[191], as described later. At a critical thickness, capillary condensation occurs, controlled by these intermolecular forces, and the gas condenses to a liquid-like phase at a pressure less than the saturation pressure of the bulk liquid, P_0. From these pore condensation measurements, the pore size distribution can then be determined.

Nitrogen adsorption measurements consist of measuring changes in the pressure of calibrated nitrogen volumes in contact with the adsorbent[175]. The sample is powdered (typically to less than 1 mm in all dimensions) and is initially outgassed by exposing it to a high vacuum at elevated temperatures to remove any physisorbed species present on the sample. A known amount of pure nitrogen is then introduced to a chamber of known volume containing the sample, which is maintained at a constant temperature of 77 K. As adsorption onto the surface of the sample occurs, the pressure of the chamber falls until an equilibrium is reached. If the amount of gas required to fill the space around the sample is known, then the amount of gas adsorbed onto the surface can be calculated from the amount of gas introduced to the chamber.

The process is repeated by introducing successive volumes of gas to the sample and a point-by-point isotherm can be constructed, as shown in Figure 2.16(a) for Clipsham limestone. The data are presented as the quantity of N_2 adsorbed against the relative pressure (P/P_0), where P is the equilibrium pressure and P_0 is the saturation vapour pressure at the adsorption temperature (in this case, atmospheric pressure). Nitrogen adsorption measurements were procured for all the stones used in this thesis by the Surface Analysis Facility, University of Oxford, and the output data has been further analysed using the following calculations, again described using Clipsham limestone as the exemplar dataset. Table 2.2 reports all the nitrogen adsorption measurements for the stones used in this thesis.

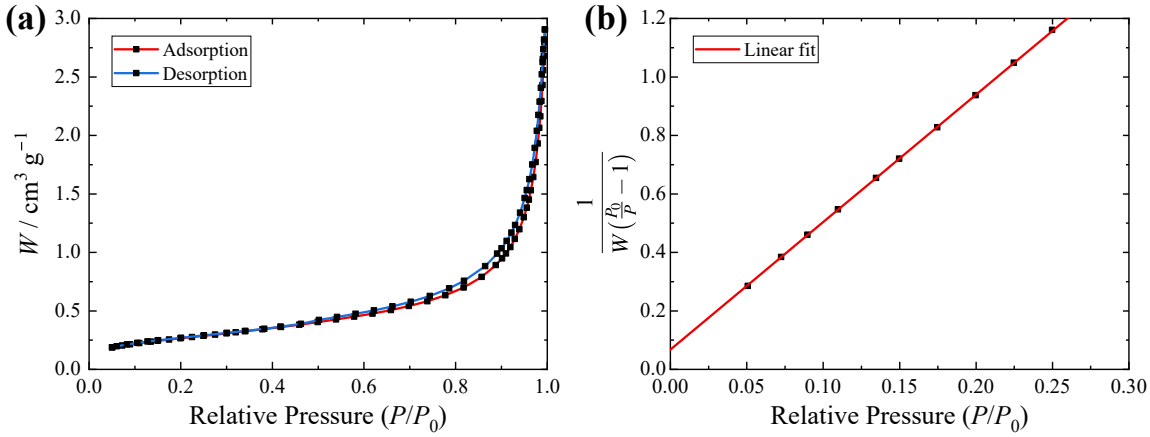


Figure 2.16: **(a)** Raw data measured using nitrogen adsorption, consisting of the quantity adsorbed, W, against relative pressure, (P/P_0); **(b)** A BET[155] linear plot for Clipsham limestone.

The isotherm shown in Figure 2.16(a), and exhibited for all the stones investigated in this thesis, is classified as a Type II isotherm with H3 hysteresis[175]. Most macroporous adsorbents, with little-to-no microporosity, exhibit Type II isotherms and the shape is a result of unrestricted monolayer–multilayer adsorption up to high relative pressures. Completion of monolayer coverage is shown by the presence of a sharp "knee" in the isotherm, as shown in Figure 2.4 when $C = 100$. The lack of a distinctive "knee" and the gradual curvature shown in Figure 2.16(a) indicates that multilayer adsorption is occurring simultaneously with monolayer coverage. The hysteresis observed arises from capillary condensation, and the lower closure limit occurs

Table 2.2: Physical properties of the stone samples used in this study determined by nitrogen adsorption. W_m = monolayer weight; C = BET constant; E_1 = average enthalpy of adsorption for first layer; SSA = BET specific surface area; A_t = t-plot surface area; V_t = t-plot micropore volume; V_{BJH} = BJH cumulative adsorption volume; A_{BJH} = BJH cumulative adsorption surface area; d_{BJH} = BJH average pore diameter.

Stone	Stoke Hall SH	Portland Whit Bed PWB	Portland Base Bed PBB	Clipsham C	Bath B	Savonnières S
W_m / cm^3 g^{-1}	0.346	0.266	0.237	0.226	0.566	0.222
C	69.981	42.682	32.309	65.340	54.151	43.564
E_1 / kJ mol^{-1}	8.330	8.013	7.834	8.286	8.166	8.026
SSA / m^2 g^{-1}	1.505	1.159	1.033	0.984	2.467	0.968
A_t / m^2 g^{-1}	1.626	1.394	1.308	1.058	2.844	1.133
V_t / $\times 10^{-4}$ cm^3 g^{-1}	−0.718	−1.362	−1.623	−0.487	−2.123	−1.004
V_{BJH} / $\times 10^{-3}$ cm^3 g^{-1}	4.249	4.113	4.540	3.963	7.009	3.963
A_{BJH} / m^2 g^{-1}	1.0218	0.889	0.756	0.905	1.769	0.786
d_{BJH} / μm	0.0166	0.0201	0.0240	0.0175	0.0159	0.0192

at a relative pressure which is independent of the adsorbent and dependent on the adsorbate[192]. The H3 hysteresis observed occurs if the macropores have not been completely filled with pore condensate.

The most common method of determining the surface area of porous materials from gas adsorption isotherms is the BET method[155]. The experimentally determined physisorption isotherm is converted into a BET plot by application of the linearised BET equation[155], Equation 2.14:

$$\frac{1}{W\left(\frac{P_0}{P}-1\right)} = \frac{1}{W_m C} + \frac{C-1}{W_m C}\left(\frac{P}{P_0}\right)$$

where W is the weight of gas adsorbed at relative pressure (P/P_0), W_m is the specific weight of adsorbate as a monolayer and C is the BET constant. Figure 2.16(b) shows the BET plot for Clipsham limestone from which W_m and C can be determined using the gradient and intercept of the linear fit. It is important to note that the applicability of the BET isotherm, that is the range of linearity, is restricted to a limited range of pressures, typically $0.05 < P/P_0 < 0.30$ for Type II isotherms.

From Figure 2.16(b), for Clipsham, W_m is equal to 0.226 cm^3 g^{-1} and C is equal to 65.340. The value of C can be used to assess the shape of the isotherm[175], that is, if $C \gtrsim 80$, then there is a well-defined transition from monolayer completion and multilayer adsorption. If, however, $C \lesssim 50$, then there is significant overlap between the monolayer and multilayer adsorption, and therefore, the interpretation of W_m is debatable. For all of the stones investigated in this thesis $C < 80$, and therefore, the results should not be over-interpreted. According to BET theory[155], C is approximately equal to $e^{(E_1 - E_L/RT)}$, where E_1 is the enthalpy of adsorption for the first layer and E_L is the enthalpy of condensation. For nitrogen, $E_L = 5.586$ kJ mol^{-1} and therefore, for Clipsham, $E_1 = 8.286$ kJ mol^{-1}. From Table 2.2, it can be observed that the values of E_1 for the different stones are relatively constant at 8.109 ± 0.171 kJ mol^{-1}. Brunauer, Emmett and Teller[155] also observed that for a given gas this value was approximately constant, irrespective of the adsorbent and its surface chemistry, and report a value of 9.08 ± 0.21 kJ mol^{-1} using nitrogen as the adsorbate. However, they noted that E_1 is the average enthalpy of adsorption and does not taken into account the most active part of the surface as the linear fit does not fit the experimental data for P/P_0 values less than 0.05. Typically, only C values are reported in the literature, with the interpretation that this value can only provide an estimate of the magnitude of the enthalpy of adsorption and not a quantitative measurement[192].

Following the determination of the monolayer weight, W_m, the specific surface area, SSA, of the porous sample can be determined using:

$$\text{SSA} = \frac{W_m N_A A_{cs}}{\overline{V_g}} \tag{2.38}$$

where N_A is Avogadro's number, A_{cs} is the cross-section of the adsorbate ($A_{cs}(\text{N}_2) = 1.62 \times 10^{-19}$ m^2[175]) and $\overline{V_g}$ is the molar gas volume (22400 cm^3 mol^{-1} at standard temperature and pressure). For Clipsham limestone, the specific surface area is 0.984 m^2 g^{-1}.

Determination of the specific surface area using Equation 2.38 requires accurate

knowledge of the adsorbate cross-section, which for nitrogen at 77 K, assuming a close-packed hexagonal monolayer, is 1.62×10^{-19} m^2. Nitrogen is the most commonly used adsorbate for measuring surface properties, partly due to the ready availability of liquid nitrogen. However, nitrogen possesses a quadrupole moment and therefore, when in contact with polar groups on the adsorbent surface, the orientation of the molecule can be affected and this has lead to uncertainty in the adsorbate cross-section [175]. The use of argon at 87 K has been proposed as an alternative [175,189,191] as it does not possess a quadrupole moment.

Although the structure of the nitrogen monolayer is dependent on the surface chemistry of the adsorbent, the multilayer adsorption is insensitive to these interactions [190], and therefore, it is possible to determine the average adsorbed film thickness, t, on pore walls. Determination of the film thickness allows the micropore volume and surface area to be calculated. The nitrogen isotherm, Figure 2.16(a), is converted to a t-plot, Figure 2.17(a), which consists of the quantity adsorbed, n, (now in moles g^{-1}) plotted against the multilayer thickness, t, which is calculated using the following equation proposed by de Boer *et al.* [193], assuming the adsorbed nitrogen layer behaves as condensed liquid with hexagonal dense packing, and provided no capillary condensation occurs and $50 < C < 100$:

$$t = \left[\frac{13.99}{0.034 - \log(P/P_0)}\right]^{\frac{1}{2}} \tag{2.39}$$

The surface area, A_t, can be determined from the gradient of the t-plot using the equation:

$$A_t = \frac{M_r n}{\rho t} \tag{2.40}$$

where $M_r(\mathrm{N_2}) = 0.028$ kg mol^{-1} and $\rho(\mathrm{N_2}) = 808$ kg m^{-3}. From Figure 2.17(a), for Clipsham limestone, A_t is 1.058 m^2 g^{-1}. Standard interpretation of the difference between the surface area determined by BET and that determined using the t-plot would be that this indicates the presence of micropores [191]. However, this difference should be accompanied with a positive y-axis intercept in the t-plot representing the micropore volume, V_t. From Figure 2.17(a), it is clear that the intercept is negative

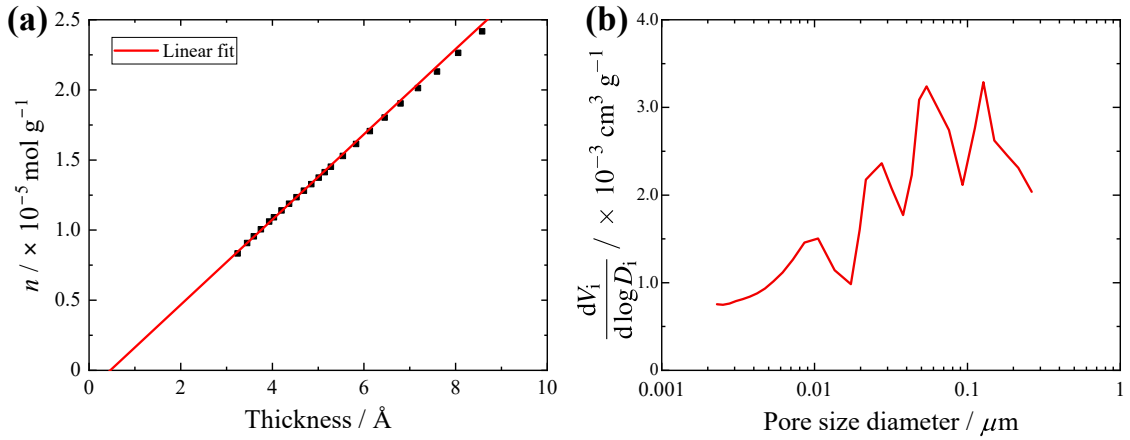


Figure 2.17: **(a)** A plot of the quantity adsorbed against the multilayer thickness, allowing determination of the micropore area; **(b)** Pore size distribution determined from the nitrogen adsorption isotherm, using the BJH method[194].

with V_t equal to -4.865×10^{-5} cm^{-3} g^{-1} for Clipsham. Clearly, a negative micropore volume is impossible and this highlights the problems associated with some of the assumptions and simplifications involved in pore size analysis, such as the applicability of the BET equation or the limit of no pore condensation.

For a given pore size, the adsorbed film has a limited thickness as a consequence of pore filling, concomitant with this and therefore at a critical amount of adsorption, surface tension effects take precedence and drive the condensation towards saturation[191]. Thus, the adsorbed volume is pore size dependent; the relationship between the pore pressure, P, and the saturation pressure, P_0, is given by the modified Kelvin equation[175]:

$$\ln\left(\frac{P}{P_0}\right) = \frac{-2\gamma\overline{V_\ell}}{RTr_k} \tag{2.41}$$

where γ is the surface tension of the liquid, $\overline{V_\ell}$ is the molar liquid volume, R is the gas constant, T is the absolute temperature, and r_k is the Kelvin radius. The pore radius, r_p, however, must take into account the adsorption that has already occurred before condensation, and therefore, is equal to the sum of the Kelvin radius and the thickness of the adsorbed multilayer film prior to condensation, *i.e.*, $r_p = r_k + t$.

Determination of the pore size distribution using gas adsorption measurements follows the Barrett, Joyner and Halenda (BJH) method[194]. The pore radius, r_p, is

determined using Equations 2.39 and 2.41. The weight of gas adsorbed is converted into a liquid volume using the equation $V_i = W_i \times (\overline{V_\ell}/\overline{V_g})$. The cumulative pore volume, V_{BJH}, is then equal to the summation of the pore volumes, and similar to mercury intrusion porosimetry, the pore size distribution is commonly determined as the lognormal derivative of cumulative pore volume against pore size diameter, as shown in Figure 2.17(b). The surface area of the pores is calculated using the relationship $A_i = 2V_i/r_p$, and the cumulative surface area, A_{BJH}, is the summation of pore surface areas. The average pore diameter, d_{BJH}, is calculated from $d_{\mathrm{BJH}} = 4V_{\mathrm{BJH}}/A_{\mathrm{BJH}}$. For example, for Clipsham limestone, $V_{\mathrm{BJH}} = 3.963$ cm^3 g^{-1}, $A_{\mathrm{BJH}} = 0.905$ m^2 g^{-1} and $d_{\mathrm{BJH}} = 0.0175$ μm. The pore size distributions determined by nitrogen adsorption for the other stones investigated in this thesis are shown in Appendix A.3.

It should be noted that the validity of the Kelvin equation in analysis of pore diameters less than 0.01 μm is questionable due to the uncertainties regarding the macroscopic concepts such as surface tension and molar volumes[175,191]. For example, assessment using the BJH method does not account for variations in the thickness of the multilayer film present before condensation, which may be altered due to curvature effects[191]. Thus, it has been reported that these Kelvin based methods, such as the BJH method, underestimate the pore diameters for narrow mesopores ($< 0.01\,\mu$m) by $20 - 30$ %[175,191]. Additionally, the BJH method is based on the theory of pore condensation, however, the isotherms for all the stones investigated in this thesis show the presence of H3 hysteresis indicating incomplete pore condensation, and therefore, this method may lead to an underestimate of the pore surface area.

2.4 Conclusions

The drying data obtained using laser-based spectroscopy presented in later chapters are interpreted with reference to the general theories described here, and in light of benchmark experiments such as MIP and gas adsorption. While both of these are destructive techniques, and therefore, can never both be carried out on the same

sample, they nevertheless provide a general picture of the petrophysical properties of the stone material. The gas adsorption method has a clear advantage over MIP in that it is not limited by the presence of narrow neck pores[189] and therefore, is able to measure narrow mesopores and micropores which MIP is unable to access. Thus, gas adsorption provides greater accuracy in determining the surface area available for vapour adsorption and desorption. However, the various methods of analysing gas adsorption data, such as BET, t-plot or BJH method, do not show very good agreement for the samples investigated in this thesis, as shown in Table 2.2. Each method has key assumptions required for the interpretation of the data, and the results obtained lead to questions regarding the applicability of these methods. Therefore, for the interpretation of the measured drying kinetics of porous media presented later, the gas adsorption measurements provide less information regarding the connectivity of the pore network which mercury intrusion porosimetry, although oversimplified, does.

Chapter 3

Development of an atmospheric pressure cavity ring-down spectrometer

The need for a high-resolution, real-time quantitative method of monitoring moisture in building materials has been highlighted in Chapter 1. This work considers the application of laser absorption spectroscopy, in the form of cavity ring-down spectroscopy, to address this aim. This chapter begins with a summary of the background theory of laser absorption spectroscopy, includes the theory of optical cavities and in particular, the principles of cavity ring-down spectroscopy. Following this, the development of the near-infrared cavity ring-down spectrometer used in this work is described, considering both optimisation of the experimental set-up and the data acquisition program. This chapter concludes with a summary of how this instrument has been used to determine important parameters concerning the spectroscopy of water, such as transition-dependent pressure broadening parameters in a nitrogen atmosphere, the water continuum absorption contribution and the relative abundances of isotopologues.

3.1 Laser absorption spectroscopy

Spectroscopy is the study of the interaction of matter and electromagnetic radiation, which provides information on molecular structure, and the interactions between molecules and their environment[195]. In the most simple case, absorption of energy is most efficient when there is resonance: molecules exist with their electrons and nuclei in discrete quantised energy levels, a transfer between which can be made by

interactions with photons carrying the appropriate amount of energy.

Consider a two-state system described by energy levels E_1 and E_2 and with populations N_1 and N_2, as shown in Figure 3.1, subjected to radiation of frequency ν. A change in the system can be imposed if the energy of radiation is equal to the energy difference between the two levels, *i.e.*, $\Delta E = E_2 - E_1 = h\nu$, where h is Planck's constant. Einstein identified three processes in which radiation may interact with the system, as illustrated in Figure 3.1: these are stimulated absorption, stimulated emission, and spontaneous emission[195,196].

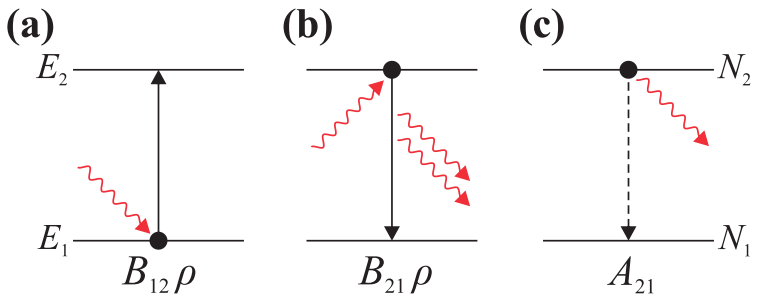


Figure 3.1: A schematic showing the interaction between a two-state system, of energies E_1 and E_2 and populations N_1 and N_2, with electromagnetic radiation of frequency ν such that $\Delta E = h\nu$: **(a)** stimulated absorption; **(b)** stimulated emission; **(c)** spontaneous emission

In stimulated absorption, the molecule absorbs a photon of energy and is excited from the lower energy level E_1 to the higher energy level E_2, Figure 3.1(a). The rate of absorption is described by:

$$\frac{\mathrm{d}N_2}{\mathrm{d}t} = N_1 B_{12} \rho(\nu) \tag{3.1}$$

where B_{12} is the Einstein coefficient of stimulated absorption [$\mathrm{m^3\ J^{-1}\ s^{-2}}$] and $\rho(\nu)$ is the spectral energy density of radiation per unit frequency [$\mathrm{J\ m^{-3}\ Hz^{-1}}$][196].

Stimulated emission occurs when upon interaction with the electromagnetic radiation, molecules in the higher energy state E_2 are transferred to the lower energy state E_1, Figure 3.1(b). In this process an additional photon of energy $h\nu$ is emitted in phase and with the same frequency as the incident photon (*i.e.*, they are coherent), and the rate of emission is given by:

$$\frac{\mathrm{d}N_2}{\mathrm{d}t} = -N_2 B_{21} \rho(\nu) \tag{3.2}$$

in which B_{21} is the Einstein coefficient of stimulated emission [m^3 J^{-1} s^{-2}], and provided the degeneracy of the two states is the same, is equal to the Einstein coefficient of stimulated absorption, *i.e.*, $B_{12} = B_{21}$.

The third process is spontaneous emission, Figure 3.1(c), in which an excited molecule spontaneously relaxes to the lower energy level and emits a photon of energy $h\nu$ in a process that occurs independently of the presence of a radiation field. Photons emitted from an ensemble of excited stated species in this case are incoherent, that is, they have no fixed phase relation. For spontaneous emission, the rate of loss from $|E_2\rangle$ is:

$$\frac{\mathrm{d}N_2}{\mathrm{d}t} = -N_2 A_{21} \tag{3.3}$$

where A_{21} is the Einstein coefficient of spontaneous emission [s^{-1}]. The overall rate of change in population of N_2 is therefore given by:

$$\frac{\mathrm{d}N_2}{\mathrm{d}t} = (N_1 - N_2)B_{12}\rho(\nu) - N_2 A_{21} \tag{3.4}$$

The photon energy flux is the product of the photon energy flow per unit area and an absorption cross-section[197], and therefore, the Einstein B_{12} coefficient is related to the absorption cross-section, $\sigma(\nu)$, and the speed of light, c, by:

$$B_{12} = \frac{c}{h\nu}\int \sigma(\nu)\mathrm{d}\nu \tag{3.5}$$

3.1.1 Beer–Lambert Law

The fact that atoms and molecules can absorb and emit light of a particular wavelength — depending on their unique set of energy levels — is encompassed, from a practical point of view, in the Beer–Lambert law. Consider a monochromatic beam with frequency ν, resonant with a molecular transition, and intensity I, passing a distance L through a sample of molecules. The density of photons in the beam could increase due to stimulated (or spontaneous) emission and decrease through the process of stimulated absorption, resulting in an overall change in the intensity of the radiation. In the most basic scenario, there is initially much more population in the lower energy level than in the upper, and the spectral energy density, $\rho(\nu)$, is

insufficient for there to be efficient 'pumping' of the ensemble of molecules between the two energy levels. In this case, the relationship between the initial intensity, I_0, and the intensity of light after it has passed through the sample, I_{tr}, is given by the Beer–Lambert law[149,195,196]:

$$I_{\mathrm{tr}} = I_0 \exp[-\alpha_{\mathrm{INT}} L] \tag{3.6}$$

where α_{INT} is the absorption coefficient integrated over the absorption profile [cm^2 cm^{-1}], and is related to the integrated absorption cross-section, σ_{INT}, for a sample of concentration N by:

$$\alpha_{\mathrm{INT}} = N\sigma_{\mathrm{INT}} = N \int_{\nu_1}^{\nu_2} \sigma(\nu) \mathrm{d}\nu \tag{3.7}$$

As given by Equation 3.5, the integrated cross-section is related to the Einstein B coefficient, and has been calculated and tabulated for many of the molecules of interest in various online databases, such as the HITRAN[198] database for atmospherically important molecules. The integrated absorption coefficient and absorption cross-section can be used directly to determine the concentration of absorbing species present in the sample provided the entire absorption profile has been measured. If, however, only the absorption coefficient at a specific frequency ν is measured, then the frequency-dependent absorption cross-section, $\sigma(\nu)$, must be used, which is dependent on the broadening mechanisms perturbing the transition or influencing the measurement. These effects are captured in various spectral line broadening mechanisms outlined in the following section.

3.1.2 The width and shape of spectral lines

In the previous discussion in Section 3.1, it was stated that the system had discrete energy levels and a change could only occur if $\Delta E = h\nu$, which would result in infinitely sharp spectral lines[197]. However, in reality this is not strictly observed and instead a distribution of frequencies is generally observed around the resonant frequency, $\nu_0 = (E_k - E_i)/h$. The shape of this distribution is dependent on the environmental conditions, and can be broadly divided into two categories[196]: homogeneous broadening which affects all molecules equally; and inhomogeneous broadening

in which the probability of absorption is not equal for all molecules, and therefore, results in different broadening depending on some physical parameter, for example, the velocity of the molecules. For the work pertinent to this thesis, the three mechanisms of broadening that need to be considered are natural, collisional and Doppler broadening.

Natural line broadening

Natural broadening is an example of homogeneous broadening, which is a fundamental quantum-mechanical contribution arising from the uncertainty in the transition energy, ΔE. This is described by the Heisenberg uncertainty principle[149,152]:

$$\Delta E \geq \frac{h}{2\pi\tau} \tag{3.8}$$

where τ is a combination of the lifetimes of the states involved in the transitions ($1/\tau = 1/\tau_1 + 1/\tau_2$). Where the lifetime of the lower state is very long, for example, if it is a ground state, then clearly ΔE is determined only by the lifetime of the upper state. The shorter the lifetime of the states involved in a transition, then the greater the uncertainty in their energies, and therefore, the broader the spectral line. However, at room temperature, and in the work described within this thesis, the natural broadening is orders of magnitude smaller than the other broadening mechanisms encountered and so can be neglected.

Collisional broadening

Another example of homogeneous broadening is pressure, or collisional, induced broadening which can be the result of both elastic and inelastic collisions[196]. In inelastic collisions, the lifetimes of the upper and lower states are potentially reduced, which from Equation 3.8, leads to an increase in the uncertainty in the energy of the transition. Elastic collisions result in a change in the phase of the transition, causing an increase in the distribution of frequencies associated with the transition and its subsequent broadening. Collisional broadening results in a Lorentzian line

shape, $L(\nu)$:

$$L(\nu) = \frac{2}{\pi} \frac{\Delta\nu_p}{\Delta\nu_p^2 + 4(\nu - \nu_0)^2} \tag{3.9}$$

where ν_0 is the central frequency of the transition and $\Delta\nu_p$ is the full-width half-maximum (FWHM) Lorentzian width. The magnitude of the broadening is dependent on the rate of collisions, and therefore, on environmental conditions such as pressure, as well as the identity of the colliding species. Thus, the Lorentzian width, $\Delta\nu_p$, is equal to:

$$\Delta\nu_p = 2 \sum_i \gamma_i p_i \tag{3.10}$$

where γ_i is the species-dependent broadening coefficient of a given transition [cm^{-1} atm^{-1}] and p_i is the partial pressure of the species i in the sample [atm]. The self-broadening coefficient, γ_{self}, is available in the HITRAN[198] database, as well as that for a standard air mixture, γ_{air}. Typical values of γ_{air} are of the order of 0.05 cm^{-1} atm^{-1}, while γ_{self} is several times larger for polar molecules. The work described in this thesis, however, was conducted in a nitrogen atmosphere, and therefore, the broadening coefficients for a nitrogen atmosphere were determined experimentally, *vide infra*.

Doppler broadening

The final contribution to spectral line broadening considered here is the inhomogeneous process of Doppler broadening, which arises from the thermal motion of molecules[196]. As the molecules in the sample move in all directions at a range of velocities, the apparent frequency of the radiation which interacts with the molecule is Doppler shifted. The shift is determined by the relative motion of the absorbing molecule with respect to the direction of propagation of the radiation. At a given temperature, the molecules have a Maxwellian, or thermal, distribution of velocities. This results in the observation, in the laboratory frame of reference, of the absorption or emission of a distribution of frequencies around the resonant frequency ν_0 which can be described by a Gaussian line shape, $G(\nu)$:

$$G(\nu) = \frac{2}{\Delta\nu_G} \sqrt{\frac{\ln 2}{\pi}} \exp\left\{ \frac{-4 \ln 2 (\nu - \nu_0)^2}{\Delta\nu_G^2} \right\} \tag{3.11}$$

where $\Delta\nu_G$ is the full-width half-maximum, which is given by:

$$\Delta\nu_G = \nu_0\sqrt{\frac{8k_BT\ln 2}{mc^2}} \tag{3.12}$$

where T is the sample temperature and m is the mass of the molecule. Equation 3.12 shows how $\Delta\nu_G$ depends on the frequency of the transition, ν_0, and thus, at room temperature is of the order of a few hundred MHz in the near-infrared spectral region relevant here.

The Voigt Profile

At atmospheric pressure and room temperature, both collisional and Doppler broadening have significant contributions to the line shape, and the resultant absorption profile is a convolution of the Lorentzian (Equation 3.9) and Gaussian (Equation 3.11) line shapes, known as the Voigt profile[199]:

$$V(\nu) = \frac{2}{\Delta\nu_G}\sqrt{\frac{\ln 2}{\pi}}\frac{y}{\pi}\int_{-\infty}^{\infty}\frac{\exp(-t^2)}{y^2+(x-t)^2}\mathrm{d}t \tag{3.13}$$

where x and y are given by:

$$x = \sqrt{\ln 2}\frac{2(\nu-\nu_0)}{\Delta\nu_G} \tag{3.14}$$

$$y = \sqrt{\ln 2}\frac{\Delta\nu_p}{\Delta\nu_G} \tag{3.15}$$

Figure 3.2 shows a comparison of these three line shapes, with the same integrated area and FWHM. In the Voigt profile shown, the Gaussian and Lorentzian contributions are equal. For the work pertinent to this thesis, the Voigt profile is the most appropriate line shape: at room temperature and atmospheric pressure the Lorentzian contribution to the Voigt profile is $\Delta\nu_p \approx 3$ GHz compared to $\Delta\nu_G \lesssim 1$ GHz.

If, as stated in Section 3.1.1, it is required to determine the concentration of a species using the absorption coefficient measured at the central frequency, ν_0, then the peak absorption cross-section, σ_p, must be calculated from the integrated absorption cross-sections tabulated in HITRAN[198] using:

$$\sigma_\mathrm{p} = \frac{\sigma_\mathrm{INT}}{\Gamma\Delta\nu_\mathrm{FWHM}} \tag{3.16}$$

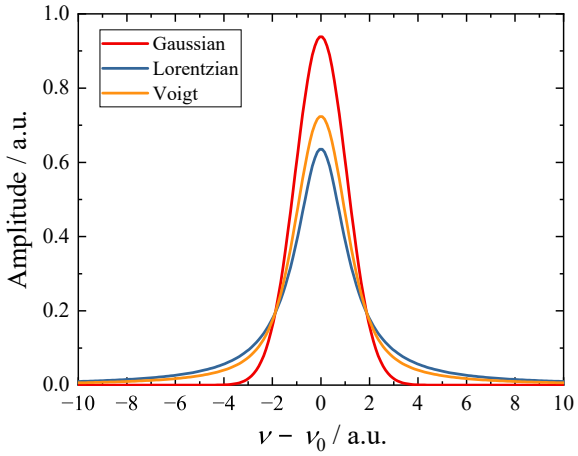


Figure 3.2: Gaussian (red), Lorentzian (blue) and Voigt (orange) line profiles. All line shapes have equal integrated areas and FWHM. For the Voigt line shape, the Gaussian and Lorentzian contributions are equal.

where $\Delta\nu_{\mathrm{FWHM}}$ is the full-width half-maximum of the absorption profile and Γ is the line shape parameter[200].

3.2 Properties of optical cavities

The Beer–Lambert law, Equation 3.6, states that the absorption of light after it passes through a sample is dependent on the concentration of the target species, N, the absorption cross-section of the transition, $\sigma(\nu)$, and the path length of absorption, L. Therefore, increasing the absorption, and thus, increasing the sensitivity, is possible by increasing one of these parameters. Often it is not feasible to increase the first parameter as it is concentration of the target species that is the desired parameter to be determined. Thus, there are two methods of increasing the sensitivity: selecting a transition for which the absorption cross-section is the highest, which is dependent on spectroscopic selection rules and the wavelength region of the laser selected; or more commonly, by increasing the path length over which the radiation passes through the sample. One method of achieving this increase in path length is through the use of a multipass cell, for example, a White cell[201] or Herriott cell[202]. These systems are designed such that the light is traverses back-and-forth between two (or more) mirrors, whose radius of curvature and separation are chosen so as to direct the light

on a different optical path following each reflection. Thus, it is possible to obtain path lengths of hundreds of metres, but this requires the use of relatively large mirrors and cell volumes.

An alternative method is the use of optical cavities which consists of two (or more) highly reflective mirrors aligned such that radiation is trapped inside the cavity and traverses along the same optical path between the mirrors. The simplest optical cavity, and one pertinent to the work described in this thesis, is a linear coaxial cavity in which two concave high reflectivity mirrors are facing each other separated by a distance L. When an optical cavity is illuminated by a coherent, white light source, the ratio of the transmitted radiation, I_{tr}, to incident radiation, I_0, is given by the Airy function[196]:

$$\frac{I_{\mathrm{tr}}}{I_0} = \frac{(1-R)^2}{(1-R)^2 + 4R\sin^2(2\pi\nu L)} \tag{3.17}$$

where R is the geometric mean mirror reflectivity and ν is the optical frequency. Figure 3.3 shows a simulation of Equation 3.17 for different mirror reflectivities, showing a comb-like transmission profile consisting of equally spaced longitudinal modes. A longitudinal mode is formed within the cavity when the separation between the cavity mirrors is equal to an integer number of half wavelengths, *i.e.*, $L = q\lambda/2$. The frequency separation between two longitudinal modes is known as the free spectral range, $\Delta\nu_{\mathrm{FSR}}$, and is given by:

$$\Delta\nu_{\mathrm{FSR}} = \frac{c}{2nL} \tag{3.18}$$

where n is the refractive index of the intracavity medium.

An important property of optical cavities is the ability for the cavity to maintain constructive interface over the extended path length upon perturbation, known as the cavity finesse, $\mathscr{F}$, which is given by:

$$\mathscr{F} = \frac{\pi\sqrt{R}}{1-R} \tag{3.19}$$

The cavity modes are described by an Airy profile and each resonance within the cavity transmission has representative FWHM, $\Delta\nu_{\mathrm{mode}}$, known as the cavity bandwidth,

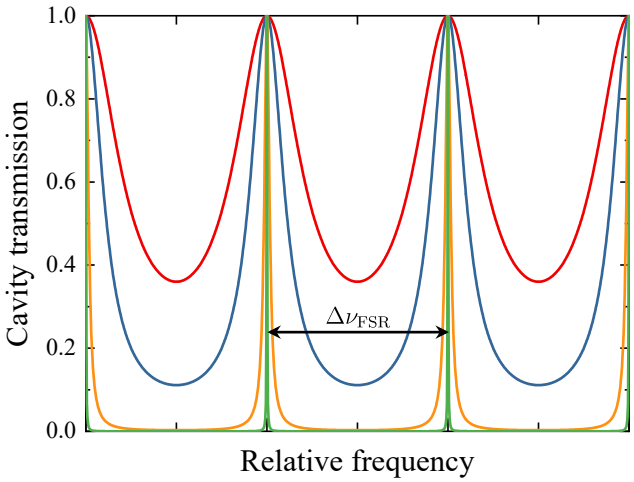


Figure 3.3: A simulation of the cavity transmission using the Airy function, Equation 3.17, with varying values of mirror reflectivity, R, of 0.25 (red), 0.5 (blue), 0.9 (orange) and 0.99 (green). The free spectral range, $\Delta\nu_{\mathrm{FSR}}$, is the frequency difference between two maxima.

which is equal to the ratio of the free spectral range to the cavity finesse:

$$\Delta\nu_{\mathrm{mode}} = \frac{\Delta\nu_{\mathrm{FSR}}}{\mathscr{F}} \tag{3.20}$$

Thus, the higher the reflectivity of the mirrors, the higher the finesse, and therefore, the narrower the cavity bandwidth. The circulating power in the cavity is proportional to the finesse[203].

To support the modes within the cavity and maintain low diffraction losses, the cavity geometry must be configured for optical stability and effectively trap the radiation during cavity round-trips[196,204]. The stability is, therefore, dependent on the mirror separation distance, L, and the radius of curvature of the mirrors, r_i, and can be quantified by the g-parameters for the mirror:

$$g_i = 1 - \frac{L}{r_i} \tag{3.21}$$

such that a cavity is defined as being optically stable if:

$$0 < g_1 g_2 < 1 \tag{3.22}$$

For a cavity consisting of two mirrors with an identical radius of curvature, this expression reduces to $0 < L < 2r$[203], and there exist certain geometries which

are on the edge of stability, such as symmetric confocal ($r_1 = r_2 = L$), concentric ($r_1 = r_2 = L/2$) and plane parallel ($r_1 = r_2 = \infty$) geometries[204].

As previously stated, the resonance condition for a longitudinal mode states that the mirror separation must be equal to an integer number of half wavelengths, which is concomitant with a round-trip phase (ϕ) invariance (*i.e.*, 2π). However, it is also possible to excite other resonant modes in a cavity which fulfil this phase criteria but have distinct spatial characteristics. These are called transverse modes, denoted as TEM_{mn} modes where TEM stands for Transverse ElectroMagnetic[203].

Generally, assuming the intracavity radiation propagates in a direction parallel to the optical axis of the cavity, the intensity distributions of the transverse modes can be described using the Hermite–Gaussian TEM_{mn} mode set, where m and n specify the number of nodes along the x- and y- Cartesian axis. The amplitude distribution, A_{mn}, is given by[196]:

$$A_{mn}(x, y, z) = \mathscr{H}_m\left(\frac{\sqrt{2}x}{w}\right)\mathscr{H}_n\left(\frac{\sqrt{2}y}{w}\right)\exp\left(\frac{-r^2}{w^2}\right)\exp[-i\phi(z, r, R)] \tag{3.23}$$

where $\mathscr{H}_m$ is the Hermitian polynomial of the m^{th} order, $r^2 = x^2 + y^2$, and w is a measure of the radial intensity distribution, known as the spot size, *vide infra*. The first Hermite polynomials are given by[204]:

$$\mathscr{H}_0(x) = 1; \quad \mathscr{H}_1(x) = 2x; \quad \mathscr{H}_2(x) = 4x^2 - 2; \quad \mathscr{H}_3(x) = 8x^3 - 12x \tag{3.24}$$

The intensity distribution $I_{mn} \propto A_{mn}A^*_{mn}$, and thus, can be derived using Equations 3.23 and 3.24. Figure 3.4 depicts theoretical intensity profiles for the fundamental mode, TEM_{00}, and higher order modes, TEM_{01} and TEM_{03}, in the xy plane.

The frequencies of resonant modes inside the cavity are given by[196,204]:

$$\nu_{qmn} = \frac{c}{2L}\left[q + \frac{m + n + 1}{\pi}\cos^{-1}\sqrt{g_1 g_2}\right] \tag{3.25}$$

where q, m, n are the mode indices, which defines the gross frequency of the mode (q) and the spatial variation of the electric field in the plane perpendicular to the cavity axis (m, n). Longitudinal modes of the same transverse order, therefore, have the same m, n indices but different q indices, and have a frequency difference equal to the free spectral range.

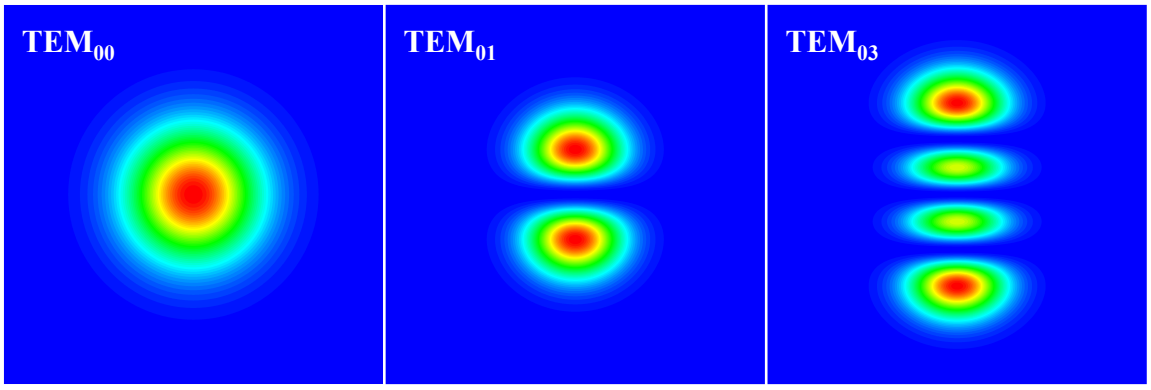


Figure 3.4: Theoretical simulation of the fundamental, TEM_{00}, and higher order, TEM_{01} and TEM_{03}, Hermite–Gaussian modes in the *xy* plane using Equations 3.23 and 3.24.

3.3 Theory of cavity ring-down spectroscopy

The use of optical cavities to enhance path lengths has been used for a variety of spectroscopic techniques, and the work reported in this thesis is largely based on the technique of cavity ring-down spectroscopy (CRDS)[203,205–208]. In cavity ring-down spectroscopy, a laser beam is focused into the optical cavity which is aligned such that resonance is achieved and constructive interference occurs causing the intracavity power to increase. A detector is positioned behind one of the cavity mirrors to monitor the intracavity power, and upon reaching a predetermined threshold level, the laser light is switched off using a fast optical switch and the temporal decay of light intensity within the cavity is measured.

For an optical cavity consisting of two mirrors of reflectivity R separated by a distance L, the light intensity during such a temporal decay inside the cavity without an absorber present is given by:

$$I(t) = I_0 \exp\left(\frac{-t}{\tau_0}\right) \tag{3.26}$$

where τ_0 is the ring-down time, which is defined as the time taken for the light intensity to decrease to $1/e$ of its original value, and is determined by the mirror reflectivity and cavity length using:

$$\tau_0 = \frac{-L}{c|\ln R|} \tag{3.27}$$

The effective path length, L_{eff}, of the cavity is given by $L_{\text{eff}} = \tau_0 c = -L/|\ln R|$, and thus, a pair of mirrors with reflectivity $R = 0.9999$ at a distance of 1 m apart results in a ring-down time $\tau_0 = 33.3$ μs and $L_{\text{eff}} = 10$ km.

The presence of an absorber within the cavity introduces an additional loss term corresponding to the absorbance as also described in the Beer–Lambert law (Equation 3.6), leading to a different temporal decay:

$$I(t) = I_0 \exp\left(\frac{-t}{\tau}\right) \tag{3.28}$$

such that the new ring-down time, τ, is given by:

$$\tau = \frac{-L}{c(\ln R - \alpha(\nu)L)} \tag{3.29}$$

Thus, using Equations 3.27 and 3.29, an expression for the absorption coefficient $\alpha(\nu)$ can be determined:

$$\alpha(\nu) = \frac{1}{c}\left(\frac{1}{\tau} - \frac{1}{\tau_0}\right) \tag{3.30}$$

and therefore, the absorption coefficient, and number densities of the absorbing species, can be determined independently of the light intensity.

The sensitivity of cavity ring-down spectroscopy is determined by the minimum detectable absorption coefficient, α_{min} [203]:

$$\alpha_{\text{min}} = \frac{\Delta\tau_{\text{min}}}{c\tau_0^2} \tag{3.31}$$

where $\Delta\tau_{\text{min}}$ is the minimum detectable change in the cavity ring-down time, which is often assumed to be equal to the standard deviation in τ_0.

3.4 Instrument development

The near-infrared cavity ring-down spectrometer used in this work is depicted in Figure 3.5(a). A continuous wave (cw) fibre-coupled distributed feedback (DFB) diode laser (NTT Electronics NLK1S5GAAA, λ = 1506 nm) is used to excite the optical cavity. The DFB laser is precisely temperature and current controlled (Thorlabs TED200C and LDC205C, respectively). The near-IR region was selected due to the coincidence of both H_2O and relatively strong isotopologue transitions, and because

it is a technologically highly developed wavelength region due to the demand of the telecommunications industry. The emission wavelength of the DFB laser is dependent on its operating temperature and current, and therefore, a wavelength calibration must be carried out to account for these dependencies. The temperature, T, of the DFB laser is measured by a thermistor of resistance, R, located in the pig-tailed butterfly laser package such that:

$$T(R) = \frac{T_0 B_{\text{val}}}{T_0 \ln\left(\frac{R}{R_0}\right) + B_{\text{val}}} \tag{3.32}$$

where $T_0 = 298.15$ K, $R_0 = 10$ kΩ and $B_{\text{val}} = 3410$ K. A wavelength calibration was carried out using a Burleigh WA-1000 wavemeter at a constant laser drive current of 120 mA, the results of which are shown in Appendix B. To ensure the regular excitation of the cavity modes, the operating current of the laser is modulated at a frequency of 5 Hz and amplitude of 200 MHz, thus ensuring the laser is scanned over more than one free spectral range[209].

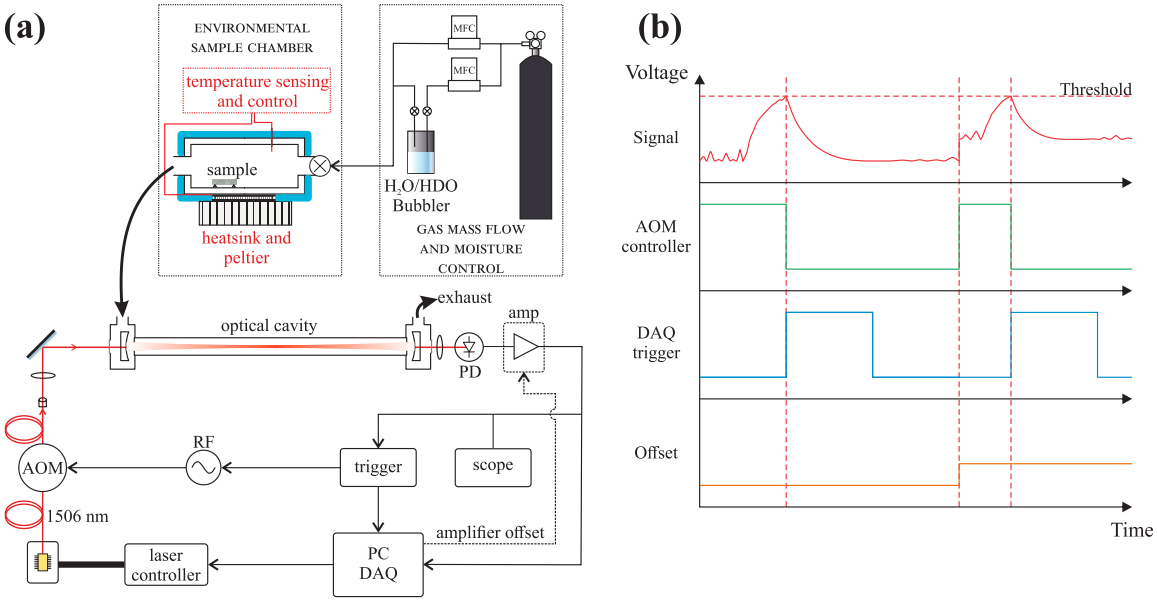


Figure 3.5: **(a)** Experimental set-up for the near-IR cavity ring-down spectrometer. AOM = acousto-optic modulator (Gooch & Housego Fiber-Q A35); RF = radio frequency generator (Gooch & Housego A35080); PD = photodetector (Thorlabs DET410); amp = amplifier (Femto DLPCA-200); PC DAQ = data acquisition system (National Instruments NI USB-6356). **(b)** Voltage-timing diagram for the measured signal, AOM controller, DAQ trigger and amplifier offset; see text for further description.

To trigger a ring-down event, the laser light within the cavity must be rapidly switched off. This is achieved by using a fast optical switch such as an acousto-optic modulator (AOM). The AOM consists of a photoelastic crystal attached to a piezoelectric acoustic transducer. A radio frequency (RF) pulse generates an acoustic wave whose interaction with the crystal results in spatially periodic changes in the crystal's refractive index, and produces a Bragg diffraction grating within the material[204]. The laser light passes through the AOM and is diffracted into multiple orders, with the 1st order diffracted beam directed into the optical cavity. When the light within the cavity reaches the predetermined threshold, as shown in Figure 3.5(b), a trigger pulse is sent to the RF generator, switching off the AOM and the 1st order beam is extinguished, resulting in a ring-down event.

The light transmitted through the cavity is focused using a short focal length lens (f = 25 mm) onto an InGaAs photodetector (PD) and the signal is amplified using a variable gain, low noise current transimpedance amplifier (amp) set to a gain of 10^7 VA^{-1} with a 400 kHz bandwidth. The signal is sent to a custom-built trigger box with which the threshold level can be set, and which triggers the AOM RF generator and the data acquisition system (PC DAQ), as described in Section 3.4.2.

The optical cavity is constructed from two highly reflective mirrors (Layertec, $R \approx 0.9999$, radius of curvature = 1 m) held in kinematic mounts (Thorlabs Polaris-K1-2AH) housed in stainless steel enclosures, separated by a distance of 86 cm, giving a corresponding $\Delta\nu_{\mathrm{FSR}}$ of 175 MHz. The enclosures are connected on one side to a borosilicate glass tube with an outer diameter of 18 mm, while the other face contains a transparent window (Thorlabs WG41050-C).

Light is coupled into the optical cavity when a mode of the incident radiation is in resonance with a mode of the cavity. Both the incident light field and the intracavity mode field (*i.e.*, the cavity eigensolution) have an associated axial dependent wavefront radius of curvature, $r_i(z)$, and spot size, $w(z)$, which is defined as the radial extent at which the field intensity decreases to $1/e^2$ of its maximum value. The intracavity power is maximised when the incident light field is mode-matched to a specific cavity mode (therefore, matching $r_i(z)$ and $w(z)$); generally, the TEM_{00} mode

is preferentially excited. Mode-matching is achieved by the use of optics to alter the radius of curvature and spot size of the incident radiation such that it matches the intracavity mode. The principle of mode-matching, therefore, requires an understanding of the propagation of light through optical components and quantification of the intracavity field.

Assuming a ray of light is travelling along the optical axis in the z-direction, the ray at a given position can be characterised by its angular, θ, and radial, y, displacements from the optical axis[210]. In the paraxial ray approximation, which applies to TEM modes, the angular displacements are considered to be small enough to allow the approximation $\sin\theta \approx \tan\theta \approx \theta$ to be made. The incident radiation (y_1, θ_1) and resultant radiation (y_2, θ_2) following interaction with an optical element are related by a linear transformation:

$$\begin{pmatrix} y_2 \\ \theta_2 \end{pmatrix} = \begin{pmatrix} A & B \\ C & D \end{pmatrix} \begin{pmatrix} y_1 \\ \theta_1 \end{pmatrix} \tag{3.33}$$

where the $ABCD$ matrix characterises the interaction of the optical element with radiation within the paraxial ray approximation. The overall transformation matrix is obtained through matrix multiplication of the $ABCD$ matrices for the individual components in the order in which they interact with the light.

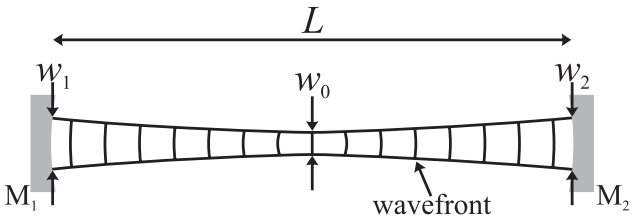


Figure 3.6: A schematic depicting how the wavefront radius of curvature and spot size w of Gaussian beam varies as a function of axial distance, where w_0 is the spot size at the cavity waist and $w_{1,2}$ is the spot size at the cavity mirrors ($M_{1,2}$).

The TEM_{00} mode is a Gaussian beam, the width and radius of curvature of which vary as a function of axial distance within the cavity, as shown in Figure 3.6. For a symmetrical cavity, in which the two mirrors are identical, and therefore, $g_1 = g_2 = g$, at the centre of the cavity the radius of curvature is infinite and the minimum spot

size occurs, which is known as the beam waist, w_0, and is given by:

$$w_0 = \sqrt{\frac{L\lambda}{\pi}}\left[\frac{1+g}{4(1-g)}\right]^{0.25} \tag{3.34}$$

where λ is the wavelength of the radiation. For the experimental set-up used in this work, the beam waist at the cavity centre is calculated to be 0.49 mm at $\lambda = 1506$ nm.

At the cavity mirrors, the radius of curvature is equal to that of the mirrors' concave faces and the spot sizes, $w_{1,2}$, are given by:

$$w_{1,2} = \sqrt{\frac{L\lambda}{\pi}}\left[\frac{1}{1-g^2}\right]^{0.25} \tag{3.35}$$

The Gaussian beam, however, can be described by the complex beam parameter, $q(z)$, which describes more generally how the spot size, $w(z)$, and radius of curvature, $r_i(z)$, varies as the beam travels along the central z-axis[204]:

$$\frac{1}{q(z)} = \frac{1}{r_i(z)} - \frac{i\lambda}{\pi w(z)^2} \tag{3.36}$$

At the beam waist (where $r_i(z) = \infty$) Equation 3.36 yields[210]:

$$q_0 = \frac{i\pi w_0^2}{\lambda} \tag{3.37}$$

The radius of curvature of the wavefront and spot size at some point z along the intracavity axis is therefore given by[196,210]:

$$r_i(z) = z\left[1 + \left(\frac{\pi w_0^2}{\lambda_z}\right)^2\right] \tag{3.38}$$

$$w^2(z) = w_0^2\left[1 + \left(\frac{\lambda_z}{\pi w_0^2}\right)^2\right] \tag{3.39}$$

The propagation of the Gaussian beam can be described using ray transfer matrix analysis and the $ABCD$ matrices for individual optical components and ray propagation, using the $ABCD$ law of Gaussian beams[210]:

$$q_2(z) = \frac{Aq_1(z) + B}{Cq_1(z) + D} \tag{3.40}$$

where $q_1(z)$ and $q_2(z)$ are the complex beam parameters before and after propagation, respectively.

Thus, mode-matching for the optical system can be performed to ensure the incident radiation matches the TEM_{00} intracavity field. For the experimental set-up used in this work, the output radiation from the AOM was passed through an adjustable fibre collimation package (Thorlabs CFC-8X-8) and two mode-matching lens, $f = 100$ mm and $f = 50$ mm (Thorlabs LB1676-C and LB1471-C, respectively) were used to focus the beam into the cavity, giving enough flexibility to find and satisfy conditions for good mode-matching.

3.4.1 Sample measurement and its relation to mass flux

The environment within the cavity is controlled and monitored *via* inlets through the stainless steel enclosures, with the pressure monitored using a pressure gauge (Leybold Vacuum CTR90, measurement range = 0.1 – 1000 Torr). Experiments were carried out in a N_2 (BOC Oxygen Free Nitrogen, 99.998 %) gas flow, controlled with calibrated mass flow controllers (MKS 1479A Mass-Flo and MKS PR 4000B-S). The gas flow could be humidified using a stainless steel bubbler through which a fraction of the gas is passed at a flow controlled by a calibrated rotameter (Cole Parmer 102-05-3T).

The gas flow further passed through a temperature controlled (range = $10.0 - 50.0$ ℃, $\delta = 0.1$ ℃) insulated stainless steel sample chamber ($13 \times 8 \times 7$ cm). The temperature within the chamber was determined using a calibrated thermocouple. The sample chamber is separated from the cavity by a valve, allowing a background spectrum of the residual water vapour in the cavity to be taken, providing a measurement of τ_0, and allowing the sample conditions to be treated independently of the optical cavity. The baseline ring-down time in a dry N_2 atmosphere is $\tau_0 \approx 150$ μs, and using Equation 3.31, the limit of detection is $\alpha_{\text{min}} \approx 1 \times 10^{-9}$ cm^{-1} in < 10 s acquisition time.

In the experiments reported in this thesis concerning the drying kinetics of stone samples, the water number density, $N(t)$, is determined within the optical cavity

which is downstream of the stone sample. To understand the drying kinetics described in Section 2.2, the mass of water released as a function of time must be determined, and therefore, the relationship between the cavity number density, $N(t)$, and sample $m(t)$ must be derived.

At a constant volumetric flow rate, f, through the experiment, if n_t is the total number of molecules in the cavity at time t, V is the volume of the cavity, and ϕ_{in} and ϕ_{out} are the molecular flux in and out of the cavity, respectively, then the following relationship can be formulated:

$$\begin{aligned} \mathrm{d}n_t &= \big(\phi_{\text{in}}(t) - \phi_{\text{out}}(t)\big)\mathrm{d}t \\ &= \left(\phi_{\text{in}}(t) - \frac{n_t f}{V}\right)\mathrm{d}t \end{aligned} \tag{3.41}$$

Rearranging Equation 3.41 and solving the first order differential equation results in the following expression:

$$n_t \exp\left(\frac{ft}{V}\right) = \int \phi_{\text{in}} \exp\left(\frac{ft}{V}\right)\mathrm{d}t + C \tag{3.42}$$

where at $t = 0$, $n_t = 0$, and therefore, $C = -\int \phi_{\text{in}}\mathrm{d}t$. Assuming $\int_0^\infty \phi_{\text{in}}\mathrm{d}t$ is a constant and manipulating Equation 3.42 gives:

$$n_t = -\exp\left(\frac{-ft}{V}\right)\int \phi_{\text{in}}\mathrm{d}t \tag{3.43}$$

Integrating Equation 3.43 over time results in:

$$\int_0^t n_t\,\mathrm{d}t = \frac{V}{f}\int_0^t \phi_{\text{in}}(t)\mathrm{d}t \tag{3.44}$$

which is equivalent to:

$$\int_0^t \phi_{\text{in}}\mathrm{d}t = f\int_0^t \frac{n_t}{V}\mathrm{d}t \tag{3.45}$$

where n_t/V is the time-dependent concentration which is equivalent to the number density, $N(t)$, which is measured. The cumulative mass of water released from the stone samples at time t is related to $\int \phi_{\text{in}}(t)\mathrm{d}t$ by:

$$m(t) = \frac{M_r}{N_A}\int_0^t \phi_{\text{in}}\mathrm{d}t = \frac{fM_r}{N_A}\int_0^t N(t)\mathrm{d}t \tag{3.46}$$

where N_A is Avogadro's number and $M_r(\mathrm{H_2O}) = 0.018$ kg mol^{-1}, and so a direct relationship between the measurement of $N(t)$ and $m(t)$ is established.

3.4.2 Control and acquisition

A crucial part of the experimental set-up shown in Figure 3.5(a) is the data acquisition system; this is constructed around a bespoke LabVIEW (National Instruments) program that both controls the experiment and acquires data with the use of a 16-bit, 1.25 MSs^{-1} DAQ card (National Instruments NI USB-6356). As shown in Figure 3.5(b), when the signal reaches the predetermined threshold level, the custom-built trigger box sends an inverted TTL pulse to the AOM to switch off the light entering the cavity while simultaneously sending a TTL pulse to the DAQ. The LabVIEW program triggers off the rising edge of the DAQ trigger and begins recording the signal from the detector. The ring-down events recorded are initially analysed within the LabVIEW program by a fitting routine which fits an exponential decay using the Levenberg–Marquardt least-squares algorithm. The average ring-down time is determined for a specified sample size, which was typically set to 10 ring-down events for this work.

The LabVIEW program filtered the acquired ring-down events to discard any outlying events, such as those resulting from noise, caused, for example, by any electrical spike which triggers the acquisition, and to remove poor ring-down data. Three filters were used in this work:

1. Amplitude of ring-down events filter — Electrical spikes in the system would present as large positive and negative deviations in the baseline, and therefore, the amplitude of the ring-down event had to lie within a set voltage range, this range could be tuned between $0 - 2$ V.

2. Ring-down time minimum and maximum filter — The excitation of different transverse cavity modes can result in different ring-down times. Although mode-matching has been carried out to ensure dominant excitation of the TEM_{00} mode, there is a low incidence of higher order modes that cause triggering. Therefore, to ensure only ring-down times for the TEM_{00} mode were used in determining the average ring-down time, a tracking filter window was added to the LabVIEW program. The minimum and maximum ring-down time allowed in the tracking window

was typically determined as ± 10 % of the previous average ring-down time.

3. Ring-down time standard deviation filter — The calculated ring-down times could be filtered to be within a set number of standard deviations of the average of all the results. In this thesis, this was typically set to ± 2 standard deviations.

As the cavity ring-down time decreases, indicating the greater concentration of absorber within the system, the amplitude of the signal and, for a given fixed threshold, the rate of acquisition also decrease which is detrimental to the practicality of the experiment. There are two ways that the experimental set-up can be adjusted to ensure the rate of acquisition remains relatively constant as the ring-down time decreases and to maintain the method's dynamic range. The first is that the trigger threshold level can be manually lowered, allowing smaller amplitudes to trigger the system. Alternatively, an offset can be applied to shift the smaller amplitudes to trigger off the same threshold level.

The current amplifier used in this experiment has an adjustable offset voltage which can be controlled remotely *via* the DAQ card and LabVIEW program. To determine the relationship between the ring-down time and the offset voltage required to maintain an acquisition rate of $\sim$ 10 Hz, the laser was tuned to the centre of a H_2O transition (further details in Section 3.5.1) and increasing amounts of water vapour were introduced to the CRDS cell. A linear relationship was determined and programmed into the LabVIEW software, ensuring the acquisition rate remains relatively constant and only the low-order modes trigger the acquisition. A schematic of this process is shown in Figure 3.5(b), illustrating the change in offset as the size of the signals decrease.

The LabVIEW program is written to allow the acquisition and analysis of three different ring-down experiments:

Subroutine One: *Acquisition of ring-down events at a single wavelength* — The laser is set to the desired wavelength. In all experiments in this thesis, the laser is driven at constant current of 120 mA, and the wavelength is set by adjusting the temperature to the desired value. The LabVIEW program acquires and fits successive ring-down events, determining the average for the specified sample size at this

fixed wavelength until stopped by the user. A plot of ring-down time versus time is created, allowing real-time monitoring of the experimental progress.

Subroutine Two: *Acquisition of a spectrum across a wavelength range* — To generate an absorption spectrum, the laser must be stepped across the required wavelength range. In this experiment, this is achieved by application of a voltage to the temperature controller, resulting in a change in the laser temperature, and thus, the wavelength. The laser is, therefore, set to an initial temperature, T_0, and a voltage tuning range and step voltage is specified within the LabVIEW program. The specified number of ring-down events is recorded at each step voltage, allowing a plot of ring-down time against wavelength to be generated using the known wavelength calibration (previously determined). In this work, the laser temperature is set probe to the centre of the water transition at $T_0 = 293.37$ K, corresponding to a thermistor resistance of 12.048 kΩ, and the voltage range is typically set to -1.25 to 0.75 V, corresponding to a wavenumber range of $6636.34 - 6640.11$ cm^{-1}, with a step voltage of 5 or 20 mV, depending on the experiment conducted.

Subroutine Three: *Acquisition of ring-down events at multiple wavelengths* — Using subroutine one, monitoring the ring-down time of only one target species is possible, and the baseline ring-down time must be measured before or after the experiment. While subroutine two allows multiple species to be monitored, providing they have transitions within a wavelength range available to the laser used, the acquisition can be a slow and time-consuming process. Therefore, the ability to switch the laser between different wavelengths is a desirable function as it would allow the monitoring of multiple target species and of the baseline ring-down time to be obtained with a high temporal resolution (seconds). The laser is set to an initial temperature, and the required voltage to tune the temperature to the desired wavelengths is set in the program. The subroutine operates similarly to subroutine one in that the average ring-down time at each wavelength is determined before the laser switches to the next position. To ensure the laser reaches and settles at the specified wavelengths, a 10 s pause is set between acquisitions. A plot of the ring-down times against time is created, and the subroutine runs in a continuous loop of the desired wavelengths until

stopped by the user. To ensure the rate of acquisition remains relatively constant, and therefore, applies the correct offset voltage to the amplifier, this subroutine specifies that the offset voltage is calculated using the previous ring-down time for the corresponding wavelength.

The LabVIEW program allows much of the acquisition and initial analyses to be controlled and undertaken. These include the number of ring-downs to acquire per average, the wavelength calibration and voltage range of the laser, the time between acquisitions following the voltage step or switch, the application and value of the filters, and the application of the offset voltage to the current amplifier. All the cavity ring-down experiments described in this thesis were carried out using this program.

3.5 Initial characterisations and measurements of water

3.5.1 Spectroscopy of water

Water is an asymmetric top molecule, with three unique moments of inertia. The quantisation of angular momentum for an asymmetric top is defined by three quantum numbers, J, the total angular momentum quantum number, K_a, the angular momentum projection quantum number along the a axis, and K_c, the angular momentum projection quantum number along the c axis. Water has three vibrational modes, depicted in Figure 3.7: ν_1 is the symmetric stretch, ν_2 is the symmetric bend, and ν_3 is the asymmetric stretch.

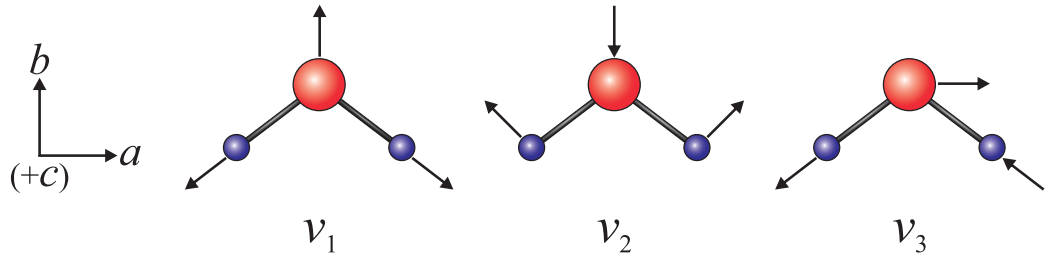


Figure 3.7: A schematic showing the three vibrational modes of water: ν_1 is the symmetric stretch, ν_2 is the symmetric bend, and ν_3 is the asymmetric stretch.

Neglecting anharmonicity, the behaviour of each mode is that of an independent harmonic oscillator, and the frequency of the mode is, therefore, proportional to $(k_F/\mu)^{1/2}$, where k_F is the force constant associated with the mode and μ is the

reduced mass of the molecule[152]. Thus, the three vibrational modes of water will have different central frequencies for the three different hydrogenic isotopologues of water, as shown in Table 3.1.

Table 3.1: The vibrational frequencies of the three hydrogenic isotopologues of water[161,211].

Isotopologue	ν_1 / cm^{-1}	ν_2 / cm^{-1}	ν_3 / cm^{-1}
H_2O	3656.65	1594.59	3755.79
HDO	2726.73	1402.20	3707.47
D_2O	2671.46	1178.33	2788.05

The ro-vibrational transitions of water are denoted by the angular momentum and vibrational quantum numbers of the upper and lower levels as the following:

$$J', K_a', K_c'(\nu_1' \ \nu_2' \ \nu_3') \leftarrow J'', K_a'', K_c''(\nu_1'' \ \nu_2'' \ \nu_3'') \tag{3.47}$$

In the wavelength range of the DFB laser, there are many accessible transitions for the three isotopologues, however, the majority of work is focused on two H_2O transitions at 6636.60 cm^{-1} and 6638.91 cm^{-1}, corresponding to the 6,0,6 (031) $\leftarrow$ 7,0,7 (010) and 10,3,7 (021) $\leftarrow$ 11,3,8 (000) ro-vibrational transitions, respectively, and an HDO transition at 6638.17 cm^{-1} corresponding to the 8,6,2 (210) $\leftarrow$ 9,6,3 (000) ro-vibrational transition[198].

3.5.2 Pressure broadening of H_2O transitions in N_2

As stated in Section 3.1.2, the broadening coefficients reported in HITRAN[198] are for a standard air mixture, and for the two H_2O transitions of interest, the Lorentzian widths at 1 atmosphere are $\Delta\nu_p(6636.60\ cm^{-1}) = 0.120\ cm^{-1}$ and $\Delta\nu_p(6636.91\ cm^{-1}) = 0.126\ cm^{-1}$. However, as the experiments in this thesis were conducted in a nitrogen atmosphere, determination of the Lorentzian width, $\Delta\nu_p$, of the H_2O transitions in nitrogen is required.

To determine the Lorentzian widths, absorption spectra for increasing H_2O concentrations were taken in the range $6636.34 - 6640.11\ cm^{-1}$ at atmospheric pressure

and a constant temperature of 294 K, an example of which is shown in Figure 3.8(a). The concentration of H_2O was increased by passing increasing amounts of a calibrated flow of N_2 through the stainless steel bubbler and mixing with a dry flow of N_2 to ensure a total flow of 1.5 standard litres per minute (slm) is maintained. The resultant spectra were fitted using a Voigt profile, with the Gaussian width determined using Equation 3.12 to be $\Delta\nu_G = 0.0192$ cm^{-1}. Figure 3.8(b) shows the Lorentzian widths for the two transitions as a function of H_2O concentration (for concentrations of H_2O $\leq 4 \times 10^{17}$ molecules cm^{-3}). The range over which $\Delta\nu_p$ could be determined was limited, either by the magnitude of the absorption becoming too large to measure at higher concentrations, in the case of the 6638.91 cm^{-1} transition, or due to the large uncertainties in the Voigt fits for the 6636.60 cm^{-1} transition due to small signal sizes at low concentrations.

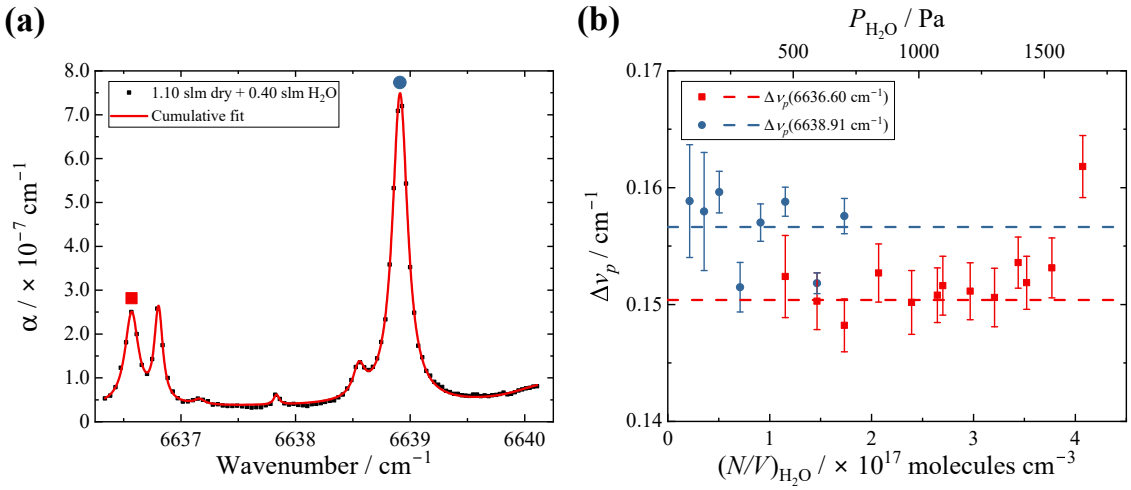


Figure 3.8: **(a)** Absorption spectrum of 0.40 slm wet N_2 in 1.10 slm dry N_2 over the range $6636.34 - 6640.11$ cm^{-1} at $T = 294$ K and $P = 102392$ Pa. The cumulative fit (red) of the data is shown, allowing determination of the Lorentzian widths, $\Delta\nu_p$, of the transition at 6636.60 cm^{-1} (marked with a red square ■), and the transition at 6689.91 cm^{-1} (marked with a blue circle ●); **(b)** The Lorentzian widths, $\Delta\nu_p$, as a function of water concentration for the two H_2O transitions. The widths and average for the transition at 6636.60 cm^{-1} are shown in red squares (■), while the data for the 6689.91 cm^{-1} transition are shown in blue circles (●).

The average Lorentzian width was determined to be $\Delta\nu_p = 0.150 \pm 0.008$ cm^{-1} and $\Delta\nu_p = 0.157 \pm 0.003$ cm^{-1} for the transitions at 6636.60 cm^{-1} and 6638.91 cm^{-1},

respectively, and these values were used to simulate the absorption cross-sections required for this work. These values are markedly different from those calculated from air broadening parameters reported in the HITRAN[198] database. It is important to also account for the self broadening, which would be expected to increase with increasing water concentration and is quantified by the self broadening coefficient, γ_{self}. In HITRAN, this is reported as $\gamma_{\text{self}}(6636.60\ \text{cm}^{-1}) = 0.352\ \text{cm}^{-1}\ \text{atm}^{-1}$ and $\gamma_{\text{self}}(6638.91\ \text{cm}^{-1}) = 0.281\ \text{cm}^{-1}\ \text{atm}^{-1}$. For the water concentrations shown in Figure 3.8(b), this corresponds to $\Delta\nu_{\text{self}} = 0.001 - 0.005\ \text{cm}^{-1}$, which is within the error of the averages reported.

Further analysis of the Lorentzian widths reported here in comparison with HITRAN[198] is needed because pure nitrogen has a greater pressure broadening effect than standard air. For standard air mixtures, the Lorentzian width is the summation of the different components, as stated in Equation 3.10, and thus has contributions from nitrogen, oxygen, argon and other trace species. The broadening coefficient in nitrogen is larger than oxygen due to several effects: firstly, nitrogen molecules have a slightly greater collision rate than oxygen molecules due to their lighter mass resulting in a higher average velocity. More significantly, however, nitrogen has a greater quadrupole moment than oxygen[212], and therefore, a larger interaction potential exists during collisions. In addition, due to nuclear spin statistics, only half the rotational states are available to oxygen for energy transfer while all states are accessible to nitrogen. Thus, the total broadening in air should be smaller than that of pure nitrogen, as is observed here. However, these effects are unlikely to account for all of the observed differences, which probably result from the more specific and efficacious measurements made here (as opposed to a more global measurement contributing to the HITRAN database).

3.5.3 Investigating the water continuum

In all the spectra recorded in Section 3.5.2, an offset in the absorptions was observed which is not captured in the HITRAN[198] database. This broad underlying absorption is known as the water continuum which can be split into two contributions: the 'self'

continuum which is due to the interaction between water molecules, and is found to scale quadratically with water number density[213]; and the 'foreign' continuum which is due to the interaction of water molecules with other gases found in the environment, such as N_2 and O_2, and is proportional to the product of the water vapour pressure and the sum of the partial pressures of the broadening gases[213].

Due to its importance in atmospheric studies, the water continuum has been widely studied and is the subject of a number of reviews[213–216], a full discussion of which is beyond the scope of this thesis. Studies of the water continuum are usually focused in the regions between absorption bands, with the majority concentrating on the mid-infrared spectral region, although a few studies have investigated the near-infrared around 1.6 μm[217–219]. To estimate the water continuum contribution in the wavelength region studied in this work, a linear regression model was used to fit the absorption spectra obtained in Section 3.5.2 with the simulated HITRAN data of the absorption cross-sections of water at atmospheric pressure in combination with a contribution representing the total water continuum, termed α_{offset}. Figure 3.9(a) shows α_{offset} determined as a function of water concentration, and a second order polynomial which was fitted to the data to allow prediction of the contribution at lower concentrations, which is given by:

$$\alpha_{\text{offset}} = 1.631 \times 10^{-25}(N/V)_{\text{H}_2\text{O}} + 2.162 \times 10^{-43}(N/V)^2_{\text{H}_2\text{O}} \tag{3.48}$$

Comparison of the water continuum contribution obtained here is in reasonable agreement with those reported in the 1.6 μm region[217–219]. Predicting a water continuum contribution for a partial water pressure of 10 Torr using the self continuum contribution from Mondelain *et al.*[218] and the foreign continuum contribution from Ptashnik *et al.*[219] gives $\alpha_{\text{offset}} = 5 \times 10^{-8}$ cm^{-1}.

3.5.4 Determination of % relative humidity (*RH*)

As stated in Section 2.1.3, the gas and liquid transport through the porous stone is dependent on the temperature and relative humidity. An investigation into the effect of relative humidity on the transport properties is described in Chapter 4, and was

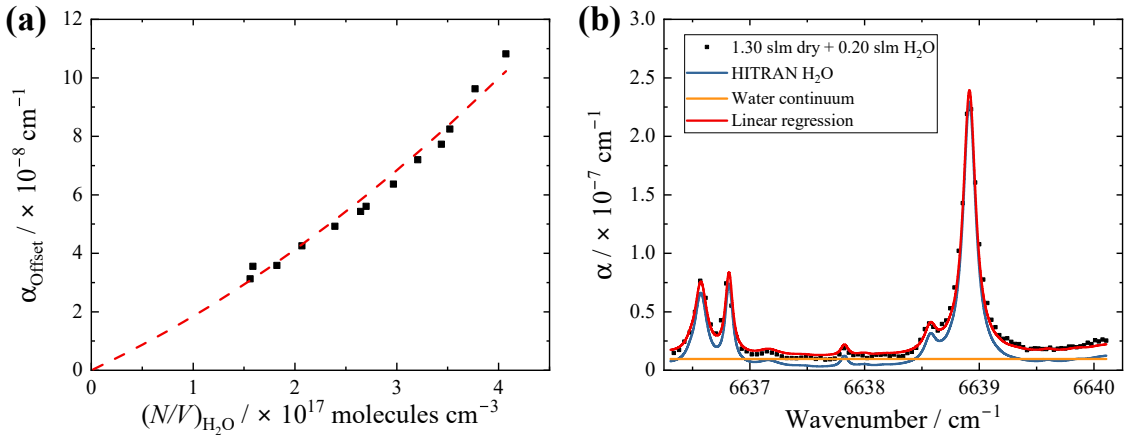


Figure 3.9: **(a)** A plot of the water continuum absorption, α_{offset}, determined using linear regression, as a function of the water concentration. The data has been fitted with a second order polynomial, shown as the red dashed line. **(b)** Absorption spectrum of 0.20 slm wet N_2 in 1.30 slm dry N_2 over the range $6634.34 - 6640.11$ cm^{-1} at $T = 293$ K and $P = 102258$ Pa. A linear regression (red) of the HITRAN simulation of the H_2O absorption coefficient (blue) over the same range and the water continuum (orange) is shown.

achieved by combining wet and dry flows of N_2, maintaining a total flow of drying gas of 1.5 slm and changing the wet component in discrete steps from 0.0 to 1.0 slm. Absorption spectra for each set of conditions were taken in the range 6636.34 – 6640.11 cm^{-1}, an example of which is shown in Figure 3.9(b). A simulation of the HITRAN[198] absorption cross-sections of H_2O in a N_2 atmosphere, at the temperature and pressure measured, was obtained using the pressure and Doppler broadening parameters determined in Section 3.5.2. Using a linear regression, the absorption spectrum was simulated using the HITRAN absorption cross-sections and the water continuum α_{offset} determined in Section 3.5.3. This linear regression, therefore, determines the number density of water, which using the ideal gas law is converted into the partial pressure of water, P_{H_2O}. The saturated water vapour pressure, $P_{v,\text{sat}}$, was determined using the method described in Section 2.1.3, and the % RH was calculated using Equation 2.17. For example, the linear regression of the spectrum shown in Figure 3.9 determines a number density of 3.57×10^{16} molecules cm^{-3}, corresponding to a partial pressure $P_{H_2O} = 144.18$ Pa. The saturated water vapour pressure at $T = 293$ K is equal to 2336.73 Pa, and therefore, for these experimental conditions, the relative humidity is 6.17 % (*i.e.*, for 0.2 slm wet N_2 and 1.3 slm dry N_2).

3.5.5 Measuring isotopically labelled species

One crucial facet of laser spectroscopy is its potential to distinguish between different isotopologues of the same molecular species. Therefore, appropriate preparation of a sample in isotopically enriched water will allow the release of water from within the limestone to be differentiated from the water present in the environment or drying gas. Of the three principal hydrogenic isotopologues of water, the low natural abundance of both HDO and D_2O (*ca.* 0.031 % and 2×10^{-6} %, respectively) validates the assumption that if either of these species are present in reasonable quantities then they must have been released from the stone sample. In the spectral region of interest, the D_2O and HDO transitions are an order of magnitude stronger than those for H_2O, as illustrated in Figure 3.10(b)−(d), and therefore, 10:1 mixtures of H_2O and D_2O were generally prepared and were left to isotopically equilibrate (producing HDO [166]) before being used to saturate samples.

The equilibrium concentrations of H_2O, D_2O and HDO in such conditions are expected to be in the ratios 83:1:16, as described in Section 2.1.3. However, for absolute determination of the equilibrium composition, an absorption spectrum of 1.25 slm dry N_2 combined with 0.25 slm wet N_2 flowed through the isotopologue mixture was measured over the range $6636.34 - 6640.11$ cm^{-1} at $T = 295$ K and $P = 102658$ Pa, as shown in Figure 3.10(a). The HITRAN [198] based absorption cross-section for H_2O over this spectral range was determined using the Doppler and pressure broadening parameters previously determined, and is shown in Figure 3.10(b). To simulate the absorption cross-sections for HDO and D_2O, the pressure broadening parameters in nitrogen were also determined. The transition at 6638.17 cm^{-1} is purely due to HDO, with a Gaussian width of $\Delta\nu_G = 0.0187$ cm^{-1} (Equation 3.12). A Voigt fit of this transition allows determination of the Lorentzian width, which was found in this gas mixture to be $\Delta\nu_p = 0.167 \pm 0.004$ cm^{-1}, and this was used to simulate the HITRAN based absorption cross-sections for HDO shown in Figure 3.10(d). From Figure 3.10, it is clear that there is no absorption that is purely from D_2O, and therefore, the Lorentzian width was unable to be directly

determined and so the HITRAN broadening value was used. Using the same linear regression routine as before (Section 3.5.3), the absorption spectrum was fitted with the HITRAN simulations along with the water continuum, and the ratios of the isotopologues were determined to be approximately 84:1:15 in H_2O, D_2O and HDO, respectively. Correction of the liquid phase equilibrium ratios of 83:1:16 to the gas phase by using the isotopic vapour pressures[220] results in the expected gas phase ratios of 84:1:15, in excellent agreement with that determined spectroscopically.

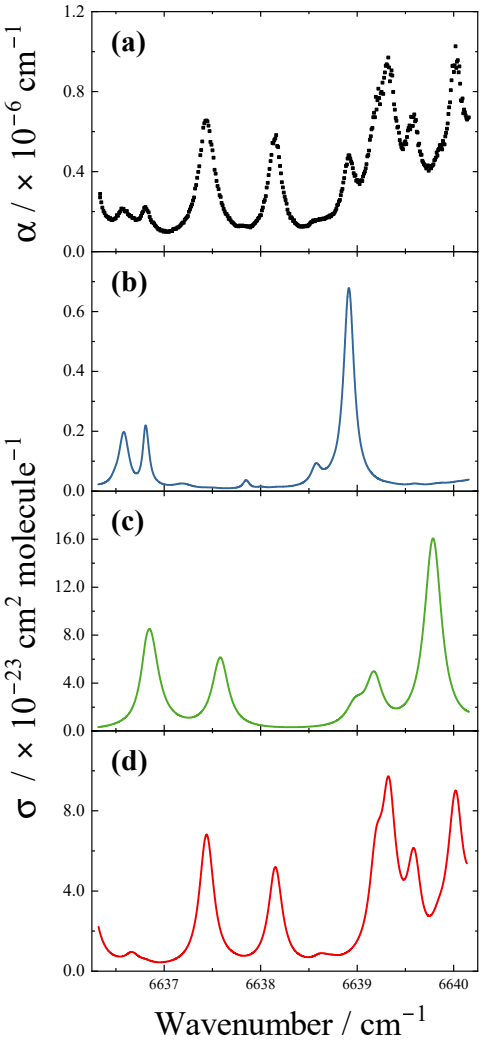


Figure 3.10: **(a)** Absorption spectrum of 1.25 slm dry N_2 with 0.25 slm wet N_2 flowed through the 10:1 mixture of H_2O and D_2O over the range 6636.11 – 6640.34 cm^{-1} at $T = 295$ K and $P = 102658$ Pa; A HITRAN simulation of the absorption cross-section over the same range and at the same temperature and pressure for **(b)** H_2O; **(c)** D_2O; and **(d)** HDO.

3.6 Conclusions

This chapter describes the principles of laser absorption spectroscopy, beginning with a consideration of the Einstein coefficients and Beer–Lambert law, before describing the influence of the environment on the spectral line shapes. A discussion of the properties of optical cavities, in particular those pertinent to the experimental method of cavity ring-down spectroscopy, is presented. Building on these foundations, the development of a near-IR cavity ring-down spectrometer is described as applied to dynamic sampling of gas constituents at atmospheric pressure. The relationship between the experimental measurements of ring-down time to the drying kinetic parameters described in Chapter 2 is detailed. Following this, a description of the acquisition software used in this work is provided, considering in detail the three subroutines utilised for recording the ring-down time at a single wavelength, at multiple wavelengths or over a range of wavelengths to obtain an absorption spectrum, while maintaining a high dynamic range for precise ring-down time determination.

This chapter concludes with initial characterisations and measurements of water vapour, beginning with a brief description of the spectroscopic nomenclature for water. As the spectroscopic measurements in this thesis were conducted in a nitrogen atmosphere, determination of the pressure broadening parameter of water in nitrogen was required to allow accurate simulation of the water absorption cross-sections from the transition-specific integrated cross-sections available in HITRAN[198]. The pressure broadening parameter was determined experimentally to be $\Delta\nu_p = 0.157 \pm 0.003$ cm^{-1} atm^{-1} for the transition at 6638.91 cm^{-1} and $\Delta\nu_p = 0.150 \pm 0.008$ cm^{-1} atm^{-1} at 6636.60 cm^{-1}, which are larger than the pressure broadening parameters reported in HITRAN for a standard air mixture.

Scrutiny of the absorption spectra obtained shows the presence of an offset that is not included in the HITRAN simulations and was determined to be contributions from the water continuum. To account for this offset, the relationship between the contribution from the water continuum and number density of water was measured, and was found to be in reasonable agreement with literature values. Using the determined

pressure broadening coefficient and water continuum contribution, the procedure for determining the relative humidity is outlined. Finally, the equilibrium isotopologue ratios in the gas phase and generated from a 10:1 mixture of H_2O and D_2O used in this work were measured spectroscopically to be 84:1:15 (H_2O; D_2O; HDO), and are in excellent agreement with the equilibrium ratios predicted from thermodynamics described in Section 2.1.3.

Chapter 4

Determining water transport kinetics in limestone by dual-wavelength cavity ring-down spectroscopy

Dáire E. Browne, Robert Peverall, Grant A. D. Ritchie and Heather A. Viles, *Analytical Chemistry*, **2022**, *94*, 3126 − 3134.

Abstract

Water plays a major role in the deterioration of porous building materials such as those widely found in built heritage, influencing many physical, chemical and biological decay processes. This paper details a proof-of-principle study using near-infrared cavity ring-down spectroscopy (CRDS) to monitor the release of water and its artificially enriched isotopologues from small (*ca.* $25 \times 25 \times 5$ mm) samples of limestone subject to drying by a fixed flow of nitrogen with varying levels of humidity and at room temperature and atmospheric pressure. Under low humidity conditions, the drying kinetics are consistent with the well-established two-phase drying process exhibited by porous materials; namely, an initial constant drying rate period (phase I) followed by a falling drying rate period (phase II). The water diffusivity during phase II, D_{II}, was measured (for Clipsham limestone) to be $3.0 \times 10^{-9} \pm 1 \times 10^{-10}$ m^2 s^{-1}. The CRDS measurements allow spectroscopic determination of the total mass of water released by the sample and the calculated values are in excellent agreement with gravimetric analysis. Importantly, the selectivity and sensitivity afforded by CRDS allows isotope analysis to be carried out, such that the flux of isotopically labelled

water out of the sample can be determined under conditions of humidified flow where there may be simultaneous ingress of water from the environment. Dual-wavelength CRDS distinguishes isotopic species, and it is demonstrated that the drying kinetics and physical properties of the samples are self-consistent when monitoring both HDO and H_2O (for HDO, D_{II} was $3.2 \times 10^{-9} \pm 4 \times 10^{-10}$ m^2 s^{-1}). As the humidity levels in the flow increase, a departure from the distinct two-phase behaviour is observed in the HDO drying curves. These new measurements of isotopically resolved mass fluxes will help refine models for drying mechanisms in porous media.

4.1 Introduction

Heritage science is a contemporary interdisciplinary subject that seeks to understand change and risk in order to preserve and maximise the cultural and socio-economic benefits of heritage for future generations[221]. Heritage materials are often very difficult to study, requiring state-of-the-art physical and chemical analysis methods, and the field has hugely benefited from the development and application of new analytical techniques[132,222,223]. One significant research area concerns the built historic environment and its conservation, and in particular how to mitigate the effects of moisture retention and transport within both traditional and new building materials. With this aim in mind, here we show how cavity ring-down spectroscopy (CRDS) can be used to monitor both the moisture content and dynamics in small samples of limestone (*ca.* $\leq$ 5 g), a sedimentary rock mainly composed of calcium carbonate, $CaCO_3$, which is a commonly used building stone across the globe[14,16,28,224,225]. This widespread use is in part due to the relative ease that it can be worked and shaped, as well as a result of its perceived durability[5].

The longevity of historic buildings constructed from limestone indicates that deterioration is a slow and gradual process, mainly occurring *via* the karst (or karstification) process[18], which is the dissolution of limestone by rainwater, normally acidified by the uptake of CO_2 or organic acids. However, in polluted metropolitan environments, dissolution markedly increases through wet and dry deposition

processes. Water is a key agent in most physical, chemical and biological decay processes[12]; there are various ways water can enter buildings, through rising damp from the soil or through the pore network, resulting in mechanical damage of the stone material due to transformational stress and various physical cycles, for example, freeze–thaw[226]. In addition, water acts as a transport medium and carries contaminants into the stone[102], leading to chemical attack, salt crystallisation and biodeterioration resulting in further mechanical damage[90,227,228]. Signatures of deterioration include flaking, powdering, and other forms of material loss, but the majority of these can be mitigated through the use of consolidants. Clearly, a consolidation treatment should not only improve the mechanical strength of the sample but also be compatible with the treated substrate and resistant to different damage mechanisms[59]. For the ongoing development and optimisation of both organic and inorganic chemical treatments, it is imperative to know the concentration and location of water within the stone as well as the net water flux in order to understand these coupled physico-chemical decay processes[44,169,229].

This paper reports the first use of CRDS as a high-resolution, non-destructive quantitative laboratory-based method to monitor moisture content and fluxes for samples of limestone. In particular, the sensitive and selective nature of CRDS when combined with isotopic enrichment of water samples allows determination of the drying kinetics within environments of varying relative humidity (% RH), key quantitative information in the area of heritage conservation. CRDS references each measurement of the ring-down time to that for an empty cavity, and as such allows absolute densities to be readily and directly determined with no instrument calibration required, as demonstrated in the equivalence of the spectroscopically and gravimetrically determined masses. In this article, the principles of the near-IR CRDS instrument that has been developed are outlined, before presentation of the proof-of-principle data from which the time-dependent water contents of limestone samples are determined. Two stages of drying are clearly observed, in agreement with conventional theories for the drying of porous materials[131]. The reproducibility and accuracy of the measurements are also discussed, before the simultaneous monitoring of water and its isotopologue,

HDO, is demonstrated in the evaluation of moisture fluxes under conditions of varying % *RH*. Prospects for this method are briefly discussed in the conclusions.

4.2 Materials and methods

4.2.1 Cavity ring-down spectroscopy

Theory: Absorption spectroscopy allows the identification of species based on their unique set of quantum-mechanical energy levels. When light passes through an absorbing species, the intensity of light decreases as a result of the resonant absorption of energy, and this attenuation in intensity is quantified by the Beer–Lambert law, $I_{\mathrm{tr}}(\nu) = I_0(\nu)\exp[-\alpha(\nu)d]$, where $I_0(\nu)$ and $I_{\mathrm{tr}}(\nu)$ are the incident and transmitted light intensities at frequency ν, respectively, $\alpha(\nu)$ is the frequency-dependent absorption coefficient of the species, and d is the path length. When the absorption is by a single species, the absorption coefficient is related to the number density, N, by $\alpha(\nu) = N\sigma(\nu)$, where $\sigma(\nu)$ is the (species-specific) absorption cross-section. Thus, absorption measurements yield absolute number densities.

The absorption intensity, $I_{\mathrm{abs}}(\nu)$, is given by the difference $\big(I_0(\nu) - I_{\mathrm{tr}}(\nu)\big)$, and it is clear that for a given absorption intensity, $I_{\mathrm{abs}}(\nu)$, increasing the path length, d, over which the light interacts with the sample allows smaller number densities to be measured, increasing the sensitivity of the absorption measurement. CRDS increases the effective path length over which the light can interact with the sample by enclosing the sample between two (or more) highly reflective mirrors[205,230]. This work utilises continuous wave (cw) CRDS in which cw laser radiation is focused into an optical cavity formed from two dielectric mirrors, aligned such that cavity modes are readily and regularly excited[203,206,208,231]. The light intensity exiting the cavity is monitored and when a certain threshold is reached, the laser radiation is switched off, causing the light intensity within the cavity to decay exponentially. This decay is characterised by a ring-down time, τ_0, which is the time taken for the light intensity to decrease to $1/e$ of its original value, I_0. If the only losses are due to the imperfect reflectively of the mirrors, then this decay time is given by $\tau_0 = \frac{d}{c|\ln R|}$, where

c is the speed of light and R the reflectivity of the mirrors. In the presence of an absorbing species, such as water (and in the absence of other loss processes), the rate of decay is faster (*i.e.*, the ring-down time of the cavity is reduced) because light is lost from the cavity, both by transmission through the mirrors and by absorption by the molecular species under investigation, resulting in a modified ring-down time, τ. The difference in the reciprocals of the ring-down times allows determination of the absorption coefficient, $\alpha(\nu)$:

$$\alpha(\nu) = \frac{1}{c}\left(\frac{1}{\tau} - \frac{1}{\tau_0}\right) \tag{4.1}$$

and hence, the the number density of the absorbing species.

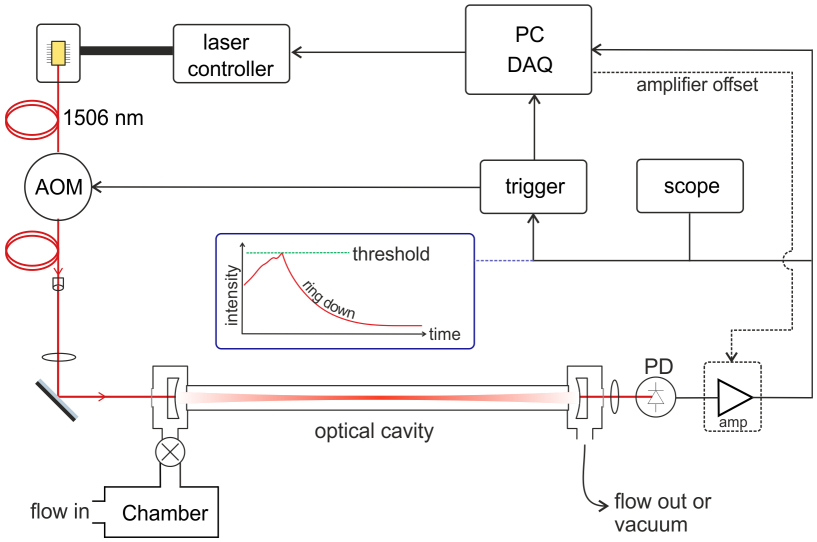


Figure 4.1: A schematic diagram of the CRDS used to measure H_2O released from limestone. AOM = acousto-optic modulator; PD = photodetector; amp = amplifier; DAQ = data acquisition system.

Instrument Design: The near-IR CRDS instrument used in this work is depicted in Figure 4.1. The laser used is a cw fibre-coupled distributed feedback diode laser (NTT Electronics NLK1S5GAAA, λ = 1506 nm) which is temperature and current controlled (Thorlabs TED200C and LDC205C). The near-IR region was selected as it is a technologically highly developed wavelength region with relatively strong H_2O and HDO absorptions. The laser beam passes through a fibre-coupled acousto-optic modulator (AOM) (Gooch & Housego Fibre-Q A35), and then through an adjustable

fibre collimation package (Thorlabs CFC-8X-C). Two mode-matching lenses, $f = 100$ mm and $f = 50$ mm (Thorlabs LB1676-C and LB1471-C, respectively), were used to focus the beam into the cavity. To form the cavity, two highly reflective mirrors (Layertec, $R \approx 0.9999$, radius of curvature = 1 m) were held in kinematic mounts (Thorlabs Polaris-K1-2AH) housed in stainless steel enclosures, a distance of 86 cm apart. One face of each enclosure is a transparent window (Thorlabs WG41050-C), whereas the other face is connected to a borosilicate glass tube with an outer diameter of 18 mm. The typical limit of detection for this apparatus is $\alpha_{\text{min}} \lesssim 1 \times 10^{-9}$ cm^{-1} in < 10 s, where α_{min} is the minimum detectable absorption coefficient. In the precise spectral region we use, around 6638 cm^{-1}, this corresponds to approximately 500 ppb of water at atmospheric pressure.

The light transmitted through the cavity is focused onto a photodetector (Thorlabs DET410 InGaAs photodiode), and the signal is amplified (current amplifier Femto DLPCA-200) and acquired using a data acquisition system (National Instruments NI-USB 6356). When the transmitted signal reaches a predetermined threshold intensity, a signal is sent to a custom-built trigger box, which both switches off the AOM (and thus stops light entering the cavity) and triggers the acquisition system. A LabVIEW (National Instruments) program has been designed to control the experiment and fit the exponential decays (of light intensity) to determine values for τ. The same program controls an offset voltage on the amplifier that depends on the previous measured ring-down time (RDT) to ensure that the rate of acquisition remains relatively constant (~ 10 Hz), and that only the low-order modes are triggered by the acquisition. The program has the capability to acquire absorption spectra using temperature tuning of the cw diode laser, as well as a dual-wavelength switching function[232]. (The temperature dependence of the wavelength under operating conditions is shown in the supplementary information.) This function automatically switches the laser between two set temperatures, providing high-resolution monitoring of two transitions of choice. To ensure the occurrence of regular CRD events, the laser is modulated at a frequency of 5 Hz and amplitude 200 MHz (an amplitude a little higher than the free spectral range of the cavity, but not too large compared to

the pressure broadened spectral line widths).

Inlets through the stainless steel enclosures allow control and monitoring of the environment inside the cavity, with pressure monitored using a pressure gauge (Leybold Vacuum CTR90, measurement range = 0.1 − 1000 Torr). Experiments are carried out in a N_2 (BOC Oxygen Free Nitrogen, 99.998 %) gas flow with preselected levels of % *RH*, controlled with calibrated mass flow controllers (MKS 1479A Mass-Flo® and MKS PR 4000B-S) and rotameters. The baseline RDT in a dry N_2 atmosphere is $\tau_0 \approx 150$ μs (corresponding to a cavity finesse of $\sim$ 160000). A separate stainless steel sample chamber (13 × 8 × 7 cm) is attached to one of the enclosures, separated by a valve. This allows a background spectrum of the residual water vapour in the cavity to be taken, providing a measure of τ_0 and allows the sample conditions to be treated independently of the optical cavity.

4.2.2 Stone samples: Clipsham limestone

Clipsham limestone is exclusively used in this work as an exemplar. Clipsham limestone is a British limestone from the Lincolnshire Limestone Formation (Middle Jurassic, Bajocian), is composed of cross-bedded oolites (characteristic spherical grains) with occasional herringbone cross-bedding[233,234], and is a very pale cream and buff colour. It is a coarse-grained ooidal and shell fragmental grainstone and was deposited in a shallow marine carbonate shelf environment[235]. Clipsham limestone has been widely used in a variety of buildings, both for construction[31] and repair[17,26]. Mercury intrusion porosimetry[188] was carried out to characterise the internal structure of the stone. The results of this analysis are available in Figure B.1 of the supplementary information. The samples have an open porosity of 20.39 % and density of 2.69 g cm^{-3}. The pore size distribution is unimodal with a median pore diameter of 1.18 μm. A sample size of *ca.* 25 × 25 × 5 mm was selected to allow relatively fast drying experiments, and a total of four different Clipsham limestone samples were used in this study.

4.2.3 Experimental procedure

For accurate analysis, it was essential to determine the water continuum contribution. To achieve this, a series of CRD spectra of increasing % *RH* were acquired over the range 6636.34 – 6640.11 cm^{-1} at a constant temperature of 294 K and a pressure of 767 Torr (*ca.* atmospheric pressure). The % *RH* was changed by passing increasing amounts of calibrated flow of N_2 through a water bubbler and mixing with a dry flow of N_2 to ensure a total flow of 1.5 standard litres per minute (slm) remained.

To monitor the release of water from the limestone samples, the samples were first immersed in distilled water for a minimum of 2 days. This is to ensure that the samples are saturated, and this time was determined as the minimum required time following a pilot study into the influence of soaking times on drying kinetics. Upon removal, excess water was sponged off of the sample, and its wet mass, m_w, recorded. The sample was then placed in the sample chamber, the valve opened to the main chamber, and a constant flow of 1.5 slm N_2 passed over the sample into the cavity. The laser was tuned to the centre of the H_2O 10,3,7 (021) ← 11,3,8 (000) transition at 6638.91 cm^{-1} (spectroscopic nomenclature is defined in the supplementary information) and the average RDT continuously measured. The procedure was stopped when the measured RDT returns to τ_0. The dry mass of the sample, m_d, was also recorded.

4.3 Results and discussion

4.3.1 Drying kinetics under dry flows

Using the CRD spectra obtained for increasing % *RH*, for each wavelength, α is calculated (Equation 4.1) from the average RDT of 10 ring-down events. Figure 4.2(a) shows the resultant CRD absorption spectrum of 0.25 slm wet N_2 mixed with 1.25 slm dry N_2 (equivalent to 7.5 % *RH*). The spectrum consists of well-resolved absorption features superimposed upon an underlying continuum absorption[213], both of which depend upon the concentration of water molecules present. Using a linear regression, the absorption spectrum was simulated with HITRAN data[198] of the absorption cross-section of water at atmospheric pressure and a contribution representing the

water continuum, termed α_{offset}. Using the increasing % *RH* spectra, the relationship between the water continuum contribution and number density of water was determined, allowing this to be accounted for in the following investigation. For example, for a 0.25 slm wet flow, as shown in Figure 4.2(a), $\alpha_{\text{offset}} = 8.8 \times 10^{-9} \pm 1.2 \times 10^{-9}$ cm^{-1}.

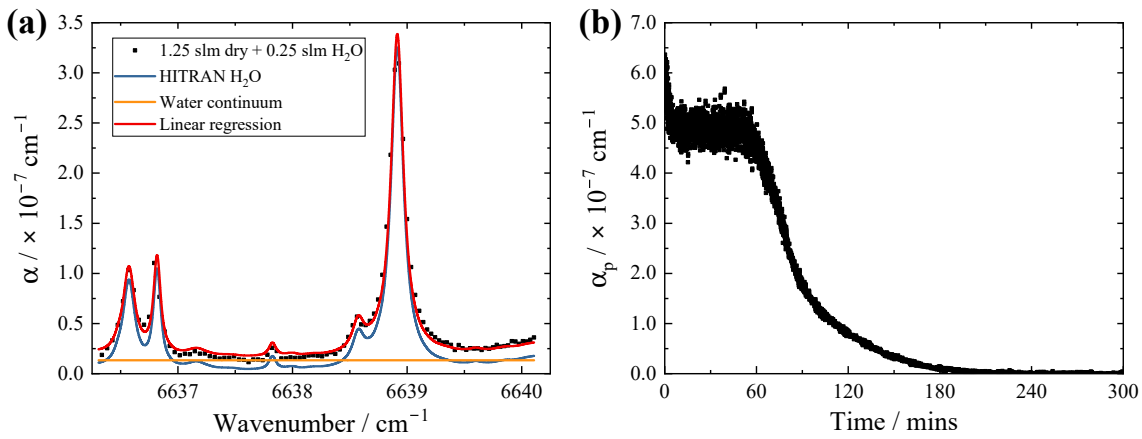


Figure 4.2: **(a)** Absorption spectrum of 0.25 slm wet N_2 in 1.25 slm dry N_2 (% *RH* = 7.5) over the range 6636.34 − 6640.11 cm^{-1} at $T = 294$ K and $P = 767$ Torr. A linear regression ($R^2 = 0.98$) of the HITRAN simulation of the absorption coefficient for H_2O (blue) over the same range and water continuum (orange) is shown. **(b)** A plot showing α_p as a function of time for a 1.5 slm N_2 flow over the Clipsham limestone *ca.* $25 \times 25 \times 5$ mm sample. α_p is obtained by tuning the laser to the centre of the H_2O 10,3,7 (021) ← 11,3,8 (000) transition at 6638.91 cm^{-1} and continuously measuring the RDT.

The time-dependent release of water from limestone samples was monitored using the method described above. Using Equation 4.1, the absorption coefficient at line centre, which we denote as α_p, is determined as a function of time as shown in Figure 4.2(b). Experiments in which extended absorption spectra were recorded as the stone dries under the same conditions described above were also performed to confirm the results obtained with monitoring at one or more fixed wavelengths, *vide infra*.

Using the spectra from a range of % *RH* values, the pressure broadening parameter for the H_2O transition was evaluated and used to determine the peak absorption cross-section, σ_p, at line centre from the integrated cross-section listed in HITRAN[198], assuming a Voigt line shape (this improves on the fit to the spectra in Figure 4.2(a), increasing the goodness-of-fit parameter R^2 from 0.98 to 0.998). Once

σ_{p} is known, the number density of water molecules is calculated using $\alpha_{\mathrm{p}} = N\sigma_{\mathrm{p}}$. Here, a small correction required to take into account the predetermined water continuum absorption is applied. To calculate the mass of water released, and allow determination of the drying kinetics, the following procedure is used.

If n_t is the total number of water molecules present in the system at time t, V the volume of the system, $\phi_{\mathrm{in}}(t)$ and $\phi_{\mathrm{out}}(t)$ are the molecular (water) flux in and out of the cavity, then for a given volumetric flow rate (f) the following relationship can be constructed:

$$\mathrm{d}n_t = \big(\phi_{\mathrm{in}}(t) - \phi_{\mathrm{out}}(t)\big)\mathrm{d}t = \left(\phi_{\mathrm{in}}(t) - \frac{n_t f}{V}\right)\mathrm{d}t \tag{4.2}$$

We measure the number density, N, which is equal to n_t/V, the time-dependent concentration, and want to determine $\int \phi_{\mathrm{in}}\mathrm{d}t$, from which the total mass of water released from the stone can be calculated. From Equation 4.2, the cumulative mass of water released by the limestone sample to a time t is then given by:

$$m_{\mathrm{H_2O}}(t) = \frac{M_r}{N_A}\int_0^t \phi_{\mathrm{in}}\mathrm{d}t = \frac{fM_r}{N_A}\int_0^t N\mathrm{d}t \tag{4.3}$$

where N_A is Avogadro's number and $M_r(\mathrm{H_2O}) = 0.018$ kg mol^{-1}. For the data shown in Figure 4.2(b), the spectroscopically determined total mass released, $m_{\mathrm{H_2O}}(\infty)$, is 0.361 ± 0.003 g. The total mass change determined by gravimetric analysis (Salter Brecknell ESA-300, max. 300 g, $\delta = 0.005$ g) is 0.360 ± 0.005 g, showing good agreement with the spectroscopically determined value.

The normalised mass difference, $\Delta m_n(t)$, is defined as:

$$\Delta m_n(t) = \frac{m_{\mathrm{H_2O}}(\infty) - m_{\mathrm{H_2O}}(t)}{m_d} \tag{4.4}$$

Figure 4.3(a) shows $\Delta m_n(t)$, illustrating the expected two-phase drying process of porous materials[12,164]. Phase I is defined as the constant drying rate period (CST) during which the rate of evaporation is controlled by the external conditions and does not depend on the transport processes within the material[90]. Water is supplied to the evaporation pores at the surface by flow through connected pathways, resulting in the air at the surface being fully saturated; diffusion from the material to the air occurs

down a constant concentration gradient which controls the rate of evaporation [236]. As the drying proceeds further, flow occurs through increasingly disconnected pathways, and the surface and mean water contents decrease such that the air at the surface is not saturated. Eventually, the unsaturated capillary flow within the sample can no longer occur at a rate sufficient to maintain a constant evaporation rate.

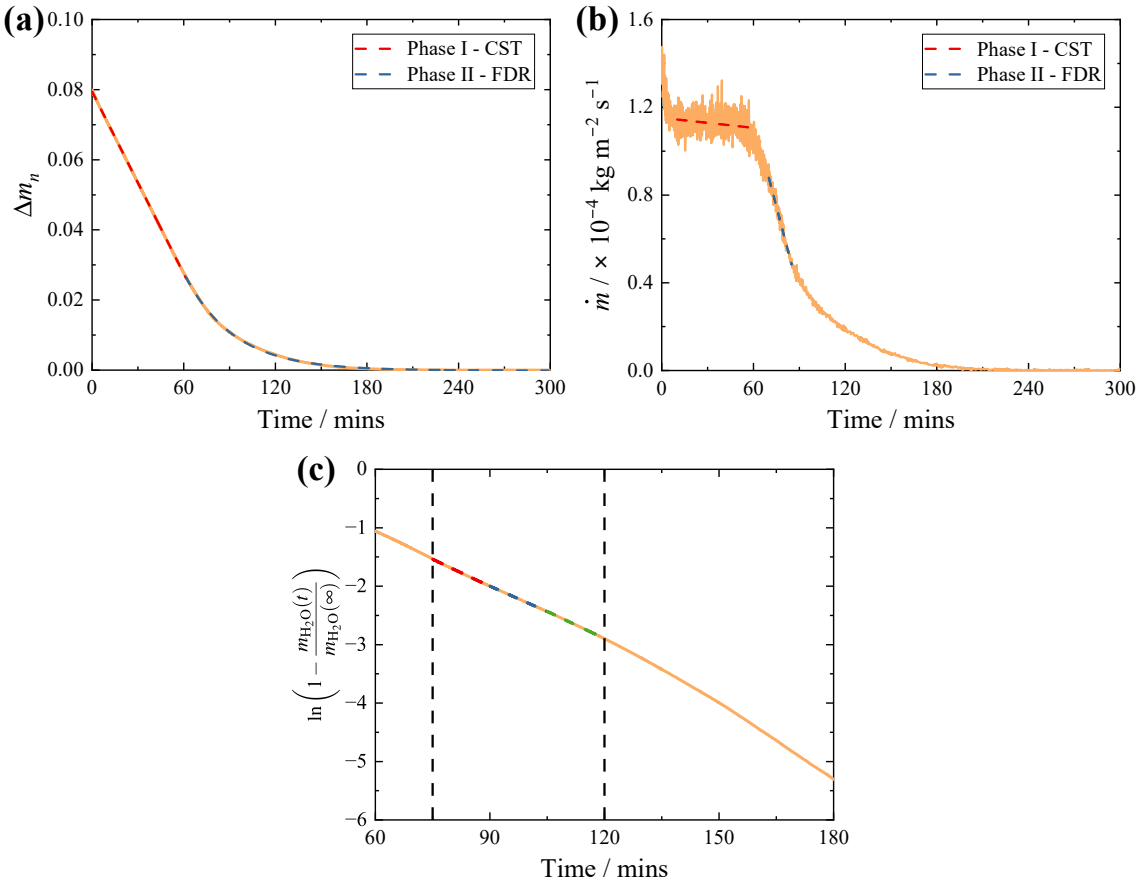


Figure 4.3: **(a)** Normalised mass difference as a function of time for a Clipsham limestone *ca.* 25 × 25 × 5 mm sample drying under a constant dry 1.5 slm N_2 flow. Phase I has been fitted with a linear function, whereas phase II has been fitted with an exponential function. **(b)** A plot of the water flux, $\dot{m}$, as a function of time, showing a linear fit to phase I, allowing $\dot{m}_{\mathrm{CST}}$ to be determined. **(c)** A plot of $\ln\left(1 - m_{\mathrm{H_2O}}(t)/m_{\mathrm{H_2O}}(\infty)\right)$ against time, allowing determination of D_{II}. The region of linear fit is indicated by two vertical lines.

Data in phase I are commonly fitted with a linear function as shown in Figure 4.3(a). The mass flux, $\dot{m}(t)$, is defined as:

$$\dot{m}(t) = \frac{1}{A}\frac{\mathrm{d}m_{\mathrm{H_2O}}(t)}{\mathrm{d}t} \tag{4.5}$$

where A is the total surface area of the sample and $\mathrm{d}m_{\mathrm{H_2O}}(t)/\mathrm{d}t$ is the gradient of a linear fit to the data. Thus, for Figure 4.3(b), the constant mass flux for phase I, $\dot{m}_{\mathrm{CST}} = (1.13 \times 10^{-4} \pm 9 \times 10^{-6})$ kg m^{-2} s^{-1}. The critical time at which phase I ends, t_c, was determined to be the intercept between two tangents fitted to $\dot{m}(t)$, shown as dashed lines in Figure 4.3(b). On the basis of the analysis described by Castro and Coelho Pinheiro[172], an iterative approach was used to determine t_c: the intercept of the two tangents was determined, and this value was then set as the upper limit for the linear fit to phase I and the process repeated until a constant t_c was determined.

As noted above, phase II drying begins as the rate of evaporation starts to fall, known as the falling drying rate period (FDR), and is regulated by the unsaturated flow within the porous material. In Figure 4.3(a), this phase has been fitted with an exponential function. Drying in this phase can be described by Fick's second law, $(\partial C/\partial t) = D_{\mathrm{II}}(\partial^2 C/\partial x^2)$, which relates the change in the moisture concentration, C, with time to the spatial variation of its concentration gradient; here, x is the distance over which moisture transfer occurs, as measured from the bottom face of the sample, and D_{II} is the phase II diffusivity. Assuming the moisture is uniformly distributed through the porous sample, and integrating over the sample thickness L, allows $m(t)$ to be written as[150]:

$$\frac{m(t)}{m(\infty)} = 1 - \sum_{n=0}^{\infty} \frac{8}{(2n+1)^2\pi^2} \exp\left\{\frac{-D_{\mathrm{II}}(2n+1)^2\pi^2 t}{4L^2}\right\} \tag{4.6}$$

In this study, we found that phase II drying begins when the moisture content falls below a critical saturation value of ~ 30 %[169]. In these later stages of drying, only the first term in Equation 4.6 needs to be considered[150], and D_{II} can therefore be determined from a linear relationship between the logarithmic terms and time:

$$\ln\left(1 - \frac{m_{\mathrm{H_2O}}(t)}{m_{\mathrm{H_2O}}(\infty)}\right) - \ln\left(\frac{8}{\pi^2}\right) = -\frac{D_{\mathrm{II}}\pi^2 t}{4L^2} \tag{4.7}$$

At even longer times (> 135 mins) slight deviations to this are seen, but we note that by this time 97 % of the water has been released.

This analysis of our data is illustrated in Figure 4.3(c): the average gradient is equal to $-5.1 \times 10^{-4} \pm 2 \times 10^{-5}$ s^{-1}, and using $L = 3.8 \times 10^{-3}$ m yields D_{II}

$= 3.0 \times 10^{-9} \pm 1 \times 10^{-10}$ m^2 s^{-1}. Using this procedure on plain cement paste, Bakhshi and Mobasher[168] obtained a diffusivity of 3.33×10^{-9} m^2 s^{-1}, whereas Zaknoune *et al.*[237] report D_{II} values between $2 - 3.5 \times 10^{-9}$ m^2 s^{-1} for lime binder and $4.5 - 6.7 \times 10^{-9}$ m^2 s^{-1} for cellular concrete. Thus, the values obtained in this work seem to be in good agreement with those reported in the literature for similar materials.

To test the reproducibility of the measurement, and also the variation between samples of the same limestone, this experiment was repeated with four *ca.* $25 \times 25 \times 5$ mm Clipsham limestone samples. Table 4.1 summarises the drying kinetics for the four samples. As expected, there are slight variations due to differences between the samples but overall good agreement between the different kinetic parameters determined. The drying kinetics are also depicted in Figure B.3 in the supplementary information.

Table 4.1: Comparison of drying kinetics using different samples of Clipsham limestone, all *ca.* $25 \times 25 \times 5$ mm. Note: $m_{\mathrm{H_2O}}(\infty)$ = spectroscopic mass; t_c = critical time; $\dot{m}_{\mathrm{CST}}$ = constant mass flux for phase I; D_{II} = phase II diffusivity.

Sample	C1	C2	C3	C4
$m_{\mathrm{H_2O}}(\infty)$ / g	0.361 ± 0.003	0.400 ± 0.003	0.393 ± 0.003	0.408 ± 0.003
Gravimetric mass / g	0.360 ± 0.005	0.390 ± 0.005	0.390 ± 0.005	0.410 ± 0.005
t_c / min	61.50	67.18	66.11	72.89
Critical saturation value / %	33	35	31	32
$\dot{m}_{\mathrm{CST}}$ / kg m^{-2} s^{-1}	$1.13 \times 10^{-4} \pm 9 \times 10^{-6}$	$1.09 \times 10^{-4} \pm 9 \times 10^{-6}$	$1.16 \times 10^{-4} \pm 9 \times 10^{-6}$	$1.08 \times 10^{-4} \pm 9 \times 10^{-6}$
D_{II} / m^2 s^{-1}	$3.0 \times 10^{-9} \pm 1 \times 10^{-10}$	$2.8 \times 10^{-9} \pm 2 \times 10^{-10}$	$3.2 \times 10^{-9} \pm 4 \times 10^{-10}$	$3.0 \times 10^{-9} \pm 2 \times 10^{-10}$

4.3.2 Isotope detection for moisture flux determination

This work utilizes a cw diode laser, an easily tunable and controllable device with high spectral purity, which is readily able to distinguish between different isotopologues that themselves exhibit unique absorption spectra. Therefore, preparing a sample in isotopically enriched water and subsequently detecting the presence of HDO or D_2O allows the release of water from within the limestone to be decoupled from the adsorption and desorption of ambient water in the environment. For example, the natural abundance of HDO is very low (*ca.* 0.031 %), and therefore, it can be assumed that any HDO measured has been released from the sample. The absorption cross-sections of D_2O and HDO transitions in the spectral region of interest are approximately an order of magnitude larger than those for H_2O[198], and thus, a 10:1 mixture of H_2O and D_2O (Sigma-Aldrich, 99.9 % atom D) was used for immersion; these species undergo isotopic substitution to produce an equilibrium mixture containing HDO, H_2O and D_2O[166], in approximately the following ratios 15:84:1.

Figure 4.4(a) shows a CRD spectrum obtained with a 1.25 slm dry N_2 flow mixed with a 0.25 slm wet N_2 flow (% $RH = 7.5$) passed through the 10:1 mixture, taken over the region $6636.34 - 6640.11$ cm^{-1} at a constant temperature of 295 K and at a pressure of 770 Torr. Using the same linear regression program as before, the spectrum was fitted with HITRAN simulations of the three dominant isotopologues along with the water continuum, as shown in Figure 4.4(a). From this, it is clear that, first, the absorption at 6638.17 cm^{-1} is due purely to the HDO 8,6,2(210) $\leftarrow$ 9,6,3(000) transition; second, the contribution from D_2O is negligible, and therefore, will not need to be taken into account when monitoring the water released from the limestone samples; and third, the measured absorptions at the H_2O transition frequencies have contributions from HDO, and therefore, this must be taken into account when determining the mass of H_2O released.

To monitor the release of both HDO and H_2O from limestone in order to confirm that HDO can be used to accurately measure limestone drying kinetics, a wavelength switching routine was used. The LabVIEW control program was set to switch be-

tween the centre of the H_2O 6,0,6(031) ← 7,0,7(010) transition at 6636.60 cm^{-1} and the centre of the HDO 8,6,2(210) ← 9,6,3(000) transition at 6638.17 cm^{-1}, with a 10 s pause between acquisitions. The same experimental procedure as described for

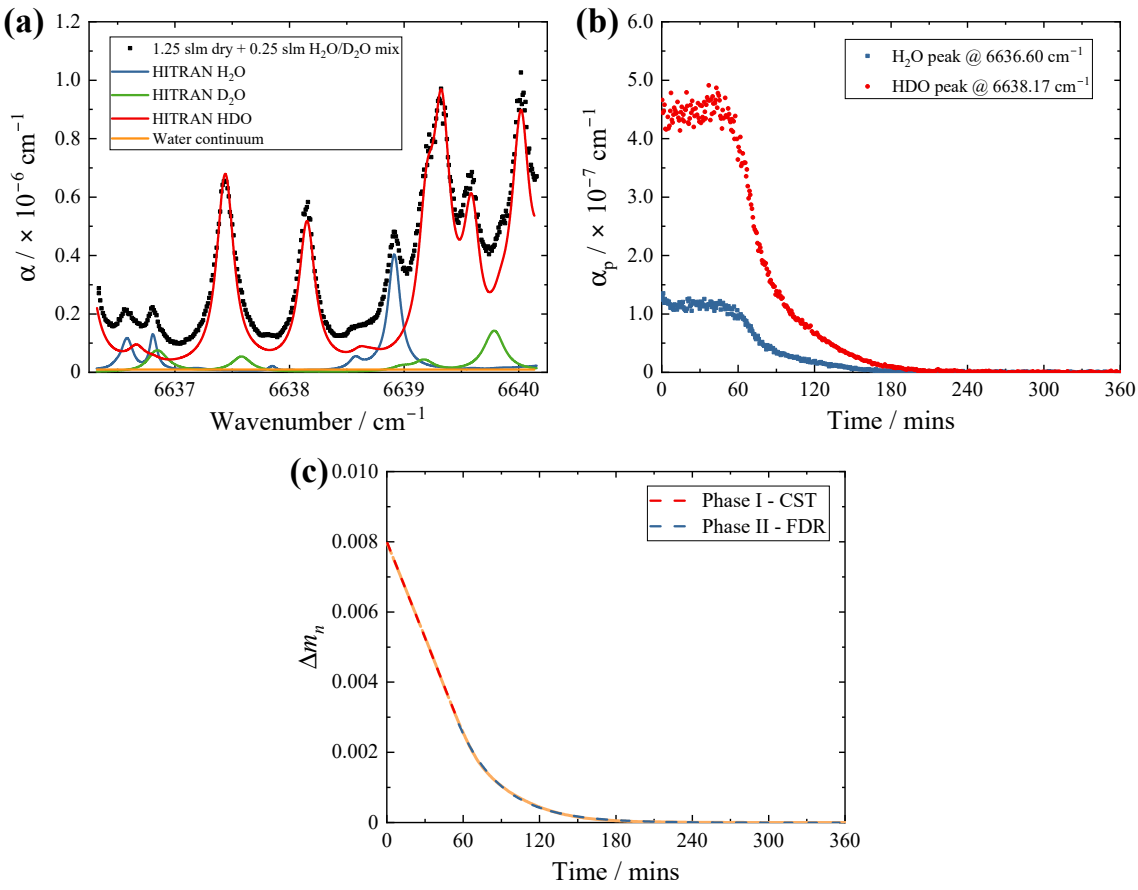


Figure 4.4: **(a)** Absorption spectrum of 1.25 slm dry N_2 mixed with 0.25 slm wet N_2 (% RH = 7.5) flowed through the 10:1 mixture of H_2O and D_2O over the range 6636.34 – 6640.11 cm^{-1} at T = 295 K and P = 770 Torr. A linear regression of the HITRAN simulation of the absorption coefficient for H_2O (blue), D_2O (green) and HDO (red) over the same range and water continuum (orange) is shown (contributing to a global fit, $R^2 = 0.99$).**(b)** A plot showing α_p as a function of time for a 1.5 slm N_2 flow over the Clipsham limestone *ca.* 25 × 25 × 5 mm sample that had been immersed in a 10:1 (H_2O/D_2O) mixture. **(c)** HDO normalised mass difference as a function of time for Clipsham limestone *ca.* 25 × 25 × 5 mm sample drying under a constant 1.5 slm N_2 flow.

H_2O was used, except the samples were immersed in the 10:1 mixture of H_2O and D_2O for 2 days (instead of distilled water). Figure 4.4(b) shows a plot of α_p for both H_2O and HDO for a Clipsham limestone *ca.* 25 × 25 × 5 mm sample dried under a 1.5 slm dry N_2 flow. From the linear regression shown in Figure 4.4(a), it was de-

termined that the HDO contribution to the absorption at 6636.60 cm^{-1} is 16.5 % of that measured at 6638.17 cm^{-1}, and this has been taken into account to produce the α_p values for H_2O shown in Figure 4.4(b). We note that the relative abundances of the isotopologues emanating from the stone can be subtly, and reproducibly, different from that in the isotopically enriched water. This effect has its origin in the residual water content of the limestone samples and occurs in samples that had not previously been subjected to an isotopic mixture — the stone samples are not oven-dried in these proof-of-principle experiments and as such there are small amounts of residual water content in the nominally dry stone that can cause small shifts in the chemical equilibrium between isotopologues.

Using Equation 4.4, Δm_n for HDO released was calculated, and Figure 4.4(c) shows a plot of $\Delta m_n(t)$. As expected, this shows the two-phase drying behaviour as previously seen in Figure 4.3(a); however, we note that Δm_n is an order of magnitude smaller in this case due to the smaller amount of HDO initially present. The data were analysed using the same procedure described for the H_2O drying kinetics, and produced the parameters listed in Table 4.2. A comparison of these values to those previously presented for a stone immersed in pure H_2O shows good consistency, with a lower amount of H_2O measured due to a lower initial amount of pure H_2O present in the stone. Because of the differences in the total masses of H_2O and HDO released from the sample, and to allow direct comparison of the constant flux, $m(t)$ can be normalised to have a maximum of 1. From this, the normalised mass flux, $\dot{m}_N$, can be calculated and the normalised constant mass flux for phase I, $\dot{m}_{NCST}$, can be determined. For H_2O, $\dot{m}_{NCST}$ is $0.332 \pm 3 \times 10^{-4}$ m^{-2} s^{-1} and for HDO it is $0.334 \pm 3 \times 10^{-4}$ m^{-2} s^{-1}. This good agreement between these values gives confidence that HDO can be used to accurately monitor limestone drying kinetics. The consistency between D_{II} for H_2O and HDO, as shown in Table 4.2, also supports the use of HDO to monitor limestone drying kinetics. We further note that the observed difference in t_c for H_2O and HDO is due to the cycling of the switching between transitions, that is, the difference in t_c values is within one period of the diode laser switching cycle, and not to any physical difference in kinetic behaviour of each isotopologue.

Table 4.2: Comparison of drying kinetics for H_2O and HDO released from a Clipsham limestone *ca.* $25 \times 25 \times 5$ mm sample under a 1.5 slm dry N_2 flow. Note: $m(\infty)$ = spectroscopic mass; t_c = critical time; $\dot{m}_{\mathrm{CST}}$ = constant mass flux for phase I; D_{II} = phase II diffusivity.

Species	H_2O	HDO
$m(\infty)$ / g	0.305 ± 0.004	0.0357 ± 0.0003
t_c / min	56.75	57.11
$\dot{m}_{\mathrm{CST}}$ / kg m^{-2} s^{-1}	1.01×10^{-4} $\pm$ 9×10^{-6}	1.19×10^{-5} $\pm$ 9×10^{-6}
D_{II} / m^2 s^{-1}	2.9×10^{-9} $\pm$ 3×10^{-10}	3.2×10^{-9} $\pm$ 4×10^{-10}

Clearly HDO can be used to accurately monitor limestone drying kinetics, but the main advantage it offers is the ability to determine drying kinetics under different environmental conditions. Specifically, this technique allows limestone drying to be monitored under conditions of increasing % *RH*. Following the same procedure as described before, experiments were conducted in which the composition of the "drying" gas was changed in steps from 0.0 to 1.0 slm wet N_2, and then combined with dry N_2 to make a constant total gas flow of 1.5 slm. Absorption spectra were taken at each composition and were analysed to determine the number density of water, from which, using the ideal gas law and saturated vapour pressure of water[160], the % *RH* can be calculated (this is also done without the sample present to characterise the wet flow). Thus, changing from 0.0 to 1.0 slm wet N_2 corresponds to increasing the humidity from 0 to 50 % *RH*. All other aspects of the experiment were kept the same, and the results are shown in Figure 4.5.

Figure 4.5(a) shows $\Delta m_n(t)$ for the HDO released, and as previously seen in Figure 4.4(c), it is an order of magnitude smaller than that for H_2O because of the smaller amount of HDO initially present. However, in Figure 4.5(a), it is apparent that as the % *RH* increases the two-phase drying behaviour becomes less distinct in the HDO drying curves. Initially, at the lower wet flows ranging from 0.0 to 0.6 slm, $\Delta m_n(t)$ does show this two-phase process, although with a decrease in the gradient of phase I and a concomitant increase in t_c as % *RH* increases. However, for the higher

wet flows of 0.8 and 1.0 slm, there are no longer two distinct phases. This change in behaviour is more apparent in the plot of normalised mass flux, $\dot{m}_{\mathrm{N}}$, which is shown in Figure 4.5(b) and the parameters reported in Table 4.3.

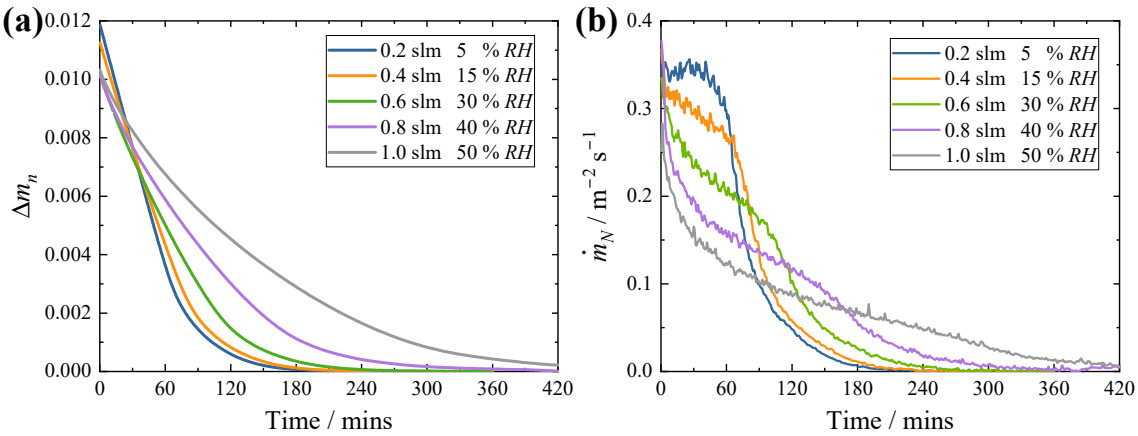


Figure 4.5: **(a)** A plot of the HDO normalised mass difference as a function of time with increasing % *RH* for the same *ca.* 25 × 25 × 5 mm Clipsham limestone sample. The total combined flow was 1.5 slm N_2. **(b)** A plot of the HDO normalised mass flux, $\dot{m}_{\mathrm{N}}$, as a function of time with increasing % *RH* for the same *ca.* 25 × 25 × 5 mm Clipsham limestone sample.

Table 4.3: Comparison of HDO drying kinetics with increasing humidity for a Clipsham limestone *ca.* 25 × 25 × 5 mm sample. Note: % *RH* = % relative humidity; t_c = critical time; $\dot{m}_{\mathrm{NCST}}$ = normalised constant mass flux for phase I; D_{II} = phase II diffusivity.

Wet flow / slm	0.0	0.2	0.4	0.6	0.8	1.0
% *RH*	0	5	15	30	40	50
t_c / min	57.11	55.85	68.66	100.44	145.55	333.76
$\dot{m}_{\mathrm{NCST}}$ / $\mathrm{m^{-2}\ s^{-1}}$	0.334 $\pm\ 4 \times 10^{-4}$	0.341 $\pm\ 4 \times 10^{-4}$	0.288 $\pm\ 7 \times 10^{-4}$	0.212 $\pm\ 1 \times 10^{-3}$	0.138 $\pm\ 8 \times 10^{-4}$	0.058 $\pm\ 5 \times 10^{-4}$
D_{II} / $\mathrm{m^2\ s^{-1}}$	3.2×10^{-9} $\pm\ 4 \times 10^{-10}$	3.2×10^{-9} $\pm\ 4 \times 10^{-10}$	2.9×10^{-9} $\pm\ 3 \times 10^{-10}$	2.5×10^{-9} $\pm\ 2 \times 10^{-10}$	1.6×10^{-9} $\pm\ 9 \times 10^{-11}$	1.1×10^{-9} $\pm\ 4 \times 10^{-12}$

As the % *RH* increases there is a resulting decrease in $\dot{m}_{\mathrm{NCST}}$, as predicted by Fick's first law[90], and this decrease in evaporation rate means that the time taken before disconnected pathways form is longer, resulting in an increase in t_c. The critical time, t_c, was determined using the same procedure as described before for pure H_2O; however, in Figure 4.5(b), it can be seen that the clear change from phase I

to phase II as seen for 0.0 and 0.2 slm becomes less defined with increasing humidity, and therefore, this leads to questions over defining discrete drying phases and t_c. Furthermore, with increasing humidity, an initial decrease in $\dot{m}_{\mathrm{N}}$ becomes apparent within the phase I drying period, and the time scale over which this occurs lengthens from approximately 10 minutes for 0.0 slm to 30 minutes for 1.0 slm. Franzen and Mirwald[12] proposed that the origin of this initial sharp decrease in $\dot{m}_{\mathrm{N}}$ is due to vaporisation, which is not influenced by the stone surface. This vaporisation, therefore, may be from a water layer on the surface of the stone, and with increasing humidity, this water layer increases in thickness, resulting in a longer time scale and greater observed decrease in $\dot{m}_{\mathrm{N}}$.

From both the data presented in Table 4.3 and Figure B.4 of the supplementary information, it can be seen that D_{II} also decreases with increasing % RH. As previously stated, phase II is determined by unsaturated flow within the material and should be independent of the external environment. However, these results imply that the external conditions influence the late stage drying behaviour. We note that the value of D_{II} at the highest % RH is broadly consistent with the self-diffusion coefficient of liquid water, reflecting the importance of water at the solid–gas interface, even at these later stages. This observation and the interpretation of late stage drying requires further investigation and quantitative modelling.

4.4 Conclusions

This paper presents the first use of cavity ring-down spectroscopy with dual-wavelength switching to quantitatively monitor the drying kinetics of Clipsham limestone. The spectroscopically deduced masses are in good agreement with those measured gravimetrically, and the drying kinetics are well described by the classic two-phase model when dry flows are employed. The ability to switch quickly and reproducibly between multiple wavelengths allows different isotopologues to be monitored, and there is excellent agreement between the measured drying kinetics and diffusivity parameters when monitoring H_2O and HDO from samples that have been isotopically enriched.

When the relative humidity of the drying gas was increased, there was an observed decrease in the phase I normalised mass flux and an increase in its time scale, as predicted using Fick's law. A clear decrease in phase II diffusivity with increasing relative humidity was also observed.

In the future, it will be interesting to use the CRDS technique to investigate the evaporation of water isotopologues under varying wet depositions within atmospheric simulation chambers of the type presented by Chabas *et al.*[238]. Further work will also investigate the influence of temperature on the drying kinetics of different classes of limestone and other porous materials which have been subject to treatment with consolidants. Finally, we note that the CRDS technique can be used to readily couple the detection of water and its isotopologues with the sensitive and selective detection of other trace gas species and pollutants; such measurements will further enhance our understanding of decay mechanisms within these heritage materials and strategies for ameliorating their effect.

Supplementary information

The supporting information is in Appendix B. This information contains details on the following:

- Mercury intrusion porosimetry results: Clipsham limestone;
- Spectroscopic nomenclature;
- Wavelength calibration;
- Reproducibility kinetics;
- Relationship between phase II diffusivity for HDO transition and % relative humidity.

Chapter 5

Direct monitoring of drying kinetics of building limestones using cavity ring-down spectroscopy

Dáire E. Browne, Robert Peverall, Grant A. D. Ritchie and Heather A. Viles, *Construction and Building Materials*, **2023**, *369*, 130554.

Abstract

Enhanced understanding of the drying kinetics of building materials is important to explain durability and improve conservation. Cavity ring-down spectroscopy has been demonstrated to be an effective method to investigate drying kinetics, and is here applied to investigate the drying behaviour of five commonly used building limestones, and one sandstone. Although the time period for phase I drying increases with increasing porosity, the constant mass flux remains essentially unchanged. This is not so for phase II drying diffusivities which are reported for Portland Whit Bed limestone, Portland Base Bed limestone, Clipsham limestone, Bath limestone, Savonnières limestone and Stoke Hall sandstone, and are found to be in the range $3.0 - 6.5 \times 10^{-9}$ m^2 s^{-1} at 25 ℃. Differences in the phase II diffusivity do not appear to be solely controlled by porosity. Activation energies associated with phase II drying for Clipsham limestone, Portland Base Bed limestone and Stoke Hall sandstone, are determined to be 31.9 ± 1.8, 29.4 ± 1.4 and 27.1 ± 2.2 kJ mol^{-1}, respectively.

5.1 Introduction

Water plays a key role in the deterioration of porous media, and understanding the effects of moisture retention and transport in construction materials continues to be an important aspect of contemporary civil and environmental engineering. The presence and fluctuations of water content can cause mechanical damage due to water undergoing various physical cycles, altering the building material[90]. The presence of water is also a requirement for different chemical and biological processes, for example, the reaction of sulfur bearing gases with limestone resulting in the formation of gypsum crusts[20]. Understanding water absorption and desorption is particularly important in explaining the deterioration of porous building stones such as limestone and sandstone, as these materials are prone to weathering from wetting and drying, and the crystallisation of soluble salts. Following the deterioration process, stone often suffers from loss of cohesion, and it is necessary to apply a consolidant to restore strength and protect the stone from suffering further decay. The moisture transport properties of the material (and in particular the drying behaviour) are important in the application and efficacy of these treatments[65]. Understanding the deterioration of limestone is also important in the field of cement and concrete research as the addition of limestone may improve cement properties, such as workability, durability and compressive strength (see, for example, Vuk *et al.*[239] and the references therein for further details).

There is a clear need to continue to develop new building conservation methods as the built environment is exposed to the increasingly extreme physico-chemical environments that accompany climate change. To achieve this aim requires ever increasing synergy between high quality laboratory studies, computational modelling, field measurements and the development and application of new analytical techniques. Within the latter area, we have recently reported on a proof-of-principle study using near-infrared continuous wave (cw) cavity ring-down spectroscopy (CRDS) to monitor the release of water and its artificially enriched isotopologues from small (*ca.* $25 \times 25 \times 5$ mm) samples of Clipsham limestone subject to drying by a fixed flow of nitrogen with

varying levels of humidity and at room temperature and atmospheric pressure[240]. Under low-humidity conditions, the drying kinetics observed are consistent with the well-established two-phase drying process exhibited by porous materials, namely, an initial constant drying rate period (phase I) followed by a falling drying rate period (phase II)[90,164]. In phase I, the surface of the porous medium is supplied with water by flow through connected pathways, and the resulting concentration gradient between the surface and the gas above controls the rate of evaporation. It is assumed that the surface of the medium is covered with a thin film of liquid and the gas above it is fully saturated leading to a relatively constant rate of evaporation. The rate of evaporation is thus controlled by the environment and is not dependent on the material properties. As the drying proceeds further, the surface water content decreases and the gas at the surface becomes unsaturated and disconnected pathways begin to form through the material. The unsaturated liquid capillary flow within the material is insufficient to maintain a constant evaporation rate and phase II drying begins. The drying of the material now occurs *via* vapour transport through the porous medium and the rate of evaporation is determined by the internal structure and properties of the material[236].

Importantly, the selectivity and sensitivity afforded by CRDS allows isotope analysis to be carried out, such that the flux of isotopically labelled water out of the sample during drying can be determined under conditions of humidified flow where there may be a simultaneous ingress of water from the environment. Dual-wavelength CRDS distinguishes isotopic species, and we have demonstrated that the drying kinetics and diffusivities are self-consistent when monitoring both HDO and H_2O.

In this paper we build upon our initial work using Clipsham limestone and present an investigation of the drying kinetics of a selection of limestones commonly used for construction and repair in the historic city of Oxford and elsewhere across the United Kingdom, and for comparison, a British sandstone also often used for new buildings and repair. We include a French limestone (Savonnières) and Portland limestone, an historic construction material which was the first designated "Global Heritage Stone

Resource" [13]. The influence of temperature on the drying kinetics is also investigated for a subset of the stones, and both heat and mass transfer coefficients and the activation energy for phase II diffusion is determined. These measurements will prove useful for future modelling of moisture dynamics and deterioration, and are a necessary prerequisite for quantitative studies of new consolidation treatments.

5.2 Materials and methods

5.2.1 Cavity ring-down spectroscopy

Each molecular species has a distinct set of quantum-mechanical energy levels which describe its translational, rotational and vibrational energy. As a consequence, molecules will absorb light at different frequencies which are particular to the identity of the molecule. Therefore, by choosing light at a specific frequency, the molecule of interest can be selectively excited — this is the underlying principle of laser absorption spectroscopy. Furthermore, by quantifying the amount of light absorption both the presence and concentration of an individual species within a complex sample can be determined. The relationship between the initial light intensity, $I_0(\nu)$, and the light intensity following absorption, $I(\nu)$, at frequency ν is given by the Beer–Lambert law [196], Equation 5.1:

$$I(\nu) = I_0(\nu) \exp[-\alpha(\nu)d] \tag{5.1}$$

where $\alpha(\nu)$ is the absorption coefficient and d the path length over which the light is absorbed. The absorption coefficient is given by $\alpha(\nu) = N\sigma(\nu)$, where $\sigma(\nu)$ is the species-dependent absorption cross-section and N is the concentration of species present in the sample. Thus, knowledge of $\sigma(\nu)$ in combination with measurements of the change in the light intensity yields concentration N.

Cavity ring-down spectroscopy allows the measurement of smaller values of $\alpha(\nu)$, and therefore, smaller values of N, by increasing the path length, d, over which the light is absorbed [203,205–208]. This is achieved by trapping the light between two highly reflective mirrors (the cavity), and monitoring the light as it leaks out. The time taken for the light intensity to decay to $1/e$ of its original value is recorded and is known as

the ring-down time, τ_0. In the presence of an absorbing species, there is an additional loss mechanism and the time taken for the light to decay is reduced, resulting in a different ring-down time, τ. The absorption coefficient can be calculated from this difference in ring-down times using the following equation:

$$\alpha(\nu) = \frac{1}{c}\left(\frac{1}{\tau} - \frac{1}{\tau_0}\right) \tag{5.2}$$

where c is the speed of light. Thus, from these two measurements the concentration of the species of interest can be determined.

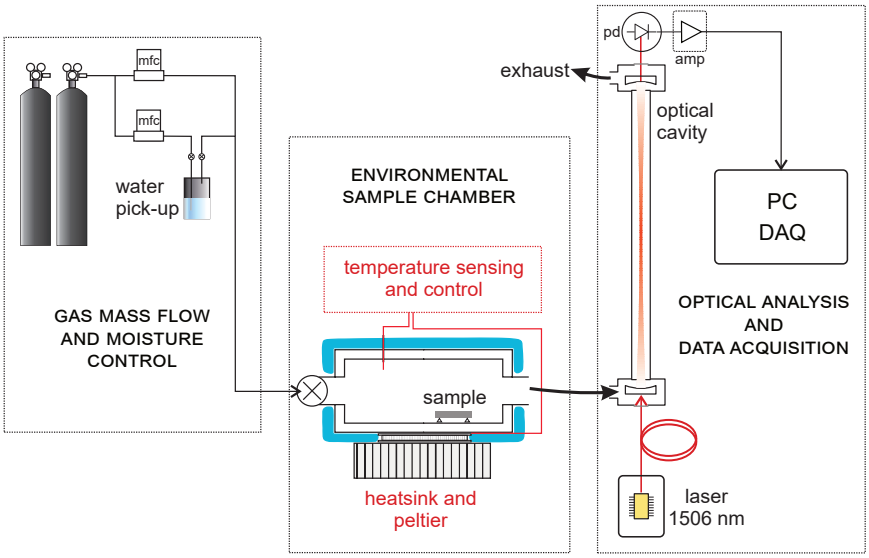


Figure 5.1: A depiction of the experimental set-up used to measure H_2O released from the stone sample. The sample is placed in a temperature controlled cell separate from the cavity ring-down spectrometer. Note: mfc = mass flow controller; pd = photodetector; amp = amplifier; DAQ = data acquisition system.

Figure 5.1 depicts the near-IR CRD spectrometer used in this work, and a full description of the instrument and theory can be found in Browne *et al.*[240]. Briefly, a cw fibre-coupled distributed feedback diode laser (NTT Electronics NLK1S5GAAA, $\lambda = 1506$ nm) was used to excite an optical cavity formed using two highly reflective mirrors (Layertec, $R \approx 0.9999$, radius of curvature = 1 m) placed 86 cm apart. The stone samples were placed in a temperature controlled (range = $10.0 - 50.0$ ℃, $\delta = 0.1$ ℃) insulated stainless steel chamber ($13 \times 7 \times 8$ cm) which was separated from the cavity by a valve. Experiments are carried out in a dry N_2 (BOC Oxygen

Free Nitrogen, 99.998 %) gas flow, controlled with calibrated mass flow controllers (MKS 1479A Mass-Flo and MKS PR 4000B-S).

5.2.2 Stone samples

This study investigated the drying kinetics of five limestones and one sandstone, all commonly used in construction and repairs of historic masonry. These were Portland limestone (Whit and Base Bed), Clipsham limestone, Bath limestone, Savonnières limestone and Stoke Hall sandstone. These stones were chosen as they cover a range of petrophysical and petrographical properties, allowing the universality of the instrument and its ability to validate porous materials drying behaviour to be fully probed. The BRE Stone List[181] was consulted for standard information regarding the stones selected. Each stone type was cut into two duplicate samples, *ca.* $25 \times 25 \times 5$ mm. To determine the pore size distribution (PSD) and characterise the internal structure of the samples, mercury intrusion porosimetry (MIP) and nitrogen adsorption measurements were carried out. These procedures were carried out on small samples which originated from the same stone blocks which provided samples for the drying experiments. The results of the subsequent analysis are shown in Figure 5.2 and Table 5.1, and are in good agreement with those reported in the literature[177,241–243]. In this analysis procedure to determine intrinsic permeability, k_{int}, we have used the experimentally measured pressure dependent cumulative volume to construct the differential $\mathrm{d}V/\mathrm{d}P$, from which the critical pressure, P_{c}, is determined. P_{c} is transformed into the characteristic length, ℓ_{c}, using the Washburn equation[146] (assuming cylindrical pore geometry), and then ℓ_{c} is scaled by the conductance formation factor, as set out by Katz and Thompson[183].

5.2.2.1 Stoke Hall sandstone

A fine to medium buff coloured sandstone from the Millstone Grit of Carboniferous age, Stoke Hall sandstone is quarried from Stoke Hall Quarry, Grindleford, Derbyshire in the U.K.[244]. Stoke Hall sandstone was used in the construction of Howden and

Table 5.1: Physical properties of the stone samples used in this study determined by mercury intrusion porosimetry and nitrogen adsorption. Note: V_p = total intrusion volume; SSA = specific surface area; ρ_b = bulk density at 3.38 kPa; ρ_s = skeletal density; ϕ_{MIP} = open porosity; d_p = peak pore diameter; d_m = mean pore diameter; k_{int} = intrinsic permeability as deduced by MIP using the rationale outlined in Katz and Thompson[183].

Stone	Stoke Hall SH	Portland Whit Bed PWB	Portland Base Bed PBB	Clipsham C	Bath B	Savonnières S
V_p / cm^3 g^{-1}	0.045	0.083	0.085	0.094	0.095	0.172
SSA / m^2 g^{-1}	1.51	1.16	1.03	0.98	2.47	0.97
ρ_b / g cm^{-3}	2.33	2.20	2.19	2.14	2.15	1.83
ρ_s / g cm^{-3}	2.60	2.69	2.69	2.68	2.70	2.66
ϕ_{MIP} / %	10.54	18.17	18.54	20.16	20.44	31.44
d_p / μm	3.84	0.28	0.18 13.95	0.84	0.55	0.15 21.33
d_m / μm	0.32	0.24	0.25	0.47	0.23	0.47
k_{int} / $\times 10^{-15}$ m^2	1.34	0.02	22.44	82.38	0.08	66.75

Derwent reservoirs and Sheffield Town Hall[245] and is often used for repairs in historic masonry. An open porosity, ϕ_{MIP}, of 10.54 % was measured for the Stoke Hall sandstone used in this study, with a peak pore diameter of 3.84 μm.

5.2.2.2 Portland limestone

Quarried on the Isle of Portland, this Upper Jurassic (Tithonian) limestone has been widely used as a building stone in the U.K., and is most known for its use in the construction of St. Paul's Cathedral, London[27]. Its use as a building stone in Oxford, U.K. has been limited, although it was used in the Taylor Institution[31] and Ashmolean Museum[23], and has experienced greater use as a repair stone, for example, in rebuilding the cupola of the Queen's college[23]. The Portland building series comprises three main beds: the Roach, the Whit Bed and the Base Bed. This study investigated the drying kinetics of the Whit and Base Bed, the more widely used building stones. The Whit Bed is a medium grained, fine to coarse bioclastic oolitic limestone[246], with a large amount of open inter-particle pores. When fresh,

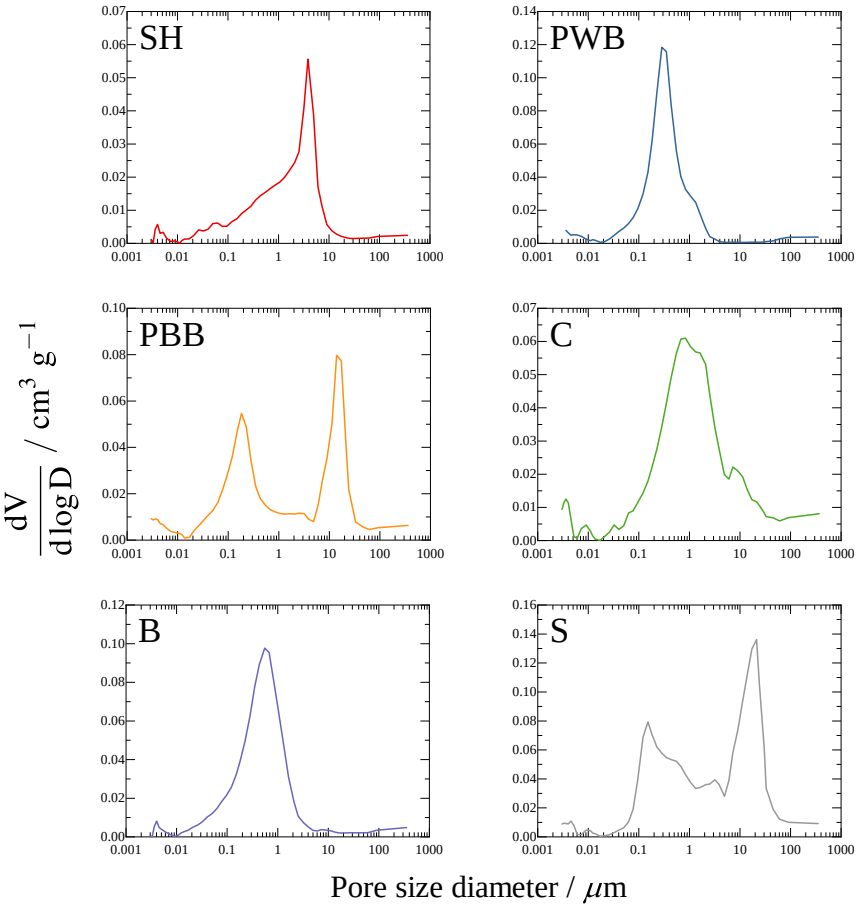


Figure 5.2: Pore size distributions (PSDs) of stone samples investigated in this study, obtained by mercury intrusion porosimetry by the British Geological Survey. Note: SH = Stoke Hall sandstone; PWB = Portland Whit Bed limestone; PBB = Portland Base Bed limestone; C = Clipsham limestone; B = Bath limestone; S = Savonnières limestone.

this limestone has a warm cream to pale brown tint, but upon exposure it becomes white[247]. The Base Bed is paler in colour than the Whit Bed, but is also a coarse bioclastic oolitic limestone. However, the Base Bed has a matrix-rich compacted texture[246], resulting in different physical properties to the Whit Bed. This difference is clear from the MIP analysis, where the Whit Bed sample has a unimodal PSD with a peak pore diameter of 0.28 μm while the Base Bed sample displays a bimodal PSD with peak pore diameters of 0.18 μm and 13.95 μm. Notably the two samples have very similar values of ϕ_{MIP}, 18.17 % and 18.54 % for Whit Bed and Base Bed samples, respectively.

5.2.2.3 Clipsham limestone

A very pale cream and buff coloured limestone, Clipsham is a course grained ooidal grainstone from the Lincolnshire Limestone Formation (Middle Jurassic, Bajocian)[233, 234]. This British limestone was deposited in a shallow marine carbonate shelf environment[235], and its first use in Oxford, U.K. was during the construction of the University of Oxford Examination Schools[31]. However, similiar to Portland limestone, it has been widely used as a repair stone, for example, in the refacing of Wadham College and Christ Church library as part of the Oxford Historic Buildings Fund programme[26], and in the restoration of the Houses of Parliament[248]. It has a broad unimodal PSD with a peak pore diameter of 0.84 μm and a ϕ_{MIP} of 20.16 %.

5.2.2.4 Bath limestone

Bath stone is an Upper Middle Jurassic (Bathonian) limestone found in the Bath region of South West England, U.K. The main Bath quarries are Box Ground, Combe Down, Hartham Park and Monk's Park[247], which exhibit slight variation in the petrophysical and petrographical properties. The majority of Bath stones are grainstones, mainly composed of ooliths (ranging from 0.2 to 0.8 mm) and larger mm-sized shell fragments[249]. The matrix of the stone is formed from low porosity crystalline calcite cement which provides the principal strength and resistance. The presence of the calcite shell fragments also provides some mechanical strength, and the presence of the weak and crumbly individual ooliths does not compromise its performance. A widely used English building stone, it first arrived in Oxford, U.K. around 1820, and has been used in a variety of buildings including the University Press building, and Balliol College on its Broad Street façade[23]. The Bath stone used in this study has a unimodal PSD with peak pore size diameter of 0.55 μm and ϕ_{MIP} of 20.44 %.

5.2.2.5 Savonnières limestone

Savonnières limestone, an Upper Jurassic (Tithonian) limestone, is quarried in the Meuse Department in northern France. It is a buff coloured oolitic grainstone[14], with a cross-bedded texture and bivalve-rich layers. Due to partial or full dissolution

of the ooids' nuclei, it is composed of intragranular macropores which are weakly connected[250]. However, partial cementation between the ooids results in a second intergranular macroporosity which is more connected. It has been used extensively as a restoration stone in France[250] and Belgium[14], and has also been used to reface the roadside façade of Magdalen College, Oxford, U.K.[26]. MIP analysis of the samples used in this study return a bimodal PSD with peak pore diameters of 0.15 μm and 21.33 μm, with a ϕ_{MIP} of 31.44 %.

5.2.3 Experiment procedure

Following the procedure described in Browne *et al.*[240], the samples were immersed in distilled water for a minimum of 2 days to ensure that they were fully saturated. Before being placed in the sample chamber, the sample's wet mass, m_w, was recorded following removal of excess surface water. Once placed in the sample chamber, the valve to the cavity was opened and a constant flow of 1.5 standard litres per minute (slm) dry N_2 passed over the sample (gas velocity = 7×10^{-3} m s^{-1}). For the stone comparison tests, the temperature of the sample chamber was set to 25 ℃, as determined using a calibrated thermocouple. The laser was tuned to the centre of the H_2O 10,3,7 (021) $\leftarrow$ 11,3,8 (000) transition at 6638.91 cm^{-1}[198] and the average ring-down time (RDT) of ten ring-down events was continuously measured; the typical ring-down acquisition rate was *ca.* $5 - 10$ s^{-1}. When the measured RDT returned to τ_0, the procedure was stopped and the dry mass of the sample, m_d, was recorded. The mass was measured using KERN PLS 420-3F mass balance (max. 420 g, δ = 0.001 g). Samples were not oven-dried in these proof-of-principle experiments, however, tests into the reproducibility using the same sample, and also different samples of the same stone, have been carried out, which showed good agreement between the kinetics parameters determined[240].

The influence of temperature on the drying kinetics for three of the samples was also investigated: two limestones (Clipsham and Portland Base Bed) and one sandstone (Stoke Hall). In these experiments, the same procedure as described above was used, except that the temperature of the sample chamber was varied from $20 - 40$

℃ in 5 ℃ steps. The same *ca.* 25 × 25 × 5 mm sample of each stone was used for measurements at each temperature.

5.3 Analysis

Using the method described in Section 5.2.3, the time-dependent release of water was monitored from the different stone samples. The absorption coefficient, $\alpha(\nu)$, is calculated using Equation 5.2 and the concentration of water released is determined using $\alpha(\nu) = N\sigma(\nu)$. The mass of water released from the sample is related to the concentration by the following equation:

$$m_{\mathrm{H_2O}}(t) = \frac{fM_r}{N_A}\int_0^t N\mathrm{d}t \tag{5.3}$$

where f is the volumetric flow rate, $M_r(\mathrm{H_2O}) = 0.018$ kg mol^{-1} and N_A is Avogadro's number. From the time-dependent mass change, the drying kinetics of the stone can be determined. The normalised mass difference, Δm_n, is calculated by:

$$\Delta m_n(t) = \frac{m_{\mathrm{H_2O}}(\infty) - m_{\mathrm{H_2O}}(t)}{m_d} \tag{5.4}$$

while the mass flux, $\dot{m}$, is defined as:

$$\dot{m} = \frac{1}{A}\frac{\mathrm{d}m_{\mathrm{H_2O}}(t)}{\mathrm{d}t} \tag{5.5}$$

where A is the surface area of the top face of the sample. The critical time, t_c, at which phase I ends is determined as the intercept between two tangents fitted to phase I and phase II in $\dot{m}(t)$. An iterative method is used in which this intercept is determined and is subsequently set as the upper limit of the phase I linear fit, and the process is repeated until a constant t_c is determined. The critical saturation value, S_c, is the percentage of water remaining in the sample following completion of phase I[82]. Using the mass of water released from the sample, $m_{\mathrm{H_2O}}(\infty)$, the dry mass, m_d, and the volume of the sample, allowed the open porosity (ϕ_{calc})[90] and the density (ρ_{calc}) to be calculated. As expected, the open porosities calculated from the release of water (and therefore, the capillary uptake under atmospheric pressure) are always less than the porosities determined by MIP[128,177,180,182,251], *vide infra*.

When the water saturation value falls below the critical saturation, the capillary flow is no longer sufficient to maintain the constant drying rate and water vapour diffusion becomes the dominant transport mechanism. In this case, phase II drying can be characterised by a diffusivity parameter, D_{II}, which originates from Fick's second law[150], Equation 5.6:

$$\left(\frac{\partial C}{\partial t}\right) = D_{\mathrm{II}}\left(\frac{\partial^2 C}{\partial x^2}\right) \tag{5.6}$$

For a porous sample, assuming a uniform distribution of moisture, integrating over the sample thickness, L, results in the following solution[150]:

$$\frac{m_{\mathrm{H_2O}}(t)}{m_{\mathrm{H_2O}}(\infty)} = 1 - \sum_{n=0}^{\infty} \frac{8}{(2n+1)^2\pi^2} \exp\left\{\frac{-D_{\mathrm{II}}(2n+1)^2\pi^2 t}{4L^2}\right\} \tag{5.7}$$

It has been found that when the sample has entered the later stages of drying and the moisture content has fallen below 40 %, then only the first term of Equation 5.7 needs to be considered and this results in the following linear relationship:

$$\ln\left(1 - \frac{m_{\mathrm{H_2O}}(t)}{m_{\mathrm{H_2O}}(\infty)}\right) - \ln\left(\frac{8}{\pi^2}\right) = -\frac{D_{\mathrm{II}}\pi^2 t}{4L^2} \tag{5.8}$$

The diffusivity, D_{II}, can be determined from the gradient of this linear relationship. A complete description of the derivations and analysis can be found in Browne *et al.*[240]

5.4 Results and discussion

5.4.1 Stone comparison data

The drying kinetics for the different stone samples are reported in Table 5.2 and shown in Figure 5.3. Figure 5.3(a) shows $\Delta m_n(t)$ for the different stone samples, showing the expected two-phase drying behaviour of porous media described in Section 5.1. This two-stage behaviour can be better represented in a plot of the mass flux, $\dot{m}(t)$, as shown in Figure 5.3(b). As previously stated, in phase I the rate of evaporation is controlled by the environment and thus, for these samples which are subjected to the same dry flow (1.5 slm) and temperature (25 ℃), the constant drying rates, $\dot{m}_{\mathrm{CST}}$,

reported are in good agreement. This agreement also indicates that the thermal properties of the saturated samples stones do not significantly differ, such that their surface temperatures can be taken as being the same.

Table 5.2: Comparison of drying kinetics for different stone samples, all *ca.* 25 × 25 × 5 mm, drying under a constant dry 1.5 slm N_2 flow at 25 ℃. Note: $m_{H_2O}(\infty)$ = spectroscopic mass; t_c = critical time; $\dot{m}_{CST}$ = constant mass flux for phase I; S_c = critical saturation value; D_{II} = phase II diffusivity; ϕ_{calc} = calculated porosity; ϕ_{MIP} = porosity determined by MIP; ρ_{calc} = calculated density; ρ_{MIP} = bulk density determined by MIP.

Sample	Stoke Hall SH	Portland Whit Bed PWB	Portland Base Bed PBB	Clipsham C	Bath B	Savonnières S
Volume / $\times 10^{-6}$ m^3	3.174	3.176	3.856	3.642	3.840	3.867
$m_{H_2O}(\infty)$ / g	0.283 ± 0.002	0.535 ± 0.004	0.493 ± 0.003	0.456 ± 0.003	0.621 ± 0.0046	0.972 ± 0.007
t_c / min	26.73	69.32	55.70	54.11	65.80	117.44
$\dot{m}_{CST}$ / kg m^{-2} s^{-1}	1.37×10^{-4} $\pm 9 \times 10^{-6}$	1.49×10^{-4} $\pm 9 \times 10^{-6}$	1.50×10^{-4} $\pm 9 \times 10^{-6}$	1.45×10^{-4} $\pm 9 \times 10^{-6}$	1.44×10^{-4} $\pm 9 \times 10^{-6}$	1.46×10^{-4} $\pm 9 \times 10^{-6}$
S_c / %	54	36	40	41	46	35
D_{II} / m^2 s^{-1}	3.171×10^{-9} $\pm 2 \times 10^{-12}$	5.945×10^{-9} $\pm 3 \times 10^{-12}$	6.335×10^{-9} $\pm 3 \times 10^{-12}$	4.465×10^{-9} $\pm 4 \times 10^{-12}$	4.195×10^{-9} $\pm 2 \times 10^{-12}$	3.990×10^{-9} $\pm 1 \times 10^{-12}$
ϕ_{calc} / %	9.77	17.76	15.46	14.54	17.27	26.74
ϕ_{MIP} / %	10.54	18.17	18.54	20.16	20.44	31.44
ρ_{calc} / g cm^{-3}	2.31	2.16	2.16	2.19	2.06	1.89
ρ_{MIP} / g cm^{-3}	2.33	2.20	2.19	2.14	2.15	1.83

From the data presented in Table 5.2, it is clear that as $\dot{m}_{CST}$ for the stones is approximately the same, the time taken to form disconnected pathways, t_c, increases with the increasing open porosity, ϕ_{calc}, of the samples. This trend is in agreement with a computational study on the influence of hydraulic properties of a porous medium (soil) on the drying kinetics[236], which specifically modelled the influence of the porosity. In that simulation, the porosity was varied from $30-50$ %, in 5 % steps, and it was found that as the porosity increased, the transition to phase II occurred at later times due to the increased amount of water present in the sample.

However, we note that this trend is not apparent when the MIP open porosities, ϕ_{MIP}, are considered. As highlighted earlier, comparison of ϕ_{calc} with ϕ_{MIP} (Table 5.1) shows that the open porosities calculated are all smaller than those measured

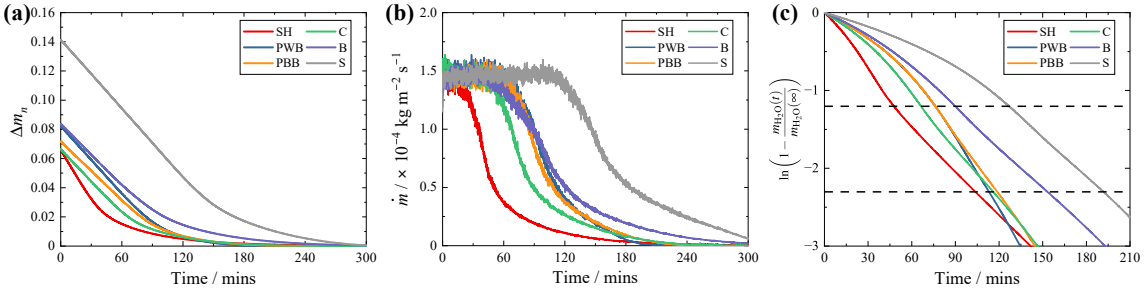


Figure 5.3: **(a)** A plot of the H_2O normalised mass differences, Δm_n, as a function of time for different stone samples, all *ca.* $25 \times 25 \times 5$ mm, drying under a constant dry 1.5 slm N_2 flow at 25 °C. **(b)** A plot of the H_2O mass flux, $\dot{m}$, as a function of time for different stone samples. **(c)** A plot of $\ln\left(1 - m_{H_2O}(t)/m_{H_2O}(\infty)\right)$ against time, allowing determination of D_{II}, for different stone samples. The region of the linear fit is indicated by two horizontal lines. Note: SH = Stoke Hall sandstone; PWB = Portland Whit Bed limestone; PBB = Portland Base Bed limestone; C = Clipsham limestone; B = Bath limestone; S = Savonnières limestone.

by MIP (and by differing amounts). The MIP process is based upon the intrusion of a non-wetting liquid (mercury) into a porous medium by application of increasing pressure (up to *ca.* 400 MPa), allowing access to pores of decreasing size[188]. The pores are assumed to have a cylindrical geometry and are accessible from the outer surface of the specimen[186]. Thus, based on this assumption, a limitation is introduced into the interpretation of PSDs derived from MIP — that of the ink-bottle effect[186,188,189] — in which the portion of smaller pores is overestimated as access to larger pore volumes is only possible through smaller pores or narrow pore throats. This offers an explanation for the discrepancy between the porosities obtained by MIP and those reported in Table 5.2. In the experiments described in this paper, water will only enter and be released from the accessible and connected pores, and to the point at which the sample comes into equilibrium with the environment. Therefore, large pores that are only accessible *via* very small pore networks will be inaccessible in our drying measurements. Thus, the static measurements reported for MIP cannot be directly related to these kinetics measurements, and this limitation must be taken into account when applying MIP analysis to the interpretation of water kinetics within "real-world" samples and conditions. We further note that the calculated densities reported in Table 5.2 are within $\pm 5\,\%$ of the reported bulk densities, giving

confidence to the dry masses used in these experiments and that there is little-to-no water trapped in the samples.

As previously stated, the critical saturation value is the moisture content determined at the end of phase I. From Table 5.2, it can be seen that Stoke Hall sandstone has a critical saturation of 54 %, which is higher than those determined for all limestones measured in this study ($\approx$ 40 %). When disconnected pathways within the stone begin to form, and the evaporation rate drops, the drying is dominated by water vapour diffusion, as reflected in the phase II kinetics. Figure 5.3(c) shows a plot of Equation 5.8 against time, which allows determination of D_{II} from the gradient of the linear fit. To ensure that only the first term of Equation 5.7 applies, the linear fit for D_{II} was taken between $10 - 30$ % saturation, as indicated by the two horizontal dashed lines in Figure 5.3(c).

The computational model reported by Mosthaf *et al.*[236] also predicts that generally higher porosities will result in higher phase II drying rates and which will be characterised by a larger effective diffusivity. From Table 5.2, it can be seen that the least porous sample, Stoke Hall sandstone, does indeed have the smallest D_{II} values and our value of 3.2×10^{-9} m^2 s^{-1} is consistent with Pichler *et al.*[252] who measured a value of 4.2×10^{-9} m^2 s^{-1} (15 mm^2 h^{-1}) for Obernkircherner sandstone ($\phi = 16.8$ %), obtained by dynamic vapour sorption experiments conducted over a range of relative humidities, upwards from 5 % *RH*. Within the limestone samples investigated, however, the phase II diffusivity does not have a clear trend as a function of porosity and other microphysical properties must be important. The highest diffusivities are for the Portland Whit Bed and Base bed samples despite PWB having a unimodal PSD and PBB having a bimodal distribution, and having large differences in the intrinsic permeability, $k_{\mathrm{int}}(\mathrm{PWB}) = 0.02 \times 10^{-15}$ m^2 vs. $k_{\mathrm{int}}(\mathrm{PBB}) = 22.44 \times 10^{-15}$ m^2. The lowest diffusivities are found in Savonnières and Bath limestone, and while the former is the most porous sample studied, the latter's porosity is very much similar to the other limestones. Repeated measurements on the same sample under identical external conditions return gradients for the linear relationship expressed in Equation

5.8 that are within $\pm 5\,\%$, giving confidence in the reproducibility of the reported diffusivity parameters.

5.4.2 Temperature dependence

The temperature dependence of the drying kinetics was investigated using three exemplar stones. Clipsham and Portland Base Bed limestone were chosen as exemplar limestones to compare the influence of a unimodal and a bimodal PSD on the drying kinetics (see Section 5.2.2) while Stoke Hall sandstone was chosen to compare the differences observed between limestones and sandstones. The results of this temperature dependent study are shown for each stone in Figure 5.4 and Table 5.3.

For all three samples, as the temperature increases, the rate of evaporation increases as shown by increasing values of $\dot{m}_{\mathrm{CST}}$. As phase I is controlled by external conditions, the higher temperature results in a higher saturated water vapour pressure, and this leads to a higher drying rate. This temperature dependent data is in agreement with the computational models of Mosthaf *et al.*[236]. The higher constant flux for phase I necessarily results in the critical time, t_c, decreasing.

From Figures 5.4(a)–(c), it can be seen that at the earliest times there is a drop in flux for the lowest temperatures (20 ℃), but an initial increase at the highest temperatures (35 and 40 ℃). This is due to differences in the initial temperature of the stone under investigation and the temperature of the sample chamber. In these experiments, as described in Section 5.2.3, the sample chamber and system are set to the temperature of interest and left undisturbed for a period of 30 min to ensure equilibrium is reached. The stones, however, are submerged in distilled water at room temperature (*ca.* 20 ℃), and thus, when first placed into the temperature controlled sample chamber, the stone samples are exposed to a temperature gradient and begin to equilibriate with the chamber environment. This can be observed as the sharp increase/decrease in $\dot{m}$ observed in Figures 5.4(a)–(c). When analysing the data to determine $\dot{m}_{\mathrm{CST}}$ and t_c, this initial change is excluded. However, as previously stated, as the temperature increases the rate of evaporation is higher and the drying front recedes beneath the surface, forming disconnected pathways. Thus, the unsaturated

capillary flow is no longer sufficient to maintain the high evaporation rate and $\dot{m}$ begins to decrease at shorter times. These two opposing effects combine to limit the period of the linear phase I previously observed in Section 5.4.1.

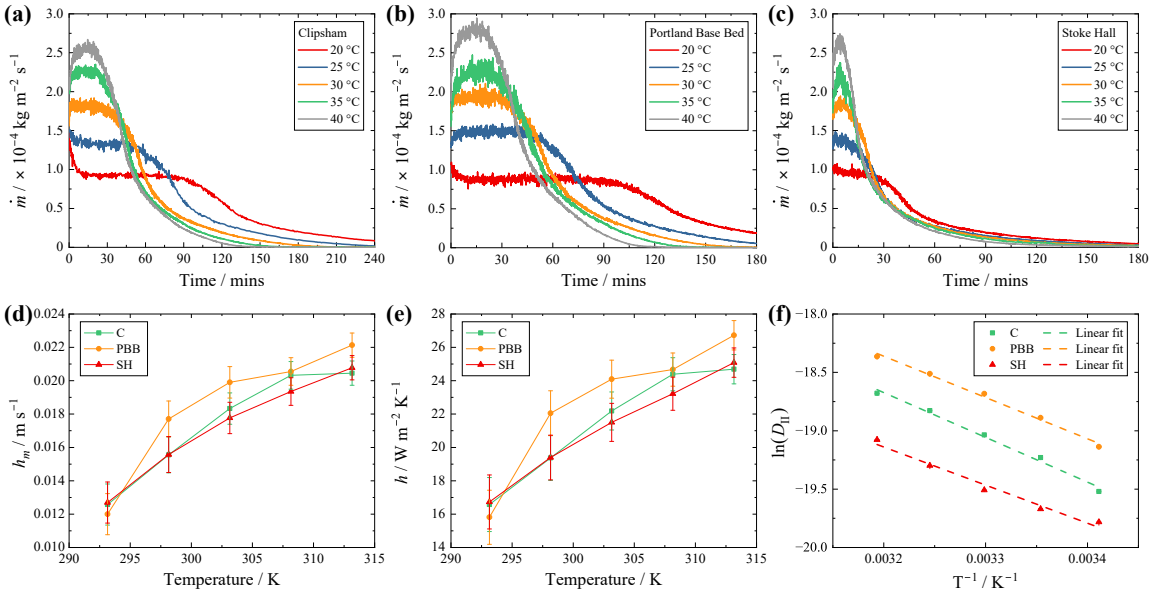


Figure 5.4: **(a)** A plot of the H_2O mass flux, $\dot{m}$, as a function of time with increasing temperature for the same *ca.* $25 \times 25 \times 5$ mm Clipsham limestone sample. **(b)** A plot of the H_2O mass flux, $\dot{m}$, as a function of time with increasing temperature for the same *ca.* $25 \times 25 \times 5$ mm Portland Base Bed limestone sample. **(c)** A plot of the H_2O mass flux, $\dot{m}$, as a function of time with increasing temperature for the same *ca.* $25 \times 25 \times 5$ mm Stoke Hall sandstone sample. **(d)** A plot of the mass transfer coefficient, h_m, as a function of temperature for the three stones investigated. **(e)** A plot of the heat transfer coefficient, h, as a function of temperature for the three stones investigated. **(f)** A plot of $\ln(D_{\mathrm{II}})$ against $1/T$ based on an Arrhenius relationship between phase II diffusivity and temperature for the three stones investigated.

5.4.2.1 Transfer coefficients

The mass flux, $\dot{m}$, is due to convection and is driven by the water content potential between the surface and the gas above[165]. It can be expressed as follows:

$$\dot{m} = h_m(\rho_{v,\mathrm{surf}} - \rho_{v,\mathrm{gas}}) \tag{5.9}$$

where h_m is the mass transfer coefficient, and $\rho_{v,\mathrm{surf}}$ and $\rho_{v,\mathrm{gas}}$ are the vapour densities at the surface of the medium and in the surrounding gas, respectively[88,165].

The net heat flux, $\dot{q}$, between the environment and the porous medium is the sum

of the convective heat exchanged between the environment and porous medium, and the heat exchanged *via* vapour flux[165], and is given by:

$$\dot{q} = h(T_{\text{gas}} - T_{\text{surf}}) - L\,\dot{m} \tag{5.10}$$

where h is the heat transfer coefficient, T_{gas} and T_{surf} the gas and surface temperatures, respectively, and L the latent enthalpy of evaporation (2.5×10^6 J kg^{-1})[88,165].

During phase I it is assumed that the gas above the surface is fully saturated and the surface temperature is equivalent to the wet bulb temperature[88], *i.e.*, $\rho_{v,\text{surf}} = \rho_{v,\text{sat}}$ and $T_{\text{surf}} = T_h$. Under these conditions there is no heat transfer to the sample but rather it is used solely to evaporate liquid water. In this limit, Equations 5.9 and 5.10 can be rearranged to the following:

$$h_m = \frac{\dot{m}_{\text{CST}}}{\rho_{v,\text{sat}} - \rho_{v,\text{gas}}} \tag{5.11}$$

$$h = \frac{L\,\dot{m}_{\text{CST}}}{T_{\text{gas}} - T_h} \tag{5.12}$$

The wet bulb temperature was calculated for the different temperatures investigated using the expression stated in Stull[163], assuming that the relative humidity (RH) was zero (dry N_2 is passed over the sample). The vapour densities were calculated using Antoine equation[160], with $\rho_{v,\text{sat}}$ determined at T_h. In general $\rho_{v,\text{gas}}$ is calculated from $\rho_{v,\text{gas}} = \rho_{v,\text{sat}} \times RH$ where $\rho_{v,\text{sat}}$ is determined at T_{gas}; in this specific case, $RH = 0$ as is $\rho_{v,\text{gas}}$.

Figures 5.4(d) and 5.4(e) show the mass and heat transfer coefficients, respectively, as a function of temperature for the three stones investigated. As predicted by the good agreement between the constant mass fluxes reported in Table 5.3, the three stones show the same trend in h_m and h with increasing temperature, and the coefficients lie in the range $0.012 - 0.023$ m s^{-1} and $15 - 27$ W m^{-2} K^{-1}, respectively. We also note that doubling the gas flow led to a 30 % increase in the transfer coefficients. For comparison, Prime *et al.*[88] reported values of h_m and h for Lixhe limestone at 50 ℃, 5 % RH, and air velocity of 0.8 m s^{-1}, and parameterised their results as a function of volume to surface area ratio. Using their parameterisation and applying

this to our samples (*i.e.*, volume to surface area ratio of 5), yields values of $h_m \approx 0.06$ m s^{-1} and $h \approx 66$ W m^{-2} K^{-1}. These higher transfer coefficients simply reflect the higher evaporation rates due to both the higher temperature and air velocity used. Ben Nasrallah and Perre[253] modelled heat and mass transfer during convective drying of a clay brick at 87 ℃ and 0 % *RH*, and reported values of $h_m = 0.014$ m s^{-1} and $h = 15$ W m^{-2} K^{-1}, which are closer to those reported in this study, despite the large difference in temperatures. Similar to Prime *et al.*[88], our data indicates that heat and moisture transfer for limestones and sandstones are relatively fast.

5.4.2.2 Phase II drying

From Table 5.3, it can be seen that as the temperature increases, the phase II diffusivity increases. It should be noted that the phase II diffusivity for Portland Base Bed limestone is consistently higher than Clipsham limestone and Stoke Hall sandstone at all temperatures, and is in keeping with the observations at 25 ℃ presented in Section 5.4.1. In phase II, the liquid water pathways have become disconnected and the drying process occurs *via* vapour transport[236]. Liquid water present on the pore surfaces must therefore evaporate in order to be removed from the sample by this mechanism. Furthermore, on average, water vapour diffusing through the porous medium will undergo many wall (surface) interactions (as the mean free path of water under atmospheric conditions is similar to the mean pore diameter). These interactions can be characterised by an effective activation energy, E_a, which can be determined if an Arrhenius type relationship for the stage II diffusivity is assumed[172,173]:

$$D_{\mathrm{II}}(T) = D_0 \exp\left(\frac{-E_a}{RT}\right) \tag{5.13}$$

Here D_0 is a temperature-independent pre-exponential factor, R is the gas constant and T is the absolute temperature. Equation 5.13 is a suitable approximation over the small range of temperatures investigated. Figure 5.4(f) shows a plot of $\ln(D_{\mathrm{II}})$ against $1/T$ for the three stones of interest, showing the predicted linear decrease in $\ln(D_{\mathrm{II}})$ with the reciprocal of absolute temperature. The activation energy, E_a, is determined from the gradient of the linear fit and reported in Table 5.3.

Table 5.3: Comparison of drying kinetics for the three exemplar stones, all *ca.* $25 \times 25 \times 5$ mm, drying under a constant dry 1.5 slm N_2 with increasing temperature. Note: t_c = critical time; $\dot{m}_{\mathrm{CST}}$ = constant mass flux for phase I; h_m = mass transfer coefficient; h = heat transfer coefficient; D_{II} = phase II diffusivity; E_a = activation energy.

Temperature / ℃	20	25	30	35	40
t_c / min	95.10	68.69	46.42	33.85	27.39
$\dot{m}_{\mathrm{CST}}$ / kg m^{-2} s^{-1}	9.2×10^{-5} $\pm 9 \times 10^{-6}$	1.30×10^{-4} $\pm 9 \times 10^{-6}$	1.75×10^{-4} $\pm 9 \times 10^{-6}$	2.21×10^{-4} $\pm 9 \times 10^{-6}$	2.53×10^{-4} $\pm 9 \times 10^{-6}$
h_m / m s^{-1}	0.0126 ± 0.0012	0.0156 ± 0.0011	0.0183 ± 0.0009	0.0203 ± 0.0008	0.0205 ± 0.0007
h / W m^{-2} K^{-1}	16.58 ± 1.62	19.37 ± 1.34	22.19 ± 1.14	24.39 ± 0.99	24.69 ± 0.88
D_{II} / m^2 s^{-1}	3.331×10^{-9} $\pm 8 \times 10^{-12}$	4.452×10^{-9} $\pm 1.2 \times 10^{-11}$	5.405×10^{-9} $\pm 4 \times 10^{-12}$	6.657×10^{-9} $\pm 3 \times 10^{-12}$	7.722×10^{-9} $\pm 2 \times 10^{-12}$
E_a / kJ mol^{-1}			31.87 ± 1.79		

(a) Clipsham limestone

Temperature / ℃	20	25	30	35	40
t_c / min	98.79	54.26	42.21	33.57	27.86
$\dot{m}_{\mathrm{CST}}$ / kg m^{-2} s^{-1}	8.8×10^{-5} $\pm 9 \times 10^{-6}$	1.48×10^{-4} $\pm 9 \times 10^{-6}$	1.90×10^{-4} $\pm 9 \times 10^{-6}$	2.24×10^{-4} $\pm 9 \times 10^{-6}$	2.74×10^{-4} $\pm 9 \times 10^{-6}$
h_m / m s^{-1}	0.0120 ± 0.0012	0.0177 ± 0.0011	0.0199 ± 0.0009	0.0206 ± 0.0008	0.0221 ± 0.0007
h / W m^{-2} K^{-1}	15.81 ± 1.62	22.06 ± 1.34	24.09 ± 1.14	24.67 ± 0.99	26.72 ± 0.88
D_{II} / m^2 s^{-1}	4.885×10^{-9} $\pm 2 \times 10^{-12}$	6.264×10^{-9} $\pm 3 \times 10^{-12}$	7.691×10^{-9} $\pm 3 \times 10^{-12}$	9.131×10^{-9} $\pm 2 \times 10^{-12}$	1.0580×10^{-8} $\pm 3 \times 10^{-12}$
E_a / kJ mol^{-1}			29.40 ± 1.44		

(b) Portland Base Bed limestone

Temperature / ℃	20	25	30	35	40
t_c / min	31.82	18.43	16.85	10.22	9.27
$\dot{m}_{\mathrm{CST}}$ / kg m^{-2} s^{-1}	9.3×10^{-5} $\pm 9 \times 10^{-6}$	1.30×10^{-4} $\pm 9 \times 10^{-6}$	1.70×10^{-4} $\pm 9 \times 10^{-6}$	2.10×10^{-4} $\pm 9 \times 10^{-6}$	2.57×10^{-4} $\pm 9 \times 10^{-6}$
h_m / m s^{-1}	0.0127 ± 0.0012	0.0156 ± 0.0011	0.0178 ± 0.0009	0.0194 ± 0.0008	0.0208 ± 0.0007
h / W m^{-2} K^{-1}	16.73 ± 1.62	19.40 ± 1.34	21.51 ± 1.14	23.22 ± 0.99	25.09 ± 0.88
D_{II} / m^2 s^{-1}	2.562×10^{-9} $\pm 1 \times 10^{-12}$	2.867×10^{-9} $\pm 2 \times 10^{-12}$	3.370×10^{-9} $\pm 3 \times 10^{-12}$	4.157×10^{-9} $\pm 3 \times 10^{-12}$	5.187×10^{-9} $\pm 4 \times 10^{-12}$
E_a / kJ mol^{-1}			27.12 ± 2.32		

(c) Stoke Hall sandstone

For Clipsham and Portland Base Bed limestone, E_a was determined to be 31.87 ± 1.79 kJ mol^{-1} and 29.40 ± 1.44 kJ mol^{-1}, respectively, whereas for Stoke Hall sandstone it was determined to be 27.12 ± 2.32 kJ mol^{-1}. For comparison, the enthalpy of vaporisation for water is 44 kJ mol^{-1} at 25 ℃. The values of E_a reported in Table 5.3 are comparable to those reported in literature for other porous media. For example, Gualtieri *et al.*[254] found E_a in the range $27 - 32$ kJ mol^{-1} for natural clay bricks, while Castro and Coelho Pinheiro[172] measured $E_a = 24$ kJ mol^{-1} for cork powder.

The activation energies determined here (and by others) are different and smaller than that for desorption from liquid water and are consistent with unsaturated conditions. We note that for pure crystalline calcite and silicate, the activation energy tends to increase as the surface coverage of water decreases[156], but that this effect can be reversed for amorphous versions of the same materials with varying surface roughness[157]. In addition, it has been reported that the presence of organic impurities can have a marked influence on the uptake of water in natural limestone[255]. The degree to which these effects, which reflect the internal micro-physico-chemical properties of the porous building materials, contribute to the phase II diffusivity warrants more detailed study.

5.5 Conclusions

This article reports an investigation into the drying kinetics for six natural building stones using a recently developed near-IR cavity ring-down spectrometer. The building materials all show the expected two-phase drying behaviour for porous media under dry flows. A clear increase in the time period for the phase I drying, from 25 to 120 min, was observed as the porosity of the samples increased from 10 to 32 %. The phase II diffusivity values, however, did not follow this trend and were found to be in the range $3.0 - 6.5 \times 10^{-9}$ m^2 s^{-1}. No clear link between the phase II diffusivity and the MIP-derived pore size distribution could be found. A study into the temperature dependence of the drying kinetics was conducted for three exemplar stones — Clipsham, Portland Base Bed limestone, and Stoke Hall sandstone — and the results

were consistent with predictions from thermodynamics and kinetic theory. That is, the phase I evaporation rate increases with temperature (and quantified by heat and mass transfer coefficients) and the phase II diffusivity displays an exponential temperature dependence. The activation energy for the phase II drying was found for the three samples to lie in the range $27 - 32$ kJ mol^{-1} and indicates subtle differences between individual porous media which reflect both the strength of binding of water to the mineral surface and slight differences in the pore structure. Further investigation into which of these stone properties determine the phase II diffusivity is required. Future studies could also seek to elucidate both water transport and (micro)mechanical properties of the stones (as they are controllably deteriorated). Another immediate area of interest is an investigation into the influence of consolidation treatments on the drying kinetics of limestones, and the effect of different environmental conditions (*e.g.*, temperature, % RH). In future, the flexible and versatile CRDS technique can be applied to the detection of other key species of interest, for example, pollutants such as SO_2 or CO_2, to increase our understanding of deterioration processes.

Chapter 6

Investigating the effect of nanolime treatment on the drying kinetics of Clipsham limestone

Dáire E. Browne, Robert Peverall, Grant A. D. Ritchie and Heather A. Viles, *Heritage Science*, **2023**, *11*, 114.

Abstract

Climate change poses an ever-increasing risk to our stone built heritage. Among conservation actions, the use of consolidant products is considered a possible response to this challenge, and the adoption of nanolimes has been widely studied showing promising results. However, while the effectiveness and method of application has been assessed, few studies have probed the changes in drying kinetics following treatment. In fact, a drastic alteration of the water transport might lead to further anomalies. This study investigates the influence of nanolimes dispersed in ethanol on the drying kinetics of Clipsham limestone using cavity ring-down spectroscopy. The degree of treatment was assessed by gravimetry, Raman spectroscopy, optical microscopy, colorimetry, optical profilometry and thin section analysis. Results showed an increase in the dry mass, observable colour changes and decrease in surface roughness. Small but reproducible increases were observed in the evaporation flux for phase I behaviour following treatment, however, no changes were observed in the total mass of water released or the phase II diffusivity. Determination of the activation energy associated with phase II drying was unchanged following treatment. These results indicate that

following treatment there has been little-to-no change in the internal surfaces and structure of the stone to affect vapour transport.

6.1 Introduction

The deterioration and conservation of stone built heritage is a significant area of research, especially due to increasing threats which accompany climate change. Deterioration of the stone can result in the loss of cohesion, leading to powdering, flaking, blistering and other forms of material loss. Therefore, it is often necessary to apply a consolidant to restore strength and provide resistance to various damage mechanisms[59]. An ideal consolidant must be compatible with the substrate, have high durability and offer retreatability[34]. Therefore, it is unsurprising that finding a suitable consolidant can be extremely difficult, and a variety of materials have been tried.

For the consolidation of limestone, inorganic lime-based consolidants should be preferably considered. Traditionally, limewater (an aqueous suspension of $Ca(OH)_2$) was widely used due to its compatibility with the substrate and high durability[34]. Consolidation of limestone occurs *via* the carbonation reaction of $Ca(OH)_2$ in the presence of CO_2 resulting in the formation of $CaCO_3$[72], the main component of the limestone matrix. However, due to the limited solubility of $Ca(OH)_2$ in water (1.65 g/L at 20 ℃[63]), large quantities of aqueous solution are required to achieve consolidation, and this poses other risks such as that of freeze–thaw weathering or salt migration[79]. Another drawback is the limited penetration depth of limewater, with the majority of the lime depositing near the surface, and in some cases, forming a white film that can be seen following application[34,48].

The use of nanolimes — dispersions of nanometre sized $Ca(OH)_2$ crystals — was proposed by Giorgi *et al.*[48] in 2000 in order to address these limitations. In their study, Giorgi *et al.*[48] compared the kinetic stability of $Ca(OH)_2$ dispersed in water versus propan-1-ol, and found that the alcohol dispersion had higher kinetic stability. The use of alcohol dispersions also offers the advantages of limiting carbonation of

the nanolimes particles by CO_2 before they have been deposited in the stone[34,63], and allowing a higher concentration of $Ca(OH)_2$, *e.g.*, commercial nanolime *CaLoSiL* (IBZ-Salzchemie GmbH & Co, Germany) is available in concentrations of 50 g/L. However, it is important to note that the use of alcohol dispersions requires appropriate health and safety precautions to carefully control the risk to the user and the environment[63].

Since then, nanolimes have been widely studied[63,256] and the literature can broadly be divided into two main groups: the first group concerns the study of the nanolimes themselves, determining the mechanism of the carbonation process[53,54,58,257] as well as improving the efficacy and synthesis of nanolime[258–262]. The second group mostly focuses on the application of these nanolimes to different substrates[59,61,67,68,70,71,73,263–265], in various environmental conditions[77–79] and with different application procedures[62,74–76,266]. Within this second group, the compatibility and effectiveness of the nanolime treatment have been assessed in terms of penetration depth, strength, hardness, surface cohesion, capillary absorption and aesthetics. However, few studies have investigated the impact of nanolime treatment on the water drying kinetics despite reports of a decrease in measured porosity and accumulation of nanolimes near the surface[60,66,69,71,72]. If this accumulation alters the water transport kinetics, and as the consolidation treatment is irreversible, this will result in a permanent and dramatic change which may result in trapped moisture leading to increased weathering[72].

Recently, we have developed and reported on the use of near-infrared continuous wave (cw) cavity ring-down spectroscopy (CRDS) to monitor the release of water from small (*ca.* $25 \times 25 \times 5$ mm) samples of Clipsham limestone[240], with a follow-up study demonstrating the universality of the technique when applied to different stone samples[267]. In these experiments, the drying kinetics showed the expected two-phase drying behaviour for porous materials, which consists of an initial constant drying rate period (phase I) followed by a falling drying rate period (phase II)[90,164]. During phase I, the rate of evaporation is controlled by the concentration gradient between the surface and the gas above. The pores at the surface are supplied with water by

flow through connected pathways, and the gas at the surface is fully saturated, leading to a constant rate of evaporation. As the drying proceeds further, disconnected pathways begin to form within the material, decreasing the surface water content and resulting in the gas at the surface becoming unsaturated. Eventually, the unsaturated capillary flow is no longer sufficient to maintain a constant rate of evaporation and phase II drying begins. Vapour transport through the material now dominates, and is controlled by the internal structure and properties of the material.

We have also demonstrated that, using CRDS, the influence of temperature on the drying kinetics can be investigated [267]. We have shown that the phase II diffusivity increases with temperature, allowing determination of an activation energy which characterises the surface interactions that occur during the diffusion of water through the porous stone. We have previously determined that for Clipsham limestone the activation energy for phase II diffusivity is 31.87 ± 1.79 kJ mol^{-1} [267], which is lower than the enthalpy of vaporisation from liquid water. Previous research has suggested that this decrease could be due to varying surface roughness [157].

The aim of this study is to use this highly sensitive technique to study the influence of ethanol-dispersed nanolime treatments on the drying kinetics of Clipsham limestone. Studies are conducted at a variety of temperatures to determine if treatment has an impact on the phase II activation energy. The degree of treatment is assessed by gravimetry, Raman spectroscopy, optical microscopy, colorimetry, optical profilometry and thin section analysis.

6.2 Materials and methods

6.2.1 Stone type: Clipsham limestone

This work focuses on the treatment of Clipsham limestone, a commonly used construction [31] and repair [26,248] stone. It is a coarse grained ooidal and shell fragmental grainstone with occasional herringbone cross-bedding (Figure 6.1(a), C0), originating from the Lincolnshire Limestone Formation (Middle Jurassic, Bajocian) [233,234]. It has a broad unimodal pore size distribution with a open porosity of 20.16 % and

peak pore diameter of 0.84 μm, as shown in Figure 6.1(b). A full characterisation of this limestone can be found in our previous research[240,267].

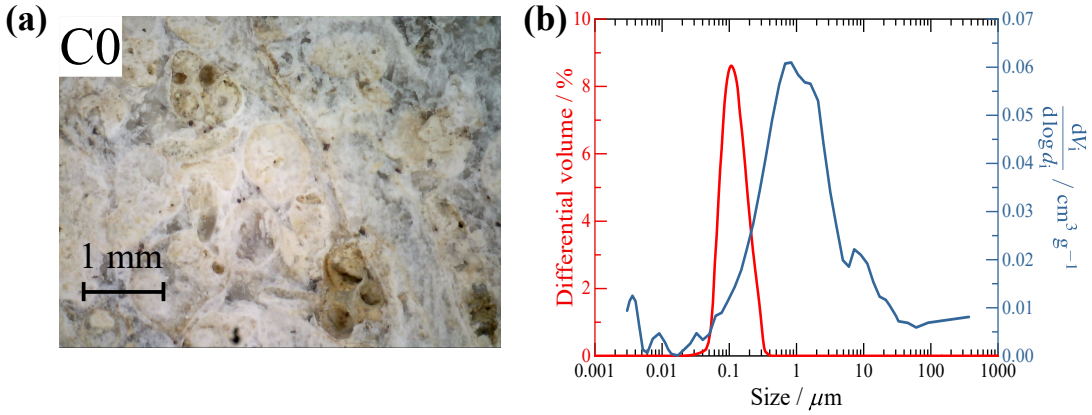


Figure 6.1: **(a)** Optical microphotograph for a control sample (C0); **(b)** Left hand axis (red): Particle size distribution of *CaLoSiL E25* (IBZ-Salzchemie GmbH & Co, Germany), provided by the manufacturer; Right hand axis (blue): Pore size distribution for Clipsham limestone, obtained by mercury intrusion porosimetry by the British Geological Survey.

Previous research on different limestones, such as Maastricht[59,60,64,65], Lecce[61], Doulting[62] and Migné[64], has reported that treatment with alcohol dispersed nanolimes results in limited penetration, and due to back-migration of the nanoparticles during solvent evaporation, the nanolime is mostly found at distances less than 1 cm from the drying face[63,76]. To ensure full treatment of the sample, as well as allow relatively fast drying experiments, the dimensions of the sample were cut to *ca.* 25 × 25 × 5 mm; eight replicate samples were investigated.

6.2.2 Consolidant and application procedure

The influence of treatment on the drying kinetics was investigated at two different concentrations. Commercially available nanolime *CaLoSiL E25* (IBZ-Salzchemie GmbH & Co, Germany) was selected due to its prevalence in nanolime research[54,68,70,71,75,258,262]. *CaLoSiL E25* (*E25* hereinafter) is a colloidal dispersion of $Ca(OH)_2$ nanoparticles in ethanol at a concentration of 25 g/L, with a particle size distribution reported between 50 and 300 nm, as shown in Figure 6.1(b), which is in agreement with literature values[55,268]. The applied suspension was well within its shelf-life and the ethanol

solvent is known to promote kinetic stability[53,64,65]. However, general consensus and advice for conservation practice promotes initially using lower concentrations of alcohol dispersed nanolimes (*e.g.*, 5 or 10 g/L), in order to prevent the formation of a white haze and improve penetration into the sample[63,74,244]. Therefore, a second concentration of 5 g/L (*E5* hereinafter) was obtained by diluting one part *E25* with four parts ethanol (Sigma Aldrich, p.a. > 99.8 %). To mitigate the Ca-alkoxide conversion, the nanolimes were stored in a refrigerator ($T \approx 5$ ℃) before and between treatments[53,54,62].

Samples were treated by full immersion, and weighed in 5 minute intervals using a KERN PLS 420-3F mass balance (max. 420 g, $\delta = 0.001$ g). The samples were wiped with a solvent dampened cloth to remove excess consolidant and prevent whitening[62,68,69,71]. The treatment was carried out for a total period of 60 minutes to ensure saturation of the sample was achieved, *i.e.*, when the weight of the sample reached a constant value. The procedure was repeated every 24 hours when the samples were dry, for a total period of 5 days. Following this, to ensure carbonation of the nanolimes, the samples were stored in an environmental chamber (Binder KBF 115) at $T = 20$ ℃, 75 % RH for 28 days[53,55,63,74,77]. Four samples were treated at each concentration to investigate reproducibility.

6.2.3 Characterisation of consolidants and their impacts

To assess application and carbonation of the treatment, Raman spectra were taken in the range $50 - 1500$ cm^{-1} using a Thermo Scientific DXR3 SmartRaman spectrometer at 785 nm. The laser output power was 5 mW with a spot size of 3.1 μm. Raman spectra were taken weekly during the carbonation period and each spectrum was taken from an average of 500 scans with a resolution of 2.3 cm^{-1}.

Optical microscopy was performed using a Dino-Lite Edge (AM7915MZT) digital microscope to evaluate the surface of the material and observe the presence of deposits. Colorimetric measurements were carried out using a Konica Minolta CM-700d spectrophotometer, using a D65 illuminant, 10° observer angle, and a 3 mm spot diameter. Measurements were taken on both the top and bottom surface of

the samples, with 20 measurements per face. The aesthetic changes were determined using CIELAB colour space[269] and the global colour change was calculated using:

$$\Delta E^*_{ab} = \sqrt{\Delta L^* + \Delta a^* + \Delta b^*} \tag{6.1}$$

where ΔL^* is the change in lightness, Δa^* is associated with changes in red–green hues and Δb^* is associated with changes in blue–yellow hues compared with a control (untreated) sample group.

Surface roughness measurements were taken on the top and bottom face of the samples following the 28 day curing period and compared with the surface roughness for control samples, measured using the same method, to assess the accumulation of the nanolime product. The changes in surface roughness were measured using an Innowep TRACEiT optical profilometer, which creates a 3D-topographical map of the surface. Measurements are taken over a 5 × 5 mm area, with a resolution of 3 μm horizontally (xy-axes) and 1.5 μm vertically (z-axis)[270]. An average of 1536 transects in the x- and y-axes are used to determine the arithmetic average height parameter, R_a, across the measuring area[271].

To examine the stone petrology, thin sections of a control sample, *E5* sample and *E25* sample were prepared according to BS EN 12407:2007[272] to 30 μm thickness and protected with a slide cover. The samples were impregnated with resin to prevent disintegration and dyed blue to help discriminate pores from the stone matrix. Samples were characterised using polarised light microscopy using an Olympus BX43 microscope with LED light source equipped with Olympus SC50 camera. In addition, scanning electron microscopy images of exemplar control and treated samples were obtained using a scanning electron microscope (JEOL JSM6010). The samples were sputter coated with carbon. These images are provided in the supplementary information.

6.2.4 Cavity ring-down spectroscopy

Molecules absorb light at different frequencies due to their unique sets of quantum-mechanical energy levels. Therefore, a molecule of interest can be selectively excited

by choosing light at a specific frequency and its concentration can be quantified by measuring the attenuation in light intensity after said radiation has passed through the absorbing sample. The Beer–Lambert law, $I_{\mathrm{tr}} = I_0 \exp[-\alpha(\nu)d]$, gives the relationship between the initial light intensity, I_0, and the transmitted light intensity, I_{tr}, at frequency ν, where $\alpha(\nu)$ is the absorption coefficient and d is the path length over which the light is absorbed. The absorption coefficient is related to the number density, N, by $\alpha(\nu) = N\sigma(\nu)$, where $\sigma(\nu)$ is the species-dependent absorption cross-section. Therefore, absolute number densities can be determined by absorption measurements.

Increasing the path length, d, over which the light interacts with the sample allows smaller values of $\alpha(\nu)$ to be measured, and therefore, increases the sensitivity of the absorption measurement. Cavity ring-down spectroscopy (CRDS) achieves this increase in path length by trapping the light between two highly reflective mirrors (the cavity)[203,205–208] and monitoring the light intensity leaking out of the cavity (after the light has been switched off; or the cavity is no longer illuminated). The time taken for the intensity to fall to $1/e$ of its original value is recorded, and is known as the ring-down time, τ_0. In the presence of an absorbing species, the rate of decay is faster as there is an additional loss mechanism, and the decay time is reduced, resulting in a different ring-down time, τ. The absorption coefficient can be determined from the difference in the reciprocals of the ring-down times:

$$\alpha(\nu) = \frac{1}{c}\left(\frac{1}{\tau} - \frac{1}{\tau_0}\right) \tag{6.2}$$

where c is the speed of light, and thus, allows the number density of the species of interest to be determined.

A schematic of the near-IR CRDS instrument used in this work is shown in Figure 6.2, and a full description of the theory and instrument can be found in Browne *et al.*[240]. The optical cavity is formed using two highly reflective mirrors (Layertec, $R \approx 0.9999$, radius of curvature = 1 m), placed 86 cm apart. The cavity is excited using a continuous wave (cw) fibre-coupled distributed feedback diode laser (NTT Electronics NLK1S5GAAA, $\lambda = 1506$ nm). A temperature controlled (range = 10−50

℃, $\delta = 0.1$ ℃) insulated stainless steel chamber ($13 \times 7 \times 8$ cm), which is separated from the cavity by a valve, is used to control the environment the stone samples are tested under. The experiments were carried out in a N_2 (BOC Oxygen Free Nitrogen, 99.998 %) gas flow, controlled with calibrated mass flow controllers (MKS 1479A Mass-Flo and MKS PR4000B-S).

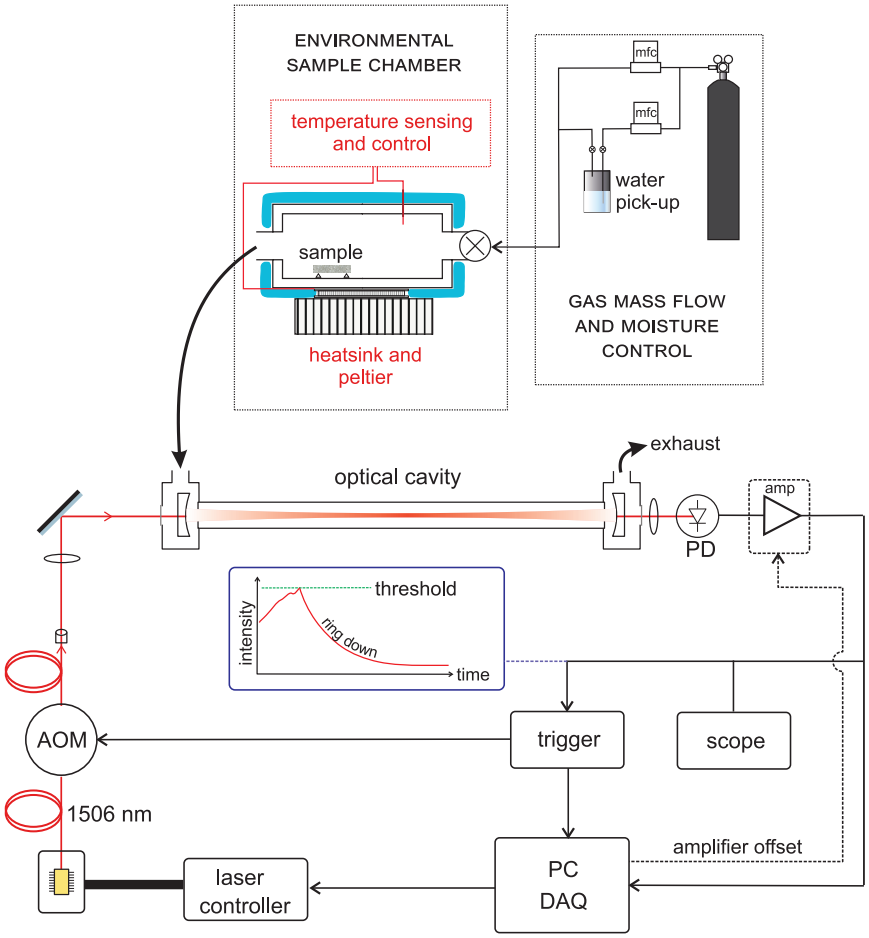


Figure 6.2: A depiction of the experimental set-up used to measure H_2O released from limestone. The sample is placed in a temperature controlled cell separate from the cavity ring-down spectrometer. Note: mfc = mass flow controller; AOM = acousto-optic modulator; PD = photodetector; amp = amplifier; PC DAQ = data acquisition system.

The same experimental procedure described in Browne *et al.*[240,267] is used. Briefly, for the reproducibility measurements, the sample chamber is set to 25 ℃ (determined using a calibrated thermocouple) and left undisturbed for 30 minutes to ensure equilibrium is reached. The samples are immersed in distilled water for 2 days

to ensure they are fully saturated, and their wet mass, m_w, is recorded before being placed in the sample chamber. The valve to the main cavity is opened and a constant flow of 1.5 standard litres per minute (slm) dry N_2 is passed over the sample (gas velocity $\simeq 7 \times 10^{-3}$ m s^{-1}). The laser is tuned to the centre of the H_2O $10,3,7(021) \leftarrow 11,3,8(000)$ transition at 6638.91 cm^{-1} [198] and the average ring-down time (RDT) of ten ring-down events is continuously measured. The procedure is stopped when the measured RDT returns to τ_0 and the dry mass of the sample, m_d, is then recorded. Measurements were taken before and after consolidation and the 28 day curing period to allow the changes in drying kinetics to be fully probed. For the investigation into the influence of temperature, the temperature of the sample chamber is changed from $20 - 40$ ℃ in 5 ℃ steps, and the rest of the procedure remains the same.

6.3 Analysis of the drying kinetics

A complete description of the analysis can be found in Browne *et al.*[240]. Following the procedure described above, the time-dependent release of water can be determined from the measured ring-down times. Using Equation 6.2, the absorption coefficient, $\alpha(\nu)$, is calculated and from this, the concentration, N, can be determined using $\alpha(\nu) = N\sigma(\nu)$. The concentration is related to the mass of water released from the sample by:

$$m_{H_2O}(t) = \frac{fM_r}{N_A} \int_0^t N \mathrm{d}t \tag{6.3}$$

where f is the volumetric flow rate, $M_r(H_2O) = 0.018$ kg mol^{-1} and N_A is Avogadro's number. The normalised mass difference, Δm_n, is defined as:

$$\Delta m_n = \frac{m_{H_2O}(\infty) - m_{H_2O}(t)}{m_d} \tag{6.4}$$

while the mass flux, $\dot{m}(t)$ is calculated by:

$$\dot{m}(t) = \frac{1}{A} \frac{\mathrm{d}m_{H_2O}(t)}{\mathrm{d}t} \tag{6.5}$$

where A is the surface area of the top face of the sample. The time at which phase I ends is denoted as the critical time, t_c, and is determined as the intercept between

two tangents fitted to phase I and II time periods in $\dot{m}(t)$. This is achieved *via* an iterative procedure, in which the intercept is set as the upper limit for the phase I linear fit, and the process repeated until a constant t_c results. An initial period in which the stone sample comes into equilibrium with the environmental chamber is observed in the mass flux, and this period (approximately 10 minutes) is excluded in the determination of the critical time and the constant mass flux, $\dot{m}_{\mathrm{CST}}$.

In phase II, the capillary flow is insufficient to maintain the constant rate of evaporation found in phase I, and the dominant transport mechanism occurs *via* vapour transport. Thus, the drying in this phase can be characterised by a diffusivity parameter, D_{II}, which originates from Fick's second law, $(\partial C/\partial t) = D_{\mathrm{II}}(\partial C/\partial x)$. Assuming a uniform distribution of moisture through the porous sample, and integrating over the sample thickness, L, results in the following solution[150]:

$$\frac{m_{\mathrm{H_2O}}(t)}{m_{\mathrm{H_2O}}(\infty)} = 1 - \sum_{n=0}^{\infty} \frac{8}{(2n+1)^2\pi^2} \exp\left\{\frac{-D_{\mathrm{II}}(2n+1)^2\pi^2 t}{4L^2}\right\} \tag{6.6}$$

When the sample has entered the later stages of drying, and the moisture content has fallen below 40 %, only the first term of Equation 6.6 needs to be considered[168], and D_{II} can be determined from the following linear relationship:

$$\ln\left(1 - \frac{m_{\mathrm{H_2O}}(t)}{m_{\mathrm{H_2O}}(\infty)}\right) - \ln\left(\frac{8}{\pi^2}\right) = -\frac{D_{\mathrm{II}}\pi^2 t}{4L^2} \tag{6.7}$$

To ensure that only the first term of Equation 6.6 applies, the linear fit for D_{II} was taken between $10 - 30$ % saturation.

As previously stated, the phase II diffusivity increases with temperature and can be characterised by an activation energy, E_a, assuming an Arrhenius type relationship:

$$\ln D_{\mathrm{II}}(T) = \ln D_0 - \frac{E_a}{RT} \tag{6.8}$$

where D_0 is a temperature-independent pre-exponential factor, R is the gas constant and T the absolute temperature. Thus, the activation energy, E_a, can be determined from the gradient of a linear fit of $\ln(D_{\mathrm{II}})$ against $1/T$.

6.4 Results and discussion

6.4.1 Characterisation of consolidation

The amount of nanolime absorbed by each sample as a result of treatment has been estimated as the difference in dry mass (Δm_d) before and after the 28 day curing period at $T = 20$ ℃ and 75 % *RH*. The results for the different samples are reported in Table 6.1, and in general show that although there was clear absorption of the consolidant, a change in dry mass of a few tens of mg at most is observed ($1 - 10$ mg is typical) which is of similar magnitude to that reported by others[60,62,71]. As expected, the samples treated with *E25* show a larger Δm_d in comparison to those treated with *E5* due to the higher concentration of $Ca(OH)_2$ present in the *E25*. Assuming complete conversion of $Ca(OH)_2$ to $CaCO_3$, the Δm_d values observed would be equivalent to a few monolayers of $CaCO_3$, and therefore, would not be expected to have resulted in large changes in the internal pore structure.

Table 6.1: Characterisation of treatment with *E5* and *E25* for different samples C1 – C8.

	Sample	Δm_d / g	$\frac{\Delta m_d}{V}$ / kg m^{-3}	ΔL^*	Δa^*	Δb^*	ΔE^*_{ab}	R_a / μm
E5	C1	−0.001 ±0.001	−0.45 ±0.45	1.71 ± 2.33 0.52 ± 2.24	-0.62 ± 0.82 -0.43 ± 0.83	1.25 ± 2.69 1.70 ± 2.60	2.21 ± 2.37 1.81 ± 2.54	2.63 ± 0.29 2.30 ± 0.17
	C2	0.008 ±0.001	2.39 ±0.30	2.40 ± 2.35 2.61 ± 2.41	-0.48 ± 0.78 -0.43 ± 0.84	-2.06 ± 2.27 -1.90 ± 2.65	3.20 ± 2.29 3.25 ± 2.48	2.78 ± 0.14 2.61 ± 0.06
	C3	0.002 ±0.001	0.62 ±0.31	5.07 ± 2.28 4.93 ± 2.43	-1.25 ± 0.77 -1.20 ± 0.73	-4.40 ± 2.34 -4.09 ± 2.35	6.83 ± 2.27 6.52 ± 2.36	2.28 ± 0.05 1.83 ± 0.11
	C4	−0.001 ±0.001	−0.28 ±0.28	0.18 ± 2.48 1.47 ± 2.28	-0.49 ± 0.88 -0.72 ± 0.91	-4.25 ± 2.71 -4.26 ± 2.66	4.28 ± 2.70 4.56 ± 2.59	2.21 ± 0.06 1.88 ± 0.08
E25	C5	0.006 ±0.001	2.56 ±0.43	2.75 ± 2.19 1.51 ± 2.42	-0.99 ± 0.79 -0.77 ± 0.83	-1.27 ± 2.55 -0.95 ± 2.47	3.19 ± 2.16 1.94 ± 2.26	2.64 ± 0.16 3.25 ± 0.29
	C6	0.010 ±0.001	2.92 ±0.29	4.87 ± 3.96 5.35 ± 2.42	-1.21 ± 1.09 -1.11 ± 0.83	-4.89 ± 2.55 -4.90 ± 2.47	7.00 ± 3.45 7.34 ± 2.26	1.97 ± 0.09 2.41 ± 0.08
	C7	0.017 ±0.001	4.88 ±0.29	7.38 ± 3.11 6.23 ± 3.07	-1.76 ± 0.82 -1.60 ± 0.86	-5.95 ± 2.44 -5.41 ± 2.48	9.64 ± 2.82 8.40 ± 2.78	2.60 ± 0.14 1.86 ± 0.01
	C8	0.032 ±0.001	8.27 ±0.26	11.70 ± 2.28 11.67 ± 2.34	-2.87 ± 0.76 -2.85 ± 0.81	-12.93 ± 2.21 -12.87 ± 2.29	17.67 ± 2.21 17.60 ± 2.29	1.67 ± 0.03 1.26 ± 0.21

Note: Δm_d = dry mass difference; $\frac{\Delta m_d}{V}$ = mass difference per unit volume; ΔL^* = change in lightness; Δa^* = change in red–green hues; Δb^* = change in blue–yellow hues; ΔE^*_{ab} = global colour change calculated using Equation 6.1; R_a = mean surface roughness. For ΔL^*, Δa^*, Δb^*, ΔE^*_{ab} and R_a, measurements are reported for top and bottom face of the sample.

As stated previously, Raman spectra were taken weekly during the carbonation period, and the results are shown in Figure 6.3. The Raman spectra show the presence of $CaCO_3$ bands at 1088 cm^{-1} (symmetric stretching vibration $\nu_1[CO_3^{2-}]$), 711 cm^{-1} (in-plane bending vibrations $\nu_4[CO_3^{2-}]$), 281 cm^{-1} (Ca–O lattice vibrations) and 154 cm^{-1} (Ca–O lattice vibrations)[273], but do not show the initial presence of the $Ca(OH)_2$ band at 359 cm^{-1} (Ca–O lattice vibrations) and its subsequent decrease, *e.g.*, as reported by Becerra *et al.*[66]. We note, however, that Becerra *et al.*[66] investigated $Ca(OH)_2$ nanoparticles doped with ZnO quantum dots, which may have an influence on the efficacy of the Raman scattering measured. From the Raman spectra we measured, there is no evidence of consolidant on the surface and thus, we are unable to use this to evaluate the extent of the carbonation process.

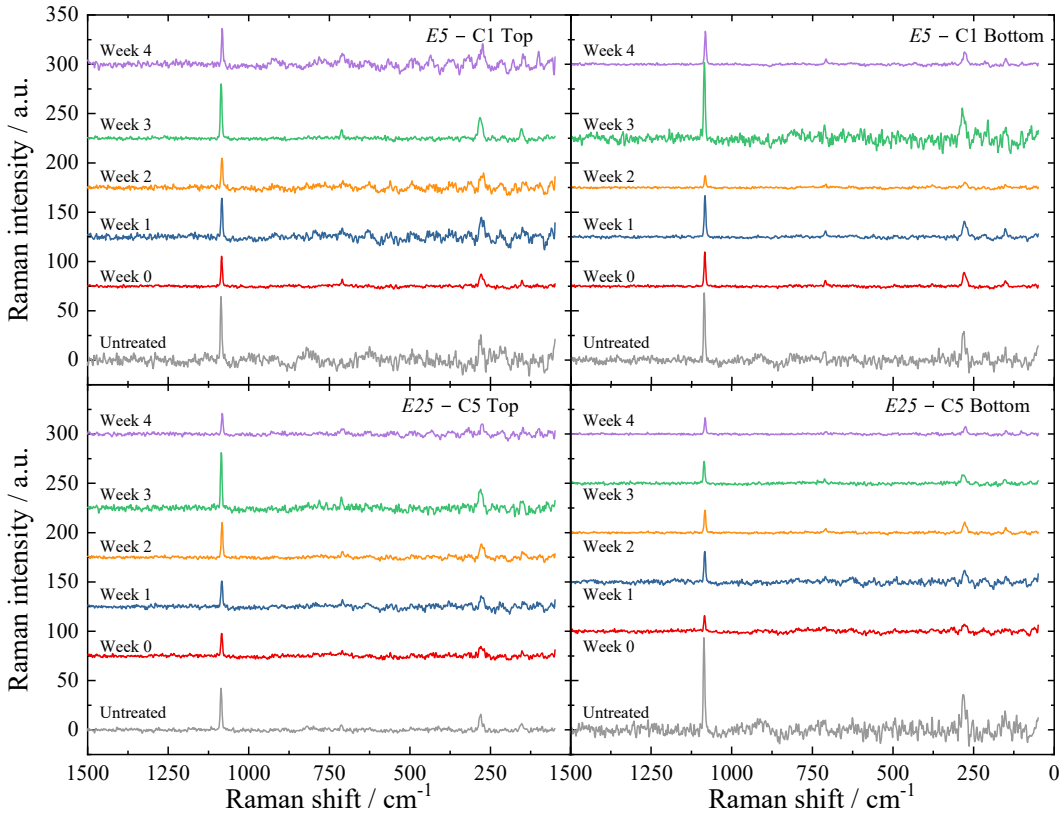


Figure 6.3: Raman spectra of the top and bottom limestone surface untreated and treated with *E5* (C1) and *E25* (C5), following each week of curing at T = 20℃, 75 % *RH*.

Figure 6.4(a) shows the optical microphotographs for a control sample (C0), the

samples treated with *E5* (C1 − C4) and those treated with *E25* (C5 − C8) following the carbonation process. From Figure 6.4(a), deposits of consolidant on the surface can be seen and visual observations confirm whitening of the samples following application, with a greater change observed for the *E25* samples.

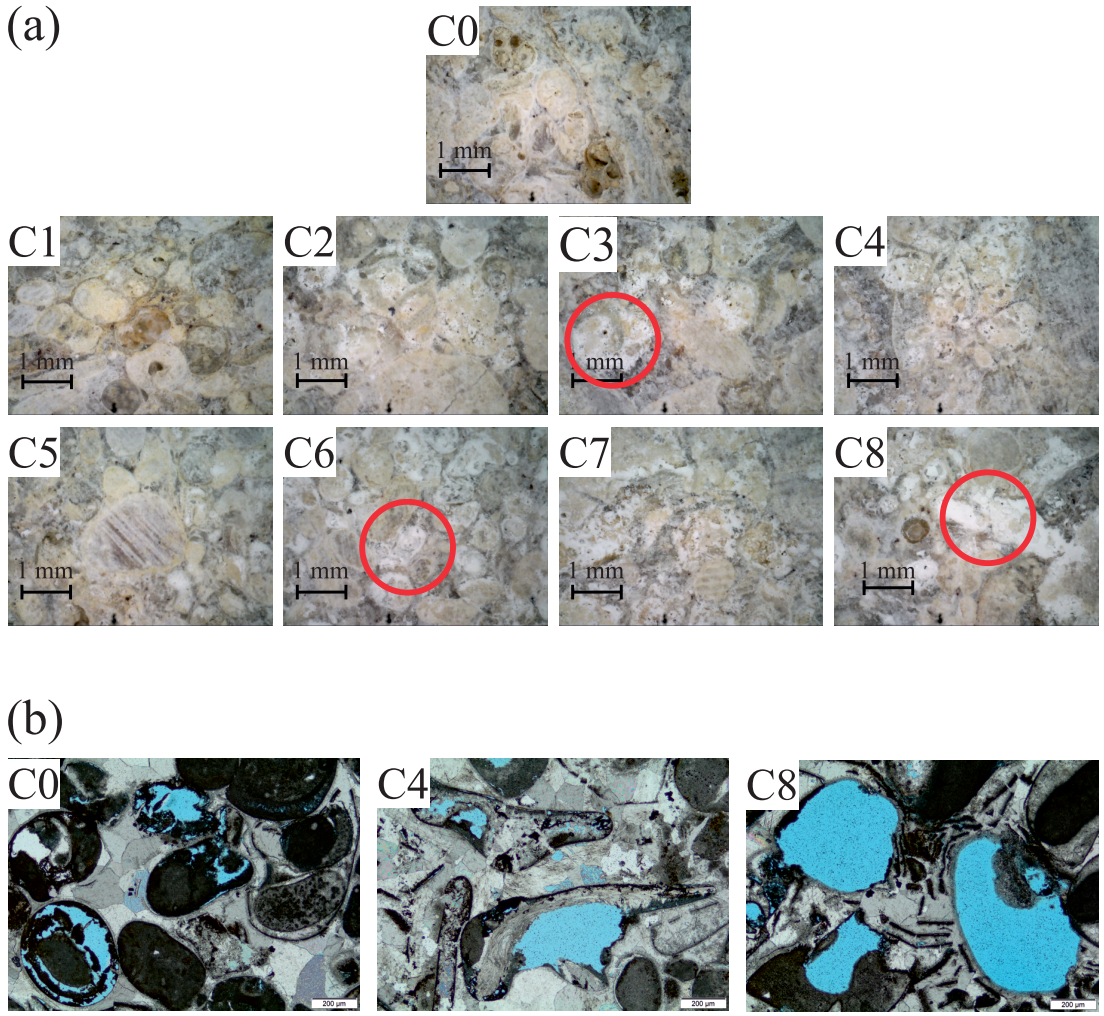


Figure 6.4: **(a)** Optical microscopy results for a control sample (C0), the samples treated with *E5* (C1 − C4) and those treated with *E25* (C5 − C8) following the 28 day curing period at $T = 20$ °C, 75 % *RH*. The red circles (○) indicate areas of nanolime deposits. **(b)** Plane polarised light microphotographs of a control (C0), *E5* sample (C4) and *E25* sample (C8) after 28 day curing period at $T = 20$ °C, 75 % *RH*. The samples were impregnated with resin to prevent disintegration and dyed blue to help discriminate pores from the stone matrix.

Examination of the thin section microphotographs shown in Figure 6.4(b) shows that there is no distinguishable difference between the control, *E5* sample and *E25* sample. A similar conclusion holds for the SEM images (see Figure C.1 in the sup-

plementary information). All samples consist of a sparite matrix containing micrite ooids and bioclasts with a calcite rind. The samples show that porosity is formed both in the ooids and the matrix. It is unsurprising that the nanolime deposits are unable to be distinguished in the thin sections as the average size of the nanoparticles found in *CaLoSiL* are between 50 and 300 nm, and for such small changes in mass as reported in Table 6.1, would be undetectable under an optical microscope.

Table 6.1 reports the colorimetric changes of the top and bottom faces of the samples following treatment and carbonation, and the results are displayed in Figure 6.5(a). The average colour values of 5 control samples (top and bottom faces) were taken as the reference $L^*a^*b^*$ values for Equation 6.1. Figure 6.5(a) shows good agreement between ΔE^*_{ab} for the top and bottom faces of the treated samples, indicating full immersion has resulted in even treatment to both large surfaces of the sample. The intersample variation for the control group is 1.89, indicating that all changes reported in Table 6.1 are likely the result of treatment. In conservation, colour changes are often assessed in comparison to an observable colour change, the threshold of which for an untrained observer is $\Delta E^*_{ab} > 3.5$[274]. Using this limit, it can be seen that two *E5* samples (C3 and C4) and three *E25* samples (C6 – C8) exhibit observable colour changes. The average ΔE^*_{ab} for samples treated with *E5* is 4.08 ± 1.73, and for *E25* is 9.10 ± 5.48, thus, on average both concentrations result in observable colour changes, with the higher concentration of nanolime (unsurprisingly) resulting in a greater change. Analysis of the ΔL^*, Δa^* and Δb^* values show that the majority of samples experienced an increase in lightness, and a negative shift in Δa^* and Δb^* towards neutral, which can be interpreted as an indication of the commonly reported whitening of samples[65,71,72,76].

The mean surface roughness values, R_a, for the samples are reported in Table 6.1, and are shown in comparison to the control group in Figure 6.5(b). The average R_a for the control samples is 2.77 ± 0.58 μm, while for *E5* is 2.31 ± 0.33 μm and *E25* is 2.20 ± 0.59 μm. A two-sample t-test on the sample groups was performed to compare the control group and the two treatment groups to determine the probability, p, of the likelihood of the null hypothesis explaining the variability. The decrease in mean

surface roughness for both the *E5* samples and *E25* samples are approaching significance at the 2σ level in comparison with the control group ($p[E5] = 0.077$; $p[E25] = 0.072$), but are not significantly different from each other ($p = 0.681$). While this suggests that there has been a decrease in surface roughness following treatment, possibly due to accumulation of the nanolime product [77], we note that the resolution of the measurement is limited to 1.5 μm [270], and therefore, we should be cautious not to over-interpret these results.

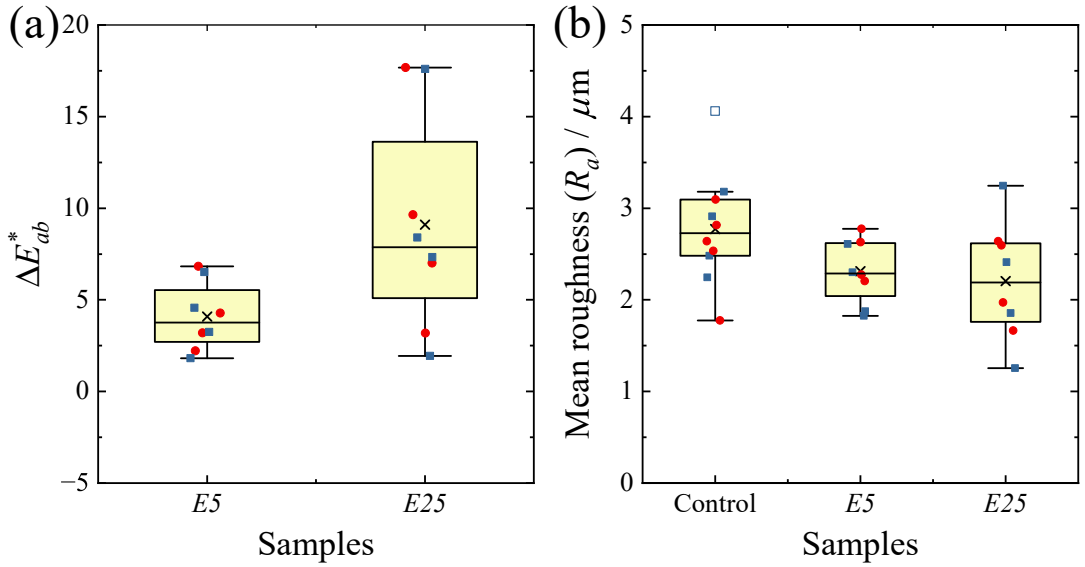


Figure 6.5: Box plots showing **(a)** the global colour change, ΔE^*_{ab}, for samples treated with *E5* and *E25*; **(b)** the arithmetic average height parameter, R_a, for control samples, *E5* samples and *E25* samples; Measurements from the top face are shown in red circles (●) and the bottom face are shown in blue squares (■), with outliers represented by hollow symbols (○/□). The box represents the interquartile range ($25^{\text{th}} - 75^{\text{th}}$ percentiles) and the whiskers are determined by the 5^{th} and 95^{th} percentiles. The median is represented by the horizontal line while the mean is indicated by ×.

6.4.2 Sample variation and reproducibility of the drying kinetics

The variation between the drying kinetics of the different samples, before and after treatment, and the reproducibility in the experimental procedure and application method, was assessed using four repeats for each concentration. Figure 6.6 shows how the drying kinetic parameters changed following treatment with *E5* and *E25* (a full report of the parameters can be found in the supplementary information, Tables

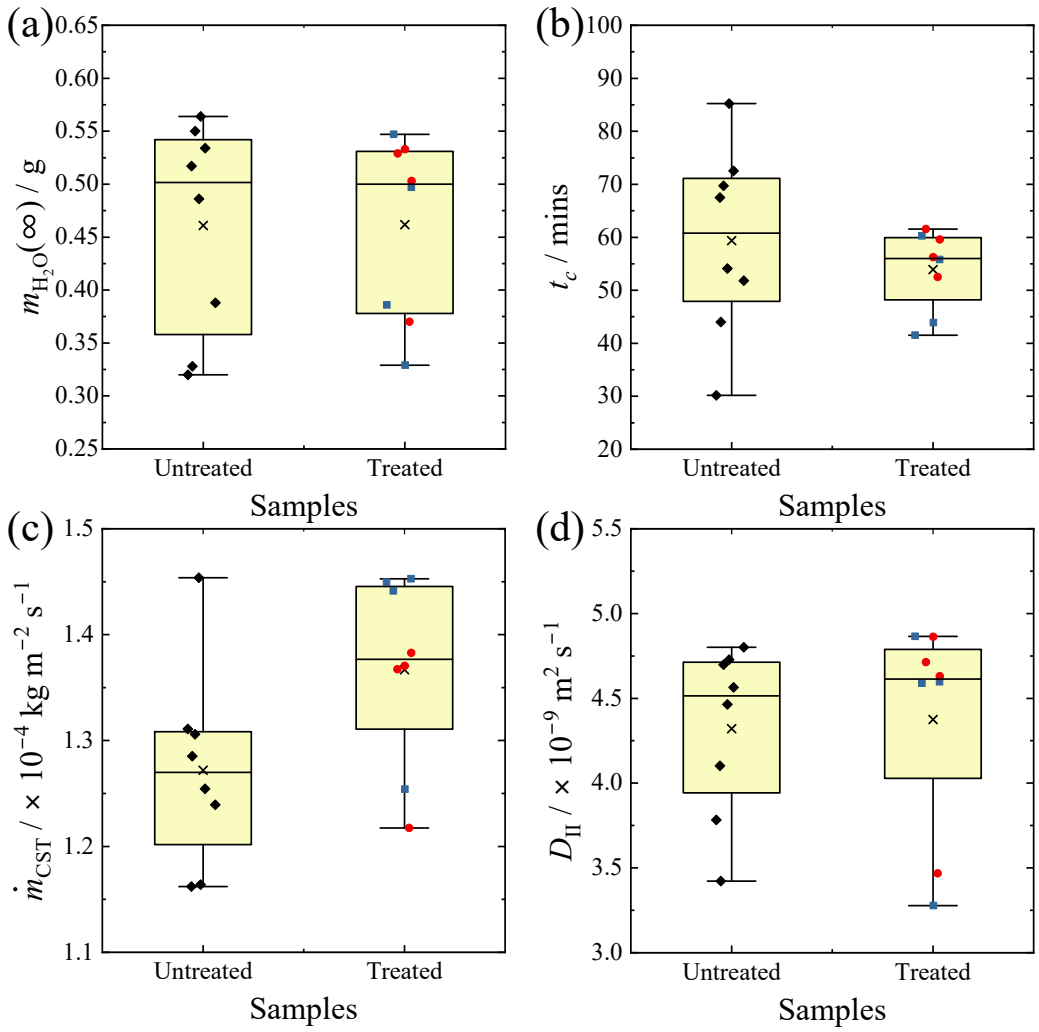


Figure 6.6: Box plots showing **(a)** the mass of water released, $m_{H_2O}(\infty)$, for untreated and treated samples ; **(b)** the critical time, t_c, for untreated and treated samples; **(c)** the constant mass flux, $\dot{m}_{CST}$, for untreated and treated samples; **(d)** the phase II diffusivity, D_{II}, for untreated and treated samples; Measurements for untreated samples are shown in black diamonds (♦), samples treated with *E5* are shown in blue squares (■) and samples treated with *E25* are shown in red circles (●). The box represents the interquartile range ($25^{th} - 75^{th}$ percentiles) and the whiskers are determined by the 5^{th} and 95^{th} percentiles. The median is represented by the horizontal line while the mean is indicated by ×.

C.1 and C.2). As expected, despite the same experimental procedure being used for all samples, there is sample variation in the drying kinetics parameters due to natural variation in the pore distributions within samples, which will result in different amounts of water being absorbed, altering the length of phase I (t_c).

The results for the drying kinetics parameters following treatment, for both *E5* and *E25*, show good agreement with the untreated samples in terms of $m_{\mathrm{H_2O}}(\infty)$, t_c and D_{II}, and two-sample t-tests show that there is no statistically significant change in these quantities ($p[m_{\mathrm{H_2O}}(\infty)] = 0.940$; $p[t_c] = 0.642$; $p[D_{\mathrm{II}}] = 0.903$). This indicates that although there is some observed surface nanolime deposits (Figure 6.4(a)), it does not contribute significant aggregation or accumulation of nanoparticles capable of blocking pore access. However, Figure 6.6(c) shows there is clear increase in $\dot{m}_{\mathrm{CST}}$ following treatment, and a two-sample t-test shows that the difference in distributions is approaching significance at the 2σ level ($p[\dot{m}_{\mathrm{CST}}] = 0.054$). As stated previously, the phase I rate of evaporation is controlled by the concentration gradient between the surface and the gas above. This increase in $\dot{m}_{\mathrm{CST}}$ may be due to subtle changes in the nano- and micro-morphology to which the TRACEiT measurements are not sensitive.

It would be expected that as $m_{\mathrm{H_2O}}(\infty)$ remains constant while $\dot{m}_{\mathrm{CST}}$ increases, then t_c should decrease. That t_c does not show a significant change may be a result of the subjective nature of its determination and the significant influence that inter- and intra-heterogeneity has on this parameter (*i.e.*, this change to phase II will not occur at the same time throughout the sample). In itself, t_c may be a relatively crude indicator of changes in the water transport kinetics as the drying process transitions from phase I to phase II.

Despite the variations in the phase I behaviour, the phase II diffusivities are in good agreement pre- and post-treatment. The phase II behaviour, as previously stated, is dominated by vapour transport within the material and is dependent on the internal structure and properties. Thus, these results indicate that there is little-to-no change in the internal surfaces and structure of the stone following treatment that affects vapour transport. One sample, C8, shows a marked increase in Δm_d

and ΔE^*_{ab} upon treatment and this is perhaps due to a higher surface deposition compared with the other samples. Despite this, there has been no impact on the ability of this sample to take up water, and its drying kinetics are in line with the other samples. The reasons for this potential deposition are unclear, although we note, visibly this sample seems to possess some large scale (100 μm) surface features (also seen in Figure 6.4(b)) and so may be a morphological outlier, at least compared with the other samples.

6.4.3 Temperature dependence of the drying kinetics

To further investigate if treatment has an impact on the internal surfaces and structure, we investigated the temperature dependence of the drying kinetics pre- and post-treatment to determine the phase II activation energy. The results of this investigation are shown in Figure 6.7, and a full report of the parameters is available in the supplementary information, Tables C.3 and C.4.

Comparison of Figures 6.7(a) and (b), and Figures 6.7(c) and (d), show that there is good agreement between the drying kinetics pre- and post-treatment. As the temperature increases, there is an increase in the rate of evaporation ($\dot{m}_{\mathrm{CST}}$) due to the increase in the concentration gradient between the surface and the environment, and this results in a decrease in the critical time (t_c). Figures 6.7(e) and (f) show plots of $\ln(D_{\mathrm{II}})$ against $1/T$ for samples pre- and post-treatment with *E5* and *E25*, respectively, and the activation energy is determined from the gradient of the linear fits. From Figure 6.7(e), E_a(untreated) = 30.30$\pm$0.60 kJ mol^{-1} and $E_a(E5)$ = 30.00$\pm$0.71 kJ mol^{-1}, and from Figure 6.7(f), E_a(untreated) = 30.31$\pm$2.07 kJ mol^{-1} and $E_a(E25)$ = 30.77$\pm$1.00 kJ mol^{-1}. We note that from Figures 6.7(e) and (f) it can be seen that the phase II diffusivities are in good agreement pre- and post-treatment, as found in the sample variation study. We also note that although the phase II diffusivities are calculated from the gradient of a linear fit using Equation 6.7 between 10 $-$ 30 % saturation, good agreement in plots of Equation 6.7 is observed to very low water saturation levels ($< 0.01\%$). This result, supported by the sample variation phase II

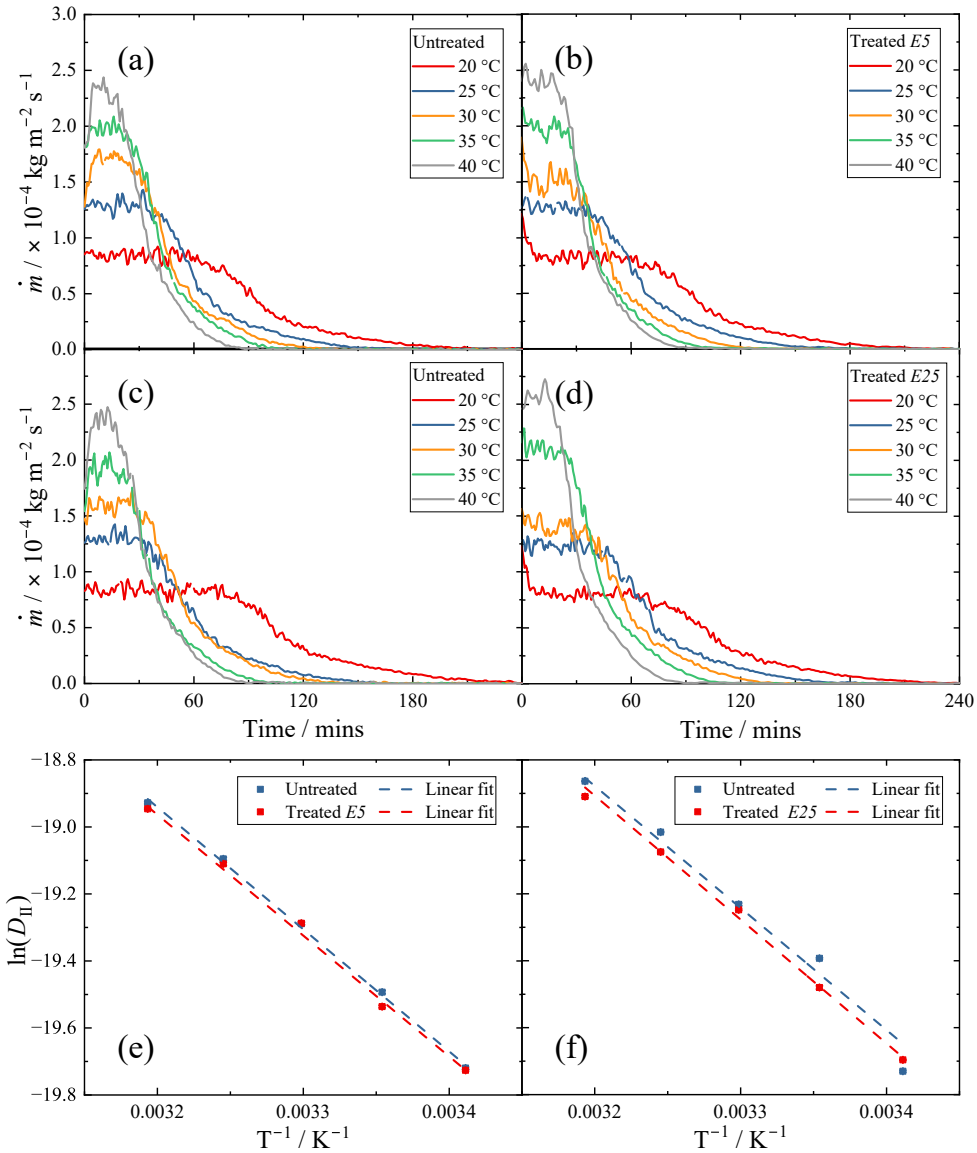


Figure 6.7: A plot of the H_2O mass flux, $\dot{m}$, as a function of time with increasing temperature for two Clipsham samples of *ca.* 25×25×5 mm **(a)** sample C1 untreated; **(b)** sample C1 treated with *E5*; **(c)** sample C5 untreated; **(d)** sample C5 treated with *E25*. A plot of $\ln(D_{II})$ against $1/T$ based on an Arrhenius relationship between phase II diffusivity and temperature for **(e)** pre- and post-treatment with *E5*; **(f)** pre- and post-treatment with *E25*.

diffusivity measurements, indicates that for Clipsham limestone treated with ethanol-dispersed nanolimes by full immersion, independent of the concentration, there is no significant change in the internal surface properties that would lead to different phase II behaviour. This preliminary result is promising as it suggests that the treatment is compatible in terms of water transport kinetics and will not result in trapped moisture and salts, leading to increased weathering. However, further investigation concerning the relationship between consolidation effectiveness and water transport kinetics is required.

6.5 Conclusions

In this article, we have investigated the impact of ethanol-dispersed nanolime treatments by full immersion at two different concentrations on the drying kinetics of Clipsham limestone, and investigated the variations in these kinetics under different temperatures. We have determined that treatment of the samples did occur as signified by changes in the dry mass and observable colour. This treatment did not result in significant changes in the mass of water released, the time for phase I to end, or the phase II diffusivity, but did result in a small but statistically significant increase to the phase I constant mass flux. Further investigation into the phase II activation energies shows that the post-treatment values are in good agreement with those found pre-treatment, and are in the range previously observed [173,254,267].

Further work into the drying kinetics of weathered samples, such as those commonly found in the need of treatment, and investigations into the impact of consolidants on their drying kinetics is required. This work has focused on treatment using ethanol dispersed nanolimes applied by full immersion, however, there are many different application procedures, *e.g.*, brushing, spraying, which may result in different distributions and penetration depths of nanoparticles within the material, and the impact of which on drying kinetics requires further study. Additionally, there are alternative treatments commonly applied in conservation and in retrofitting, for example, water repellent treatments, which are also an area of interest for future

investigations. Cavity ring-down spectroscopy can also monitor other species of interest, such as key agents of deterioration, *e.g.*, SO_2 or CO_2, allowing investigations into the weathering mechanisms to be carried out.

Supplmentary information

The supporting information is in Appendix C. This information contains details on the following:

- Scanning electron microscopy results;
- Sample variation and reproducibility of the drying kinetics;
- Temperature dependence of the drying kinetics.

Chapter 7

Discussion, conclusions and future work

7.1 Discussion and conclusions

The main aim of this thesis was the development and application of laser absorption spectroscopic techniques as a new method of exploring the interactions of water with porous building stones and assessing conservation treatments. The technique of cavity ring-down spectroscopy (CRDS) has been shown to be a highly sensitive and selective method which is capable of quantitatively detecting moisture, and can be adapted to allow simultaneous detection of other degrading species.

Before CRDS could be applied to investigating moisture transport within limestones, initial characterisations and measurements of the materials and instrument were required. Chapter 2 described the background theory of gas and liquid transport within porous media, including a description of the two-phase drying behaviour observed for stone materials. Following this, methods of characterising the pore network were evaluated, and measurements for the stones used in this thesis were obtained using mercury intrusion porosimetry (MIP) and nitrogen adsorption, with the physical properties determined showing good agreement with those reported in the literature[177,241–243].

Chapter 3 introduced the theory of laser absorption spectroscopy, in particular optical cavities and cavity ring-down spectroscopy, before presenting the development of the near-IR cavity ring-down spectrometer used in this work. A continuous wave DFB diode laser at 1506 nm was used to excite the optical cavity, and the baseline ring-down time in a nitrogen atmosphere was determined to be 150 μs, with

an $\alpha_{\text{min}} = 1 \times 10^{-9}$ cm^{-1} in a < 10 s acquisition time. The pressure broadening parameters for the two water transitions were measured in a nitrogen atmosphere: 0.150 ± 0.008 cm^{-1} atm^{-1} for the H_2O 6,0,6 (031) $\leftarrow$ 7,0,7 (010) transition, and 0.157 ± 0.003 cm^{-1} atm^{-1} for the H_2O 10,3,7 (021) $\leftarrow$ 11,3,8 (000) transition. A broad underlying absorption was observed in the water absorption spectra which was identified as the water continuum, and a second order polynomial relationship was determined between the number density of water and the water continuum contribution. These pressure broadening parameters allow accurate simulation of the absorption cross-section, which in combination with the water continuum contribution, ensures absolute conversion of the experimentally measured ring-down times into the drying kinetic parameters detailed in Chapter 2.

In Chapter 4, the first measurements of the moisture released from a limestone using cavity ring-down spectroscopy were presented. These measurements were benchmarked against the traditional method of gravimetric analysis, and good agreement was shown between the spectroscopic mass (0.361 ± 0.003 g) and the gravimetric mass (0.360 ± 0.005 g) of water. The capabilities of the instrument were assessed, and a good dynamic range was found, allowing measurements to be obtained over three orders of magnitude, equivalent to measuring from $0.5 - 500$ ppm of water at atmospheric pressure in this spectral region around 6638 cm^{-1}. The selectivity of CRDS was shown through the use of isotopically labelled water, which showed good agreement between the drying kinetics for H_2O and HDO. This technique, therefore, can separate the moisture released from the stone from the ambient water in the environment, and measurements to determine the flux of isotopically labelled water out of the stone under increasing relative humidity were conducted. A departure from the classic two-phase drying behaviour and a linear decrease in the phase II diffusivity from $3.2 \times 10^{-9} \pm 4 \times 10^{-10}$ m^2 s^{-1} at 0 % RH to $1.1 \times 10^{-9} \pm 4 \times 10^{-12}$ m^2 s^{-1} at 50 % RH was observed.

Comparison of these results with those presented in the literature using other techniques, such as gravimetric analysis or NMR, is limited as environmental conditions, such as relative humidity, are not always reported. In the select studies which

do record conditions, these are conducted at one constant % RH [12,82,127,169], and it is not always clear how these humidities were controlled or determined. Additionally, the drying curves for these studies are not always presented and this prevents making conclusive comparisons with the results in Chapter 4. The definite changes in the desorption and drying behaviour observed in Chapter 4 through the use of isotopologues cannot be observed gravimetrically due to its inability to decouple the ambient moisture from that which has been released by the stone. Therefore, to obtain definitive stone parameters regarding the water transport kinetics, such as phase II diffusivity, which accounts for, but is not hidden by, the relative humidity requires a specific and sensitive technique, such as the cavity ring-down spectrometer developed in this work.

Further development of the CRDS apparatus was presented in Chapter 5 through the addition of a temperature controlled cell, allowing manipulation and control of the environment, and measurement of the temperature dependence of the processes described in Chapters 2 and 4. The universality of the CRDS was tested by measuring the drying kinetics of different types of limestone, and in comparison with a sandstone. The phase I constant mass flux was in good agreement across the different stone types, with the length of phase I increasing with open porosity. The phase II diffusivities, however, did not follow this trend and were found to be in the range $3.0 - 6.5 \times 10^{-9}$ m^2 s^{-1} at 25 ℃. Comparison of these drying kinetics results with the well-established standard technique of MIP identified apparent inconsistencies in the deductions of parameters, such as porosity, due to the ink-bottle effect. Thus, care needs to be taken when using MIP to interpret "real-world" water kinetic measurements. Using the temperature controlled cell, the temperature dependence of the drying kinetics was investigated and the results were consistent with thermodynamic and kinetic theory predictions. An increase in the phase II diffusivities was observed with increasing temperature, and assuming an Arrhenius relationship, an effective activation energy for the water vapour diffusion was determined to be in the range $27 - 32$ kJ mol^{-1}, comparable with those reported in literature for other porous media [172,254].

Having developed a cavity ring-down spectrometer which can quantitatively measure drying kinetics under controlled environmental conditions, and determined its sensitivity, selectivity and reproducibility through testing on different samples of the same limestone (Chapter 4) and different types (Chapter 5), an investigation into the effect of conservation treatments, specifically an ethanol based nanolime consolidant, on water transport kinetics of limestone was conducted and presented in Chapter 6. Treatment was assessed and determined to have occurred due to the increase in dry mass, observable colour change and decrease in surface roughness. The application of ethanol based nanolime showed a small but statistically significant increase in the phase I constant mass flux and highlighted that parameters such as length of phase I, t_c, have a subjective element which must be considered when used as a comparative parameter. The phase II activation energies determined post-treatment were in good agreement with those pre-treatment and in the range previously observed in Chapter 5, indicating no significant change in the internal properties of the stones.

The results presented in Chapter 6 are not in agreement with those reported by Borsoi *et al.*[60] and Otero, Starinieri and Charola[72], discussed in Section 1.2, who both report an increase in drying times following consolidation. However, there are several differences between these three studies which must be taken into account when comparing the results. Firstly, the study presented in Chapter 6 was conducted using smaller samples and the consolidant applied by full immersion. In comparison, Borsoi *et al.* and Otero, Starinieri and Charola used larger samples and different application methods, for example, brushing applied to one face of the substrate[72]. Thus, the distribution of nanolimes in the three studies may be different, with the smaller samples used in Chapter 6 potentially having a more uniform distribution. Additionally, the study in Chapter 6 was conducted on sound Clipsham limestones samples, whereas Borsoi *et al.* and Otero, Starinieri and Charola investigated weathered limestones, the internal structure and properties of which will be more varied and which the consolidant, therefore, may interact with differently. Thus, it is clear that there is a need to look at the local microscopic changes that the consolidant has made in order to make a complete comparison. Lastly, it should also be noted that

complete understanding and comparison of the results reported by Otero, Starinieri and Charola is limited as they do not report the drying environmental conditions. Overall, for deeper understanding of the impact of consolidants on transport kinetics requires further experimentation, which will be discussed in Section 7.2.

In conclusion, this thesis presents proof-of-principle, laboratory-based measurements of water transport kinetics using the highly sensitive, selective and quantitative technique of cavity ring-down spectroscopy. In comparison to the techniques discussed in Section 1.3, cavity ring-down spectroscopy allows high-resolution and versatile temporal studies to be conducted. Although this thesis focused on the study of water transport under different environmental conditions, CRDS offers the ability to selectively monitor other species of interest, as demonstrated in the simultaneous monitoring of different isotopologues which would not be distinguished using techniques such as gravimetry. As previously mentioned, the ability to use isotopologues provides the potential for greater understanding of the desorption behaviour under different environmental conditions. While this could be considered a destructive technique, similar to gravimetry, in that it requires stone fragments or surrogate samples, it can be used to determine high-resolution and reproducible stone transport properties in controlled environmental conditions. Thus, it provides useful experimental data which can be used by conservators, for example, to evaluate the properties of a potential replacement stone and compare to the original material or evaluate conservation treatments, and for the testing and improvement of moisture transport and deterioration models for porous media such as WUFI[275], LAGAMINE[276], GLASTA[277], and PHREEQC[278].

7.2 Future work

This thesis provides the foundation for future work in three main areas of study concerning water transport kinetics, other degrading chemicals, and conservation treatments.

Continuing the study of water transport kinetics, further work concerning the en-

vironmental conditions, such as temperature, relative humidity and gas flow, could be conducted using the CRDS developed in this work. A small pilot study using the developed CRDS instrument into the combined effect of temperature and relative humidity was conducted on Clipsham limestone, and the results are shown in Figure 7.1. The phase II diffusivity showed the same linear relationship to relative humidity with constant temperature, Figure 7.1(a), which is consistent with the results reported in Chapter 4. Slight differences were observed in the phase II diffusivity as a function of temperature at constant relative humidities, as shown in Figure 7.1(b), however, the apparent activation energies were determined to be $E_a(0\ \%\ RH) = 32.95 \pm 1.32$ kJ mol^{-1} and $E_a(40\ \%\ RH) = 34.90 \pm 1.08$ kJ mol^{-1}. Therefore, further work is required to determine if the activation energy does increase with relative humidity, and if so, if this is a result of above monolayer surface coverage as reported by others[156–158].

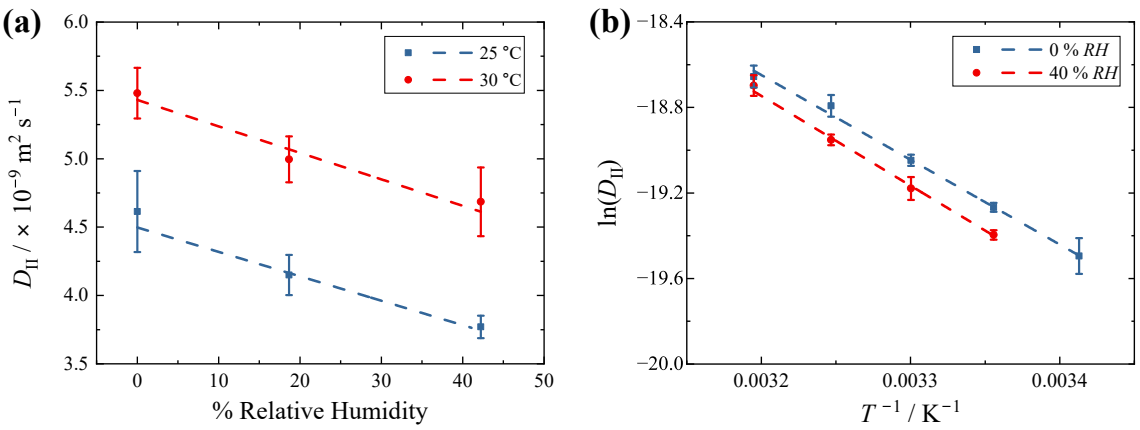


Figure 7.1: **(a)** A plot of the phase II diffusivity, D_{II}, as a function of increasing humidity for the same *ca.* $25 \times 25 \times 5$ mm Clipsham sample at 25 ℃ (blue squares) and 30 ℃ (red circles); **(b)** A plot of $\ln(D_{\mathrm{II}})$ against $1/T$ based on an Arrhenius relationship between phase II diffusivity and temperature for the same *ca.* $25 \times 25 \times 5$ mm Clipsham sample at 0 % *RH* (blue squares) and 40 % *RH* (red circles).

In this thesis, the environmental conditions were varied over relatively limited ranges, $20 - 40$ ℃ and $0 - 50$ % *RH*, and were maintained at a constant value over the course of each drying experiment. Thus, work over a wider range may provide greater insight into the potential change in activation energy shown in Figure 7.1, and potential investigations into varying conditions, such as those to simulate diurnal cycles, could provide information on "real-world" processes and conditions.

In Chapter 5 initial work into understanding the relationship between the water transport kinetics and the pore network properties was presented, however, no clear link to the phase II diffusivity was found. Thus, further work into determining which of the pore network properties determine water transport, using additional techniques such as micro-computed tomography which provide high-resolution images of the internal structure, is required. This could include CRDS investigations into the characteristic length, as discussed in Section 2.2, which controls the transition from phase I to phase II. These findings and experimental data will help to improve and test the moisture models and predictions previously mentioned.

As demonstrated with the isotopologue study presented in Chapter 4, CRDS can sensitively and selectively monitor different chemical species simultaneously. As discussed in Section 1.1, the deterioration of natural stone materials can occur through reaction with pollutants, such as SO_2 and CO_2, in the presence of water. The carbonation of nanolimes, discussed in Section 1.2, can also only occur in the presence of CO_2 and water. Thus, work into understanding the diffusion of CO_2 through stone materials, as a function of both temperature and relative humidity, may prove extremely useful. The near-IR region, which was used in this work for H_2O and HDO detection, also contains relatively strong CO_2 transitions. A HITRAN[198] simulation of the absorption cross-sections for CO_2, H_2O and HDO over the range $6480 - 6490$ cm^{-1} at $T = 298$ K and $P = 1$ atm is shown in Figure 7.2, showing that the developed LabVIEW switching programme could be used for simultaneous detection of all three species.

All the work presented in this thesis has concerned the water transport kinetics of sound stone samples, that is samples obtained from freshly quarried stone. It would be extremely interesting, and beneficial, to study the effect of weathering on transport kinetics and stone properties, both for a greater understanding of how heritage materials behave, and to allow greater assessment of the effects of conservation treatments, as discussed in Section 7.1. A potential method of ensuring greatest understanding and comparison would consist of weathering and then consolidating initially sound samples, measuring the transport kinetics at each stage of the process. As stated in

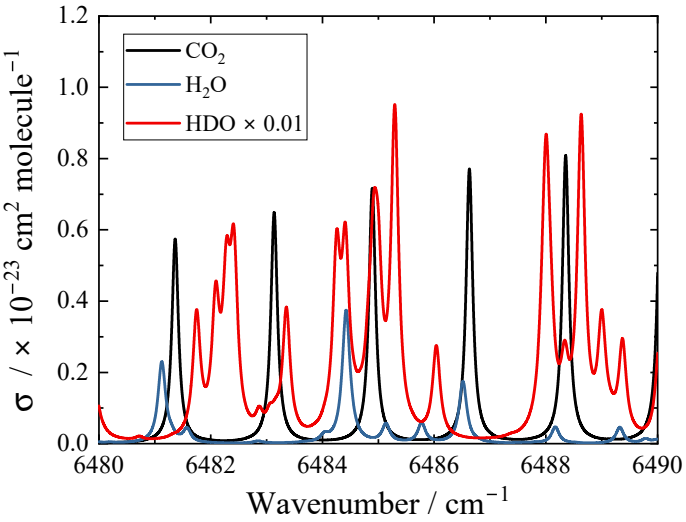


Figure 7.2: A HITRAN simulation of the absorption cross-section over the range $6480 - 6490$ cm^{-1} at $T = 298$ K and $P = 1$ atm for CO_2 (black), H_2O (blue) and HDO (red; scaled by a factor of 0.01).

Section 7.1, the microscopic properties for the three stages should also be assessed using surrogate samples and techniques such as MIP and micro-computed tomography, with a large sample size to assess statistical significance.

The area of conservation treatments offers a wide range of potential studies, for example, the influence of application procedure which may alter the depth of penetration, and therefore, heterogeneously alter the water transport kinetics. The work presented in this thesis focused on the pure ethanol based *CaLoSiL*, however, further work could investigate the differences observed for the different solvents and mixes discussed in Section 1.2. These studies could be conducted using the further developed CO_2 and H_2O CRDS instrument, and under varying environmental conditions to potentially study the carbonation process. The use of CRDS could expand past the study of nanolimes, and investigate some of the conservation treatments discussed in Section 1.2, for example, the effect of TEOS which forms a hydrophobic gel, and therefore, could influence water transport properties.

Bibliography

[1] Shadmon, A. *Stone: an introduction*, 2nd ed.; London: Intermediate Technology Publications, **1996**.

[2] Fitzner, B.; Heinrichs, K. Damage diagnosis on stone monuments – weathering forms, damage categories and damage indices. In *Understanding and managing of stone decay (SWAPNET)*. **2001**, pp 11–56.

[3] Brimblecombe, P.; Camuffo, D. In *The Effects of Air Pollution on the Built Environment*; Brimblecombe, P., Ed.; Air Pollution Reviews; Imperial College Press, **2003**, Vol. 2; Chapter 1, pp 1–30.

[4] Siegesmund, S.; Weiss, T.; Vollbrecht, A. Natural stone, weathering phenomena, conservation strategies and case studies: Introduction. *Geol. Soc. London, Spec. Publ.* **2002**, *205*, 1–7.

[5] Smith, B. J.; Gomez-Heras, M.; Viles, H. A. Underlying issues on the selection, use and conservation of building limestone. *Geol. Soc. London, Spec. Publ.* **2010**, *331*, 1–11.

[6] Přikryl, R. Understanding the Earth scientist's role in the pre-restoration research of monuments: An overview. *Geol. Soc. London, Spec. Publ.* **2007**, *271*, 9–21.

[7] Deprez, M.; De Kock, T.; De Schutter, G.; Cnudde, V. A review on freeze–thaw action and weathering of rocks. *Earth-Sci. Rev.* **2020**, *203*, 103143.

[8] Alves, C.; Figueiredo, C. A. M.; Sanjurjo-Sánchez, J.; Hernández, A. C. Salt weathering of natural stone: A review of comparative laboratory studies. *Heritage* **2021**, *4*, 1554–1565.

[9] Trudgill, S. T.; Goudie, A. S.; Viles, H. A. Weathering processes and forms. *Geol. Soc. London, Mem.* **2022**, *58*, 173–189.

[10] Grossi, C. M.; Brimblecombe, P. Effect of long-term changes in air pollution and climate on the decay and blackening of European stone buildings. *Geol. Soc. London, Spec. Publ.* **2007**, *271*, 117–130.

[11] Sass, O.; Viles, H. Heritage hydrology: A conceptual framework for understanding water fluxes and storage in built and rock-hewn heritage. *Heritage Sci.* **2022**, *10*, 66.

[12] Franzen, C.; Mirwald, P. W. Moisture content of natural stone: Static and dynamic equilibrium with atmospheric humidity. *Environ. Geol.* **2004**, *46*, 391–401.

[13] Hughes, T.; Lott, G. K.; Poultney, M. J.; Cooper, B. J. Portland Stone: A nomination for "Global Heritage Stone Resource" from the United Kingdom. *Episodes* **2013**, *36*, 221–226.

[14] De Kock, T.; Dewanckele, J.; Boone, M.; De Schutter, G.; Jacobs, P.; Cnudde, V. Replacement stones for Lede stone in Belgian historical monuments. *Geol. Soc. London, Spec. Publ.* **2014**, *391*, 31–46.

[15] Fort, R.; Varas-Muriel, M. J.; Alvarez de Buergo, M.; Perez-Monserrat, E. M. Colmenar Limestone, Madrid, Spain: Considerations for its nomination as a Global Heritage Stone Resource due to its long term durability. *Geol. Soc. London, Spec. Publ.* **2015**, *407*, 121–135.

[16] Shaffer, N. R. Indiana limestone: America's building stone. *Geol. Soc. London, Spec. Publ.* **2020**, *486*, 77–101.

[17] Basu, S.; Orr, S. A.; Aktas, Y. D. A geological perspective on climate change and building stone deterioration in London: Implications for urban stone-built heritage research and management. *Atmosphere* **2020**, *11*, 788.

[18] Livingston, R. A. Acid rain attack on outdoor sculpture in perspective. *Atmos. Environ.* **2016**, *146*, 332–345.

[19] Huggett, R.; Shuttleworth, E. *Fundamentals of Geomorphology*, 5th ed.; Routledge Fundamentals of Physical Geography; London: Routledge, **2022**, Chapter 16, pp 449–495.

[20] Sabbioni, C. In *The Effects of Air Pollution on the Built Environment*; Brimblecombe, P., Ed.; Air Pollution Reviews; Imperial College Press, **2003**, Vol. 2; Chapter 3, pp 63–106.

[21] Charola, A. E.; Ware, R. Acid deposition and the deterioration of stone: A brief review of a broad topic. *Geol. Soc. London, Spec. Publ.* **2002**, *205*, 393–406.

[22] Steiger, M. In *Urban Pollution and Changes to Materials and Building Surfaces*; Brimblecombe, P., Ed.; Air Pollution Reviews; Imperial College Press, **2016**, Vol. 5; Chapter 3, pp 65–102.

[23] Arkell, W. J. *Oxford stone*; Faber & Faber, **1947**.

[24] Gomez-Heras, M.; Smith, B. J.; Viles, H. A. Oxford stone revisited: Causes and consequences of diversity in building limestone used in the historic centre of Oxford, England. *Geol. Soc. London, Spec. Publ.* **2010**, *333*, 101–110.

[25] Sass, O.; Viles, H. A. Two-dimensional resistivity surveys of the moisture content of historic limestone walls in Oxford, UK: Implications for understanding catastrophic stone deterioration. *Geol. Soc. London, Spec. Publ.* **2010**, *331*, 237–249.

[26] Tyack, G. *Oxford: An Architectural Guide*; Oxford University Press, **1998**, Chapter 8, pp 299–334.

[27] Inkpen, R. J.; Viles, H. A.; Moses, C.; Baily, B.; Collier, P.; Trudgill, S. T.; Cooke, R. U. Thirty years of erosion and declining atmospheric pollution at St. Paul's Cathedral, London. *Atmos. Environ.* **2012**, *62*, 521–529.

[28] Smith, B. J.; Viles, H. A. Rapid, catastrophic decay of building limestones: Thoughts on causes, effects and consequences. In *Heritage Weathering and Conservation.* **2006**, pp 191–197.

[29] Tucker, M. E. *Sedimentary Petrology: An Introduction to the Origin of Sedimentary Rocks*, 3rd ed.; Wiley-Blackwell, **2001**.

[30] Leary, E. *The building limestones of the British Isles*; Building Research Establishment report; H.M.S.O. [for] Building Research Establishment: London, **1983**.

[31] Salter, H. E.; Lobel, M. D. *A History of the County of Oxford: Volume 3, the University of Oxford*; Victoria Country House, London, **1954**, Chapter 10, pp 56–60.

[32] Hall, C.; Hamilton, A.; Hoff, W. D.; Viles, H. A.; Eklund, J. A. Moisture dynamics in walls: Response to micro-environment and climate change. *Proc. R. Soc. A* **2011**, *467*, 194–211.

[33] Clifton, J. R. *Stone Consolidating Materials: a Status Report*; National Bureau of Standards, **1980**.

[34] Doehne, E.; Price, C. A. *Stone Conservation: An Overview of Current Research*, 2nd ed.; Research in Conservation; Getty Conservation Institute, **2010**.

[35] Vitruvius In *Vitruvius: 'Ten Books on Architecture"*; Rowland, I. D., Noble Howe, T., Eds.; Cambridge University Press, **1999**, pp 85–95.

[36] Wheeler, G. *Alkoxysilanes and the Consolidation of Stone*, 1st ed.; Research in Conservation; Getty Conservation Institute, **2005**.

[37] Scherer, G. W.; Wheeler, G. S. Silicate consolidants for stone. *Key Eng. Mater.* **2009**, *391*, 1–25.

[38] Pápay, Z.; Török, A. Physical changes of porous Hungarian limestones related to silicic acid ester consolidant treatments. *Geol. Soc. London, Spec. Publ.* **2010**, *331*, 147–155.

[39] Briffa, S.; Vella, D. The behaviour of as-applied and artifically weathered silica-epoxy consolidants on a typical Mediterranean porous limestone: A comparison with TEOS. *Heritage Sci.* **2019**, *7*, 30.

[40] Sena da Fonseca, B.; Ferreira Pinto, A.; Rodrigues, A.; Piçarra, S.; Santos, C.; Montemor, M. Effect of the pore network and mineralogy of stones on the behavior of alkoxysilane-based consolidants. *Constr. Build. Mater.* **2022**, *345*, 128383.

[41] Celik, S. E.; Gulen, J.; Viles, H. A. Evaluating the effectiveness of DAP as a consolidant on Turkish building stones. *Constr. Build. Mater.* **2020**, *262*, 120765.

[42] Mosquera, M. J.; Pozo, J.; Esquivias, L. Stress during drying of two stone consolidants applied in monumental conservation. *J. Sol-Gel Sci. Technol.* **2003**, *26*, 1227–1231.

[43] Hansen, E.; Doehne, E.; Fidler, J.; Larson, J.; Martin, B.; Matteini, M.; Rodriguez-Navarro, C.; Pardo, E. S.; Price, C.; de Tagle, A.; *et al.* A review of selected inorganic consolidants and protective treatments for porous calcareous materials. *Stud. Conserv.* **2003**, *48*, 13–25.

[44] Gonçalves, T. D.; Brito, V.; Musacchi, J. The whole and the parts: Can lime coatings enhance the drying of salt laden materials? *Constr. Build. Mater.* **2014**, *57*, 179–189.

[45] Boynton, R. S. *Chemistry and Technology of Lime and Limestone*; Wiley, New York, **1980**.

[46] Haynes, W. M.; Lide, D. R.; Bruno, T. J. *CRC handbook of chemistry and physics: a ready-reference book of chemical and physical data*, 95$^{\text{th}}$ ed.; Boca Raton: CRC Press, **2014**.

[47] Delgado Rodrigues, J.; Ferreira Pinto, A. P. Laboratory and onsite study of barium hydroxide as a consolidant for high porosity limestones. *J. Cult. Heritage* **2016**, *19*, 467–476.

[48] Giorgi, R.; Dei, L.; Baglioni, P. A new method for consolidating wall paintings based on dispersions of lime in alcohol. *Stud. Conserv.* **2000**, *45*, 154–161.

[49] Chelazzi, D.; Camerini, R.; Giorgi, R.; Baglioni, P. In *Advanced Materials for the Conservation of Stone*; Hosseini, M., Karapanagiotis, I., Eds.; Springer International Publishing, **2018**, pp 151–173.

[50] Ambrosi, M.; Dei, L.; Giorgi, R.; Neto, C.; Baglioni, P. Stable dispersions of $Ca(OH)_2$ in aliphatic alcohols: Properties and application in cultural heritage conservation. In *Trends in Colloid and Interface Science XV*. **2001**, pp 68–72.

[51] Daehne, A.; Herm, C. Calcium hydroxide nanosols for the consolidation of porous building materials – Results from EU-STONECORE. *Heritage Sci.* **2013**, *1*, 11.

[52] Lazzeri, A.; Coltelli, M.-B.; Castelvetro, V.; Bianchi, S.; Chiantore, O.; Lezzerini, M.; Niccolai, L.; Weber, J.; Rohatsch, A.; Gherardi, F.; Toniolo, L. European Project "NANO-CATHEDRAL: Nanomaterials for conservation of European architectural heritage developed by research on characteristic lithotypes". In *Science and Art: A Future for Stone: Proceedings of the 13th International Congress on the Deterioration and Conservation of Stone, Volume II*. **2016**, pp 847–854.

[53] Rodriguez-Navarro, C.; Suzuki, A.; Ruiz-Agudo, E. Alcohol dispersions of calcium hydroxide nanoparticles for stone conservation. *Langmuir* **2013**, *29*, 11457–11470.

[54] Rodriguez-Navarro, C.; Vettori, I.; Ruiz-Agudo, E. Kinetics and mechanism of calcium hydroxide conversion into calcium alkoxides: Implications in heritage conservation using nanolimes. *Langmuir* **2016**, *32*, 5183–5194.

[55] Rodriguez-Navarro, C.; Elert, K.; Ševčík, R. Amorphous and crystalline calcium carbonate phases during carbonation of nanolimes: Implications in heritage conservation. *CrystEngComm* **2016**, *18*, 6594–6607.

[56] van Santen, R. A. The Ostwald step rule. *J. Phys. Chem.* **1984**, *88*, 5768–5769.

[57] Beruto, D. T.; Botter, R. Liquid-like H_2O adsorption layers to catalyze the $Ca(OH)_2/CO_2$ solid–gas reaction and to form a non-protective solid product layer at 20 ℃. *J. Eur. Ceram. Soc.* **2000**, *20*, 497–503.

[58] Daniele, V.; Taglieri, G.; Quaresima, R. The nanolimes in cultural heritage conservation: Characterisation and analysis of the carbonation process. *J. Cult. Heritage* **2008**, *9*, 297–301.

[59] Borsoi, G.; Lubelli, B.; van Hees, R.; Veiga, R.; Silva, A. S. Understanding the transport of nanolime consolidants within Maastricht limestone. *J. Cult. Heritage* **2016**, *18*, 242–249.

[60] Borsoi, G.; Lubelli, B.; van Hees, R.; Veiga, R.; Silva, A. S. Evaluation of the effectiveness and compatibility of nanolime consolidants with improved properties. *Constr. Build. Mater.* **2017**, *142*, 385–394.

[61] Licchelli, M.; Malagodi, M.; Weththimuni, M.; Zanchi, C. Nanolimes for conservation of bio-calcarenite stone. *Appl. Phys. A: Mater. Sci. Process.* **2014**, *114*, 673–683.

[62] Otero, J.; Pozo-Antonio, J. S.; Montojo, C. Influence of application method and number of applications of nanolime on the effectiveness of the Doulting limestone treatments. *Mater. Struct.* **2021**, *54*, 41.

[63] Rodriguez-Navarro, C.; Vettori, I.; Ruiz-Agudo, E. Nanolimes: From synthesis to application. *Pure Appl. Chem.* **2018**, *90*, 523–550.

[64] Borsoi, G.; Lubelli, B.; van Hees, R.; Veiga, R.; Silva, A. S.; Colla, L.; Fedele, L.; Tomasin, P. Effect of solvent on nanolime transport within limestone: How to improve in-depth deposition. *Colloids Surf., A* **2016**, *497*, 171–181.

[65] Borsoi, G.; Lubelli, B.; van Hees, R.; Veiga, R.; Silva, A. S. Optimization of nanolime solvent for the consolidation of coarse porous limestone. *Appl. Phys. A: Mater. Sci. Process.* **2016**, *122*, 846.

[66] Becerra, J.; Ortiz, P.; Martín, J. M.; Zaderenko, A. P. Nanolimes doped with quantum dots for stone consolidation assessment. *Constr. Build. Mater.* **2019**, *199*, 581–593.

[67] Otero, J.; Starinieri, V.; Charola, A. E.; Taglieri, G. Influence of different types of solvent on the effectiveness of nanolime treatments on highly porous mortar substrates. *Constr. Build. Mater.* **2020**, *230*, 117112.

[68] D'Armada, P.; Hirst, E. Nano-lime for consolidation of plaster and stone. *J. Archit. Conserv.* **2012**, *18*, 63–80.

[69] Taglieri, G.; Otero, J.; Daniele, V.; Gioia, G.; Macera, L.; Starinieri, V.; Charola, A. E. The biocalcarenite stone of Agrigento (Italy): Preliminary investigations of compatible nanolime treatments. *J. Cult. Heritage* **2018**, *30*, 92–99.

[70] Tzavellos, S.; Pesce, G. L.; Wu, Y.; Henry, A.; Robson, S.; Ball, R. J. Effectiveness of nanolime as a stone consolidant: A 4-year study of six common UK limestones. *Materials* **2019**, *12*, 1–17.

[71] Gherardi, F.; Otero, J.; Blakeley, R.; Colston, B. Application of nanolimes for the consolidation of limestone from the medieval Bishop's Palace, Lincoln, UK. *Stud. Conserv.* **2020**, *65*, P90 – P97.

[72] Otero, J.; Starinieri, V.; Charola, A. E. Influence of substrate pore structure and nanolime particle size on the effectiveness of nanolime treatments. *Constr. Build. Mater.* **2019**, *209*, 701–708.

[73] Otero, J.; Charola, A. E.; Starinieri, V. Preliminary investigations of compatible nanolime treatments on Indiana limestone and weathered marble stone. *Int. J. Archit. Herit.* **2022**, *16*, 394–404.

[74] Arizzi, A.; Gomez-Villalba, L. S.; Lopez-Arce, P.; Cultrone, G.; Fort, R. Lime mortar consolidation with nanostructured calcium hydroxide dispersions: The efficacy of different consolidating products for heritage conservation. *Eur. J. Mineral.* **2015**, *27*, 311–323.

[75] Niedoba, K.; Slížková, Z.; Frankeová, D.; Lara Nunes, C.; Jandejsek, I. Modifying the consolidation depth of nanolime on Maastricht limestone. *Constr. Build. Mater.* **2017**, *133*, 51–56.

[76] Pozo-Antonio, J. S.; Otero, J.; González, N. The influence of using wet cellulose poultice on nanolime consolidaton treatments applied on a limestone. *Constr. Build. Mater.* **2022**, *337*, 127615.

[77] López-Arce, P.; Gomez-Villalba, L. S.; Pinho, L.; Fernández-Valle, M. E.; Álvarez de Buergo, M.; Fort, R. Influence of porosity and relative humidity on consolidation of dolostone with calcium hydroxide nanoparticles: Effectiveness assessment with non-destructive techniques. *Mater. Charact.* **2010**, *61*, 168–184.

[78] Ruffolo, S. A.; La Russa, M. F.; Aloise, P.; Belfiore, C. M.; Macchia, A.; Pezzino, A.; Crisci, G. M. Efficacy of nanolime in restoration procedures of salt weathered limestone rock. *Appl. Phys. A: Mater. Sci. Process.* **2014**, *114*, 753–758.

[79] Pozo-Antonio, J. S.; Otero, J.; Alonso, P.; Mas i Barberà, X. Nanolime- and nanosilica-based consolidants applied on heated granite and limestone: Effectiveness and durability. *Constr. Build. Mater.* **2019**, *201*, 852–870.

[80] Hall, K. Rock moisture content in the field and the laboratory and its relationship to mechanical weathering studies. *Earth Surf. Processes Landforms* **1986**, *11*, 131–142.

[81] Tournier, B.; Jeannette, D.; Destrigneville, C. Stone drying: An approach of the effective evaporating surface area. In *Proceedings of the 9th International Congress on Deterioration and Conservation of Stone*. **2000**, pp 629–635.

[82] Rousset-Tournier, B.; Mazerolle, F.; Géraud, Y.; Jeannette, D. Rock drying tests monitored by X-ray computed tomography – The effect of saturation methods on drying behaviour. *Geol. Soc. London, Spec. Publ.* **2003**, *215*, 117–125.

[83] Sass, O. Rock moisture measurements: Techniques, results, and implications for weathering. *Earth Surf. Processes Landforms* **2005**, *30*, 359–374.

[84] Phillipson, M. C.; Baker, P. H.; Davies, M.; Ye, Z.; McNaughtan, A.; Galbraith, G. H.; McLean, R. C. Moisture measurement in building materials: An overview of current methods and new approaches. *Building Serv. Eng. Res. Technol.* **2007**, *28*, 303–316.

[85] Pinchin, S. E. Techniques for monitoring moisture in walls. *Stud. Conserv.* **2008**, *53*, 33–45.

[86] Lehmann, P.; Assouline, S.; Or, D. Characteristic lengths affecting evaporative drying of porous media. *Phys. Rev. E* **2008**, *77*, 056309.

[87] van der Zanden, A. J. J.; de Wit, M. H. A procedure to measure the diffusion coefficient of water in brick as a function of the water concentration. *Drying Technol.* **2012**, *30*, 526–534.

[88] Prime, N.; Housni, Z.; Fraikin, L.; Léonard, A.; Charlier, R.; Levasseur, S. On water transfer and hydraulic connection layer during the convective drying of rigid porous material. *Transp. Porous Media* **2015**, *106*, 47–72.

[89] McAllister, D.; Warke, P.; McCabe, S.; Gomez-Heras, M. Evaporative moisture loss from heterogeneous stone: Material-environment interactions during drying. *Geomorphol.* **2016**, *273*, 308–322.

[90] Hall, C.; Hoff, W. D. *Water transport in brick, stone and concrete*, 3rd ed.; CRC Press, **2021**.

[91] Sandrolini, F.; Franzoni, E. An operative protocol for reliable measurements of moisture in porous materials of ancient buildings. *Build. Environ.* **2006**, *41*, 1372–1380.

[92] Sass, O.; Viles, H. A. How wet are these walls? Testing a novel technique for measuring moisture in ruined walls. *J. Cult. Heritage* **2006**, *7*, 257–263.

[93] Hassine, M. A.; Beck, K.; Brunetaud, X.; Al-Mukhtar, M. Use of electrical resistance measurement to assess the water saturation profile in porous limestones during capillary imbibition. *Constr. Build. Mater.* **2018**, *165*, 206–217.

[94] Schnepfleitner, H.; Sass, O.; Fruhmann, S.; Viles, H.; Goudie, A. A multimethod investigation of temperature, moisture and salt dynamics in tafoni (Tafraoute, Morocco). *Earth Surf. Processes Landforms* **2016**, *41*, 473–485.

[95] Weiss, T.; Sass, O. The challenge of measuring rock moisture – A laboratory experiment using eight types of sensors. *Geomorphol.* **2022**, *416*, 108430.

[96] Martínez-Garrido, M. I.; Fort, R.; Gómez-Heras, M.; Valles-Iriso, J.; Varas-Muriel, M. J. A comprehensive study for moisture control in cultural heritage using non-destructive techniques. *J. Appl. Geophys.* **2018**, *155*, 36–52.

[97] Ruiz Valero, L.; Flores Sasso, V.; Prieto Vicioso, E. *In situ* assessment of superficial moisture condition in façades of historic building using non-destructive techniques. *Case Stud. Constr. Mater.* **2019**, *10*, e00228.

[98] Barbosa, M. T. G.; Rosse, V. J.; Laurindo, N. G. Thermography evaluation strategy proposal due moisture damage on building façades. *J. Build. Eng.* **2021**, *43*, 102555.

[99] Barreira, E.; Almeida, R. M. S. F.; Simões, M. L. Emissivity of building materials for infrared measurements. *Sensors* **2021**, *21*, 1961.

[100] Frodella, W.; Elashvili, M.; Spizzichino, D.; Gigli, G.; Nadaraia, A.; Kirkitadze, G.; Adikashvili, L.; Margottini, C.; Antidze, N.; Casagli, N. Applying close range non-destructive techniques for the detection of conservation problems in rock-carved cultural heritage sites. *Remote Sens.* **2021**, *13*, 1040.

[101] Proietti, N.; Calicchia, P.; Colao, F.; De Simone, S.; Di Tullio, V.; Luvidi, L.; Prestileo, F.; Romani, M.; Tatì, A. Moisture damage in ancient masonry: A multidisciplinary approach for *in situ* diagnostics. *Minerals* **2021**, *11*, 406.

[102] Basheer, P.; Srinivasan, S.; Smith, B. J.; Gomez-Heraz, M. Micro-environmental monitoring of temperature & moisture changes in building stones using embedded electrical sensors. In *Proceedings of the 12th International Conference on Structural Faults and Repair*. **2008**.

[103] Eklund, J. A.; Zhang, H.; Viles, H. A.; Curteis, T. Using handheld moisture meters on limestone: Factors affecting performance and guidelines for best practice. *Int. J. Archit. Herit.* **2013**, *7*, 207–224.

[104] Cutler, N. A.; Viles, H. A.; Ahmad, S.; McCabe, S.; Smith, B. J. Algal 'greening' and the conservation of stone heritage structures. *Sci. Total Environ.* **2013**, *442*, 152–164.

[105] Wilhelm, K.; Viles, H.; Burke, Ò. The influence of salt on handheld electrical moisture meters: Can they be used to detect salt problems in porous stone? *Int. J. Archit. Herit.* **2016**, *10*, 735–748.

[106] Egartner, I.; Sass, O.; Viles, H.; Dietzel, M. A multi proxy investigation of moisture, salt, and weathering dynamics on a historic urban boundary wall in Oxford, UK. *Stud. Conserv.* **2020**, *65*, 172–188.

[107] Franzoni, E.; Bassi, M. A new sensorized ceramic plug for the remote monitoring of moisture in historic masonry walls: First results from laboratory and onsite testing. *Struct. Control Health Monit.* **2022**, *29*, e3126.

[108] Sass, O.; Viles, H. A. Wetting and drying of masonry walls: 2D-resistivity monitoring of driving rain experiments on historic stonework in Oxford, UK. *J. Appl. Geophys.* **2010**, *70*, 72–83.

[109] Mol, L. Investigations into the relationship between changes in internal moisture regimes and rock surface deterioration in cavernous sandstone features. *Earth Surf. Processes Landforms* **2014**, *39*, 914–927.

[110] Sass, O. Investigating rock moisture at a sandstone massif in the Saxonian Switzerland climbing area. *J. Geomorphol.* **2022**, *1*, 25–41.

[111] Černý, R. Time-domain reflectometry method and its application for measuring moisture content in porous materials: A review. *Measurement* **2009**, *42*, 329–336.

[112] Cataldo, A.; De Benedetto, E.; Cannazza, G.; D'Amico, S.; Farrugia, L.; Mifsud, G.; Dimech, E.; Sammut, C. V.; Persico, R.; Leucci, G.; De Giorgi, L. Dielectric permittivity diagnostics as a tool for cultural heritage preservation: Application on degradable globigerina limestone. *Measurement* **2018**, *123*, 270–274.

[113] Stingl Freitas, T.; Guimarães, A. S.; Roels, S.; Peixoto de Freitas, V.; Cataldo, A. Is the time-domain reflectometry (TDR) technique suitable for moisture content measurement in low-porosity building materials? *Sustainability* **2020**, *12*, 7855.

[114] Orr, S. A.; Young, M.; Stelfox, D.; Leslie, A.; Curran, J.; Viles, H. An 'isolated diffusion' gravimetric calibration procedure for radar and microwave moisture measurement in porous building stone. *J. Appl. Geophys.* **2019**, *163*, 1–12.

[115] Orr, S. A.; Fusade, L.; Young, M.; Stelfox, D.; Leslie, A.; Curran, J.; Viles, H. Moisture monitoring of stone masonry: A comparison of microwave and radar on a granite wall and a sandstone tower. *J. Cult. Heritage* **2020**, *41*, 61–73.

[116] Taye, B.; Viles, H.; Orr, S. A. Seasonality in moisture dynamics in the walls of the rock-cut churches in Lalibela, Ethiopia: Implications for weathering. *Int. J. Archit. Herit.* **2022**, 1–14.

[117] Srinivasan, S.; Basheer, P. A.; Smith, B. J.; Gomez-Heras, M.; Grattan, K. T.; Sun, T. Use of fiber optic and electrical resistance sensors for monitoring moisture movement in building stones subjected to simulated climatic conditions. *J. ASTM Int.* **2010**, *7*, 1–11.

[118] Sun, T.; Grattan, K. T. V.; Srinivasan, S.; Basheer, P. A. M.; Smith, B. J.; Viles, H. A. Specially designed compensated optical fiber humidity sensors. *IEEE Sen. J.* **2012**, *12*, 1011–1017.

[119] Chai, J.; Liu, Q.; Liu, J.; Zhang, D. Optical fiber sensors based on novel polyimide for humidity monitoring of building materials. *Opt. Fiber Technol.* **2018**, *41*, 40–47.

[120] Caponero, M.; D'Amato, R.; Polimadei, A.; Terranova, G. Polymer-coated FBG humidity sensors for monitoring cultural heritage stone artworks. *Measurement* **2018**, *125*, 325–329.

[121] Ketelaars, A.; Pel, L.; Coumans, W.; Kerkhof, P. Drying kinetics: A comparison of diffusion coefficients from moisture concentration profiles and drying curves. *Chem. Eng. Sci.* **1995**, *50*, 1187–1191.

[122] Hassanein, R.; Meyer, H. O.; Carminati, A.; Estermann, M.; Lehmann, E.; Vontobel, P. Investigation of water imbibition in porous stone by thermal neutron radiography. *J. Phys. D: Appl. Phys.* **2006**, *39*, 4284–4291.

[123] Vlassenbroeck, J.; Cnudde, V.; Masschaele, B.; Dierick, M.; van Hoorebeke, L.; Jacobs, P. A comparative and critical study of X-ray CT and neutron CT as non-destructive material evaluation techniques. *Geol. Soc. London, Spec. Publ.* **2007**, *271*, 277–285.

[124] Cnudde, V.; Dierick, M.; Vlassenbroeck, J.; Masschaele, B.; Lehmann, E.; Jacobs, P.; van Hoorebeke, L. High-speed neutron radiography for monitoring the water absorption by capillarity in porous materials. *Nucl. Instrum. Methods Phys. Res., Sect. B* **2008**, *266*, 155–163.

[125] Dewanckele, J.; De Kock, T.; Fronteau, G.; Derluyn, H.; Vontobel, P.; Dierick, M.; Van Hoorebeke, L.; Jacobs, P.; Cnudde, V. Neutron radiography and X-ray computed tomography for quantifying weathering and water uptake processes inside porous limestone used as building material. *Mater. Charact.* **2014**, *88*, 86–99.

[126] Carpenter, T. A.; Davies, E. S.; Hall, C.; Hall, L. D.; Hoff, W. D.; Wilson, M. A. Capillary water migration in rock: Process and material properties examined by NMR imaging. *Mater. Struct.* **1993**, *26*, 286–292.

[127] Pel, L.; Brocken, H.; Kopinga, K. Determination of moisture diffusivity in porous media using moisture concentration profiles. *Int. J. Heat Mass Transfer* **1996**, *39*, 1273–1280.

[128] Gonçalves, T. D.; Pel, L.; Rodrigues, J. D. Drying of salt-contaminated masonry: MRI laboratory monitoring. *Environ. Geol.* **2007**, *52*, 293–302.

[129] Camaiti, M.; Casieri, C.; De Luca, F.; Fantazzini, P.; Terenzi, C. The use of portable single-sided relaxometry and laboratory imaging NMR devices in stone conservation. *Stud. Conserv.* **2007**, *52*, 37–49.

[130] Peysson, Y.; Fleury, M.; Blázquez-Pascual, V. Drying rate measurements in convection- and diffusion-driven conditions on a shaly sandstone using nuclear magnetic resonance. *Transp. Porous Media* **2011**, *90*, 1001–1016.

[131] Thiery, J.; Rodts, S.; Weitz, D. A.; Coussot, P. Drying regimes in homogeneous porous media from macro- to nanoscale. *Phys. Rev. Fluids* **2017**, *2*, 074201.

[132] Rehorn, C.; Blümich, B. Cultural heritage studies with mobile NMR. *Angew. Chem., Int. Ed.* **2018**, *57*, 7304–7312.

[133] Edelmann, M.; Zibold, T.; Grunewald, J. Generalised NMR-moisture correlation function of building materials based on a capillary bundle model. *Cem. Concr. Res.* **2019**, *119*, 126–131.

[134] Turkington, A.; Martin, E.; Viles, H.; Smith, B. Surface change and decay of sandstone samples exposed to a polluted urban atmosphere over a six-year period: Belfast, Northern Ireland. *Build. Environ.* **2003**, *38*, 1205–1216.

[135] Richards, J.; Zhao, G.; Zhang, H.; Viles, H. A controlled field experiment to investigate the deterioration of earthen heritage by wind and rain. *Heritage Sci.* **2019**, *7*, 51.

[136] Franzen, C.; Mirwald, P. W. Moisture sorption behaviour of salt mixtures in porous stone. *Chem. Erde Geochem.* **2009**, *69*, 91–98.

[137] Browne, D. E. *A comparative assessment of the performance of moisture meters and dowels in measuring the drying characteristics of building limestones*; MRes Coursework, University College London, **2019**.

[138] Archie, G. E. The electrical resistivity log as an aid in determining some reservoir characteristics. *Trans. Am. Inst. Min., Metall. Pet. Eng.* **1942**, *146*, 54–62.

[139] Kaatze, U. Complex permittivity of water as a function of frequency and temperature. *J. Chem. Eng. Data* **1989**, *34*, 371–374.

[140] Othonos, A. Fiber Bragg gratings. *Rev. Sci. Instrum.* **1997**, *68*, 4309–4341.

[141] Yeo, T.; Sun, T.; Grattan, K.; Parry, D.; Lade, R.; Powell, B. Characterisation of a polymer-coated fibre Bragg grating sensor for relative humidity sensing. *Sens. Actuators, B* **2005**, *110*, 148–156.

[142] Eidmann, G.; Savelsberg, R.; Blümler, P.; Blümich, B. The NMR MOUSE, a Mobile Universal Surface Explorer. *J. Magn. Reson., Ser. A* **1996**, *122*, 104–109.

[143] Manz, B.; Coy, A.; Dykstra, R.; Eccles, C.; Hunter, M.; Parkinson, B.; Callaghan, P. A mobile one-sided NMR sensor with a homogeneous magnetic field: The NMR-MOLE. *J. Magn. Reson.* **2006**, *183*, 25–31.

[144] Israelachvili, J. *Intermolecular & Surface Forces*, 2nd ed.; Academic Press, **1991**.

[145] Castellan, G. W. *Physical Chemistry*, 2nd ed.; Addison–Wesley Publishing Company, **1971**.

[146] Washburn, E. W. Note on a method of determining the distribution of pore sizes in a porous material. *Proc. Natl. Acad. Sci. U. S. A.* **1921**, *7*, 115–116.

[147] Muskat, M. *The Flow of Homogenous Fluids Through Porous Media*, 1st ed.; McGraw–Hill Book Company, **1937**.

[148] Landau, L.; Lifshitz, E. *Fluid Mechanics*, 2nd ed.; Pergamon, **1987**.

[149] Laidler, K. J.; Meiser, J. H.; Sanctuary, B. C. *Physical Chemistry*, 4th ed.; Houghton Mifflin Company, **2003**.

[150] Crank, J. *The Mathematics of Diffusion*, 2nd ed.; Oxford University Press, **1975**.

[151] Daniels, F.; Alberty, R. A. *Physical Chemistry*, 2nd ed.; Wiley, **1961**.

[152] Atkins, P. W. *Physical Chemistry*, 3rd ed.; Oxford University Press, **1986**.

[153] Denbigh, K. *The Principles of Chemical Equilibrium*, 3rd ed.; Cambridge University Press, **1971**.

[154] Berry, R. S.; Rice, S. A.; Ross, J. *Physical Chemistry*, 2nd ed.; Oxford University Press, **2000**.

[155] Brunauer, S.; Emmett, P. H.; Teller, E. Adsorption of gases in multimolecular layers. *J. Am. Chem. Soc.* **1938**, *60*, 309–319.

[156] Hackerman, N.; Hall, A. C. The adsorption of water vapor on quartz and calcite. *J. Phys. Chem.* **1958**, *62*, 1212–1214.

[157] Meyer, D. E.; Hackerman, N. Adsorption thermodynamics of the interaction of water and various silica powders. *J. Phys. Chem.* **1966**, *70*, 2077–2086.

[158] Okhrimenko, D. V.; Nissenbaum, J.; Andersson, M. P.; Olsson, M. H. M.; Stipp, S. L. S. Energies of the adsorption of functional groups to calcium carbonate polymorphs: The importance of –OH and –COOH groups. *Langmuir* **2013**, *29*, 11062–11073.

[159] Antoine, C. Tension des vapeurs: nouvelle relation entre les tension et les temperatures. *C. R. Seances Acad. Sci.* **1888**, *107*, 681–684, 778–780, 836–837.

[160] Bridgeman, O. C.; Aldrich, E. W. Vapor pressure tables for water. *J. Heat Transfer* **1964**, *86*, 279–286.

[161] Thermodynamics Research Center, NIST Boulder Laboratories, Chris Muzny director. *Thermodynamics Source Database, NIST Chemistry WebBook, NIST Standard Reference Database Number 69*; National Institute of Standards and Technology, **2022**.

[162] Dunlop, S. *A Dictionary of Weather*, 2nd ed.; Oxford University Press, **2008**.

[163] Stull, R. Wet-bulb temperature from relative humidity and air temperature. *J. Appl. Meteorol. Climatol.* **2011**, *50*, 2267–2269.

[164] Scherer, G. W. Theory of drying. *J. Am. Ceram. Soc.* **1990**, *73*, 3–14.

[165] Kowalski, S. J. *Thermomechanics of Drying Processes*; Lecture Notes in Applied and Computational Mechanics; Springer Berlin Heidelberg, **2003**, Vol. 8; Chapter 8, pp 137–156.

[166] Simonson, J. M. The enthalpy of the isotope-exchange reaction: $H_2O + D_2O = 2HDO$ at temperatures to 673 K and at pressures to 40 MPa. *J. Chem. Thermodyn.* **1990**, *22*, 739–749.

[167] Hall, C.; Hoff, W. D.; Nixon, M. R. Water movement in porous building materials – VI. Evaporation and drying in brick and block materials. *Build. Environ.* **1984**, *19*, 13–20.

[168] Bakhshi, M.; Mobasher, B. Experimental observations of early-age drying of Portland cement paste under low-pressure conditions. *Cem. Concr. Compos.* **2011**, *33*, 474–484.

[169] Karagiannis, N.; Karoglou, M.; Bakolas, A.; Krokida, M.; Moropoulou, A. Drying kinetics of building materials capillary moisture. *Constr. Build. Mater.* **2017**, *137*, 441–449.

[170] Gonçalves, T. D.; Brito, V.; Pel, L. Water vapor emission from rigid mesoporous materials during the constant drying rate period. *Drying Technol.* **2012**, *30*, 462–474.

[171] Gonçalves, T. D.; Brito, V.; Vidigal, F.; Matias, L.; Faria, P. Evaporation from porous building materials and its cooling potential. *J. Mater. Civ. Eng.* **2015**, *27*, 1–10.

[172] Castro, L. M.; Coelho Pinheiro, M. N. A simple data processing approach for drying kinetics experiments. *Chem. Eng. Commun.* **2016**, *203*, 258–269.

[173] Fiorentini, C.; Demarchi, S. M.; Quintero Ruiz, N. A.; M, T. R.; Giner, S. A. Arrhenius activation energy for water diffusion during drying of tomato leathers: The concept of characteristic product temperature. *Biosyst. Eng.* **2015**, *132*, 39–46.

[174] Fitzner, B.; Basten, D. In *Jahresberichte Steinzerfall-Steinkonservierung*; Snethlage, R., Ed.; Verlag Ernst & Sohn, **1994**, pp 19–32.

[175] Thommes, M.; Kaneko, K.; Neimark, A. V.; Oliver, J. P.; Rodriguez-Reinoso, F.; Rouquerol, J.; Sing, K. S. W. Physisorption of gases, with special reference to the evaluation of surface area and pore size distribution (IUPAC Technical Report). *Pure Appl. Chem.* **2015**, *87*, 1051–1069.

[176] Carniglia, S. C. Construction of the tortuosity factor from porosimetry. *J. Catal.* **1986**, *102*, 401–418.

[177] Hall, C.; Hamilton, A. Porosities of building limestones: Using the solid density to assess data quality. *Mater. Struct.* **2016**, *49*, 3969–3979.

[178] American Petroleum Institute *API RP 40: Recommended Practices for Core Analysis*; API Publishing Services, **1998**, Chapter 5, pp 5–1 – 5–23.

[179] Tamari, S. Optimum design of the constant-volume gas pycnometer for determining the volume of solid particles. *Meas. Sci. Technol.* **2004**, *15*, 549–558.

[180] Beck, K.; Al-Mukhtar, M.; Rozenbaum, O.; Rautureau, M. Characterization, water transfer properties and deterioration in Tuffeau: Building material in the Loire valley — France. *Build. Environ.* **2003**, *38*, 1151 – 1162.

[181] BRE The BRE Stone List. https://projects.bre.co.uk/ConDiv/stonelist, **2001**, Accessed: 24 November 2022.

[182] Hall, C.; Hamilton, A. Porosity–density relations in stone and brick materials. *Mater. Struct.* **2015**, *48*, 1265–1271.

[183] Katz, A. J.; Thompson, A. H. Quantitative prediction of permeability in porous rock. *Phys. Rev. B* **1986**, *34*, 8179–8181.

[184] Katz, A. J.; Thompson, A. H. Prediction of rock electrical conductivity from mercury injection measurements. *J. Geophys. Res.: Solid Earth* **1987**, *92*, 599–607.

[185] Thompson, A. H.; Katz, A. J.; Krohn, C. E. The microgeometry and transport properties of sedimentary rock. *Adv. Phys.* **1987**, *36*, 625–694.

[186] Diamond, S. Mercury porosimetry: An inappropriate method for the measurement of pore size distributions in cement-based materials. *Cem. Concr. Res.* **2000**, *30*, 1517–1525.

[187] Roels, S.; Elsen, J.; Carmeliet, J.; Hens, H. Characterisation of pore structure by combining mercury porosimetry and micrography. *Mater. Struct.* **2001**, *34*, 76–82.

[188] Giesche, H. Mercury porosimetry: A general (practical) overview. *Part. Part. Syst. Charact.* **2006**, *23*, 9–19.

[189] Benavente, D.; Such-Basañez, A., Fernandez-Cortes; Pla, C.; Cazorla-Amoros, D.; Cañaveras, J. C.; Sanchez-Moral, S. Comparative analysis of water condensate porosity using mercury intrusion porosimetry and nitrogen and water adsorption techqniues in porous building stones. *Constr. Build. Mater.* **2021**, *288*, 123131.

[190] Sing, K. The use of nitrogen adsorption for the characterisation of porous materials. *Colloids Surf., A* **2001**, *187-188*, 3–9.

[191] Lowell, S.; Shields, J. E.; Thomas, M. A.; Thommes, M. *Characterisation of Porous Solids and Powders: Surface Area, Pore Size and Density*, 1st ed.; Springer Science+Business Media, **2004**.

[192] Sing, K. S. W.; Everett, D. H.; Haul, R. A. W.; Moscou, L.; Pierotti, R. A.; Rouquérol, J.; Siemieniewska, T. Reporting physisorption data for gas/solid systems with special reference to the determination of surface area and porosity (Recommendations 1984). *Pure Appl. Chem.* **1985**, *57*, 603–619.

[193] de Boer, J. H.; Lippens, B. C.; Linsen, B. G.; Broekhoff, J. C. P.; van den Heuvel, A.; Osinga, T. J. The *t*-curve of multimolecular N_2-adsorption. *J. Colloid Interface Sci.* **1966**, *21*, 405–414.

[194] Barrett, E. P.; Joyner, L. G.; Halenda, P. P. The determination of pore volume and area distributions in porous substances. I. Computations from nitrogen isotherms. *J. Am. Chem. Soc.* **1951**, *73*, 373–380.

[195] Hollas, J. M. *Modern Spectroscopy*, 4th ed.; Wiley, **2014**.

[196] Demtröder, W. *Laser Spectroscopy 1: Basic Principles*, 5th ed.; Springer, **2014**.

[197] Corney, A. *Atomic and Laser Spectroscopy*, 1st ed.; Oxford University Press, **1977**.

[198] Gordon, I. E. *et al.* The HITRAN2020 molecular spectroscopic database. *J. Quant. Spectrosc. Radiat. Transfer* **2022**, *277*, 107949.

[199] Armstrong, B. Spectrum line profiles: The Voigt function. *J. Quant. Spectrosc. Radiat. Transfer* **1967**, *7*, 61–88.

[200] Rehle, D.; Leleux, D.; Erdelyi, M.; Tittel, F.; Fraser, M.; Friedfeld, S. Ambient formaldehyde detection with a laser spectrometer based on difference-frequency generation in PPLN. *Appl. Phys. B* **2001**, *72*, 947–952.

[201] White, J. U. Long optical paths of large aperture. *J. Opt. Soc. Am.* **1942**, *32*, 285–288.

[202] Herriott, D.; Kogelnik, H.; Kompfner, R. Off-axis paths in spherical mirror interferometers. *Appl. Opt.* **1964**, *3*, 523–526.

[203] Mazurenka, M.; Orr-Ewing, A. J.; Peverall, R.; Ritchie, G. A. D. Cavity ring-down and cavity enhanced spectroscopy using diode lasers. *Annu. Rep. Prog. Chem., Sect. C: Phys. Chem.* **2005**, *101*, 100–142.

[204] Siegman, A. E. *Lasers*, 1st ed.; Oxford University Press, **1986**.

[205] O'Keefe, A.; Deacon, D. A. G. Cavity ring-down optical spectrometer for absorption measurements using pulsed laser sources. *Rev. Sci. Instrum.* **1988**, *59*, 2544–2551.

[206] Romanini, D.; Kachanov, A. A.; Stoeckel, F. Diode laser cavity ring down spectroscopy. *Chem. Phys. Lett.* **1997**, *270*, 538–545.

[207] Wheeler, M. D.; Newman, S. M.; Orr-Ewing, A. J.; Ashfold, M. N. Cavity ring-down spectroscopy. *J. Chem. Soc., Faraday Trans.* **1998**, *94*, 337–351.

[208] Berden, G.; Peeters, R.; Meijer, G. Cavity ring-down spectroscopy: Experimental schemes and applications. *Int. Rev. Phys. Chem.* **2000**, *19*, 565–607.

[209] Schulz, K.; Simpson, W. Frequency-matched cavity ring-down spectroscopy. *Chem. Phys. Lett.* **1998**, *297*, 523–529.

[210] Svelto, O.; Hanna, D. C. *Principles of Lasers*; Plenum Press, **2007**.

[211] Shimanouchi, T. *Tables of Molecular Vibrational Frequencies, Consolidated Volume I*; National Bureau of Standards, **1972**.

[212] Buckingham, A. D.; Disch, R. L.; Dunmur, D. A. Quadrupole moments of some simple molecules. *J. Am. Chem. Soc.* **1968**, *90*, 3104–3107.

[213] Paynter, D. J.; Ptashnik, I. V.; Shine, K. P.; Smith, K. M.; McPheat, R.; Williams, R. G. Laboratory measurements of the water vapor continuum in the 1200 – 8000 cm^{-1} region between 293 K and 351 K. *J. Geophys. Res.* **2009**, *114*, D21301.

[214] Ptashnik, I.; Shine, K.; Vigasin, A. Water vapour self-continuum and water dimers: 1. Analysis of recent work. *J. Quant. Spectrosc. Radiat. Transfer* **2011**, *112*, 1286–1303.

[215] Ptashnik, I. V.; Petrova, T. M.; Ponomarev, Y.; Solodov, A. A.; Solodov, A. M. Water vapour continuum absorption in near-IR atmospheric windows. *Atmos. Oceanic Opt.* **2015**, *28*, 115–120.

[216] Shine, K. P.; Campargue, A.; Mondelain, D.; McPheat, R. A.; Ptashnik, I. V.; Weidmann, D. The water vapour continuum in near-infrared windows – Current understanding and prospects for its inclusion in spectroscopic databases. *J. Mol. Spectrosc.* **2016**, *327*, 193–208.

[217] Mondelain, D.; Aradj, A.; Kassi, S.; Campargue, A. The water vapour self-continuum by CRDS at room temperature in the 1.6 μm transparency window. *J. Quant. Spectrosc. Radiat. Transfer* **2013**, *130*, 381–391.

[218] Mondelain, D.; Manigand, S.; Kassi, S.; Campargue, A. Temperature dependence of the water vapor self-continuum by cavity ring-down spectroscopy in the 1.6 μm transparency window. *J. Geophys. Res.: Atmos.* **2014**, *119*, 5625–5639.

[219] Ptashnik, I. V.; McPheat, R. A.; Shine, K. P.; Smith, K. M.; Williams, R. G. Water vapour foreign-continuum absorption in near-infrared windows from laboratory measurements. *Philos. Trans. R. Soc., A* **2012**, *370*, 2557–2577.

[220] Wahl, M. H.; Urey, H. C. The vapor pressures of the isotopic forms of water. *J. Chem. Phys.* **1935**, *3*, 411–414.

[221] Select Committee on Science and Technology *Science and Heritage: a follow-up, HL Paper 291*; House of Lords, **2012**.

[222] Madariaga, J. M. Analytical chemistry in the field of cultural heritage. *Anal. Methods* **2015**, *7*, 4848–4876.

[223] Rousaki, A.; Vandenabeele, P. *In situ* Raman spectroscopy for cultural heritage studies. *J. Raman Spectrosc.* **2021**, 1–12.

[224] Siegesmund, S.; Grimm, W.-D.; Dürrast, H.; Ruedrich, J. Limestones in Germany used as building stones: An overview. *Geol. Soc. London, Spec. Publ.* **2010**, *331*, 37–59.

[225] Calvo, J. P.; Reguerio, M. Carbonate rocks in the Mediterranean region – From classical to innovative use of building stone. *Geol. Soc. London, Spec. Publ.* **2010**, *331*, 27–35.

[226] Ruedrich, J.; Kirchner, D.; Siegesmund, S. Physical weathering of building stones induced by freeze–thaw action: A laboratory long-term study. *Environ. Earth Sci.* **2011**, *63*, 1573–1586.

[227] Gázquez, F.; Rull, F.; Medina, J.; Sanz-Arranz, A.; Sanz, C. Linking groundwater pollution to the decay of 15th-century sculptures in Burgos Cathedral (northern Spain). *Environ. Sci. Pollut. Res.* **2015**, *22*, 15677–15689.

[228] Gómez-Laserna, O.; Prieto-Taboada, N.; Morillas, H.; Arrizabalaga, I.; Olazabal, M. A.; Arana, G.; Madariaga, J. M. Analytical study to evaluate the origin and severity of damage caused by salt weathering in a historical Palace House: The attack of infiltration water. *Anal. Methods* **2015**, *7*, 4608–4615.

[229] Brito, V.; Gonçalves, T. D. Drying kinetics of porous stones in the presence of NaCl and $NaNO_3$: Experimental assessment of the factors affecting liquid and vapour transport. *Transp. Porous Media* **2013**, *100*, 193–210.

[230] Lehmann, K. K.; Berden, G.; Engeln, R. In *Cavity Ring-Down Spectroscopy: Techniques and Applications*; Berden, G., Engeln, R., Eds.; Wiley, **2009**, Chapter 1, pp 1–26.

[231] Morville, J.; Romanini, D.; Kachanov, A. A.; Chenevier, M. Two schemes for trace detection using cavity ringdown spectroscopy. *Appl. Phys. B: Lasers Opt.* **2004**, *78*, 465–476.

[232] Chen, T.-L.; Ober, D. C.; Miri, R.; Bui, T. Q.; Shen, L.; Okumura, M. Optically switched dual-wavelength cavity ring-down spectrometer for high-precision isotope ratio measurements of methane δD in the near infrared. *Anal. Chem.* **2021**, *93*, 6375–6384.

[233] Ashton, M. The stratigraphy of the Lincolnshire Limestone Formation (Bajocian) in Linconshire and Rutland. *Proc. Geol. Assoc.* **1980**, *91*, 203–223.

[234] Emery, D.; Dickson, J. A. D. A syndepositional meteoric phreatic lens in the Middle Jurassic Lincolnshire Limestone, England, U.K. *Sediment. Geol.* **1989**, *65*, 273–284.

[235] Barron, A. J. M.; Lott, G. K.; Riding, J. B. *Stratigraphical framework for the Middle Jurassic strata of Great Britain and the adjoining continental shelf, RR/11/06*; British Geological Survey Research Report, **2012**.

[236] Mosthaf, K.; Helmig, R.; Or, D. Modeling and analysis of evaporation processes from porous media on the REV scale. *Water Resour. Res.* **2014**, *50*, 1059–1079.

[237] Zaknoune, A.; Glouannec, P.; Salagnac, P. Estimation of moisture transport coefficients in porous materials using experimental drying kinetics. *Heat Mass Transfer* **2012**, *48*, 205–215.

[238] Chabas, A.; Sizun, J. P.; Gentaz, L.; Uring, P.; Phan, A.; Coman, A.; Alfaro, S. C.; Saheb, M.; Pangui, E.; Zapf, P.; Huet, F. Water content of limestones submitted to realistic wet deposition: a CIME2 chamber simulation. *Environ. Sci. Pollut. Res.* **2018**, *25*, 23973–23985.

[239] Vuk, T.; Tinta, V.; Gabrovšek, R.; Kaučič, V. The effects of limestone addition, clinker type and fineness on properties of Portland cement. *Cem. Concr. Res.* **2001**, *31*, 135–139.

[240] Browne, D. E.; Peverall, R.; Ritchie, G. A. D.; Viles, H. A. Determining water transport kinetics in limestone by dual-wavelength cavity ring-down spectroscopy. *Anal. Chem.* **2022**, *94*, 3126–3134.

[241] Ioannou, I.; Charalambous, C.; Hall, C. The temperature variation of the water sorptivity of construction materials. *Mater. Struct.* **2017**, *50*, 208.

[242] Hall, C.; Pugsley, V. Spontaneous capillary imbibition of water and nonaqueous liquids into dry quarry limestones. *Trans. Porous Med.* **2020**, *135*, 619–631.

[243] Wang, Y.; Viles, H.; Desarnaud, J.; Yang, S.; Guo, Q. Laboratory simulation of salt weathering under moderate ageing conditions: Implications for the deterioration of sandstone heritage in temperate climates. *Earth Surf. Processes Landforms* **2021**, *46*, 1055–1066.

[244] Thomas, I. *Strategic Stone Study: A Building Stone Atlas of Derbyshire and the Peak National Park*; Historic England, **2017**.

[245] Lott, G. Geology and building stones in the East Midlands. *Mercian Geol.* **2001**, *15*, 97–122.

[246] Dubelaar, C. W.; Engering, S.; van Hees, R. P. J.; Koch, R.; Lorenz, H.-G. Lithofacies and petrophysical properties of Portland Base Bed and Portland Whit Bed limestone as related to durability. *Heron* **2003**, *48*, 221–229.

[247] Allen Howe, J. *The Geology of Building Stones*; Arnold's Geological Series; Edward Arnold, London, **1910**, Vol. 4; Chapter 6, pp 173–272.

[248] Schaffer, R. J. II. The weathering, preservation and restoration of stone buildings. *J. R. Soc. Arts* **1955**, *103*, 843–867.

[249] Palmer, T. Limestone petrography and durability in English Jurassic freestones. In *Proceedings of England's Heritage in Stone.* **2005**, pp 65 –78.

[250] Eyssautier-Chuine, S.; Vaillant-Gaveau, N.; Charpentier, E.; Reffuveille, F. Comparison of biofilm development on three building and restoration stones used in French monuments. *Int. Biodeterior. Biodegrad.* **2021**, *165*, 105322.

[251] Boone, M. A.; De Kock, T.; Bultreys, T.; De Schutter, G.; Vontobel, P.; Van Hoorebeke, L.; Cnudde, V. 3D mapping of water in oolithic limestone at atmospheric and vacuum saturation using X-ray micro-CT differential imaging. *Mater. Charact.* **2014**, *97*, 150–160.

[252] Pichler, C.; Lacker, R.; Bader, T.; Perfler, L. Water vapor diffusion properties of Obernkirchener sandstone: Analysis of DVS data. *Constr. Build. Mater.* **2022**, *347*, 128554.

[253] Ben Nasrallah, S.; Perre, P. Detailed study of a model of heat and mass transfer during convective drying of porous media. *Int. J. Heat Mass Transfer* **1988**, *31*, 957–967.

[254] Gualtieri, A. F.; Ricchi, A.; Lassinantti Gualtieri, M.; Maretti, S.; Tamburini, M. Kinetic study of the drying process of clay bricks. *J. Therm. Anal. Calorim.* **2016**, *123*, 153–167.

[255] Ioannou, I.; Hoff, W. D.; Hall, C. On the role of organic adlayers in the anomalous water sorptivity of Lépine limestone. *J. Colloid Interface Sci.* **2004**, *279*, 228–234.

[256] Zhu, J.; Zhang, P.; Ding, J.; Dong, Y.; Cao, Y.; Dong, W.; Zhao, X.; Li, X.; Camaiti, M. Nano $Ca(OH)_2$: A review on synthesis, properties and applications. *J. Cult. Herit.* **2021**, *50*, 25–42.

[257] Camerini, R.; Poggi, G.; Chelazzi, D.; Ridi, F.; Giorgi, R.; Baglioni, P. The carbonation kinetics of calcium hydroxide nanoparticles: A boundary nucleation and growth description. *J. Colloid Interface Sci.* **2019**, *547*, 370–381.

[258] Nuño, M.; Pesce, G. L.; Bowen, C. R.; Xenophontos, P.; Ball, R. J. Environmental performance of nano-structured $Ca(OH)_2/TiO_2$ photocatalytic coatings for buildings. *Build. Environ.* **2015**, *92*, 734–742.

[259] Samanta, A.; Chanda, D. K.; Das, P.; Ghosh, J.; Mukhopadhyay, A.; Dey, A. Synthesis of nano calcium hydroxide in aqueous medium. *J. Am. Ceram. Soc.* **2016**, *99*, 787–795.

[260] Taglieri, G.; Daniele, V.; Macera, L.; Mondelli, C. Nano $Ca(OH)_2$ synthesis using a cost-effective and innovative method: Reactivity study. *J. Am. Ceram. Soc.* **2017**, *100*, 5766–5778.

[261] Martínez-Ramírez, S.; Higueruela, L. R.; Cascales, I.; Martín-Garrido, M.; Blaco-Varela, M. T. New approach to nanolime synthesis at ambient temperature. *SN Appl. Sci.* **2019**, *1*, 105.

[262] Ševčík, R.; Viani, A.; Machová, D.; Lanzafame, G.; Mancini, L.; Appavou, M. S. Synthetic calcium carbonate improves the effectiveness of treatments with nanolime to contrast decay in highly porous limestone. *Sci. Rep.* **2019**, *9*, 1–13.

[263] Daniele, V.; Taglieri, G.; Macera, L.; Rosatelli, G.; Otero, J.; Charola, A. Green approach for an eco-compatible consolidation of the Agrigento biocalcarenites surface. *Constr. Build. Mater.* **2018**, *186*, 1188–1199.

[264] Macera, L.; Daniele, V.; Duchetta, F.; Casciardi, S.; Taglieri, G. New nanolimes for eco-friendly and customized treatments to preserve the biocalcarenites of the "Valley of Temples" of Agrigento. *Constr. Build. Mater.* **2021**, *306*, 124811.

[265] Elert, K.; Jroundi, F.; Benavides-Reyes, C.; Correa Gómez, E.; Gulotta, D.; Rodriguez-Navarro, C. Consolidation of clay-rich earthen building materials: A comparative study at the Alhambra fortress (Spain). *J. Build. Eng.* **2022**, *50*, 104081.

[266] Zornoza-Indart, A.; López-Arce, P.; Gomez-Villalba, L.; Varas-Muriel, M.; Fort, R. Consolidation of deteriorated carbonate stones with $Ca(OH)_2$ nanoparticles. In *12th International Congress on the deterioration and conservation of stone.* **2012**.

[267] Browne, D. E.; Peverall, R.; Ritchie, G. A. D.; Viles, H. A. Direct monitoring of drying kinetics of building limestones using cavity ring-down spectroscopy. *Constr. Build. Mater.* **2023**, *369*, 130554.

[268] Ziegenbalg, G.; Dietze, C.; Ziegenbalg, G. *Nanomaterials in Architecture and Art Conservation*, 1st ed.; Pan Standford Publishing, **2018**, Chapter 4, pp 131–166.

[269] ISO/CIE 11664-4:2019(E) *Colorimetry — Part 4: CIE 1976 L*a*b* colour space*; International Organization for Standardization: Geneva, Switzerland, **2019**.

[270] INNOWEP *TRACEiT® User Manual*; INNOWEP GmbH, **2015**.

[271] Gadelmawla, E. S.; Koura, M.; Maksoud, T.; Elewa, I.; Soliman, H. Roughness parameters. *J. Mater. Process. Technol.* **2002**, *123*, 133–145.

[272] BS EN 12407:2007 *Natural stone test methods – Petrographic examination*; British Standards Institution, **2007**.

[273] Kaszowska, Z.; Malek, K.; Staniszewska-Slezak, E.; Niedzielska, K. Raman scattering or fluorescence emission? Raman spectroscopy study on lime-based building and conservation materials. *Spectrochim. Acta, Part A* **2016**, *169*, 7–15.

[274] Mokrzycki, W. S.; Tatol, M. Colour difference ΔE – A survey. *Mach. Graph. Vis.* **2011**, *20*, 383–411.

[275] Künzel, H. M. *Simultaneous Heat and Moisture Transport in Building Components: One- and two-dimensional calculation using simple parameters*; Fraunhofer IRB, **1995**.

[276] Collin, F.; Chambon, R.; Charlier, R. A finite element method for poro mechanical modelling of geotechnical problems using local second gradient models. *Int. J. Numer. Methods Eng.* **2006**, *65*, 1749–1772.

[277] Physibel GLASTA diffusion-condensation-drying extended glaser method. https://www.physibel.be/en/products/glasta, **2007**, Accessed: 13 February 2023.

[278] Parkhurst, D. L.; Appelo, C. A. J. *Description of input and examples for PHREEQC version 3: a computer program for speciation, batch-reaction, one-dimensional transport, and inverse geochemical calculations*; U.S. Geological Survey Report, **2013**, pp 519.

[279] Riley, K. F.; Hobson, M. P.; Bence, S. *Mathematical Methods for Physics and Engineering*; Cambridge University Press, **2006**, Chapter 5, pp 151–186.

Appendix A

Supplementary Information – Gas and liquid transport in porous media

A.1 Derivation of the Langmuir isotherm

The Langmuir isotherm, described in Section 2.1.3, has two key assumptions[153]:

(a) Adsorption of a gas molecule can only occur at a finite number of sites on the surface of the solid, *i.e.*, only monolayer coverage is possible – This assumes that the surface is atomic in structure with potential energy wells as the sites of adsorption. If the depth of the wells $\ll k_B T$ then the assumption will break down;

(b) The ability for a gas molecule to bind to a site is independent of neighbouring molecules and the quantum states of the molecule are the same for all sites – If the adsorbed molecules have significant attractive or repulsive interactions, or the surface is significantly heterogeneous, this assumption will break down.

The Langmuir isotherm can be derived from statistical thermodynamics as follows[153]:

Let the fractional coverage of a surface, θ be given by $\theta = n/N$, where n is the total number of gas molecules adsorbed and N is the total number of available sites. The entropy (per mole) for molecules in the gas phase can be represented as S_g while for the adsorbed molecules it will be S. Thus, the total entropy change for adsorption must take into account the moles of adsorbed gas (n/N_A), the difference in entropies between the gas and adsorbed phase, and account for the configurational entropy

which is a result of the number of arrangements of n molecules on N sites. Therefore, the total entropy change for adsorption is given by:

$$\Delta S = \frac{n}{N_A}(S - S_g) + k_B \ln \Omega_c \tag{A.1}$$

where Ω_c is the number of arrangements of n molecules on N sites, that is:

$$\Omega_c = \frac{N!}{n!(N-n)!} \tag{A.2}$$

If the number of adsorbed molecules increases by $\mathrm{d}n$ then the entropy of the adsorbed layer will increase by $(\partial \Delta S/\partial n)\mathrm{d}n$. Assuming the entropy is independent of the fractional surface coverage, θ, and using Stirling's theorem [279], $\ln n! \approx n \ln n - n$, the differential entropy per mole, ΔS_m, is therefore given by:

$$\Delta S_m = S - S_g - R \ln \frac{\theta}{1-\theta} \tag{A.3}$$

Let the chemical potential of the adsorbed layer be given by μ and that of the gas be given by μ_g. Assuming the molar enthalpy of adsorption, ΔH_m, is also independent of θ and the pressure, P, if it is a perfect gas, then the molar Gibbs free energy of adsorption can be given by:

$$\begin{aligned} \mu - \mu_g &= \Delta H_m - T\Delta S_m \\ &= \Delta H_m - T(S - S_g) + RT \ln \frac{\theta}{1-\theta} \end{aligned} \tag{A.4}$$

Equilibrium between adsorption and desorption occurs at pressure P_θ and the corresponding chemical potential of the gas is given by $\mu(P_\theta)$. Thus, for a perfect gas at equilibrium:

$$\mu = \mu_g + RT \ln P_\theta \tag{A.5}$$

Combining Equations A.4 and A.5, therefore, results in the following expression:

$$P_\theta = \frac{\theta}{1-\theta} \exp\left(\frac{\Delta H_m}{RT} - \frac{S - S_g}{R}\right) \tag{A.6}$$

which may be rearranged, assuming ΔH_m and S are independent of θ, to:

$$\theta = \frac{KP_\theta}{1 + KP_\theta} \tag{A.7}$$

which is the Langmuir isotherm where K is the equilibrium constant.

A.2 Mercury intrusion porosimetry measurements

Mercury intrusion porosimetry measurements were obtained by the British Geological Survey for all the stone samples used in this thesis, and the pore size distributions, shown in Figure A.1, were determined using the method described in Section 2.3.2.

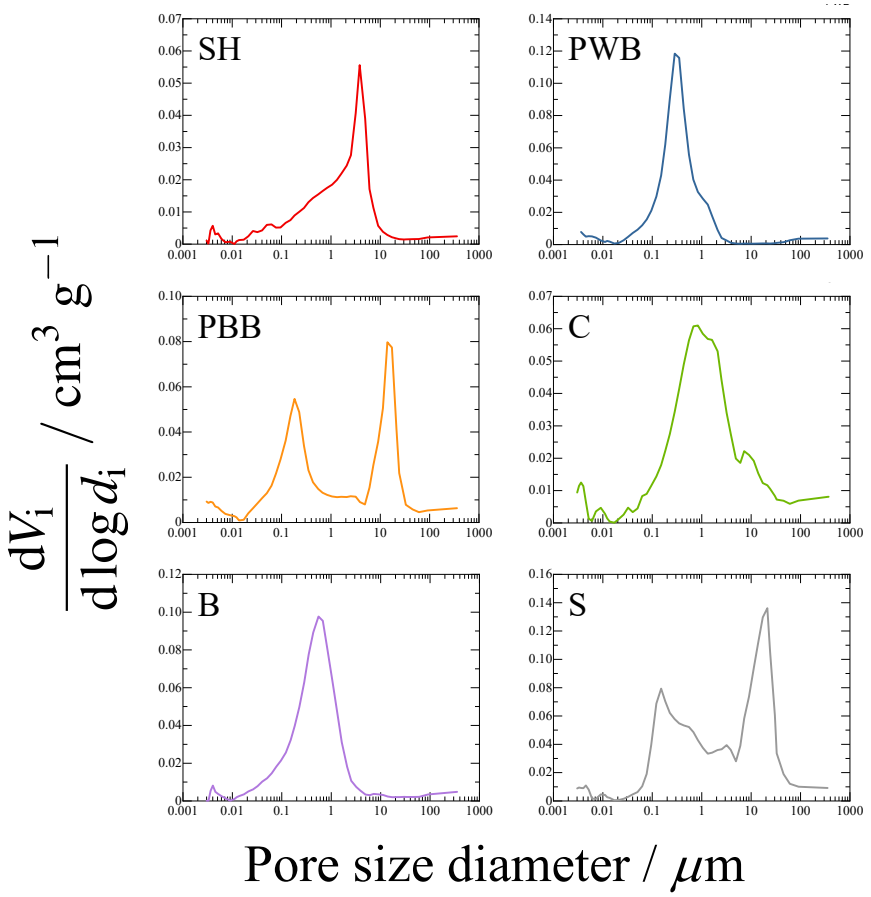


Figure A.1: Pore size distributions of stone samples investigated in this thesis, obtained by mercury intrusion porosimetry. Note: SH = Stoke Hall sandstone; PWB = Portland Whit Bed limestone; PBB = Portland Base Bed limestone; C = Clipsham limestone; B = Bath limestone; S = Savonnières limestone.

A.3 Nitrogen adsorption measurements

Nitrogen adsorption measurements for all the stone samples used in this thesis were procured by the Surface Analysis Facility, University of Oxford, and the pore size distributions were determined using the Barrett, Joyer and Halenda method[194] described in Section 2.3.2 and are shown in Figure A.2.

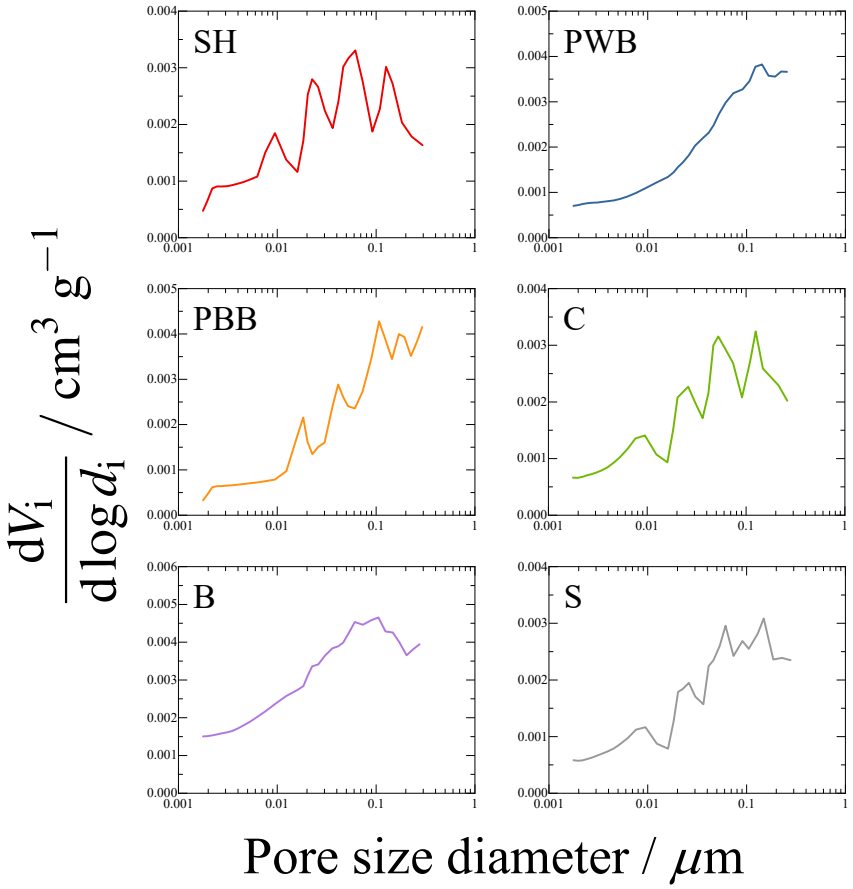


Figure A.2: Pore size distributions of stone samples investigated in this thesis, obtained by N_2 adsorption. Note: SH = Stoke Hall sandstone; PWB = Portland Whit Bed limestone; PBB = Portland Base Bed limestone; C = Clipsham limestone; B = Bath limestone; S = Savonnières limestone.

Appendix B

Supplementary Information – Determining water transport kinetics in limestone by dual-wavelength cavity ring-down spectroscopy

B.1 Stone samples: Clipsham limestone

This study investigated the use of CRDS to monitor moisture release using Clipsham limestone as the exemplar limestone. Mercury intrusion porosimetry[188] was carried out by the British Geological Survey to characterise the internal structure of the stone, and determine the open porosity of the sample. The pore size distribution is presented in Figure B.1 and shows that the Clipsham limestone used in this study has a unimodal pore distribution, with a median pore diameter of 1.18 μm. The Clipsham limestone samples have a density of 2.69 g mL^{-1} and an open porosity of 20.39 %.

B.2 Spectroscopic nomenclature

Water is an asymmetric top molecule, with three unique moments of inertia. The rotational levels for water are reported in terms of J, the total angular momentum quantum number, K_a, the projection quantum number along the a axis, and K_c, the projection quantum number along the c axis. Water has three vibrational modes: ν_1 is the symmetric stretch, ν_2 is the symmetric bend and ν_3 is the asymmetric stretch. The ro-vibrational transitions are reported by the angular momentum and vibrational

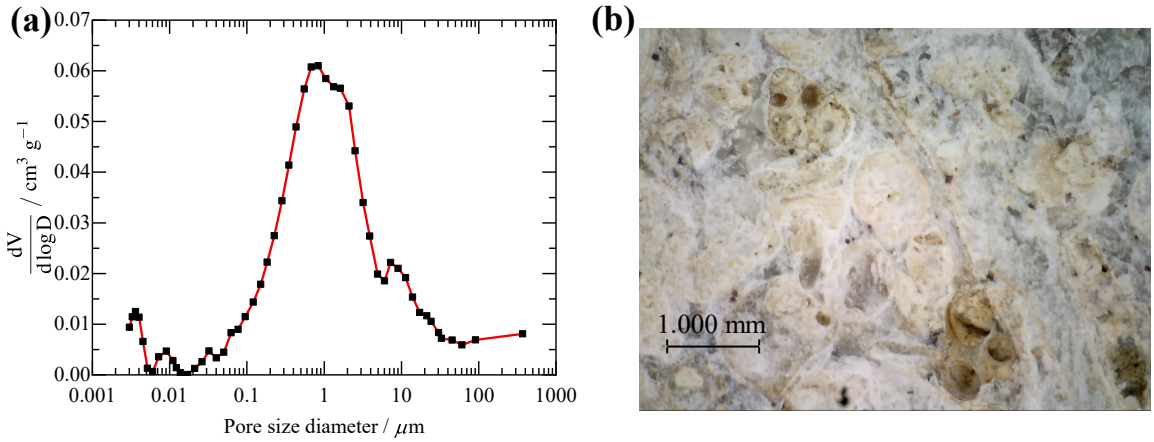


Figure B.1: **(a)**Pore size distribution of Clipsham obtained by mercury intrusion porosimetry carried out by the British Geological Survey. **(b)** Micrograph of Clipsham limestone.

quantum numbers of the lower and upper levels as the following:

$$J', K'_a, K'_c\ (\nu'_1\ \nu'_2\ \nu'_3)\ \leftarrow\ J'', K''_a, K''_c\ (\nu''_1\ \nu''_2\ \nu''_3) \tag{B.1}$$

The transitions of interest in this work are the:

- H_2O 10,3,7 (021) $\leftarrow$ 11,3,8 (000) transition at 6638.91 cm^{-1};
- H_2O 6,0,6(031) $\leftarrow$ 7,0,7(010) transition at 6636.60 cm^{-1};
- HDO 8,6,2(210) $\leftarrow$ 9,6,3(000) transition at 6638.17 cm^{-1}.

B.3 Wavelength calibration

The emission wavelength of the DFB laser is strongly dependent on its temperature and operating current, and in this experiment the fine tuning of the wavelength was made by controlling the laser temperature. Wavelength calibration has been carried out using a Burleigh WA-1000 wavemeter at constant laser drive current of 120 mA. This is shown in Figure B.2.

B.4 Reproducibility

To test the reproducibility of the CRDS measurement, and also variation between samples of the same limestone, the experiment of measuring α_p as a function of time

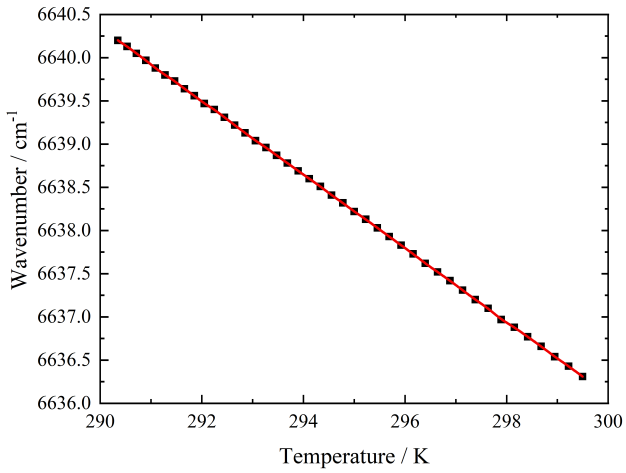


Figure B.2: Wavelength calibration curve for the 1506 nm DFB laser as a function of temperature, measured at constant current of 120 mA. This was measured using the Burleigh WA-1000 wavemeter and fitted with a fourth order polynomial.

with a 1.5 slm dry N_2 flow was repeated with four *ca.* $25 \times 25 \times 5$ mm Clipsham limestone samples. Figure B.3 shows the normalised mass difference curves for the four samples. As expected there are slight variations due to differences between the samples but overall good agreement between the different parameters determined.

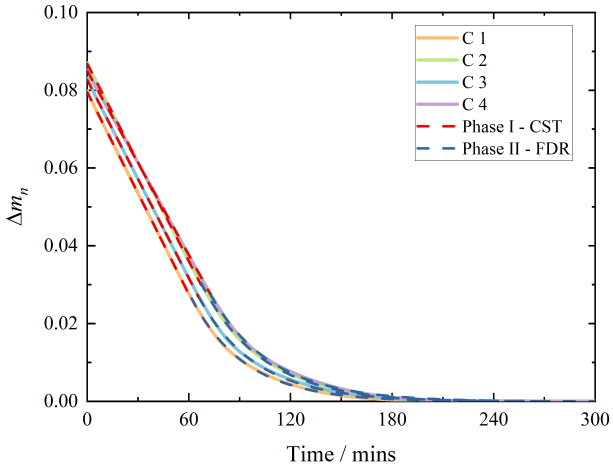


Figure B.3: A plot of normalised mass difference as a function of time for four *ca.* $25 \times 25 \times 5$ mm samples of Clipsham limestone drying under a constant 1.5 slm N_2 flow.

B.5 Phase II diffusivity and % relative humidity

Phase II diffusivity is determined by unsaturated flow within the material[90] and D_{II} can therefore be determined from a linear relationship between the logarithmic terms and time[150]:

$$\ln\left(1-\frac{m_{\mathrm{H_2O}}(t)}{m_{\mathrm{H_2O}}(\infty)}\right)-\ln\left(\frac{8}{\pi^2}\right)=-\frac{D_{\mathrm{II}}\pi^2 t}{4L^2} \tag{B.2}$$

Figure B.4 shows D_{II} as a function of % relative humidity for the HDO 8,6,2(210) ← 9,6,3(000) transition at 6638.17 cm^{-1}, measured for two *ca.* $25 \times 25 \times 5$ mm samples of Clipsham limestone. The results shown in Figure B.4 indicate that D_{II}(HDO) decreases with increasing humidity, implying that the external conditions still have an influence on the drying behaviour observed during phase II. Thus, this raises a question about the interpretation of the later drying times, especially with increasing % *RH*.

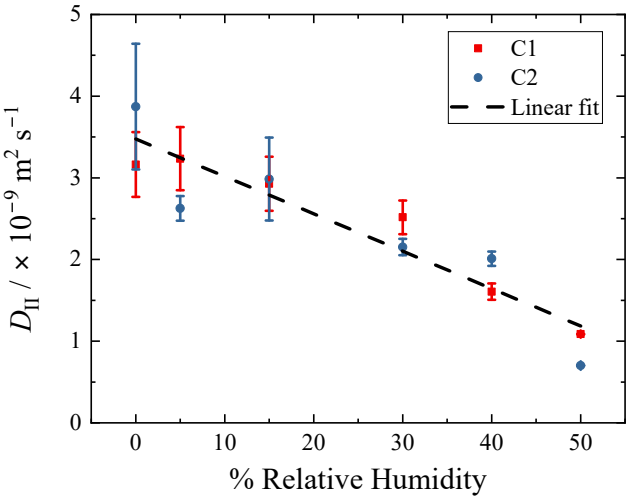


Figure B.4: A plot of the phase II diffusivity, D_{II}, as a function of increasing humidity for two samples of *ca.* $25 \times 25 \times 5$ mm Clipsham limestone samples.

Appendix C

Supplementary Information – Investigating the effect of nanolime treatment on the drying kinetics of Clipsham limestone

C.1 Scanning electron microscopy results

The surface topographies of a control sample (C0), *E5* sample (C2) and *E25* sample (C6) were studied using a scanning electron microscope (JEOL JSM6010). The samples were sputter coated with carbon.

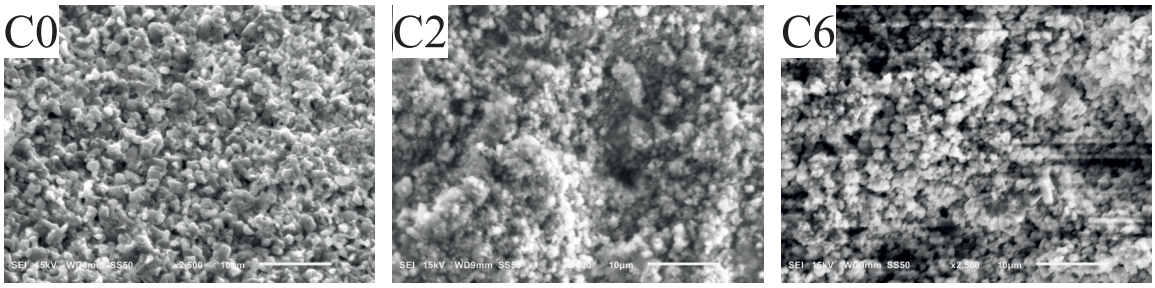


Figure C.1: Scanning electron microscopy images of a control sample (C0), E5 sample (C2) and E25 sample (C6) after 28 day curing period at $T = 20$ °C, 75 % *RH*.

C.2 Sample variation and reproducibility of the drying kinetics

The drying kinetic parameters for four different samples of Clipsham limestone, all *ca.* $25 \times 25 \times 5$ mm, drying under a constant dry 1.5 slm N_2 flow at $T = 25$ °C, before and after treatment with *E5* and *E25* are reported in Tables C.1 and C.2, respectively.

Table C.1: Sample variation, pre- and post-treatment with *E5*.

	Sample	C1	C2	C3	C4
Untreated	$m_{H_2O}(\infty)$ / g	0.328 $\pm$ 0.001	0.486 $\pm$ 0.001	0.550 $\pm$ 0.001	0.388 $\pm$ 0.001
	t_c / min	44.02 $\pm$ 2.46	54.11 $\pm$ 0.87	69.70 $\pm$ 0.71	51.80 $\pm$ 0.91
	$\dot{m}_{CST}$ / kg m^{-2} s^{-1}	$1.29 \times 10^{-4} \pm 9 \times 10^{-6}$	$1.45 \times 10^{-4} \pm 9 \times 10^{-6}$	$1.31 \times 10^{-4} \pm 9 \times 10^{-6}$	$1.24 \times 10^{-4} \pm 9 \times 10^{-6}$
	D_{II} / m^2 s^{-1}	$3.422 \times 10^{-9} \pm 1.6 \times 10^{-11}$	$4.465 \times 10^{-9} \pm 4 \times 10^{-12}$	$4.699 \times 10^{-9} \pm 5 \times 10^{-12}$	$4.802 \times 10^{-9} \pm 5 \times 10^{-12}$
Treated	$m_{H_2O}(\infty)$ / g	0.329 $\pm$ 0.001	0.497 $\pm$ 0.001	0.547 $\pm$ 0.001	0.386 $\pm$ 0.001
	t_c / min	43.90 $\pm$ 2.71	55.78 $\pm$ 0.53	60.27 $\pm$ 0.67	41.52 $\pm$ 0.60
	$\dot{m}_{CST}$ / kg m^{-2} s^{-1}	$1.25 \times 10^{-4} \pm 9 \times 10^{-6}$	$1.45 \times 10^{-4} \pm 9 \times 10^{-6}$	$1.44 \times 10^{-4} \pm 9 \times 10^{-6}$	$1.45 \times 10^{-4} \pm 9 \times 10^{-6}$
	D_{II} / m^2 s^{-1}	$3.277 \times 10^{-9} \pm 1.2 \times 10^{-11}$	$4.597 \times 10^{-9} \pm 5 \times 10^{-12}$	$4.589 \times 10^{-9} \pm 5 \times 10^{-12}$	$4.865 \times 10^{-9} \pm 4 \times 10^{-12}$

Table C.2: Sample variation, pre- and post-treatment with *E25*.

	Sample	C5	C6	C7	C8
Untreated	$m_{H_2O}(\infty)$ / g	0.320 $\pm$ 0.001	0.534 $\pm$ 0.001	0.564 $\pm$ 0.001	0.517 $\pm$ 0.001
	t_c / min	30.17 $\pm$ 3.32	72.53 $\pm$ 0.72	85.24 $\pm$ 0.71	67.49 $\pm$ 0.92
	$\dot{m}_{CST}$ / kg m^{-2} s^{-1}	$1.31 \times 10^{-4} \pm 9 \times 10^{-6}$	$1.25 \times 10^{-4} \pm 9 \times 10^{-6}$	$1.16 \times 10^{-4} \pm 9 \times 10^{-6}$	$1.16 \times 10^{-4} \pm 9 \times 10^{-6}$
	D_{II} / m^2 s^{-1}	$3.783 \times 10^{-9} \pm 9 \times 10^{-12}$	$4.565 \times 10^{-9} \pm 6 \times 10^{-12}$	$4.728 \times 10^{-9} \pm 3 \times 10^{-12}$	$4.102 \times 10^{-9} \pm 5 \times 10^{-12}$
Treated	$m_{H_2O}(\infty)$ / g	0.370 $\pm$ 0.001	0.503 $\pm$ 0.001	0.529 $\pm$ 0.001	0.533 $\pm$ 0.001
	t_c / min	52.51 $\pm$ 2.98	59.60 $\pm$ 0.39	61.55 $\pm$ 0.54	56.24 $\pm$ 0.47
	$\dot{m}_{CST}$ / kg m^{-2} s^{-1}	$1.22 \times 10^{-4} \pm 9 \times 10^{-6}$	$1.38 \times 10^{-4} \pm 9 \times 10^{-6}$	$1.37 \times 10^{-4} \pm 9 \times 10^{-6}$	$1.37 \times 10^{-4} \pm 9 \times 10^{-6}$
	D_{II} / m^2 s^{-1}	$3.467 \times 10^{-9} \pm 1.7 \times 10^{-11}$	$4.631 \times 10^{-9} \pm 5 \times 10^{-12}$	$4.713 \times 10^{-9} \pm 4 \times 10^{-12}$	$4.863 \times 10^{-9} \pm 5 \times 10^{-12}$

C.3 Temperature dependence of the drying kinetics

The drying kinetic parameters for two different Clipsham limestone samples, *ca.* $25 \times 25 \times 5$ mm, drying under a constant dry 1.5 slm N_2 flow with increasing temperature, before and after treatment with *E5* and *E25* are reported in Tables C.3 and C.4, respectively.

Table C.3: Temperature dependence for pre- and post-consolidation with *E5*.

Temperature / ℃	20	25	30	35	40
$m_{H_2O}(\infty)$ / g	0.347 ±0.001	0.328 ±0.001	0.327 ±0.001	0.347 ±0.001	0.323 ±0.001
t_c / min	71.82 ±3.08	44.02 ±2.46	32.16 ±2.14	28.71 ±1.73	20.99 ±1.33
$\dot{m}_{CST}$ / kg m^{-2} s^{-1}	8.4×10^{-5} $\pm 9 \times 10^{-6}$	1.29×10^{-4} $\pm 9 \times 10^{-6}$	1.69×10^{-4} $\pm 9 \times 10^{-6}$	1.96×10^{-4} $\pm 9 \times 10^{-6}$	2.29×10^{-4} $\pm 9 \times 10^{-6}$
D_{II} / m^2 s^{-1}	2.728×10^{-9} $\pm 9 \times 10^{-12}$	3.422×10^{-9} $\pm 1.6 \times 10^{-11}$	4.197×10^{-9} $\pm 1.45 \times 10^{-11}$	5.093×10^{-9} $\pm 2.4 \times 10^{-11}$	6.021×10^{-9} $\pm 2.0 \times 10^{-11}$
E_a / kJ mol^{-1}			30.30 ± 0.60		

(a) Untreated

Temperature / ℃	20	25	30	35	40
$m_{H_2O}(\infty)$ / g	0.322 ±0.001	0.329 ±0.001	0.311 ±0.001	0.329 ±0.001	0.345 ±0.001
t_c / min	73.23 ±4.11	43.90 ±2.71	34.02 ±5.84	26.68 ±1.98	24.29 ±1.89
$\dot{m}_{CST}$ / kg m^{-2} s^{-1}	8.2×10^{-5} $\pm 9 \times 10^{-6}$	1.25×10^{-4} $\pm 9 \times 10^{-6}$	1.49×10^{-4} $\pm 9 \times 10^{-6}$	1.97×10^{-4} $\pm 9 \times 10^{-6}$	2.37×10^{-4} $\pm 9 \times 10^{-6}$
D_{II} / m^2 s^{-1}	2.710×10^{-9} $\pm 6 \times 10^{-12}$	3.277×10^{-9} $\pm 1.2 \times 10^{-11}$	4.203×10^{-9} $\pm 1.8 \times 10^{-11}$	5.018×10^{-9} $\pm 2.2 \times 10^{-11}$	5.913×10^{-9} $\pm 1.4 \times 10^{-11}$
E_a / kJ mol^{-1}			30.00 ± 0.71		

(b) Treated with *E5*

Table C.4: Temperature dependence for pre- and post-consolidation with *E25*.

Temperature / ℃	20	25	30	35	40
$m_{H_2O}(\infty)$ / g	0.376 ±0.001	0.320 ±0.001	0.368 ±0.001	0.318 ±0.001	0.335 ±0.001
t_c / min	82.73 ±4.97	30.17 ±3.32	32.79 ±2.84	21.67 ±4.21	23.35 ±2.67
$\dot{m}_{CST}$ / kg m^{-2} s^{-1}	8.3×10^{-5} $\pm\ 9 \times 10^{-6}$	1.31×10^{-4} $\pm\ 9 \times 10^{-6}$	1.59×10^{-4} $\pm\ 9 \times 10^{-6}$	1.93×10^{-4} $\pm\ 9 \times 10^{-6}$	2.31×10^{-4} $\pm\ 9 \times 10^{-6}$
D_{II} / m^2 s^{-1}	2.700×10^{-9} $\pm 8 \times 10^{-12}$	3.783×10^{-9} $\pm 9 \times 10^{-12}$	4.444×10^{-9} $\pm 1.8 \times 10^{-11}$	5.516×10^{-9} $\pm 1.0 \times 10^{-11}$	6.421×10^{-9} $\pm 7 \times 10^{-12}$
E_a / kJ mol^{-1}			30.31 ± 2.07		

(a) Untreated

Temperature / ℃	20	25	30	35	40
$m_{H_2O}(\infty)$ / g	0.356 ±0.001	0.370 ±0.001	0.344 ±0.001	0.361 ±0.001	0.325 ±0.001
t_c / min	77.33 ±4.03	52.51 ±2.98	39.34 ±3.64	26.71 ±1.54	19.22 ±1.46
$\dot{m}_{CST}$ / kg m^{-2} s^{-1}	8.0×10^{-5} $\pm 9 \times 10^{-6}$	1.22×10^{-4} $\pm\ 9 \times 10^{-6}$	1.39×10^{-4} $\pm\ 9 \times 10^{-6}$	2.09×10^{-4} $\pm\ 9 \times 10^{-6}$	2.59×10^{-4} $\pm\ 9 \times 10^{-6}$
D_{II} / m^2 s^{-1}	2.793×10^{-9} $\pm 5 \times 10^{-12}$	3.467×10^{-9} $\pm 1.7 \times 10^{-11}$	4.373×10^{-9} $\pm 1.0 \times 10^{-11}$	5.197×10^{-9} $\pm 1.5 \times 10^{-11}$	6.133×10^{-9} $\pm 2.1 \times 10^{-11}$
E_a / kJ mol^{-1}			30.77 ± 1.00		

(b) Treated with *E25*

Appendix D

Statements of authorship for multi-authored papers

This appendix includes signed statements from co-authors of the papers included in this thesis confirming that, as represented by first authorship, the candidate has made a substantive contribution to each publication.

Statement of Authorship for multi-authored papers

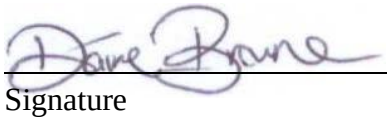
Title of Paper: Determining Water Transport Kinetics in Limestone by Dual-Wavelength Cavity Ring-Down Spectroscopy

Publication Status: Published

Publication Details: Dáire E. Browne, Robert Peverall, Grant A. D. Ritchie and Heather A. Viles, "Determining Water Transport Kinetics in Limestone by Dual-Wavelength Cavity Ring-Down Spectroscopy", *Analytical Chemistry*, **2022**, *94*, 3126 – 3134.

Student Confirmation
Student Name: Dáire E. Browne

Contribution to the paper: Methodology, validation, data acquisition and analysis, interpretation and visualisation of data, manuscript preparation and final editing.



Signature 27/02/2023 Date

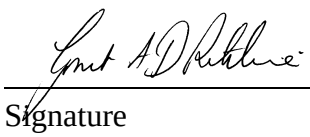
Co-authors confirmation
By signing the Statement of Authorship, you are certifying that the candidate made a substantial contribution to the publication, and that the description above is accurate.

Co-author name and title: Dr. Robert Peverall, Senior Research Fellow, Physical and Theoretical Chemistry, Department of Chemistry, University of Oxford



Signature 27/02/2023 Date

Co-author name and title: Professor Grant Ritchie, Head of Physical and Theoretical Chemistry, Department of Chemistry, University of Oxford



Signature 01/03/2023 Date

Co-author name and title: Professor Heather Viles, Professor of Biogeomorphology and Heritage Conservation, School of Geography and the Environment, University of Oxford



Signature 01/03/2023 Date

Statement of Authorship for multi-authored papers

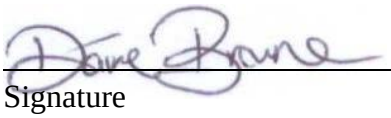
Title of Paper: Direct monitoring of drying kinetics of building limestones using cavity ring-down spectroscopy

Publication Status: Published

Publication Details: Dáire E. Browne, Robert Peverall, Grant A. D. Ritchie and Heather A. Viles, "Direct monitoring of drying kinetics of building limestones using cavity ring-down spectroscopy", *Construction and Building Materials*, **2023**, *369*, 130554.

Student Confirmation
Student Name: Dáire E. Browne

Contribution to the paper: Methodology, validation, data acquisition and analysis, interpretation and visualisation of data, manuscript preparation and final editing.



Signature — Date: 27/02/2023

Co-authors confirmation
By signing the Statement of Authorship, you are certifying that the candidate made a substantial contribution to the publication, and that the description above is accurate.

Co-author name and title: Dr. Robert Peverall, Senior Research Fellow, Physical and Theoretical Chemistry, Department of Chemistry, University of Oxford



Signature — Date: 27/02/2023

Co-author name and title: Professor Grant Ritchie, Head of Physical and Theoretical Chemistry, Department of Chemistry, University of Oxford



Signature — Date: 01/03/2023

Co-author name and title: Professor Heather Viles, Professor of Biogeomorphology and Heritage Conservation, School of Geography and the Environment, University of Oxford



Signature — Date: 01/03/2023

Statement of Authorship for multi-authored papers

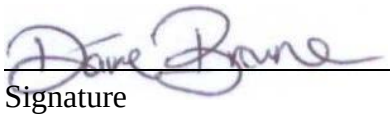
Title of Paper: Investigating the effect of nanolime treatment on the drying kinetics of Clipsham limestone

Publication Status: Published

Publication Details: Dáire E. Browne, Robert Peverall, Grant A. D. Ritchie and Heather A. Viles, "Investigating the effect of nanolime treatment on the drying kinetics of Clipsham limestone", *Heritage Science*, **2023**, *11*, 114

Student Confirmation
Student Name: Dáire E. Browne

Contribution to the paper: Methodology, validation, data acquisition and analysis, interpretation and visualisation of data, manuscript preparation and final editing.



Signature 23/05/2023 Date

Co-authors confirmation
By signing the Statement of Authorship, you are certifying that the candidate made a substantial contribution to the publication, and that the description above is accurate.

Co-author name and title: Dr. Robert Peverall, Senior Research Fellow, Physical and Theoretical Chemistry, Department of Chemistry, University of Oxford



Signature 23/05/2023 Date

Co-author name and title: Professor Grant Ritchie, Head of Physical and Theoretical Chemistry, Department of Chemistry, University of Oxford



Signature 23/05/2023 Date

Co-author name and title: Professor Heather Viles, Professor of Biogeomorphology and Heritage Conservation, School of Geography and the Environment, University of Oxford



Signature 23/05/2023 Date